MSc Thesis

Multidisciplinary Design Analysis and Optimisation of Inflatable Stacked Toroid Decelerators:

A Novel Framework Advancing Mars Exploration

Claudio Rapisarda

2023

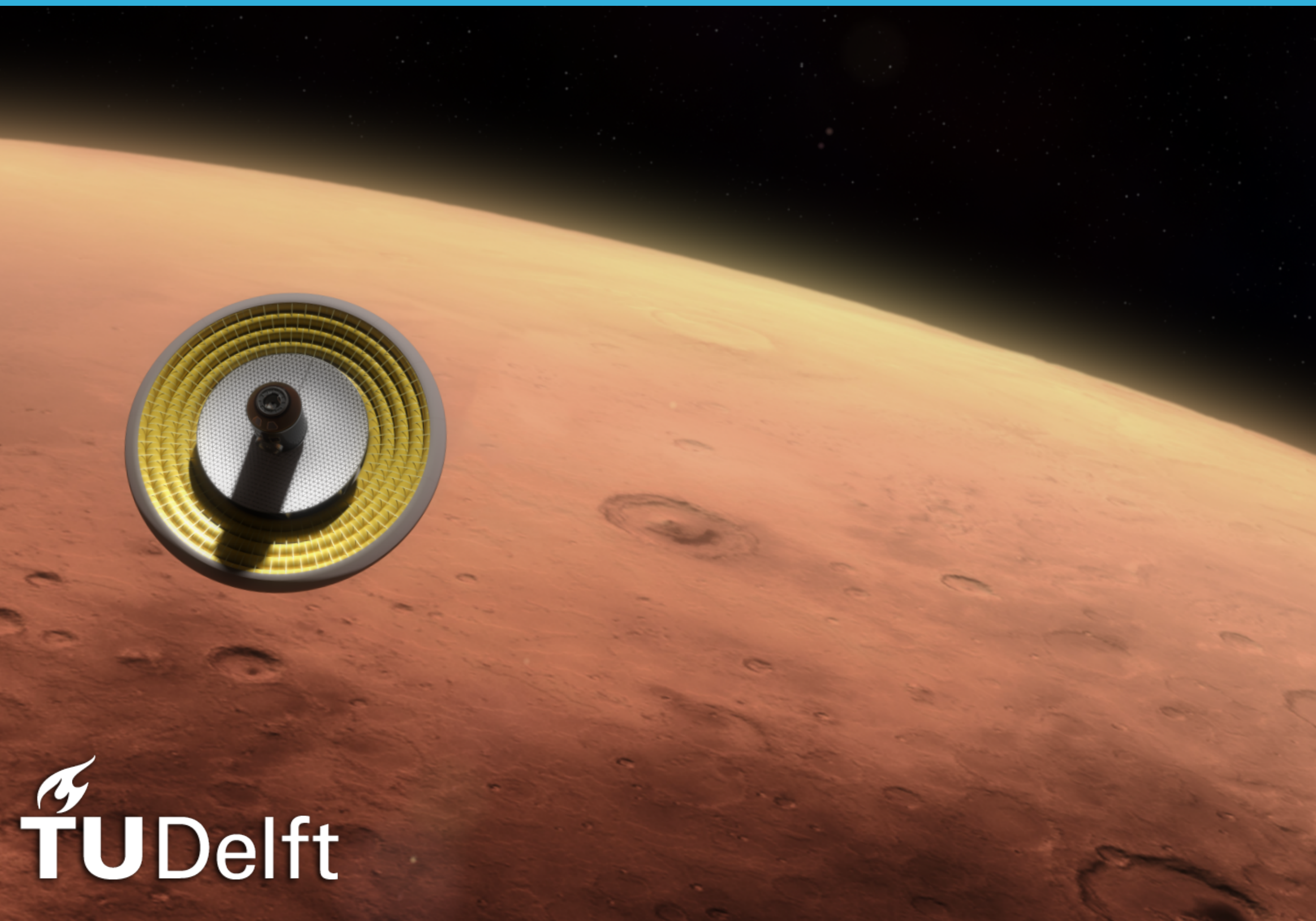

TU Delft

MSc Thesis

Multidisciplinary Design Analysis and Optimisation of Inflatable Stacked Toroid Decelerators: A Novel Framework Advancing Mars Exploration

Claudio Rapisarda

August 2023

A thesis submitted to the Delft University of Technology in partial fulfilment of the requirements for the degree of Master of Science in Aerospace Engineering

TU Delft

Dr. Angelo Cervone	Astrodynamics & Space Missions
Dr. Stefano Speretta	Space Systems Engineering
Dr. Jyoti Botchu	Space Systems Engineering

Claudio Rapisarda: Multidisciplinary Design Analysis and Optimisation of Inflatable Stacked Toroid Decelerators: A Novel Framework Advancing Mars Exploration (2023)

Executive Summary

The long-term exploration of Mars requires delivering scientific instruments to its surface for conducting investigations. Landing these instruments has been challenging due to constraints on payload mass, volume, and landing region requirements. The MiniPINS study proposes a solution using penetrating probes, also known as penetrators. These probes are designed to impact the planetary surface at relatively high velocities and then come to rest in the subsurface. Conventional heritage technologies for Mars Entry, Descent, and Landing (EDL) face limitations in landing larger payloads due to payload fairing or deployment constraints. However, a promising technology that has emerged in recent years is the inflatable stacked toroid decelerator. This innovative design involves stacking concentric bladders of toroidal shape with increasing diameter, which are then wrapped in a thermal protection layer to create a smooth surface.

Research studies have demonstrated that the flexible aeroshell shape significantly influences various design aspects of space entry vehicles. The aerothermal environment has a major impact on the design space, affecting the layout and design of the Flexible Thermal Protection System (F-TPS), as well as the aerodynamic characteristics that influence deceleration, maneuverability, trajectory shaping, and the resulting aerodynamic loading on the structural subsystem. Additionally, the flexibility of the aeroshell leads to deflections known as scallops, which alter the aerodynamic and aerothermal performance of the vehicle. To comprehensively explore the design of stacked toroid configurations for conceptual studies, considering the overall mission perspective and identifying the optimal design within given requirements and constraints, a Multidisciplinary Design Analysis and Optimization (MDAO) environment is needed. The objective of this work is to address the interconnected design dependencies among the identified disciplines by proposing a fully-integrated MDAO framework tailored specifically to the stacked toroid configuration.

To efficiently optimize the design of stacked toroid configurations, the framework employs parametric modelling, which allows for the effective use of gradient-based optimizers. The design space is divided into six key design variables: the half-cone angle, the number of tori, the inner tori radius, outer torus radius, payload height, and payload radius. A noteworthy addition to the design space is the outer torus radius, which was initially introduced in the IRVE-3 flight vehicle and later adopted for LOFTID and other conceptual vehicles. Including this variable as part of the design space contributes a novel aspect to the optimization process. This parametric approach facilitates the establishment of parametric constraints on the deployed and stowed dimensions of the decelerator. Analytical relations are also incorporated to determine the structural loading on the internal tori, the spar fabric, and the restraint wrap components. Furthermore, the structural mass of the stacked toroid is evaluated based on the specific inputs provided within the design space, utilizing a nondimensional mass model developed by NASA specifically for Inflatable Aerodynamic Decelerators (IADs). When compared to technologically-mature flight vehicles, the parametrization correctly models the aeroshell but generates slight discrepancies of 4-7.5% in the centre body when antennas or additional components are present.

The Mars Climate Database (MCD) v.6.1 is utilized to simulate the Mars atmosphere. This database incorporates mean solar conditions and provides averaged profiles of density, pressure,

and temperature across various latitudes and longitudes. To evaluate the entry trajectory of the vehicle, the atmospheric model is integrated with the planar equations of motion for a specified entry altitude, speed and angle. The planar trajectory is therefore successfully implemented, with errors between 2-7% compared to IRVE-II's flight trajectory.

To calculate the aerodynamic forces exerted on the decelerator, necessary for the equations of motion, the surface mesh generated during the parametrization process facilitates the application of local surface inclination panel methods. A shading algorithm is implemented to account for the presence of the centrebody. In the continuum regime, the modified Newtonian method is employed to determine the aerodynamic coefficients for each panel. The model performs well against numerical and flight data, showing errors lower than 3.4% in the hypersonic region and in the order of 18-28% at subsonic speeds. In rarefied conditions, several candidate models, including Sentman, Schaaf and Chambre, Cercignani-Lampsi-Lord, Storch and Cook's models, are initially considered to identify the most suitable one for the stacked toroid during the verification stages. Schaaf and Chambre's model emerges as the most suitable one as it presents the lowest percentage error when compared to higher fidelity data. For the transitional regime, Wilmoth's formula is employed to bridge the aerodynamic coefficients between continuum and rarefied regimes, unveiling excellent agreement with independent data over a wide range of angles of attack. Additionally, the aerostability of the decelerator is determined by analyzing the moment coefficients, ensuring a positive static margin to maintain stability during the entry phase. The adequacy of the model is verified for all flight regimes. Shortcomings are observed at 90° of angle of attack, but it is considered beyond the desired region of applicability.

The aerothermal discipline incorporates well-established and widely-used analytical relationships for stagnation-point heat flux, which have been extensively validated for entry applications and are documented in the literature. These relationships serve as a foundation for determining the convective heat flux. In the continuum regime, several models, including Fay-Riddell, Detra-Kemp-Riddell, Van-Driest, Chapman and Sutton, and Graves' models, are considered as candidates. From this set, the Sutton-Graves relation is chosen as it is the most conservative in terms of peak heat flux and heat load when compared to flight data. In rarefied conditions, Schaaf and Chambre's model is utilized as it is widely accepted in the field. Due to the lack of available aerothermal data in free-molecular flow, results are extrapolated from numerical databases, showing an error of approximately 11%. Transitioning between the continuum and rarefied regimes, the Wilmoth function is employed to bridge the heat transfer coefficient, which is directly related to the heat flux. The aerothermodynamic discipline incorporates validated engineering models to determine radiative heating for low and high entry speeds on Mars, with acceptable error levels for conceptual design stages mostly between 4% and 12%. The heat distribution is then evaluated based on the stagnation heat flux using the local inclination method. A combination of the SCARAB combination for the nose-cone and torus shoulder, along with the Krasnov correlation for conical shells, is integrated to account for the heat distribution across the decelerator's surface, showing improved correlations than SCARAB alone.

The framework introduces a novel aspect by addressing the scalloping effect, which significantly influences the aerodynamic and aerothermal performance of the decelerator. Unlike previous literature that assumes rigid models with no corrections, this framework incorporates corrective measures: empirically-fit polynomials dependent on the freestream dynamic pressure are proposed and validated to correct the aerodynamic coefficients. These polynomials are fitted based on dynamic pressure, allowing for accurate adjustments to the aerodynamic performance of the decelerator. The augmented heat flux is modelled by means of semi-empirical correlations retrieved from the literature as a function of the scallop depth.

The F-TPS is modelled using a 1D Finite Difference Method (FDM) explicit scheme that considers temperature-dependent thermal properties. The chosen layup, comprising Nicalon SiC, Pyrogel 3350, and Kapton, is selected based on its experimental qualification performance, allowing it to withstand heat fluxes ranging from 50-100 W/cm^2. Given the sharp variation in layer thickness across the F-TPS, harmonic weighted averaging is employed at the layer interfaces. Mean percentage errors lower than 9% are measured against experimental tests. This technique ensures an accurate representation of the thermal behavior and provides a more precise analysis. To minimise the F-TPS mass, an inner optimizer is employed, taking the heat flux history generated by the aerothermal discipline as input.

The framework is implemented in the context of a novel EDL architecture proposed for the MiniPINS mission. Building upon the MetNet heritage, adjustments are made to accommodate the use of stacked-toroid configurations, which offer significant advantages over conventional rigid entry capsules. The optimization problem aims to minimize the overall system mass, which includes both the structural mass and the F-TPS mass. To ensure feasibility and meet EDL requirements, the optimization process incorporates constraints related to stage deployment, impact speed, tank radius, structural loading, aerostability, and compliance with the launcher fairing. A combination of gradient-based and genetic algorithms is utilized to solve the outer optimization problem. These algorithms work synergistically to explore and exploit the design space efficiently, seeking the optimal solution that minimizes system mass while meeting all the specified constraints.

The results reveal that the optimization successfully converges and that all constraints are satisfied. The genetic algorithm rapidly narrows down the design search within 15 generations but converges to a near global optimum. A gradient-based solver is used to further refine the search and converge to a global optimum in 30 iterations. The optimised design, weighing 3.7 kg, presents a reduction in mass of 58% when compared to the original rigid vehicle. The optimization unveils preference towards designs with larger numbers of tori but with smaller torus diameters. Remarkably, the optimum design does not present an outer shoulder torus. The trajectory of the optimised decelerator is found to be robust with respect to entry conditions and trimmed angle of attack, as a sensitivity analysis is conducted. With the exceptions of specific cases, particularly when atmospheric density is reduced in which the impact speed is excessive, no changes are required to comply with the EDL requirements.

In the final stage, a Monte Carlo study is conducted, encompassing more than 8000 simulations to thoroughly explore the design space. This study enables the examination of individual changes in trajectory parameters, such as peak heat flux, heat load, and peak dynamic pressure, by tracing them back to the specific variations in design inputs. This analysis facilitates decision-making processes for future Mars missions that involve stacked toroid configurations. The inflated radius, serving as a comprehensive representation of all design variables, exhibits one-to-one relationships with the performance parameters. This inflated radius can be viewed as a global variable, simplifying the design space and allowing for rapid estimations of performance characteristics. However, given the reduced amount of information contained in this variable, genetic optimization mainly leads to near-optimum results. These advancements empower the optimization of the vehicle's performance characteristics based on desired outcomes and trade-offs. The framework is applicable to feasibility and conceptual studies, enabling mission assessments to evaluate the feasibility and viability of stacked toroid configurations across various applications.

Abstract

Future Mars exploration missions require safe and controlled landing on the planet's surface. Conventional entry, descent and landing (EDL) technologies, such as parachutes and rigid aeroshells, face limitations in meeting increasing demands for heavier payloads, harsher entry conditions, and desired landing locations due to their limited deployment windows or geometry constraints set by current launchers. The stacked-toroid inflatable aerodynamic decelerator (IAD) has emerged as a promising EDL technology which has the potential to enable new and ambitious applications. Unlike conventional aeroshells, it utilizes flexible, high-temperature resistant materials that can be folded during orbital injection and transportation, and subsequently deployed before entering the Martian atmosphere. To address the complex interdependence of design variables and the multidisciplinary nature of stacked-toroid analysis, this research proposes a novel Multidisciplinary Design Analysis and Optimization (MDAO) framework. The framework integrates aerodynamics, aerothermodynamics, structural analysis, mass estimation, and Flexible-Thermal Protection System (F-TPS) sizing with trajectory simulations for a parametrized stacked-toroid. The major design variables are parameterized to trace model responses back to the design space. An additional novel contribution is the inclusion of a smaller torus on the IAD's shoulder. For aerodynamics and aerothermodynamics modelling, the local-inclination panel method is implemented, separately addressing the continuum, rarefied, and transitional flow regimes using well-established analytical methods and bridging functions. The scalloping phenomenon of the deflected surface is accounted for through semi-empirical expressions and experimentally-fitted correlations, capturing the additional aerodynamic and aerothermal contribution. F-TPS sizing employs a 1D Finite Difference Method (FDM) with harmonic weighted averaging of material characteristics to accommodate abrupt thickness variations. Results from each discipline are compared to experimental, flight, and high-fidelity numerical data, showing consistent agreement under various conditions. All disciplines present mean percentage errors in the order of 10-20% which are deemed acceptable for early design stages. The framework is applied to the ESA MiniPINS study, to demonstrate its applicability to a novel EDL architecture for a penetrating probe. The proposed environment efficiently evaluates the stacked-toroid optimum design for minimum mass, weighing only 3.72 kg whilst complying with mission requirements and optimisation constraints. The design remains robust against variations in entry parameters and atmospheric density, requiring minor adjustments for the penetrator impact speed. The framework enables design space exploration, revealing trends favoring stacked-toroids with low inner torus radii and large numbers of tori to minimize aerothermal loads while ensuring sufficient aerobraking. The inflated radius remarkably results in a global variable that can further simplify the design space to a single input for near-optimum rapid evaluations. The feasible parameter ranges identified through the design space search expedite the evaluation and optimization of stacked-toroids' multidisciplinary performance, aiding decision-making in early design stages of future Mars missions

Preface

The motivation for this research stems from my internship in the Flight Vehicles and Aerothermodynamics section (TEC-MPA) at ESA ESTEC. Over the course of six months preceding my thesis, I had the privilege of actively participating in research activities focused on the Entry, Descent, and Landing phases of Mars exploration. Under the expert guidance of Luca Ferracina, I gained valuable insights into the advantages of both conventional and unconventional EDL technologies for Mars missions, ultimately leading me to select the topic of inflatable aerodynamic decelerators for my research. The need for alternative EDL systems became apparent during my internship at ESA, coinciding with the final presentation of the MiniPINS mission. In defining the case study for this work, I received generous support from Víctor Fernández Villacé, who worked on MiniPINS. Additionally, I express my gratitude to my academic supervisor, Angelo Cervone, who not only nurtured the initial idea but also committed to providing continuous guidance throughout the project. Their unwavering support formed the foundation of this thesis, which aims to make a significant contribution to the future advancements in EDL within the realm of space exploration.

Acknowledgements

Amongst the most valuable lessons I have acquired throughout my academic journey is the recognition that successful scientific contributions are the result of collective effort, rather than individual endeavor. It is by standing on the shoulders of Giants that we see further. I am privileged to have received the exceptional mentorship of highly professional and highly expert researchers and engineers. This section briefly acknowledges some of the most influential contributions who played a significant role towards the completition of this thesis.

First and foremost, I am deeply thankful to my academic supervisor, Angelo Cervone, for his guidance, expertise, and trust. His unwavering support throughout my Master's program has been invaluable. The constructive feedback he has provided has contributed not only to the technical development of this thesis but also to my academic growth. I am also thankful to Stefano Speretta and Jyoti Botchu for their expertise as members of the assessment committee.

I would like to express my utmost gratitude to the TEC-MPA section in ESA ESTEC, who warmly welcomed me from day one and transformed my dream into a reality. It is through the opportunity provided by Jamila Mansouri and Guillermo Ortega that I had the privilege of working in an engineering team unparalleled in the world on some of the most fascinating engineering endeavours ever undertaken by humankind. I would therefore like to thank the entire section: Cristina, Csaba, Dirk, Eva-Marie, Frederik, Jeroen, Johan, Louis, Luca, Orr, Richard, Stephan and Victor. I also thank Andrew Ball, who dedicated a great deal of his work to planetary landers and entry probes. The fascinating conversations I had with him were not only stimulating but also fruitful in comprehensively exploring the literature on inflatable aerodynamic decelerators and penetrator missions. A special acknowledgement goes to Víctor Fernández Villacé who has worked on MiniPINS and has provided me with valuable information on the case study of this work. Most importantly, it is thanks to Luca Ferracina's supervision and constructive feedback that this thesis was proposed in the first place, and I am immeasurably thankful to him. His unmatched professionalism and boundless expertise have taught me life lessons beyond the technical realm that will always remain with me.

I would like to extend my gratitude to the numerous friends from across the globe who have played a pivotal role throughout this journey. The adventures I shared with Franco, from Bremen to Paris, with Andrea, from San Francisco to Los Angeles, and with Vincenzo, from Delft to Sicily, will forever be etched in my memory. Meeting them during my time in Delft has been one of the most meaningful events in my personal life. I would also like to express my appreciation to Sahir, Benji, Oliver, Alex, Sabin, Thommy and Nachiket. Our shared endeavours within the Delft Aerospace Rocket Engineering society have transformed into enriching friendships. While it would be impossible to individually name all the other friends who have helped me throughout this journey, I extend my heartfelt appreciation to all of them.

My final words go to my sister, Chiara, and my parents. I could never find enough words to express my gratitude for everything my family has done for me. Therefore, I will simply thank them for perhaps the single most significant thing they have done: ensuring that the only limits to my dreams were my very dreams themselves.

Contents

List of Figures

List of Tables

Nomenclature

Acronyms

1D One Dimensional

2D Two Dimensional

2U Two Functional Units

3D Three Dimensional

CAD Computer-aided Design

CFD Computational Fluid Dynamics

CLL Cercignani-Lampsi-Lord

CoG Centre of Gravity

CoP Centre of Pressure

DGB Disk-Gap-Band

DOF Degrees of Freedom

DSMC Direct-Simulation Monte Carlo

EDL Entry, Descent and Landing

ESA European Space Agency

EUV Extreme UltraViolet

F-TPS Flexible Thermal Protection System

FDM Finite Difference Method

FMF Free Molecular Flow

FSI Fluid-Structure Interaction

GA Genetic Algorithm

GSI Gas-Surface Interaction

HEART High-Energy Atmospheric Reentry test

HIAD Hypersonic Inflatable Aerodynamic Decelerator

IAD Inflatable Aerodynamic Decelerator

ID Identifier

IRDT Inflatable Re-entry and Descent Technology

IRT Inflatable Re-entry Technologies

IRVE Inflatable Reentry Vehicle Experiment

ISS International Space Station

JAXA Japan Aerospace Exploration Agency

LHMEL Laser-Hardened Materials Evaluation Laboratory

LOFTID Low Earth Orbit Flight Test of an Inflatable Decelerator

MATLAB Matrix Laboratory program

MCD The Mars Climate Database

MDAO Multidisciplinary Design, Analysis and Optimisation

MetNET Mars Network Lander

MiniPINS Miniature Planetary Insitu Sensor Packages for Mars and Moon

MINS Mars In-Situ Sensors

MRC Moment reference centre

MTI Finnish Meteorological Institute

NASA National Aeronautics and Space Administration

NetCDF Network Common Data Form

PAIDAE Program to Advance Inflatable Decelerators for Atmospheric Entry

RMSE Root-mean-square Deviation

RQ Research Question

SD Standard Deviation

SiC Silicon Carbide

STL Stereolithography

TC Thermocouple

THOR	Terrestrial HIAD Orbital Reentry	
TLR	Technology Readiness Level	
TPS	Thermal Protection System	
UTC	Universal Time Coordinated	
V&V	Verification and Validation	
VHS	Variable Hard Sphere	

Greek Symbols

α	Angle of Attack	rad
α_E	Energy Accommodation coefficient	-
β	Ballistic Coefficient	$\mathrm{N/m^2}$
β_{fiber}	Braided fiber bias angle	rad
δ	Complementary panel angle	rad
δ_s	Structural Displacement	-
$\delta_{\%}$	Percentage Error	%
ϵ	Emissivity	-
ϵ_e	Material Strain	-
η_g	Growth Allowance Parameter for leaks and ullage	-
η_{axial}	Design Safety factor for Axial straps	-
η_{fiber}	Design Safety factor for fibers	-
η_{radial}	Design Safety factor for Radial straps	-
η_{torus}	Design Safety factor for Tori	-
Γ	Flight Path Angle	rad
γ	Ratio of specific heat	-
λ	Mean Free Path	m
μ_0	Sutherlands' Coefficient	$\mathrm{Pa \cdot s}$
μ_S	Sutherlands' Viscosity Coefficient	$\mathrm{Pa \cdot s}$
μ_{EC}	Enskog-Chapman Viscosity Coefficient	$\mathrm{Pa \cdot s}$

ω	Viscosity Index	-
ϕ	Angle of Revolution	rad
ψ	Auxiliary Angle	rad
σ	Stefan–Boltzmann constant	$W/(m^2 \cdot K)$
σ_N	Normal Momentum Transfer coefficient	-
σ_T	Tangent Momentum Transfer coefficient	-
σ_y	Yield strength	Pa
σ_{spar}	Spar fabric stress	Pa
σ_{toroid}	Toroid fabric stress	Pa
σ_{wrap}	Restraint wrap stress	Pa
Θ	Complementary Angle	rad
θ_c	Half-cone Angle	rad
Ξ	Mole Fraction	-
m_{radial}	Mass of radial straps	kg
n_0	Number density	m^3

Roman Symbols

$\bar{a}$	Deceleration	m/s^2
$\bar{G}$	Inflation Gas Metric	-
$\bar{m}_g$	Mean gas mass	kg
$\bar{R}$	Specific Gas Constant	$J/(mol \cdot K)$
ρ	Density nomunitkg/m^3	
A	Cross-sectional Area	m^2
A_{gores}	Gores Area	m^2
A_{nose}	Area of nose cone	m^2
A_{shell}	Area of bottom shell	m^2
$A_{shoulder,link}$	Area of the connection between the shell to its shoulder	m^2

$A_{shoulder}$	Shoulder area	m^2
AR	Aspect Ratio	-
b_x	Nondimensionalized mass parameter for dynamic pressure	-
C	Total Toroid Circumference	m
C_D	Drag Coefficient	-
C_L	Lift Coefficient	-
c_p	Heat capacity at constant pressure	$J/(kg \cdot K)$
c_x	Nondimensionalized fabric mass parameter	-
D	Drag Force	N
d_f	Nondimensionalized fabric mass parameter	-
d_m	Molecular diameter	m
g	Gravitational Acceleration	m/s^2
h_{pay}	Payload height	m
h_{shell}	Shell Slanted Height	m
h_{stowed}	Height of launcher fairing	m
h_{stowed}	Packed height of decelerator	m
I	Number of radial straps	-
Kn	Knudsen Number	-
L_r	Radial Straps Length	m
$L_{enclosure}$	Distance between outer shell and payload wall	m
L_{ref}	Reference Length	m
L_{shell}	Outer shell length	m
$L_{shoulder,link}$	Distance connecting the shell to its shoulder	m
$L_{shoulder}$	Arc length of shoulder	m
m	Mass	kg
M_w	Molar mass	g/mol
m_{gas}	Gas mass	kg

m_{gores}	Gores Mass	kg
m_{IAD}	Structural mass of inflatable aerodynamic decelerator	kg
m_{pay}	Payload mass	kg
m_{torus}	Torus mass	kg
N	Number of tori	-
N_A	Avogadro's number	1/mol
$p_{inflation}$	Inflation Pressure	Pa
p_{min}	Minimum Inflation Pressure	Pa
p_{tank}	Tank Pressure	Pa
q	Dynamic Pressure	Pa
R	Gas Universal Constant	$\mathrm{J/(mol \cdot K)}$
R^2	Coefficient of determination	-
r_c	Base radius	m
r_N	Nose-cone radius	m
$r_{fairing}$	Radius of launcher fairing	m
$r_{inflated}$	Total inflated radius	m
$r_{out,torus}$	Radius of shoulder torus	m
r_{pay}	Payload radius	m
r_{tank}	Tank radius	m
r_{torus}	Radius of inner tori	m
S	Surface toroid area	$\mathrm{m^2}$
s	Speed Ratio	-
SM	Static margin	%
T	Temperature	K
t	Time	s
T_f	Final Temperature	K
T_i	Initial Temperature	K

T_{gas}	Gas temperature	K
V	Velocity	m/s
V_{tank}	Tank Volume	m^3
V_{toroid}	Total volume of tori	m^3

Superscripts

$\bar{}$	Nondimensionalized
eq	Equalities
g	Global
ineq	Inequalities
m	Spatial Discretization
t	Temporal Discretization

Subscripts

∞	Freestream
a	Wind-frame
b	Body-frame
c	Convective
E	Entry
I	Impact
i	Number of panels index
j	Number of gas species index
k	Layer of Thermal Protection System
m	Mars
r	Radiative
s	Stagnation
w	Wall
x	Horizontal Axis
y	Vertical Axis

z	Rotational Axis
0	Total
2	Post-shock
avg	Average
CoG	Centre of Gravity
cond	Conduction
cont	Continuum Regime
CoP	Centre of Pressure
F-TPS	Flexible Thermal Protection System
fmf	Free-Molecular Flow
FR	Fay-Riddel
lam	Laminar
LB	Lower Bound
max	Maximum
min	Minimum
post	After
pre	Before
ref	Reference
rerad	Reradiation
tot	Total
turb	Turbulent
UP	Upper Bound

1. Introduction

The advent of interplanetary space flight has opened up a wealth of opportunities for research in the field of space sciences. Long-term exploration of celestial bodies in our Solar system, using tools such as landers and flyers, has provided unprecedented access to data and information. The exploration of Mars, in particular, has highlighted the need for delivering scientific instruments to its surface. In the past, the problem of landing scientific instruments on Mars has been addressed by ensuring a soft landing for robotic vehicles. However, the constraints on payload mass and volume, as well as the strict requirements for landing regions, can make the mission more complex. An alternative approach to landing scientific instruments on a planet's surface is to use penetrating probes, also known as penetrators. These self-contained vehicles are designed to impact a planet's surface at high velocities and come to rest in its subsurface. They use their kinetic energy to traverse a certain distance within a solid target. Despite the potential benefits of using penetrating probes, previous space missions that have proposed their use, such as Mars-96, Deep Space 2 and Lunar-A, have yet to be successful. Recently, the Miniature Planetary In-situ Sensor Packages for Mars and Moon (MiniPINS) study [1] led by the Finnish Meteorological Institute has sparked renewed interest in miniaturized surface penetrators to enable simultaneous distributed in-situ measurements and network studies.

Currently, the study is in the preliminary design stage, presenting opportunities for the definition and analysis of its entry, descent, and landing (EDL) system to ensure the delivery and emplacement of the penetrators on the Martian surface in accordance with the system requirements. Amongst the viable EDL concepts for Mars exploration, early studies [2–5] on unmanned Mars entry uncovered three main candidate systems based on the mission requirements, the entry vehicle and operational constraints: parachute descent systems, rigid aeroshells and inflatable aerodynamic decelerators (IADs). In particular, Disk-Gap-Band (DGB) parachutes have long been used because of their heritage in supersonic flight test data. In fact, wind tunnel testing, both sub-scale and full-scale, has enabled the design and qualification of parachute systems. Nevertheless, the success of parachute applications for planetary exploration comes with the limitation of staying within this heritage as their performance limits are being approached [5]. Gillis [3] marked the limited operating conditions at which parachutes can be used for Martian entry, reaching Mach numbers up to 2 and dynamic pressures up to 960 Pa. Rigid aeroshells have also been used in previous missions to protect the vehicle during Martian descent, however, the performance of these devices is constrained by the size of the vehicle itself, in addition to leading to large mass increases. Hence, in most cases, aeroshells do not offer sufficient drag area. Mission studies [2, 6] reveal that when compared to a rigid aeroshell, inflatable decelerators can relax the stringent deployment conditions for a second-stage decelerator. Furthermore, they can significantly increase the landed payload mass without increasing the size of the entry vehicle [6]. To provide the needed drag area and Mach number required by future planetary exploration missions, including penetrator concepts, the application of inflatable decelerators is addressed in this work.

The concept, first proposed in the 1960s by National Aeronautics and Space Administration (NASA) for planetary exploration, indicated three-dimensional gas-pressurised bodies that are inflated by an internal gas-generating source, ram-air or a combination of both, to improve their aerodynamic performance for EDL applications. Current conventional entry technologies are limited in terms of landed mass by the ballistic coefficient which is itself constrained by the diameter of the aeroshell which is capable of fitting within the launcher fairing. EDL system analysis studies by NASA [7, 8] recognise that the existing heritage technology for Mars's EDL lacks the capacity to land increasing payload masses.

The studies retrieved on IADs do not only include spherical objects similar to balloons [9–13] and inflatable spherical drag objects [14, 15], but also extends to tension shells [16–21], conical bodies [22, 23], lentils [24] and toroidal shapes [25]. While the initial efforts on decelerators aimed at advancing the state of the art by developing empirical databases through wind tunnel and free flight testing, the technological investment made in recent years has unveiled a specific configuration as being the most promising one for application to planetary mission: the stacked toroid blunted cone [26]. A rendering of the concept is shown in Figure 1.1. This configuration, also referred to as stacked toroid, is constructed by stacking a series of concentric bladders of toroidal shape with an increasing diameter which is wrapped in a thermal protection layer to create a smooth surface [26].

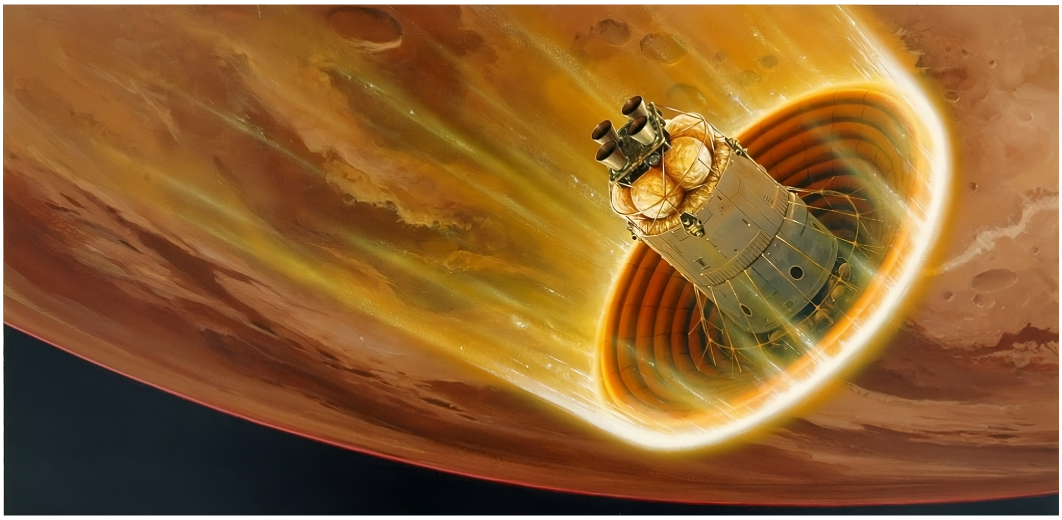

Figure 1.1.: Artist impression of Stacked-toroid Decelerator for Mars Exploration [27]

The several research studies performed on EDL architectures utilizing this configuration have revealed the complex interdependence of the many design variables that affect its performance and the multidisciplinary nature of the design process, branching into aerodynamics [28], thermodynamics [29], material science [30–33], structures [34–37] and flight mechanics [38, 39]. Due to this inherent multidisciplinary and tightly-coupled character, the system-level performance is driven by convoluted interactions that cannot be captured from individual subsystems without sacrificing fidelity. This limitation is further accentuated by the inadequate design tools for modelling and analysing IADs, as identified by NASA in their EDL Systems Analysis study for Mars exploration [7, 8].

Although analytical design methodologies exist for alternative IADs such as the isotensoid [40] and tension cone [41] configurations, the stacked torus design is based upon its construction method. This highlights the lack of a generalised design methodology that requires a strategy to optimise the chosen system. The argument of utilizing the classical 70° sphere-cone design because of its heritage [42–46] is rather weak, especially because it is non-optimal from an aerothermal standpoint given the presence of boundary layer instabilities driven by the expansion around the nose cone, along with early transition and high heating levels.

This research, therefore, aims to address the intertwined design dependencies [47] branching into aerodynamics, aerothermodynamics, structural engineering, material science and flight mechanics by developing a multidisciplinary design analysis and optimisation (MDAO) framework that can be applied to EDL architectures for future Mars missions to identify the system most suited to a given set of requirements and constraints. Because of the multitudinous design variables intrinsic in a stacked toroid, the framework shall utilize parametric modelling, which would enable the use of efficient gradient-based optimizers [48, 49]. Although the parametrization of a vehicle's design by simplifying its configuration into a reduced number of inputs is a common approach in the aeronautical industry, where each design parameter is evaluated against its performance imprint [50], the method is yet to fully emerge for space applications. Previous efforts in hypersonic vehicle design, in fact, employed empirical regressions to size conceptual aerial vehicles, without needing a defined outer mold line [51], resulting in overly simplified relationships mandating the need for large design margins. The need for such a framework is also supported by NASA' EDL system analysis [7, 8], recognising the immaturity of the current modelling tools for flexible aeroshells and emphasising the importance of alternative computational models for better productivity and verifiability.

While a similar MDAO architecture to that proposed in this work has recently been described by Decker and Mavris [49] and employed by Dean, Robertson and Mavris [52], its applicability is limited to the continuum regime since it is intended for hypersonic aerial systems. As such, the geometries are treated as rigid bodies which lack any type of deformations, typical of IADs. The augmented aeroheating due to the presence of scalloping phenomena is therefore neglected [53]. Moreover, the architecture proposed by Decker and Mavris consists of multiple wrappers to industry tools, such as CBaero and FIAT, which are licensed under U.S. release only [54], thus constraining accessibility to the environment. On the contrary, an open-source tool that accounts for the transition from rarefied to continuum conditions has been proposed by Falchi et al. [55], referred to as FOSTRAD. Nevertheless, this does not present the capabilities to parametrize a vehicle and is only applicable to Earth re-entry scenarios. As for the previous case, no modelling of body deformations is in place.

Leveraging on the recent advancements in numerical methods and reduced order modelling, coupled with the advanced technological development of IADs, the aim of this work is that of developing a fully-integrated framework capable of generating the optimal design of a stacked toroid IAD for a Mars mission. Specifically, the MiniPINS penetrator mission is investigated as the case study of this work. The novel contributions are manifold and consist of tailoring the parametrization of the geometry to the chosen IAD configuration, investigating the effect of the outer shoulder torus, validating the numerical model of a 1D heat diffusion problem for the flexible-thermal protection system (F-TPS), evaluating both the continuum and rarefied aerothermal and aerodynamic effects in a Mars entry trajectory and accounting for the flexible IAD deflections along with their aerothermal augmentation, proposing and assessing a novel EDL architecture comprising a stacked toroid and a tension cone for a penetrator mission. Each of these contributions, combined into a fully-integrated MDAO environment, aims to deliver an optimal EDL architecture for the MiniPINS mission and ultimately to address the pressing challenges faced by space engineers in design space exploration, sensitivity analysis and optimisation within reasonably short time frames.

1.1. Motivation

The stacked-toroid configuration has gained significant interest in the last decade due to its distinct advantages over conventional EDL technologies. This mission-enabling technology offers lower ballistic coefficients and higher drag levels at higher Mach speeds, expanding the deployment Mach number envelope and enabling the accommodation of larger landed masses and the selection of higher altitude landing sites [26]. Additionally, these configurations of IADs generate lower heat fluxes on the system, reducing the thermal requirements on the vehicle's Thermal Protection System (TPS). In response to the limitations of current EDL devices, the renewed research efforts in designing inflatable entry systems highlight the importance of this work [30].

Amongst the most significant motivations driving this research endeavour is the need to fill a knowledge gap on the intricate interdependencies between the design parameters influencing the performance of stacked toroids. By tailoring the parametrization specifically to the chosen IAD configuration, this research enables systematic exploration of the design space, allowing for optimized EDL configurations to be obtained efficiently. While the technique is still yet to be fully explored for space applications, it is considered a standard procedure in the aeronautical industry to parametrize a vehicle's design by collapsing its configuration into fewer inputs [50]. Therefore, creating a comprehensive framework that uses reduced-order parametric modelling methods would make it possible to use effective gradient-based optimizers for creating stacked toroid IADs, enhancing the state-of-the-art in entry vehicle design.

The proposed research aims to incorporate both the continuum and rarefied aerodynamic and aerothermodynamic effects in the analysis, enabling more accurate and reliable predictions of the lift and drag coefficients, heat transfer and surface temperatures. In fact, the application of existing hypersonic aerodynamic databases for similar geometric configurations is not appropriate for stacked-toroids in rarefied conditions [56]. Moreover, given the fundamental dependency of the aerothermal performance on the flexible deformation of the IAD during entry and descent, semi-empirical and analytical correlations are implemented to estimate the heat augmentation caused by the scalloping phenomenon across the surface of the stacked-toroid and by the onset of turbulence. Similar correlations are also proposed for the aerodynamic performance. This contribution simplifies the complex dynamics involved in the operation of stacked-toroid IADs, thereby enabling the multidisciplinary design of optimal decelerators for Mars penetrator missions and other space exploration applications.

The proposed MDAO framework is not only academically significant but also holds practical implications for industry and space agencies. By providing a methodology for parametrizing the stacked-toroid IAD, this research establishes a standardized approach that can be adopted and explored both by researchers and engineers for efficient design space exploration, sensitivity analysis, and optimization studies. The open-source nature of the framework proposed makes it accessible to the scientific community and industries, thereby fostering collaborative research and enabling the next generation of space engineers to engage in the early design stages of EDL without highly-sophisticated computational equipment.

The application of the framework to the MiniPINS mission aims to demonstrate the suitability of IADs for penetrators. The main motivation for leading scientific research on the EDL of a Martian penetrator mission is its remarkable scientific relevance that such an endeavour would enable for the ultimate benefit of humankind. Due to the penetration achieved, such probes would enable the measurements of regional geometric gradients as well as the thermal flows arising from the interior of a planet at depths that would not be otherwise reached by other equipment [57]. Furthermore, the emplacement of the probes in the subsurface guarantees that the scientific instrumentation would be isolated from the meteorological conditions affecting the surface, making it an ideal candidate for seismometry measurements. The direct contact with the soil makes scientific observations very reliable for geochemical studies. Besides the scientific output, the use of a penetrator system for the exploration of Mars is the most compelling and advantageous option from a technical standpoint. While the application of these systems has been advocated for celestial bodies such as the Moon [58–65], Galilean satellites and Mercury [66], Europa, Ganymede and Enceladus [67, 68], Vesta [69–71] and comets [72–74], Mars is the ideal candidate because of its environmental characteristics [57].

The application of stacked toroids extends beyond Mars missions. The versatility of this design opens up possibilities for various other space exploration applications where deceleration and controlled descent are crucial. Previous feasibility studies have proposed the utilization of these IADs for satellite de-orbiting [75], space-debris removal [76], cargo missions to orbiting space stations [77]. Exploring the potential of stacked toroids as decelerators not only offers practical benefits but also contributes to the advancement of aerospace engineering by expanding the design space and fostering innovation in the field.

1.2. Research Questions

The needs associated with the gaps identified in chapter 2 serve the purpose of providing a baseline for the definition of the following research questions (RQ):

RQ1 How can a robust MDAO framework be developed to effectively integrate aerothermoelastic models for a parametrized stacked-toroid IAD design?

  a) How can optimisation of a stacked-toroid be effectively integrated into the holistic mission design process?

  b) What is the extent of agreement between the simulated aerodynamic performance and the high-fidelity results from the literature?

  c) How does the accuracy of the simulated aerothermal performance compare to high-fidelity results retrieved from the literature?

RQ2 What is the optimal conceptual design of a stacked toroid for the MiniPINS penetrator that minimizes the total mass of the decelerator?

  a) How can the design space of a stacked-toroid be described?

  b) What is the most suitable characterisation of the EDL design space that complies with the MiniPINS requirements?

  c) How does the variation of design space impact the responses of the MDAO model?

RQ3 How robust is the entry performance of the optimised stacked-toroid design space?

  a) How do the trajectory entry conditions of the MiniPINS mission affect the design choices of the stacked-toroid?

  b) How does the trimmed angle of attack influence the entry trajectory of the optimized stacked-toroid design?

  c) How does the variation in atmospheric density impact the entry trajectory of the optimized stacked-toroid design?

1.3. Thesis Outline

The aim and objectives of this research are outlined in chapter 1, highlighting the advantages offered by stacked-toroids over conventional EDL technologies, as well as the wide range of applications they enable. The MiniPINS mission is introduced as a case study to demonstrate the application of the IAD to penetrating probes.

Chapter 2 presents a comprehensive review of the major technological developments in stacked-toroids. It covers both initial and recent advancements found in the Russian, American, and European literature. The multidisciplinary nature of the stacked-toroid concept is addressed, and existing gaps in the research are identified.

Chapter 3 outlines the novel fully-integrated framework. It provides an overview of the interfaces between different disciplines, describes the parametrization process, and presents an analytical structural model for determining the mass of the IAD. The atmospheric model used is discussed in section 3.3, while the planar equations of motion are explained in section 3.4. The local inclination panel method, including the mesh generation approach and shading algorithm, is discussed in section 3.5. Analytical methods for determining aerodynamic and aerothermodynamic performance in different regimes are presented. Additionally, semi-empirical correlations to correct for aeroshell deflection and an associated F-TPS performance modelling approach are introduced.

Chapter 4 focuses on the verification and validation of each individual discipline within the proposed MDAO framework. This is done by comparing the results against high-fidelity data and experimental data retrieved from the literature. The limitations and range of applicability of the proposed methodologies are identified, and the successful implementation and accuracy of the methods for early design stages are demonstrated.

In chapter 5, the case study of this thesis is discussed. An overview of the predecessor mission is provided, serving as the foundation for the MiniPINS mission. A modified mission is proposed, where a stacked-toroid configuration is utilized instead of a conventional capsule. The EDL requirements, defined in section 5.4, are used to formulate the optimization problem. The constraints and objective function of the optimization problem are presented in section 5.6.

Chapter 6 presents the results and discussion. It focuses on the optimization results and the converged design space. The performance of the optimized stacked-toroid configuration is contextualized, and a comparison with the baseline MiniPINS trajectory is provided. The sensitivity analysis results are discussed in terms of entry conditions and atmospheric density. Finally, the exploration of the design space is addressed.

In conclusion, chapter 7 summarizes the findings of the research and provides answers to the research questions. Additionally, recommendations for future work are provided.

2. Literature Review

This chapter presents a comprehensive literature review of the historical technological developments of stacked-toroids, expanding from previous work in [78], that encompass their multidisciplinary nature by focusing on the gaps in current design, modelling and simulation methods.

2.1. Inflatable Re-entry and Descent Technology (IRDT)

The first descent vehicle consisting of conical layers made of internal toroids, at least for one of the vehicle's stages, was developed by Lavochkin Association in 1999-2000 [79], leading to the collaboration with ESA for the Inflatable Re-entry and Descent Technology (IRDT) [80–83], depicted in Figure 2.1. A three-layer ablating TPS composed of silica-organic polymer was analytically designed by Finchenko [84] for IRDT to withstand peak heat fluxes of 38.9 W/cm^2, with the requirements of occupying the minimum volume in a stowed position without any hindrance [85]. Despite the initial design, thermal tests using plasma jet flow conducted by Finchenko et al. [33] revealed significant damage to the first two layers. This highlighted the importance of conducting further research on multilayer ablation and TPS layer vibration at aerodynamic loading. A successful qualification flight of IRDT-1 was conducted in February 2000 [86]; the first stage survived a peak heat flux of 35 W/cm^2 and g-load of 15g, but measured instabilities that led to a structural collapse associated with a failure in the TPS later in the flight, whereas the second stage did not inflate. Subsequent suborbital flights (IRDT-2 and IRDT-3) failed due to envelope damage, revealing issues with analysis tools and thermal protection structures. It appears evident that the application of soft structural materials raised the need to explore various research directions. These include investigations into design methods and analysis techniques for structures incorporating unique properties of soft materials, such as anisotropy and non-linear elasticity. Alifanov [87] immediately realised that such developments necessitated adjustments in the traditional scientific disciplines and particularly recognised the areas of strength analysis, aeroelasticity, thermal physics, technology, and reliability.

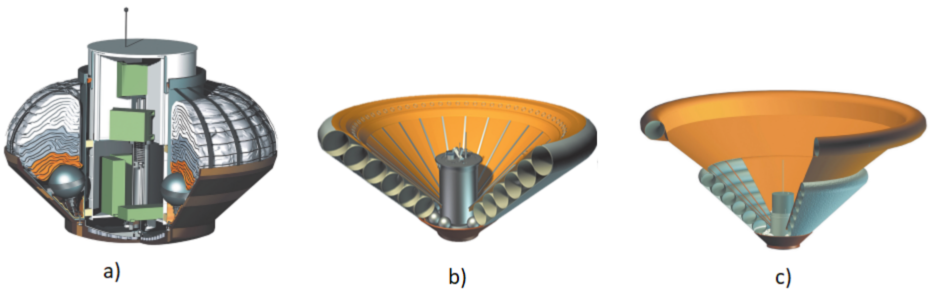

Figure 2.1.: IRDT in stowed (a), first-stage (b) and second-stage (c) configurations [88]

Given the flexible contour of IADs, aerodynamic scaling is not achievable, necessitating costly full-scale testing of mock-ups [33]. To overcome the obstacle of rapidly evaluating the aerodynamic performance of IRDT, a recent numerical study was conducted by Wang, Hou, and Niu [89]. The study utilized computational fluid dynamics (CFD) and a ballistic trajectory code to assess the impact of the decelerator's half-taper angle on the drag coefficient at different speeds. The findings revealed that increasing the half-taper angle resulted in a decreased drag coefficient, leading to lower peak heat flux and absorption while achieving higher deceleration. Increasing the reentry angle, under a fixed half-taper angle, was found to increase peak heat flux and maximum deceleration but reduce heat absorption. Integrating aerodynamics and trajectory analysis offers valuable insights into geometric design, aerodynamic performance, structural characteristics, and aerothermal loads. This emphasizes the intricate decision-making process involved in designing such vehicles, where various disciplines are interconnected and interdependent.

2.2. Inflatable Re-entry Technologies (IRT)

Following the IRDT failures, a study called IRT was conducted by Wilde, Tausche, and Orth [90] for OHB-System AG (see Figure 2.2). Using improved engineering tools like LS-Dyna, the study focused on technology research, conceptual design, and thermal/structural analysis. Limited resources restricted the study to three configurations with different ballistic parameters. Finchenko [91] designed and validated the TPS, but testing revealed failures due to thermal shrinkage of the fabric. This incident highlighted the limited understanding of aeroheating and the need to address interconnections between disciplines for the IAD's success. Finchenko et al. [92] also proposed landing a multi-ton module of a manned space station on Mars, as shown in Figure 2.2 (b), where instead of a single layer of tori, Finchenko suggested connecting two layers with compressive elements to securely hold large cargoes and reduce deflection. The stacked-toroid IAD also found applications in satellite de-orbiting [75], ISS-cargo re-fuelling, and space debris removal [76], showcasing its wide range of applicability. The possibility of trimming the vehicle at a positive angle of attack was also proposed to generate lift and improve the descent control [92, 93]. The concept of stacked toroids has even been explored for Venus exploration [94, 95], expanding its potential beyond Earth.

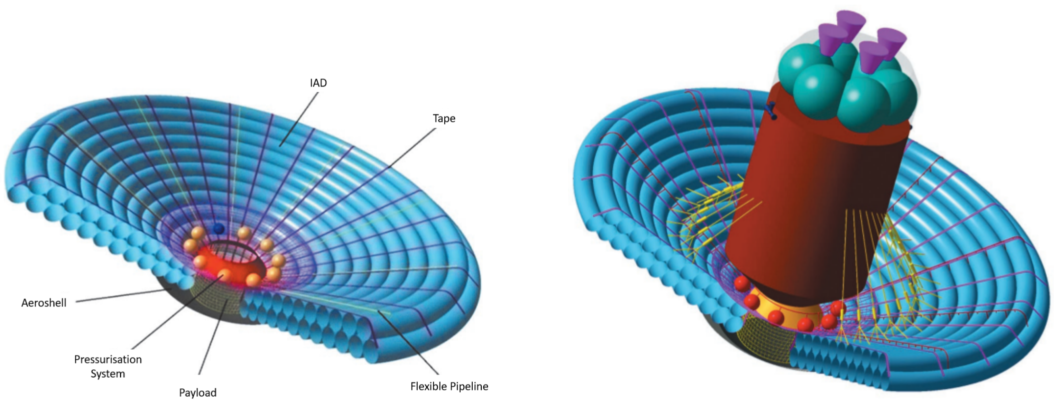

(a) without payload [96]

(b) with payload for manned Mars mission [92]

Figure 2.2.: IRT Vehicle

2.3. Program to Advance Inflatable Decelerators for Atmospheric Entry (PAIDAE)

Building upon the valuable lessons learned from the material failures of the IRDT, advancements were made through the Program to Advance Inflatable Decelerators for Atmospheric Entry (PAIDAE). This program successfully increased the Technology Readiness Level (TLR) of the stacked-toroid to 6, indicating progress in both design and manufacturing processes.

The initial studies conducted within the PAIDAE program were carried out by Yates and Chapman [97], focusing on the experimental aerodynamic performance of a 60° sphere-cone forebody. The ground tests confirmed the aerodynamic stability of the vehicle across various Mach speeds. However, later high-fidelity numerical simulations conducted by Murman [98] revealed the presence of hysteresis in the unsteady wake profile due to the intensified load of a stronger shock. The need for enhanced analysis tools and more comprehensive experimental data served as a driving force behind the development of IRVE, HEART, THOR, and LOFTID.

2.3.1. Inflatable Reentry Vehicle Experiment (IRVE)

The stacked toroid concept has seen significant progress with the Inflatable Reentry Vehicle Experiment (IRVE) [44–46]. IRVE aimed to raise the TRL to 6 and was designed for exoatmospheric deployment on Earth. Hughes et al. [99] provided an overview of the 3 m inflatable aeroshell used in Mars entry simulations. The system consisted of four main elements: inflatable bladder, structural restraint, gas barrier, and thermal protection layer. The bladder, made of silicone-coated Kevlar, maintained pressurization during descent and had redundant compartments to prevent catastrophic failures. The dry Kevlar fabric restraint attached the bladder to the centerbody structure and facilitated the mounting of the gas barrier and thermal protection layer. The gas barrier ensured that hot gases did not penetrate the Nextel 312 cloth layers of the thermal protection layer. Compared to IRDT, the IRVE design is well-documented and accessible, making it valuable for future research and investigations.

Lindell et al. [88] conducted a preliminary structural analysis of the vehicle using analytical functions to calculate loads on key components. A comparison with high-fidelity finite element analysis showed differences below 10-12%, indicating good agreement between the approaches. While both methods involve assumptions and may not yield exact solutions, their consistency allows for effective correlation of design parameters with system loads. This understanding aids trade-off assessments during the design phase and enables rapid evaluation of structural integrity for similar vehicles. The development of simplified analytical expressions is valuable for efficient structural integrity assessments and can be utilized in a MDAO environment for design space constraints or optimization.

2.3.2. Inflatable Reentry Vehicle Experiment (IRVE) II

Despite the initial setback of the unsuccessful flight of IRVE-I, which experienced a mishap during separation from the sounding rocket, its successor, IRVE-II, was launched in 2009. The flight provided invaluable telemetry data that facilitated post-flight trajectory reconstruction, performed by O'Keefe and Bose [100]. The analysis of the reconstructed aerodynamic coefficients revealed the presence of high-frequency instabilities during the deployment phase, as well as unexpected low-frequency oscillations near the peak dynamic pressure. Interestingly, these instabilities were not anticipated in the pre-flight aerodynamic database, which was generated using high-fidelity simulations with a rigid model of IRVE-II. The significant discrepancy between the predicted and actual magnitude of these oscillations was attributed to the fact that the aerodynamic assessment had modelled the IAD as a rigid vehicle, whereas it became apparent that IRVE-II flexed during the dynamic pressure pulse. While the vehicle demonstrated sufficient stability throughout the flight until the aeroshell lost the necessary pressure to maintain inflation, the remarkable insight gained from the reconstructed aerodynamic flight data highlighted the crucial need to accurately model the deflection of the stacked-toroid design.

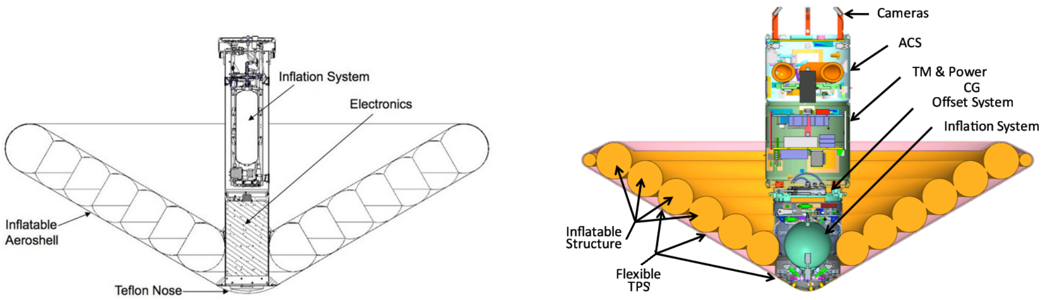

(a) IRVE-II [100] (b) IRVE-3 [39]

Figure 2.3.: IRVE Vehicle upgrade

The flight performance analysis conducted by Dillman et al. [39] confirmed the observation of inflation for a few seconds during the mission, although quantitative measurements were not provided. It was discovered that despite the initial prediction of a maximum Mach number of 5.5, the post-flight data revealed a peak Mach number of 6.2. This deviation was attributed to variations in atmospheric properties that were not adequately accounted for in the initial atmosphere models. Moreover, the uncertainty in the performance flight data was linked to the anisotropy of the fabric seams [101], indicating a need for improved analysis tools to accurately predict the trajectory and structural behaviour of IRVE. Throughout the entry phase, the IAD experienced oscillations in the angle of attack ranging from 14 to 22°, which later reduced to 5-9° at peak pressure and peak heating. This suggests the presence of flight disturbances that must be considered when modelling the trajectory of a stacked-toroid entry vehicle. Ground radar tracking, aligned with the study of a Mars penetrator aiming for a verticalized trajectory, revealed that the trajectory was nearly straight down at an altitude of 2 km from impact.

Although the aerodynamic data was collected solely in the continuum regime, Moss et al. [56] extended the analysis to the rarefied and transitional regimes using high-fidelity simulations. These calculations generated a comprehensive database of axial, normal, and static pitching coefficients for angle of attacks ranging from 0° to 180°. The findings, of significant relevance to this study, underscored the sensitivity of IRVE's aerodynamic performance to the relatively low speeds encountered in the rarefied and near-continuum regime. Proper modelling of these conditions is essential, as the existing hypersonic aerodynamic databases for similar geometric configurations are inadequate for stacked-toroids.

2.3.3. Inflatable Reentry Vehicle Experiment (IRVE) 3

Lichodziejewski et al. [102] present the design and fabrication details of the flight unit for the successor of IRVE-II, known as the IRVE-3 decelerator shown in Figure 2.3. IRVE-4 was also proposed to gather more experimental data but never launcher [103]. Drawing from the lessons learned from the previous flight, significant surface deflections encountered during IRVE-II's mission prompted the adoption of stronger materials and structural enhancements. Consequently, Kevlar braid tubes were selected for IRVE-3's seven tori, while braided tubes with a silicon liner were employed as the gas retention barrier to reduce flexing of the structures. Additionally, radial straps were added to the centerbody to tie the tori together and minimize oscillations. Notably, a novel configuration was introduced, featuring a smaller-diameter torus at the shoulder of the vehicle to further enhance structural rigidity. The thermal protection system was also further improved with a novel lay-up consisting of outer Nextel layers with high-temperature Pryogel insulation and inner Kapton-encapsulated Kevlar material [30].

In order to avoid the previous mistake of de-linking the structural and aerodynamic performance of the IAD, high-fidelity numerical modelling was employed to capture the coupled behaviour between the structure and flow distribution around the decelerator. The modelling efforts revealed that under a pressure loading of 8 kPa, deflections of up to 9 cm would occur [102]. This finding emphasizes the importance of employing coupled methods that integrate structural and flow analysis tools for accurate prediction of the performance of inflatable stacked tori. Although other analytical relationships were developed for IRVE-3, such as the estimation of minimum inflation pressure proposed by Brown [104], or Samareh's model to evaluate the IAD mass [105], the implementation of such low-accuracy methods often fails to capture the complete physical processes involved. Consequently, safety factors and arbitrary multipliers are frequently utilized to quantify performance [106]. This highlights the ongoing challenge of achieving a trade-off between computational complexity and the desired level of accuracy in modelling inflatable stacked tori, underscoring the need for continued advancements in multidisciplinary design approaches.

The launch and post-flight reconstruction of IRVE-3, presented by Old et al. [39], thoroughly examines the aerodynamic deflections experienced by the aeroshell, resulting in a reduction in the decelerator's actual half-cone angle. The additional flight data collected for IRVE-3 holds immense significance in validating the applicability of low-fidelity aerodynamic models for stacked toroids. These models should incorporate the effects of the reduced half-cone angle or vehicle deflection. However, due to the computational demands associated with conducting a comprehensive aeroelastic study coupling the vehicle's aerodynamics with structural behaviour throughout the full trajectory, an aerodynamic database was established for subsonic, supersonic, and rarefied flow conditions using a simplified rigid model of IRVE-3 [39]. To address the simplification of treating the geometries as rigid models, the calculated aerodynamic coefficients included a correction term that accounted for the freestream dynamic pressure. While detailed information on the reproducibility of the cone-sharpening model is lacking, the concept of calculating aerodynamic coefficients with rigid models and subsequently applying corrections proves to be highly valuable due to its simplicity and computational efficiency.

To investigate the impact of stacked toroid rigidity on performance, the CFD Research Corporation conducted a comprehensive study on the aeroelastic behaviour of various stacked toroid configurations [107]. A multidisciplinary integrated computational environment was employed, establishing FSI models through the coupling of finite element method in NASTRAN and ABAQUS with average constant aerodynamic loading. Both one-way and two-way FSI coupling approaches were implemented, yielding comparable results. The study revealed cyclic fluctuations in deformation and stresses with consistent mean values, and stress levels remained significantly below yield values. However, notable deflections were observed in the IADs due to the omission of modelling the radial straps. Interestingly, it was found that the stacked toroid configuration exhibited robustness to pressure variations across the fluid interface. This suggests that a high-fidelity CFD analysis does not necessarily lead to improved FSI results when compared to lower-fidelity models. Moreover, no significant variation in pressure distribution was observed between the double-stack and single-stack IAD configurations. Considering the increased complexity and mass associated with the double-stacked design, as depicted in Figure 2.2, no aerodynamic benefit was identified for the alternative configuration. Therefore, a single-stacked design seems to be favoured for its simpler construction and lack of aerodynamic disadvantages.

The importance of structural flexibility in stacked toroid design has been extensively investigated by Hollis and Hollingsworth [53] who conducted a wind tunnel test program specifically focusing on the stacked toroid's F-TPS. In fact, its deflection caused scalloping of the flexible structure, which led to early boundary layer transition and increased heating levels in both laminar and turbulent flow. The study highlighted the crucial aerothermal perspective that needs to be addressed alongside the structural-aerodynamic coupling, further emphasizing the multidisciplinary nature of the problem. In a subsequent wind tunnel campaign conducted by Hollis et al. [108], rigid bodies with fixed inherent degrees of deformation were used. The investigation revealed that the characteristics of the scalloping phenomenon were influenced by the specific design of the stacked toroid and the flow characteristics. The intricate flow field surrounding these deformations resulted in shock wave reflections and complex interaction patterns. To further understand and characterize this phenomenon, a parametric numerical study was conducted, which was grounded on the wind tunnel campaign results. Hollis and Hollingsworth [53] thus developed semi-empirical correlations that provided a low-fidelity description of the aerodynamic heating associated with the scalloping phenomenon. These correlations can be readily implemented in a multidisciplinary environment, aiding in the comprehensive analysis of stacked toroid aerothermodynamics.

The comprehensive investigation conducted by Hollis and Hollingsworth [53] shed light on the significant impact of structural deflection on both the aerodynamic performance and aerothermodynamics of IAD, particularly in relation to turbulence transition. The research revealed that depressions on the surface of the IAD promote higher convective heat rates. While Schneider [109] published a review of available flight transition data for (re-)entry capsules and proposed low-accuracy correlations for predicting turbulence onset, none of these correlations have been validated for IADs, especially in a Mars environment. In addressing the convective heat transfer characteristics of scalloped surfaces as a function of the cone angle, two numerical studies by Zhao et al. [110, 111] proved insightful. The two studies demonstrated the sensitivity of stacked toroids to sphere-cone angles under varying Mach numbers, with larger angles leading to weaker cross-flow and a higher tendency for flow separation. Zhao et al. [112] also observed the greatest heat transfer at the transition zone. Although the modelled deflections in these studies were unrealistic and assumed rigidity, they confirmed the aerothermal augmentation and laid the groundwork for establishing a parametric correlation to predict transition onset based on the design and scalloped surface of stacked toroids. However, a key challenge that remains unaddressed in the literature is the development of a low-fidelity method capable of predicting the scallop radius. Such a method would enable the determination of aerothermal performance using Hollis' heat-augmented relationships. The high-fidelity method advocated by Zhao et al [110, 111] would in fact result computationally prohibitive for a MDAO framework. Resolving this challenge would significantly contribute to enhancing the predictive capabilities for stacked toroid aerodynamics and aerothermodynamics.

McNamara and Friedmann [113] acknowledged the limited existing work in the literature regarding aeroelasticity and aerothermoelasticity in the context of IADs. The authors emphasize the necessity for systematic studies that integrate multidisciplinary aerodynamics and structural analysis, while also considering the intricate heat transfer problem. Furthermore, the challenge of accurately modelling the aerothermodynamic environment, including rarefied aerodynamics and the transition from rarefied to continuum flow, highlights the importance of fully-integrated methods in the analysis and development of IADs. Notably, McNamara and Friedmann observed that a more refined flow approach does not necessarily guarantee higher accuracy in high-fidelity strategies for stacked toroids. These decelerators are not highly sensitive to pressure distributions, indicating that efforts should be focused on the comprehensive characterization of all relevant disciplines involved in the analysis. The insights provided by the IRVE studies underscore the need for a holistic and integrated approach that considers the interplay between aerodynamics, aerothermodynamics, and structural behaviour.

2.3.4. High-Energy Atmospheric Reentry Test (HEART)

Within the PAIDAE development program encompassing the IRVE vehicles mentioned thus far, the High-Energy Atmospheric Reentry Test (HEART) project was also proposed in an effort to scale the diameter of a HIAD and to investigate its effects on the IAD performance when subjected to more relevant entry conditions in terms of dynamic pressure, heat flux and heat load [114]. The mission, outlined by Wright et al. [115], fulfilled the need of landing a larger mass on the surface of Mars whilst offering a low ballistic coefficient with a 2.5 m-diameter IAD. While the design relies heavily on the IRVE program, the configuration presents eleven structural tori and an additional smaller diameter shoulder torus which initiates the tri-torus configuration. These components, resembling the burble fence of isotensoids, are intended to reduce the degree of oscillation due to vortex shedding. Furthermore, this prevents resistance against axial deflection and buckling while allowing for reduced inflation pressure. This configuration was also investigated by Cassell et al. [116] for a linearly scaled IRVE-3 design with a diameter of 6 m. The data measured in the wind tunnel campaign showed that the tri-torus configuration produced an increase in drag coefficient between 5% and 15% when compared to the baseline configuration. The models tested at higher inflation pressures also resulted in a slightly larger drag coefficient. The added mass and complexity to the system, therefore, seems justified by the enhanced aerodynamic performance. However, such an increase should also be investigated in other aerodynamic regimes.

To maximize HEART's mass efficiency, lightweight and high-strength materials are crucial. The deployable structure must be efficiently packed within the available fairing volume, with minimal material degradation from thermal cycling. To achieve this, a bias-braided Kevlar sheath coated with a silicone-based RTV is used. Mazaheri's aerothermal analysis [117, 118] optimized the nose geometry to reduce aeroheating, assuming a rigid body and a fully-catalytic surface. The catalytic mechanism generated heat fluxes up to 67% higher than the non-catalytic case. Comparing it to a super-catalytic model showed a nearly identical match, supporting the claim of 100% catalytic efficiency. Guo et al. [119] further investigated the relationship between wall temperature and heat flux, finding a non-linear correlation that becomes more complex for complex geometries. Both Mazaheri [118] and Guo's [119] analyses did not consider the effect of scalloping caused by uneven heat distribution on a smooth surface.

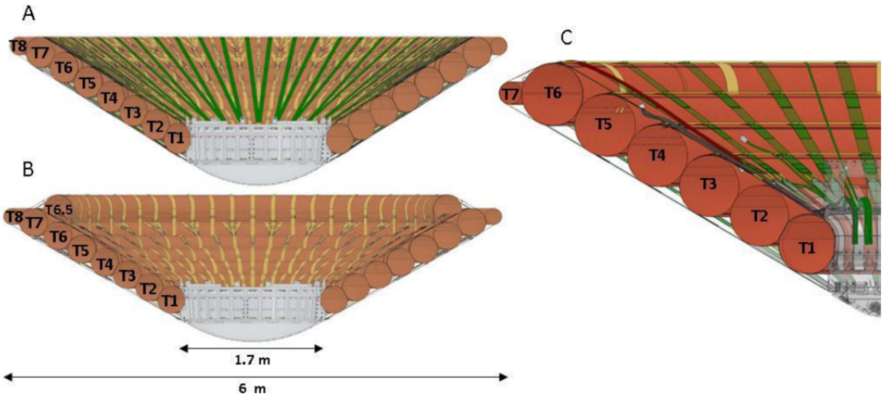

Figure 2.4.: A) 6m HIAD scaled configuration, B) 6m tri-torus configuration and C) 3m baseline configuration [116]

2.3.5. Terrestrial HIAD Orbital Reentry (THOR)

A concept similar to HEART was proposed by Hughes et al. [120], followed by a test proposal by Dillman et al. [39] as a secondary payload on a commercial resupply mission to the International Space Station (ISS). This concept was called Terrestrial HIAD Orbital Reentry (THOR) and featured a 3.7 m diameter inflatable with a 70° half-cone angle designed for a 315 kg vehicle. THOR maintained the toroidal configuration of the IRVE-3 concept, but with an increased half-cone angle of 70°. This modification improved vehicle stability and increased the inflation volume. However, the larger angle also resulted in higher heat flux, necessitating the use of Zylon instead of Kevlar braid and structural straps. Zylon was found to be more effective in withstanding harsh environmental conditions.

Notably, wind tunnel testing conducted by Hollis et al. [53] on THOR revealed that the convective heating environment on the back-face of the vehicle was relatively benign. This finding allowed for the reduction of thickness in the F-TPS on the back faces, resulting in weight savings and simplified packaging of the aeroshell. The experimental data collected in the wind tunnel campaign were used to develop semi-empirical correlations for evaluating the heat on the payload and back-face, enabling low-fidelity aeroheating analysis which is in line with the scope of a MDAO framework.

2.3.6. Low Earth Orbit Flight Test of an Inflatable Decelerator (LOFTID)

In November 2022, NASA developed and launched the Low Earth Orbit Flight Test of an Inflatable Decelerator (LOFTID) [121, 122], a 6-meter-diameter, 70° sphere-cone aeroshell with six structural tori and one shoulder torus. Although the flight has been successfully conducted, no flight data has been publicly released at the time of writing. Nevertheless, the vehicle retrieval demonstrated the survivability and feasibility of the largest IAD ever flown to date. In a preliminary presentation by Herath et al. [123], enhanced analytical techniques used in the design stage provided insights into the aerodynamics and aerothermodynamics of the wake flow environment. While this contribution aligns with the research goals of this thesis, the specific tools used are mentioned without sufficient detail. Recently, Thompson et al. [124] pointed out that resolving the flow field over the inflation toroids, which are exposed to the flow on the back of the vehicle, poses a challenge. The data and predictions mostly agree, although there are some discrepancies in local toroid heating peaks due to the scalloped shape that increases turbulence. Once the performance flight data becomes available, it is expected to provide valuable information on the aeroheating environment during Earth reentry under more realistic aerothermal loading conditions. This information will enable the correlation and refinement of predictive models for the exploration of Mars, contributing to the advancement of Mars mission planning and design.

2.4. Outlook

The literature survey on the developments of stacked-toroids, summarized in Table B.1, has revealed the significance of multidisciplinary analysis in evaluating the performance of the complex interwoven interactions between different parameters and engineering branches. The nominal design trajectory is, in fact, dependent on the aerodynamic and aeroheating properties of the vehicle. In particular, the lift and drag forces, its ballistic coefficient and peak heating. Flight dynamics constraints should also be imposed on the aeroshell structures, such as the gravitational loading on the vehicle. The disciplines highlighted in blue in Figure 2.5 can be identified as follows in relation to the design space, coloured in red:

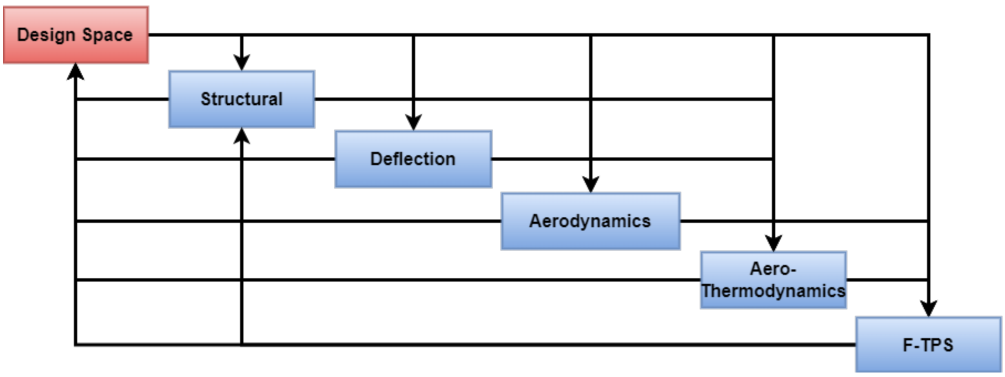

Figure 2.5.: Design Disciplines for Stacked-toroid configuration

- Structures: the utilization of flexible fabric materials poses challenges, which were recognized from the early stages of development. The structure of the aeroshell is particularly sensitive to the vehicle configuration as it is driven by the aeroshell geometry, aerodynamic loading, vehicle scale and payload configuration. Several low-fidelity expressions have been developed to evaluate the structural response and associated mass of the vehicle which can be leveraged upon. The scalability of structural elements has also been addressed in the literature for design optimization. Within this discipline, it is also needed to define the structural mass of the vehicle. Three traditional options are identified in the literature: 1) applying available mass estimating relations 2) extrapolating from comparable vehicles 3) parametrising the mass model. While the third is the most demanding one, it is also the most suitable one.

- Deflection: the importance of considering the deflection of flexible structures became evident after the IRVE-II and IRVE-3 flights. Computational FSI efforts have improved the accuracy of modeling the deflection of structural membranes. However, low-fidelity models still struggle to adequately represent the scalloping phenomenon observed on the IAD surface. This affects not only the aerodynamics but also the aerothermodynamics performance of the decelerator. Correction factors to aerodynamic models of rigid bodies can be included, incorporating available analytical and semi-empirical correlations to determine the aerothermal augmentation due to scalloping

- Aerodynamics: traditionally, high fidelity methods based on physics equations yield accurate solutions. Most missions still rely on aerodynamic databases of rigid blunt capsules, which are inaccurate in rarefied conditions. There is a need for extended databases that cover near-continuum and rarefied flows. However, their computational requirements are prohibitive for rapid simulations, where engineering methods could be used instead. The literature provides an extensive dataset of wind tunnel and flight-testing data on stacked-toroids, which can be used to verify and validate aerodynamics models of varying fidelity.
- Aerothermodynamics: similar considerations to the aerodynamics discipline apply to aerothermodynamics, where high-fidelity simulations are typically employed in the literature ranging from CFD to DSMC methods depending on the regime. However, extensive experimental campaigns have established semi-empirical models to determine not only the convective heat flux on the front but also on the back faces and centerbody. Engineering and analytical methods can therefore replace more computationally expensive alternatives with reasonable accuracy.
- Thermal Protection System: the aerothermal discipline provides information on the total heat flux and absorption experienced by the IAD to determine the F-TPS layup and required characteristics to maintain the desired payload temperature. Advances in IAD technologies have led to three generations of TPS with increasing performance. NASA commonly utilizes Pyrogel and Kapton, while ablative layers are often used in Russian literature. In general, materials with low thermal transport and outer fabrics with high emissivity and low catalyticity are desired. However, thermal studies on the suitability of the layup should be conducted.

The technology and computational advancements highlighted in this literature review have paved the way for addressing the need for an engineering framework capable of handling the multidisciplinary nature of stacked-toroids for design optimization and analysis. The examination of current available engineering codes for (re-)entry applications in Appendix A and Table A.1 reveals the absence of a code specifically tailored to this class of vehicles. Such a code should be capable of rapidly generating optimized designs that meet given requirements or constraints while considering the various disciplines identified in this study across all flow regimes.

The development of an integrated engineering framework for stacked-toroids poses a significant opportunity to leverage the advancements in computational tools and techniques. By incorporating parametrization, structural considerations, aeroelasticity, aerodynamics, aerothermodynamics, flight mechanics, and thermal protection systems, this framework can effectively address the challenges associated with the design and analysis of stacked-toroids. It would enable the rapid exploration of the design space and the identification of optimal solutions that meet the desired performance objectives. The absence of a dedicated code emphasizes the need for further research and development efforts to create a comprehensive engineering tool for stacked-toroids. Such a tool would enhance the efficiency and accuracy of the design process, enabling engineers to optimize the performance of these complex vehicles while considering the interplay of multiple disciplines.

3. Methodology

The novel framework that this research aims to develop mandates the definition of different disciplines and their corresponding interactions. The common platform in Figure 2.5 illustrates the top-level interfaces between the models of interest which are further explored in the following sections, following the example set by Clark's design methodology [43]. The methodology described in this chapter develops from the logic outlined in Figure 3.1, where the disciplines in Figure 2.5 are addressed individually.

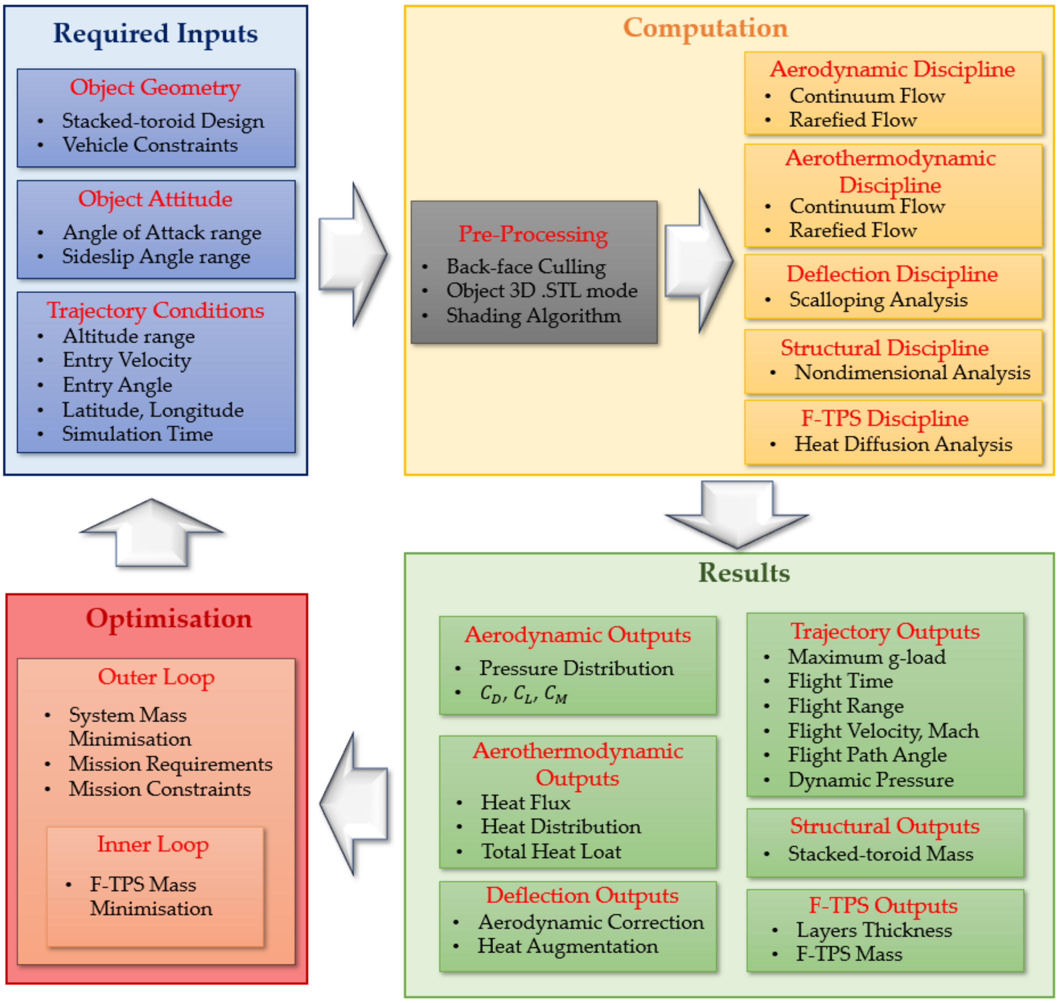

Figure 3.1.: Flow-chart of the proposed environment

Each simulation initiates with the definition of the required inputs, in the blue box, consisting of the vehicle design space, its attitude and the trajectory entry conditions. The first inputs, concerned with the parametrisation of the geometry, stem from the design space of a stacked-toroid described in section 3.1 and include vehicle constraints associated with the tank size and the maximum launcher fairing dimensions. Further constraints can be defined on the structural loads and g-load experienced by the vehicle. On the other hand, the trajectory entry conditions are defined by the mission of interest and the IAD's attitude by the desired flight profile.

The computation phase is then initiated where the methodology to evaluate the aerodynamic loading, described in section 3.5, and the aerothermal loading in section 3.6, perceived by the stacked toroid are used iteratively at each trajectory point. The planar motion described in section 3.4 is used in conjunction with the atmospheric model in section 3.3 to compute the environmental characteristics of the flow and the vehicle's position and velocity along the EDL phases. The maximum deceleration is also computed and recorded to constrain the optimisation, depending on the mission requirements. The heat flux and heat load predicted in section 3.6 are thus employed to design the F-TPS according to section 3.8, yielding the minimum mass of the F-TPS layers. At the same time, the structural mass of the IAD is computed following the approach outlined in section 3.2 for the parametrised vehicle and expected aerodynamic loading. At the same time, the aeroelastic deflection of the stacked toroid's surface is evaluated in section 3.7 to determine the scallop's radius and associated aeroheating augmentation. The results are then recorded and the design space is optimised according to the desired objective function, which could be expanded to a multi-objective function for more complex problems.

Given the recursive nature of the approach, the trajectory variables are recomputed at each iteration. The atmospheric data is imported prior to starting the optimisation process and maintained consistent across all scenarios. The aerodynamic database is then computed for a given design only once per trajectory and the aerodynamic coefficients are interpolated for the given atmospheric conditions at each point along the trajectory. This reduces the storage requirements for the 64 bits double-precision arrays.

While the definition of the optimisation process may be changed in the proposed environment depending on the requirements and desired optimisation variable, the aim of this research is that of minimising the decelerator's mass for the MiniPINS case study. Therefore, the structural and F-TPS mass must be minimised whilst ensuring compliance with the system requirements and mission constraints. Thus, the F-TPS and IAD mass are stored at each iteration along with the design parameters, entry conditions, maximum heating and maximum deceleration.

The MDAO framework is established within the Matlab R2022b toolbox. This programming environment is extensively utilized and well-established in the scientific, academic, and engineering communities, with most students having access to academic licenses. Furthermore, its user-friendly interface, extensive collection of built-in functions, and self-contained toolboxes establish it as the prevailing standard for technical computing. Alternative coding environments are viable, such as Python, however, they might not offer the domain-specific toolboxes, such as the aerospace and optimization functions employed throughout this work.

The following sections will detail the different methodologies implemented for each discipline. Starting from the parameterization of the design space and proposed constraints, the structural mass model is outlined. Consequently, the atmosphere model and planar motion equations are defined. Then, the aerodynamic and aerothermodynamic models are presented along with the meshing and shading algorithm adopted. Corrections for the deflections are proposed. Finally, the numerical approach to evaluate the F-TPS dimensions is outlined and discussed.

3.1. Geometry Parametrization

Amongst the novelties that this research aims to present, the optimisation of a reduced-order model IAD requires the definition of a parametrised geometry that decreases the number of adjustable variables down to a practical set of inputs. The approach, commonly used in the aeronautical sector to design aircraft, enables several queries to be performed rapidly whilst keeping the computing cost under control [125]. The closure of the problem can thus be attained for a constructed geometry by implementing a solver, such as gradient-based optimiser known in the literature for being highly efficient at converging when compared to other families of algorithms [126].

The problem of parametrisation comes down to selecting the most suitable design variables that most affect the topology of the vehicle and its performance. To enable design space exploration of the stacked-toroid, the outer aeroshell may be treated in a similar manner as a sphere-cone geometry, commonly adopted in re-entry and EDL applications [127, 128]. The simplification of the geometry is illustrated in Figure 3.2, where the axisymmetric contour is shown. The geometry may be described by three design variables, namely the half-cone angle θ_c, the nosecone radius r_N and the base radius r_c.

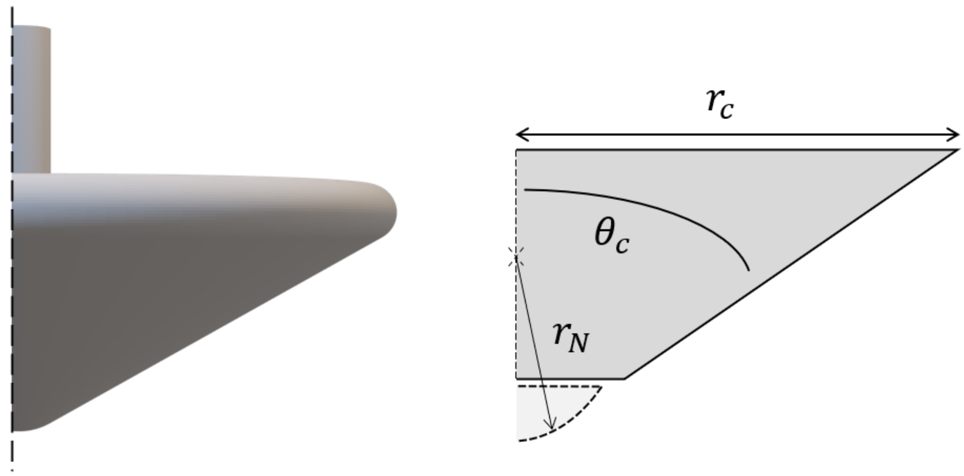

Figure 3.2.: Stacked-toroid outer shell (left) and simplified sphere-cone (right)

While this first approach may be sufficient for preliminary approximations, an improved design space is treated in this work. In fact, this forebody simplification lacks a description of the shoulder curvature and neglects the payload. Moreover, the base of the decelerator should not be treated as a closed surface, as it is erroneously reported in [52, 129] since the conventional stacked-toroid configuration presents a concave topology in the aft-body due to its inflated nature. In addition, the base radius should be related to the number of internal tori and their corresponding diameter. The improved model of the stacked-toroid forebody cross-section is shown in Figure 3.3, where the effect of the axial and radial straps is neglected.

The toroidal structure shown in Figure 3.3 is equivalent to the initial iterations of the IRVE program [44–46] and Soviet developments [33, 79, 84] mentioned in chapter 2. However, the more recent design configurations of the stacked-toroid include an additional torus, around the IAD's shoulder as shown in Figure 3.4, which has a smaller diameter than the inner ones. Although the

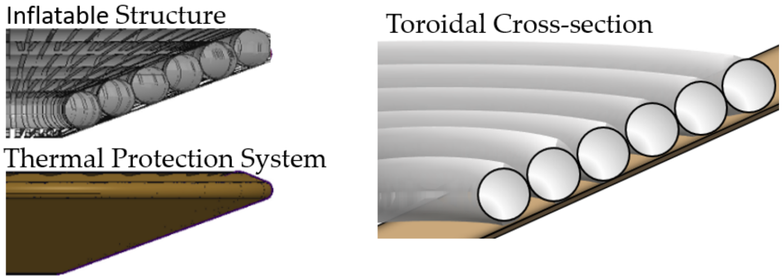

Figure 3.3.: Stacked-toroid forebody layers (left) and toroidal cross-section (right)

advantages introduced by this auxiliary torus are mainly structural and aerodynamic, as opposed to aerothermal, the revisited architecture is investigated in this work. This is an additional novelty that has not been addressed in previous parametrisation studies.

The inflation tank indicated in Figure 3.4 can be parametrised by assuming a predefined geometry type. Given that the stress concentration in a spherical tank is minimised as the stress resistance is uniform over its surface area, a sphere is often used in the development of IADs [99, 122, 123]. This parametrisation strategy has also been adopted by Cornick et al. [129]. The tank radius r_{tank} can be estimated by using the ideal gas equation in Equation 3.1, by assuming that the internal volume of the tank is completely filled with gas. When the inflation process occurs exoatmospherically prior to entering the atmosphere of the planet of interest, a one-off slow expansion process can be established. Therefore, by assuming an isothermal expansion for which the final temperature equals the initial temperature ($T_f = T_i = T$), the gass mass in Equation 3.1 is defined as $m_{\text{gas}} = \rho_{gas} V_{gas} = p_f V_{tank}/RT$ such that the product of the internal pressure in the tori p_{toroid} with their total volume V_{toroid} can be equated to the product of the tank pressure p_{tank} with its corresponding spherical volume $V_{tank} = 4/3\pi r_{tank}^3$ as in Equation 3.2. In case of rapid expansion during the inflation process, the gass mass could be computed assuming an isentropic expansion with $m_{\text{gas}} = \frac{p_f V_{tank}}{RT_i}\left(\frac{T_i}{T_f}\right)^{\frac{\gamma-1}{\gamma}}$. Given that the case study of this work advocates for exoatmospheric inflation, sufficient expansion time is ensured to utilize Equation 3.2.

$$pV = m_{\text{gas}}\, RT_{\text{gas}} \tag{3.1}$$

$$p_{\text{tank}}\, \frac{4}{3}\pi r_{\text{tank}}{}^{3} = p_{\text{toroid}}\, V_{\text{toroid}} \rightarrow r_{\text{tank}} = \frac{(6 p_{\text{toroid}}\, V_{\text{toroid}})^{\frac{1}{3}}}{2\,(p_{\text{tank}}\, \pi)^{\frac{1}{3}}} \tag{3.2}$$

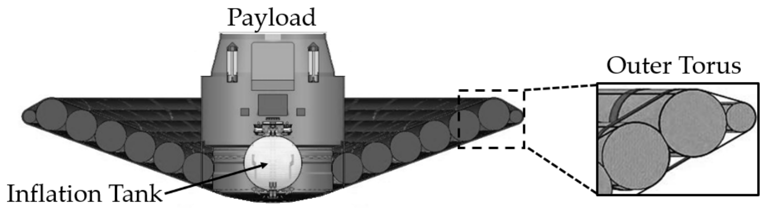

Figure 3.4.: Stacked-toroid configuration with outer torus; Adapted from [121]

The radius of the tank can be used as a constraint to the number of toroid shells, their diameter, toroidal inflation pressure, inflation gas or payload dimensions. The final parameterised geometry is shown in Figure 3.5, where parameters required to describe the geometry are highlighted. It is remarked that only the half-cone angle θ_c and nose-cone radius r_N are preserved from the first simplification in Figure 3.2.

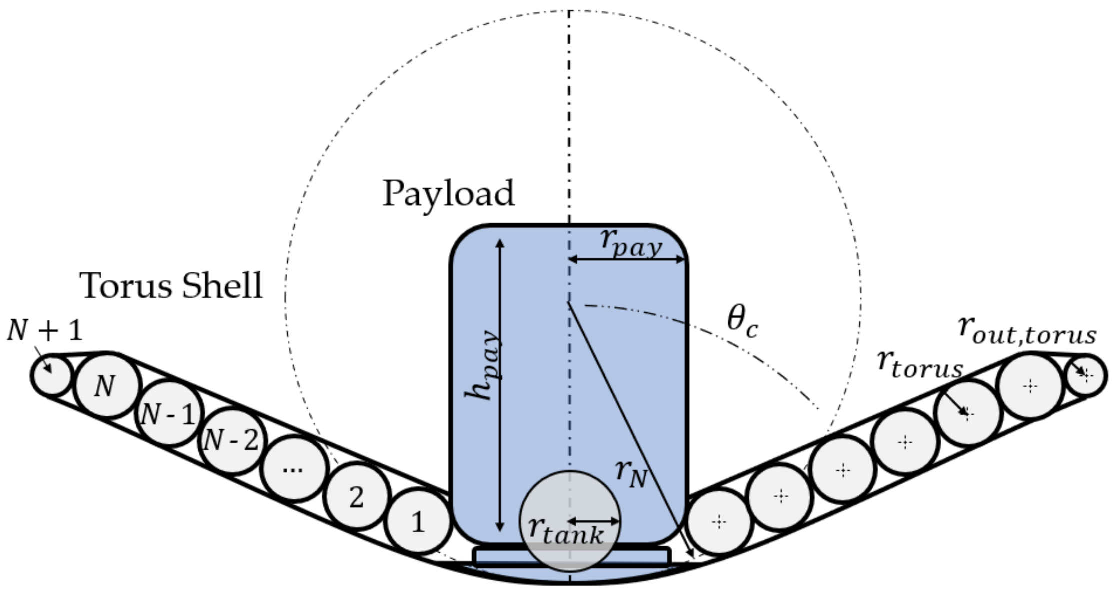

Figure 3.5.: Parametrized Inflatable

In addition to the tank radius r_{tank} derived in Equation 3.2, used as a constraint, the payload is described as a cylindrical centre-body of height h_{pay} and radius r_{pay}. The shape adopted may be easily modified for future studies, depending on the configuration of interest. However, based on the conventional designs identified in the literature survey and further supported by the shape of a penetrating probe, the cylindrical approximation is deemed appropriate for this framework. By assuming that all the internal tori N have the same radius r_{torus} , and the radius $r_{\text{out,torus}}$ of the outer torus $N+1$ is either known or not used, the inflated radius of the IAD r_{inflated} can be computed in Equation 3.3

$$r_{\text{inflated}} = 2r_{\text{torus}} \sin(\theta_c) N + 2r_{\text{out,torus}} \sin(\theta_c) + 2r_{\text{torus}} (1 - \sin(\theta_c)) + r_N \cos(\theta_c) \quad (3.3)$$

From trigonometry, the tangency point shown in Figure 3.6 is identified as the point where the spherical nose cap encounters the conical shape of the vehicle's shell. This allows a further reduction in the number of input parameters that can be obtained for a given half-cone angle and payload radius such that the nose-cone radius results fixed as in Equation 3.4.

$$r_N = \frac{r_{\text{pay}}}{\cos(\theta_c)} \quad (3.4)$$

For a given payload size, the number of design inputs is therefore reduced to four for the configuration with an outer torus whose diameter is smaller than the inner tori's, namely the half-cone

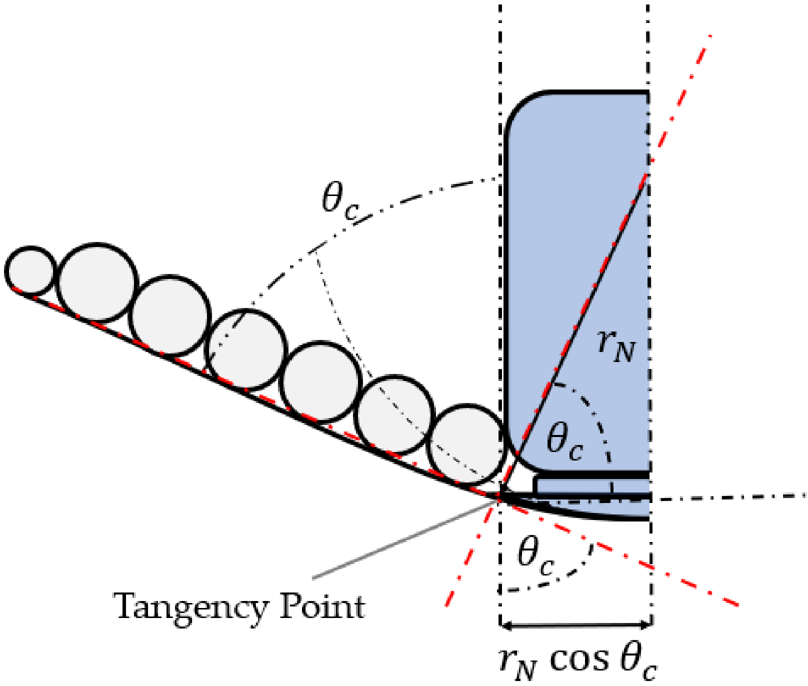

Figure 3.6.: Tangency point

angle θ_c, the radius of the internal tori r_{torus} , the number of internal tori N and the radius of the outer torus $r_{\text{out,torus}}$. However, if further analysis reveals the unsuitability of the outer torus adopted in the more recent configurations of the stacked toroid, the number of parameters is lowered to three: θ_c, r_{torus} , N. The inflation tank size may also be used to constrain the dimensions of the tori and their pressurisation strategy.

Inputs	Half-cone Angle	Number of Tori	Inner Tori Radius	Outer Torus Radius	Payload Height	Payload Radius
Symbol	θ_c	N	r_{torus}	$r_{out,torus}$	h_{pay}	r_{pay}
Units	$[rad]$	$[-]$	$[m]$	$[m]$	$[m]$	$[m]$

Table 3.1.: Design Space of Parametrised Stacked-toroid

The dimensions of the IAD can be calculated purely from the design space variables reported in Table 3.1. A complete derivation is provided in section C.1 not only to construct the geometry, but also to obtain values for the reference dimensions required in the aerothermal calculations.

A significant advantage of IADs over more conventional EDL technologies is their compact and flexible storage capability when they are stowed in the launcher fairing. Since they are inflatable structures, they can be packed into a relatively small volume, allowing for efficient use of space during launch as illustrated in the deployment sequence in Figure 3.7. However, it is important to note that there are still fairing geometrical constraints that need to be considered. The first one can be imposed on the height of the payload based on the launcher size to ensure that the folded IAD may be stowed within the available volume in the launcher's fairing.

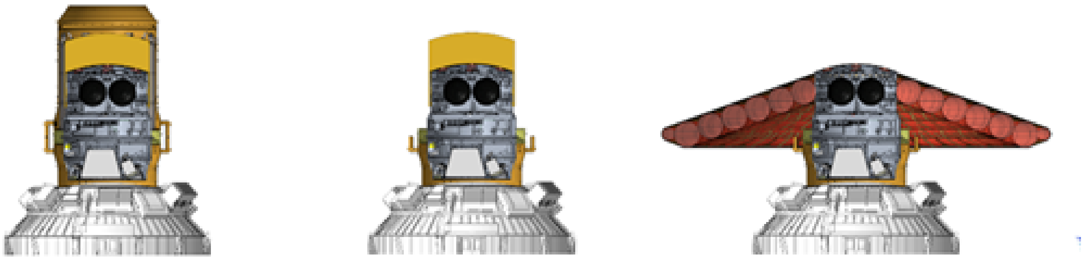

Figure 3.7.: Deployment sequence of Inflatable Stacked-Toroid from Launcher Fairing [123]

Based on the configuration suggested by Cornick et al. [129] and shown in Figure 3.8, while the minimum payload diameter can be constrained by the inflation tank in the absence of other design requirements, the upper bound may be set by the base diameter of the launcher fairing as described in Equation 3.5.

$$\begin{aligned} min(r_{pay}) &\geq r_{tank} \\ max(r_{pay}) &\leq r_{fairing} \end{aligned} \tag{3.5}$$

At the same time, the maximum height of the payload may be constrained by the maximum payload fairing height $h_{max,fairing}$ as well as the packaged height of the inflatable h_{stowed}, the diameter of the inflation tank and the base diameter of the fairing nose as in Equation 3.6. In fact, while the upper bound to the payload diameter is given by the payload fairing height, the lower limit is a combination of the inflation tank diameter and the height of the stowed inflatable. Reference values for the base diameter and the maximum height of the launcher fairings that have been or are planned to be employed for Mars exploration are given in Table 3.2. The list is by no means exhaustive and only serves the purpose of providing some reference bounds for the choice of constraints.

$$h_{pay} + 2r_{tank} + h_{stowed} \leq h_{max,fairing} \tag{3.6}$$

Launcher Fairing	Delta IV [130]	Starship [131]	New Glenn [132]	Atlas V [133]	Ariane 5 [134]
Base Diameter $[m]$	4.572	~ 8.0	6.35	4.57	5.4
Max. Height $[m]$	16.485	17.24	17.836	12.927	17.0

Table 3.2.: Launcher Fairing Dimensions as Constraints

To estimate the diameter of the inflatable in its stowed configuration within the launcher, the packing efficiency of previous missions in Table 3.3 is used for reference. This assumes that the ratio of the deployed-to-stowed radius of the inflatable would follow the same trends as previously obtained. It is noted that while the IRVE flight experiments and IRDT present comparable efficiencies, LOFTID exhibits a lower radius ratio likely due to the non-linear structural upscaling of the inflated tori with respect to the centrebody.

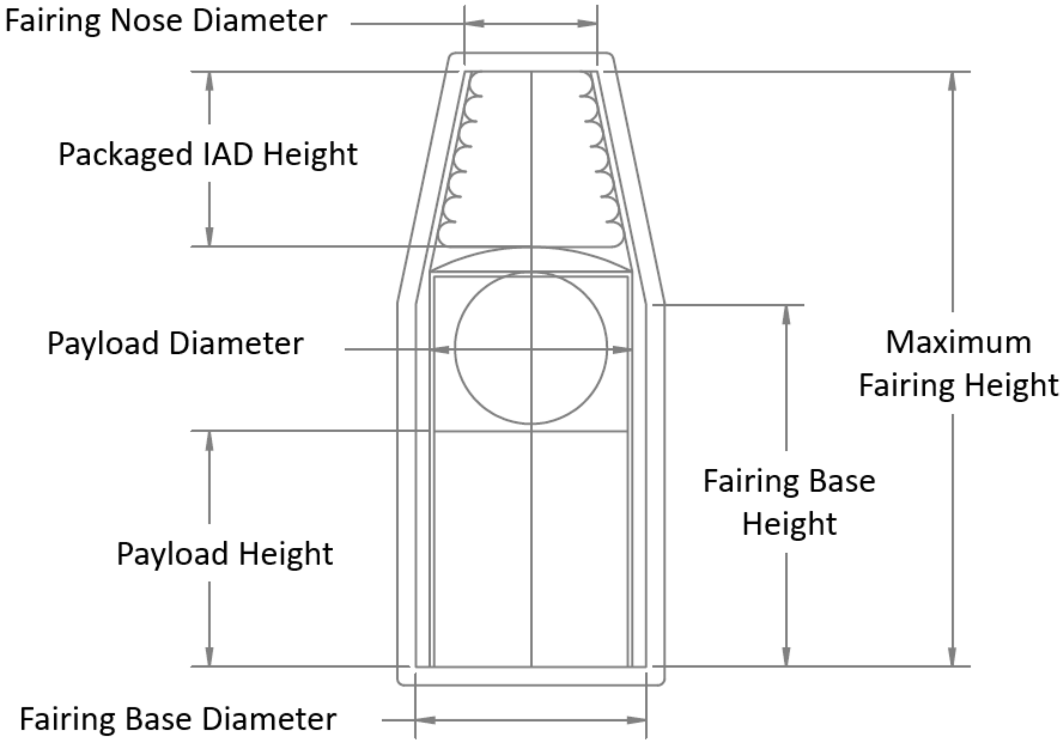

Figure 3.8.: Launch configuration Parametrization Visual; Adapted from [129]

It is crucial to acknowledge that every launch possesses unique constraints, including interfaces with other payloads, making it impractical to include all of them in a comprehensive analysis applicable to every scenario. Nonetheless, within the context of this research, the framework has been designed to address the primary requirements of all missions while remaining adaptable for future implementations to incorporate additional constraints effortlessly.

Vehicle	Inflated Radius $r_{inflated}$ $[m]$	Payload Radius r_{pay} $[m]$	$\frac{r_{inflated}}{r_{pay}}$
IRVE-II [100]	1.465	0.2095	6.993
IRVE-3 [38, 106]	1.500	0.2360	6.383
LOFTID [122, 123]	3.00	1.240	2.419
IRDT [81]	1.500	0.212	7.075

Table 3.3.: Packaging Efficiency of Stacked-Toroid Vehicles

Further constraints that may be applied to the parametric exploration of a stack toroid are concerned with the structural limitations of the decelerator's fabric. The structural analysis conducted by Lindell et al. [88] presents three closed-form analytical expressions to calculate the fabric loads in the aeroshell which have been validated against finite element, showing percentage differences between 1.8% and 13.6% which are reasonably accurate for conceptual design stages. The loads on the inflatable structure are generated by the internal inflation pressure and by the dynamic pressure of the entry phase with associated deceleration. As remarked by Brown [104], since the actual internal pressure distribution is unknown in conceptual design phases, the pressure requirement to react to the compression created by the aerodynamic pressure on the forward surface can instead be utilized. Defined in Equation C.23, such inflation pressure is computed for the most critical conditions when the drag force is at its peak during flight. The safety factory recommended by Lindell [88] of 2.5 is applied to compensate for material discontinuities, manufacturing tolerances and stress concentrations which are neglected by the simple relations but also for the simplified pressure relation which does not account for the presence of compression and bending.

The first expression, presented in Equation 3.7, is used to estimate the maximum fabric load $\sigma_{toroid,max}$ as a function of the payload diameter, inner torus diameter and inflation pressure $p_{inflation}$. The maximum load, which is a consequence of the aerodynamic force acting on the flexible outer shell, is found to occur in the inner radius of the innermost toroid [88].

$$\sigma_{toroid,max} = \frac{p_{inflation} r_{torus}}{2} \left[2 + \frac{r_{torus}}{r_{pay}} \right] \tag{3.7}$$

Then, the maximum load experienced by the spar fabric can be evaluated. This component is particularly important as it partitions the individual tori from one another. Differently from the toroidal structures that are directly affected by the aerodynamic loading, the spar is mainly subject to the internal inflation pressure such that the maximum loading is expected to occur in the innermost section with the spar end closest to the axis of symmetry of the vehicle [88]. The equation to evaluate the maximum loading $\sigma_{spar,max}$ is given in Equation 3.8. The expression assumes a continuous distribution of the spar around the circumference, whereas segmented discontinuities are likely to be created in the manufacturing stages of the decelerator.

$$\sigma_{spar,max} = p_{inflation} r_{torus} \left[1 + \frac{1}{1 - \frac{r_{torus} \cos(\theta_c)}{r_{pay} + r_{torus}(1+\sin(\theta_c))})} \right] \tag{3.8}$$

The loads acting on the restraint wrap used to hold the tori in place is computed from the deceleration experienced throughout the entry trajectory, as in Equation 3.23 later detailed. By assuming that the load is equally shared between the outer and inner interfaces of the wrap, and by neglecting the internal pressure on the nose cone, force equilibrium on the cylindrical payload yields the running load. The maximum load, in this case, is expected to be found at the interface between the fabric and the centrebody as the running length of the fabric is at its minimum [88]. The expression for the maximum load on the restraint wraps $\sigma_{wrap,max}$ is given in Equation 3.9, where m_{pay} is the payload mass. A slightly larger value of the payload radius may yield more accurate results to account for attachment interfaces [88].

$$\sigma_{wrap,max} = \frac{m_{pay} \bar{a} g}{\pi r_{pay} \cos(\theta_c)} \tag{3.9}$$

The analytical expressions in Equation 3.7, Equation 3.8, Equation 3.9 are thus employed as constraints to the parametrisation strategy hereby outlined by ensuring that all maximum loads are below the yield strength σ_y of the chosen materials (i.e. $\sigma_{toroid,max} < \sigma_y$, $\sigma_{spar,max} < \sigma_y$ and $\sigma_{wrap,max} < \sigma_y$).

3.2. Structural Mass Model

The design and assessment of different IADs require the evaluation of the system mass, which is one of the most important figures of merit in sensitivity and trade studies. The MDAO framework proposed dictates the need for rapid and accurate parametric approaches to estimate the structural mass of different architectures. The first merit function to relate the structural and aerodynamic parameters was proposed by Anderson [135] for a generic IAD to determine its efficiency. Equation 3.10 outlines the mathematical definition of the decelerator's efficiency as intended by Anderson, where the ratio of the system's mass m to its drag area CdA is set equal to the square root of the drag area itself multiplied by the dynamic pressure term q and a parameter b_x summed to the fabric mass per unit area d_f multiplied by a second constant c_x. Besides the form of the expression, which was originally defined to encompass the mass of suspension lines for detached IADs, the relevance of Equation 3.10 is that the structural mass is related to the desired drag area and the design loading condition. According to Anderson [135], the determination of dynamic pressure should consider the deployment conditions. Nevertheless, when dealing with exoatmospheric inflation, a more appropriate choice would be to use the maximum dynamic pressure experienced during the flight, denoted as q_{max}.

$$\frac{m}{C_D A} = b_x q \left(C_D\right)^{1/2} + c_x d_f \tag{3.10}$$

Anderson's merit function [135] was later adapted by Samareh [105] who described a dimensional analysis technique to estimate the mass of a stacked toroid. The proposed method accounts for the presence of the inflatable tori, the gores and radial straps. Specifically, Samareh speculated that the structural mass of IADs is a function of the maximum dynamic pressure q_{max} and the IAD's projected area A_{IAD}. The nondimensional function Π is therefore constructed in Equation 3.11, where the gravitational's acceleration of the planet g of interest is included for the units' consistency. While Samareh [105] utilizes the Earth's gravitational acceleration, the Martian value will be utilized in this work $g_m = 3.721 m/s^2$. The exponents $b_1 - b_4$ are determined through dimensional analysis to provide an implicit relation for the dimensionless mass $\bar{m}_{IAD}$.

$$\Pi\left(m_{IAD}, q_{\max}, A_{\mathrm{IAD}}, g_m\right) = m^{b_1} q_{\max}^{b_2} A_{\mathrm{IAD}}^{b_3} g_m^{b_4} \rightarrow \bar{m}_{IAD} = \frac{m_{IAD} g_m}{A_{IAD} q_{max} C_D} \tag{3.11}$$

The approach adopted to rapidly estimate the mass of a parametrised stacked toroid first defines a set of dimensionless geometry parameters to be used throughout the analysis. It then calculates the inflation pressure and inflation gas mass to then estimate the toroid, gore and radial strap mass. The mathematical approach is detailed in section C.2, where the novel contribution of expanding Samareh's model [105] to account for the shoulder torus is presented. Following the procedure outlined in section C.2, the total nondimensional mass of the IAD can at last be obtained by adding the individual nondimensionalised mass contributions of the IAD components shown in Equation 3.12, namely the gas mass, the axial and radial straps, the tori and gores. The $\bar{m}_{IAD}$ can hence be dimensionalised by substitution in Equation 3.11, such that the final value is multiplied by the scaling mass factor as in Equation 3.13.

$$\bar{m}_{IAD} = \bar{m}_{gas} + \bar{m}_{axial} + \bar{m}_{torus} + \bar{m}_{radial} + \bar{m}_{gores} \tag{3.12}$$

$$m_{IAD} = \bar{m}_{IAD} A_{IAD} q_{max} C_D / g_m \tag{3.13}$$

3.3. Atmospheric Model

Accurately predicting spacecraft aerodynamic and aerothermodynamic loading during atmospheric entry requires describing the environmental properties such as density, temperature, pressure, and composition. Planetary atmospheres are complex and dynamic systems that change over time. To address this complexity, a reference atmospheric model is used to characterize these variations primarily with altitude. This model is crucial for accurate flight simulations and mission design [136]. This study focuses on investigating the EDL system for a Martian penetrator, but similar modelling approaches can be applied to other planetary atmospheres.

The Mars Climate Database (MCD) is the most reputable database of atmospheric data compiled from the simulations of the Martian atmosphere generated with state-of-the-art global climate models [137]. These are capable of computing the three-dimensional atmospheric circulation while taking into consideration both the presence of dust and ice particles and gas radiative transfer. The model may also replicate the transport of dust particles and photochemistry in the atmosphere in addition to the condensation and sublimation cycle of CO_2 and water [137]. The MCD has been extensively validated with the available measurements retrieved by the thermal emission spectrometer onboard Mars Global Surveyor [138], by the Mars climate sounder onboard Mars Reconnaissance Orbiter [139], by the Emirates Mars infrared spectrometer onboard Emirates Mars Mission [140] and by the measurements made by the Viking landers, InSight and Perseverance [141].

The latest version of the MCD at the time of writing is the v6.1, released in October 2022 [142]. The database is accessed from the Fortran source code, which is compiled in a virtual Linux environment on a Windows system through the gfortran compiler in the Cygwin environment. Because the MCD is written as a Network Common Data Form (NetCDF) file, the associated library is installed from the Unidata website [143]. The model inputs are the spatial coordinates expressed in latitude, longitude and altitude, the date and local time, and the dust and Extreme UltraViolet (EUV) conditions. In the absence of a specific trajectory window for the case study of this work, the 1st of January 2028 with local time of 12:00 UTC is chosen (Mars Solar longitude of 225.2°) in an effort for the results of the study to remain relevant for the Mars missions of this decade [144, 145]. The average EUV conditions in the "Climatology" scenario represent a standard Martian year without the planet-encircling global dust storm. These conditions are reconstructed based on observations from Mars Years 24 to 35. The relevant outputs for this methodology include atmospheric pressure, density, temperature, and volume mixing ratios of several constituents such as CO_2, N_2, Ar, CO, O, O_2, and H in mol/mol_{air}.

To further generalize the atmospheric model, latitude and longitude are sampled from -180° to +180° and -90° to +90° respectively, with 5° increments, and then averaged. This approach, commonly used in the literature [146], provides representative data for trajectory analysis while decoupling atmospheric parameters from specific locations. The pressure, temperature and density distribution over latitude and longitude are shown in Figure B.1 at 120 km. The averaged pressure, temperature and density profiles are plotted in Figure 3.9 as a function of altitude. At the same time, the volumetric fraction of each atmospheric constituent is shown in Figure 3.10. Mars' atmosphere is much thinner than Earth's, primarily composed of carbon dioxide, with trace amounts of oxygen and other species depending on altitude. Trace gases like O_2, O_3, He, and H_2 are present in negligible quantities. The average surface pressure is below 600 Pa, less than 1% of Earth's, and the temperature ranges from about 210 K at the surface to 120 K in the upper mesosphere.

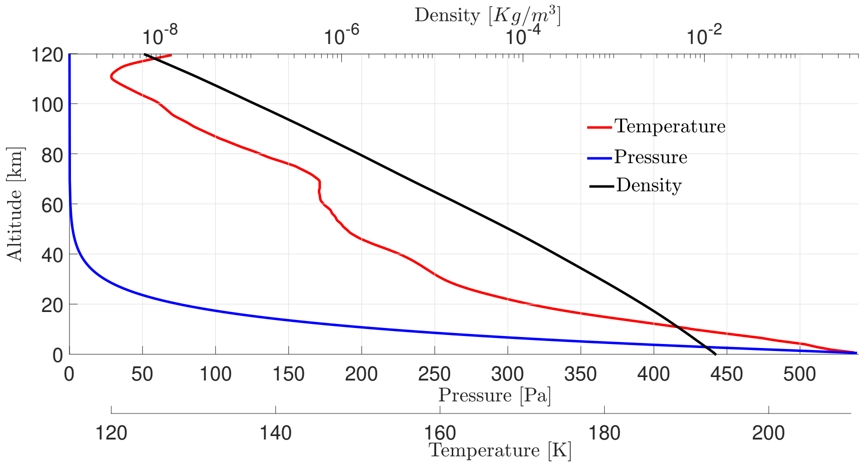

Figure 3.9.: Latitude- and longitude-averaged temperature, pressure and density over altitude

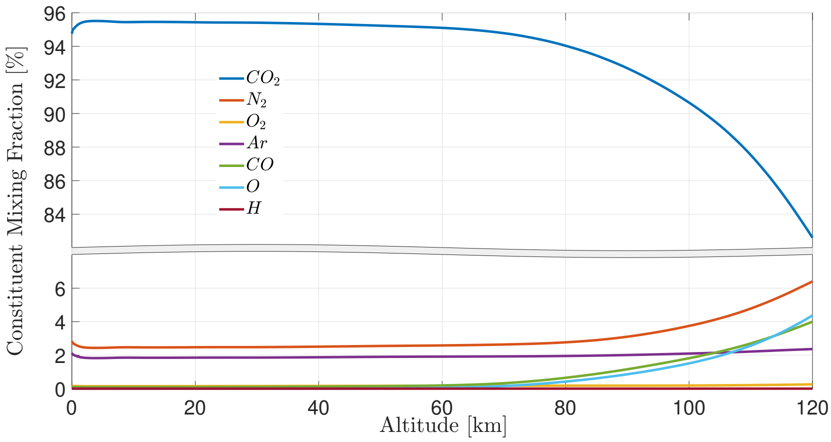

Figure 3.10.: Volume mixing ratio of the individual atmospheric constituents

According to multi-species gas dynamic theory, the number density of individual constituents n_0 in Figure 3.11 relates to their molecular weight M_w and atmospheric density as in Equation 3.14, where Avogadro's number is $N_A = 6.02214 \cdot 10^{23}\ mol^{-1}$ [147]. The abundance of atmospheric gases generally decreases with altitude, except for H and CO which peak at the mesosphere.

$$\rho = \frac{\sum_{j=1}^{J} n_{0_j} \cdot M_{w_j}}{N_A} \tag{3.14}$$

The mass of a single molecule is obtained by dividing the molecular weight of the gas by Avogadro's number in Equation 3.15. The molecular weights of the Martian gas constituents are given in Table B.4. The mean gas mass $\bar{m}_g$ can be calculated from the number of particles for each species according to Equation 3.15.

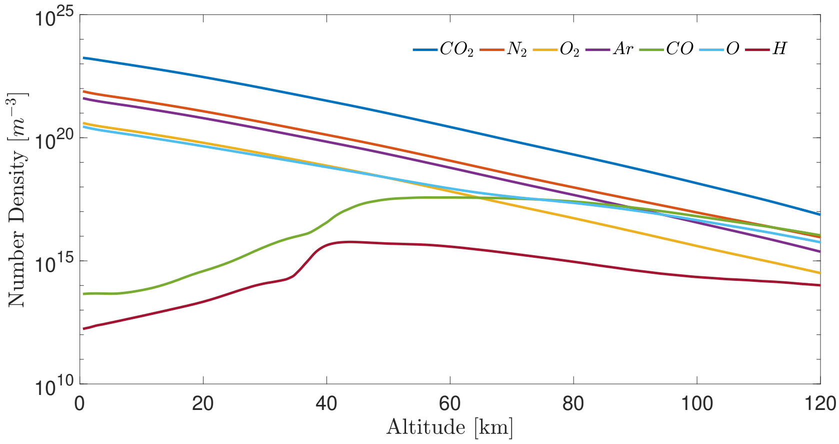

Figure 3.11.: Number density of the individual atmospheric constituents

$$m = M_w / N_A \qquad \bar{m}_g = \frac{\sum_{j=1}^{J} M_{w_j} \cdot n_{0_j}}{\sum_{i=1}^{J} n_{0_j}} \tag{3.15}$$

The transport properties of the gas are modelled with the available fourth-order polynomial equations retrieved from the literature [148], expressed as a function of flow temperature in the form of Equation 3.16. It is pointed out that the universal gas constant R is defined as 8.3145 $Jmol^{-1}K^{-1}$, and the specific gas constant as $\bar{R} = R/M_w$. The coefficients employed to evaluate the heat capacity at constant pressure c_p of each individual species. The fitted coefficients $a_1 - a_5$ are reported in Table B.5.

$$\frac{c_p(T)}{\bar{R}} = a_1 + a_2 T + a_3 T^2 + a_4 T^3 + a_5 T^4 \tag{3.16}$$

Determining the degree of rarefaction in the gas is crucial for the aerodynamic and aerothermal analysis in this study. The Knudsen Number Kn, defined in Equation 3.17, is used to quantify rarefaction, with λ representing the mean free path and L_{ref} as the reference length [149]. Flow regimes are categorized based on the Knudsen number, as shown in Table 3.4 using thresholds defined by Bird [149]. Classical Navier-Stokes equations are applicable in the continuum regime but fail at extremely low densities, requiring alternative molecular models.

$$Kn = \lambda / L_{ref} \tag{3.17}$$

While the definition of L_{ref} is trivial and only depends on the topology of the geometry investigated in the flow analysis, λ is hereby defined according to the Enskog-Chapman viscosity coefficient for non-continuum conditions and Variable Hard Sphere (VHS) model illustrated in Equation 3.18 with the viscosity coefficient μ_{EC} in Equation 3.19 [150, 151]. Moreover, the viscosity of the gas in the continuum flow can be determined with Sutherlands' law μ_S also in Equation 3.19. The values required for the VHS model and Sutherlands' law are also reported in Table B.4 in terms of the viscosity index ω, Sutherlands' coefficient μ_0, reference temperature T_{ref} and molecular diameter d_m. In the notation adopted, the subscript ∞ refers to the freestream flow conditions and the mean quantities are indicated by the bar and take the same form as Equation 3.15 such that $\bar{\omega} = \frac{\sum_{j=1}^{J} \omega_j \cdot n_{0_j}}{\sum_{i=1}^{J} n_{0_j}}$ and $\bar{d}_m = \frac{\sum_{j=1}^{J} d_{m_j} \cdot n_{0_j}}{\sum_{i=1}^{J} n_{0_j}}$.

$$\lambda_{VHS} = \left(\frac{2\mu_{EC}}{15\rho}\right)(7-2\bar{\omega})(5-2\bar{\omega})\frac{1}{\sqrt{2\pi R T_\infty}} \tag{3.18}$$

$$\mu_{EC} = \frac{5\bar{m}}{16\pi \bar{d}_m^2}\sqrt{\pi R T_\infty} \qquad \mu_S = \frac{\mu_0 T_\infty^{1.5}}{T_\infty + T_{ref}} \tag{3.19}$$

Figure 3.12 shows the Knudsen Number for different L_{ref} representative of the decelerator's radius, indicating that a pure continuum flow characterization is inadequate during its EDL phases[149]. While the free-molecular-flow (FMF) regime is only encountered at the beginning of the entry phase for small systems, Near-continuum and transitional flow effects prevail at altitudes below 100-120 km and above 70-100 km, depending on system dimensions.

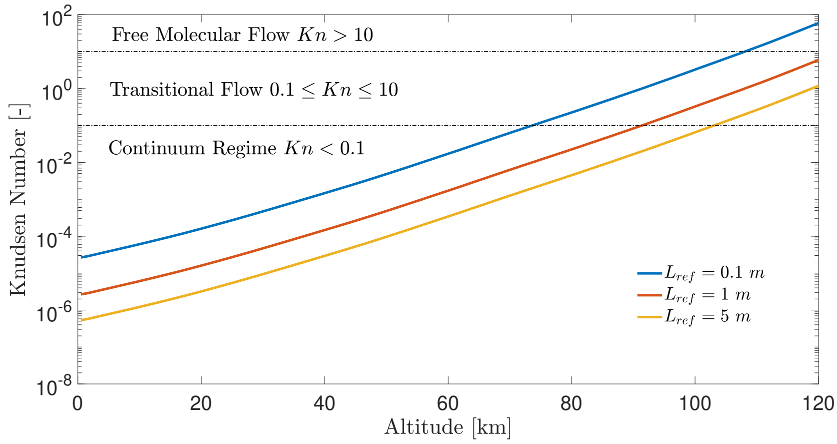

Figure 3.12.: Knudsen number as a function of altitude for varying reference lengths

Flow Regime	Knudsen Number
Continuum	$Kn < 10^{-1}$
Transitional	$10^{-1} \leq Kn \leq 10^1$
Free Molecular Flow	$Kn > 10^1$

Table 3.4.: Gas flow regimes based on the Knudsen number

The speed ratio, given by Equation 3.20, compares the bulk velocity of the flow to its thermal speed, representing the most probable molecular speed of the gas. It is used to assess aerodynamic characteristics in rarefied conditions, later discussed in subsection 3.5.3 and subsection 3.6.2. Figure B.2 shows the variation of the speed ratio with altitude on Mars for a constant V_∞.

$$s = \frac{V_\infty}{\sqrt{2TR/M_w}} \tag{3.20}$$

3.4. Planar Motion Trajectory

The determination of the aerodynamic, aerothermodynamic and deceleration loading experienced by the IAD vehicle during the EDL phases requires the definition of a trajectory profile. Given the absence of propulsive devices and assuming that no skipping flight occurs, the trajectory can either be considered a ballistic or gliding flight. In this work, the equations of planar motions are adopted since they enable closed-form expressions which are particularly useful in evaluating the performance of entry vehicles [152, 153]. However, planar motion equations do reduce the accuracy of gliding flight when lift is modelled, even though they do not impose any restrictions on ballistic flights. In fact, the vehicle's trajectory is constrained to a flat 2D plane in which no transverse forces are regarded. Moreover, the model assumes that the planet of interest is perfectly spherical and does not rotate. This neglects the centripetal and Coriolis accelerations. While the former is generally negligible when compared to the gravitational acceleration, the latter only generates an error in the initial phases of flight [154]. However, the error rapidly decreases as the aerodynamic forces dominate throughout flight [154]. No atmospheric winds are modelled in order to maintain the focus on the difference in atmospheric density, which is regarded as a more relevant parameter when assessing the robustness of the EDL architecture. Despite this approach is typically employed in the literature [155], the effect of zonal wind is further presented in section B.7 to show only slight variations to the trajectory profile, g-load and heat flux. When the velocity of the wind is the same as the vehicle's velocity, a greater inertial deceleration is experienced by the IAD [156], also leading to a higher impact speed which should be taken into account in the design process.

The derivation of the equations of motions for an entry vehicle, such as a stacked toroid, that has a constant mass with no thrust stems from the inertial reference frame in Figure 3.13. In the convention adopted, the velocity vector is oriented with respect to the local horizontal plane by the flight-path angle Γ, which is positive when the velocity vector is below the local horizontal [157]. The auxiliary angle ψ is also defined to determine how the velocity vector is oriented with regard to the inertial frame's fixed axis orientation. The complementary angle Θ is also defined to simplify the derivation [157]. Since the motion is assumed to be planar, the aerodynamic forces acting on the vehicle, namely lift and drag, can be resolved along the two coordinate axes $X - Y$ with the weight $W = mg$ component of the vehicle. By applying Newton's second law in the flightpath reference frame of the vehicle, the equations of motion are given in Equation 3.21 and Equation 3.22.

$$\frac{dV}{dt} = -\frac{D}{m} + g\sin(\Gamma) \tag{3.21}$$

$$mV\frac{d\psi}{dt} = L - mg\cos(\Gamma) \tag{3.22}$$

The deceleration experienced by the vehicle $\bar{a}$ may also be obtained by assuming equilibrium flight from Equation 3.23 [154] by re-arranging of Equation 3.21, which is normalised using the gravitational acceleration g.

$$\frac{\bar{a}}{g} = -\frac{1}{g}\frac{dV}{dt} = \frac{D}{W} + \sin(\Gamma) \tag{3.23}$$

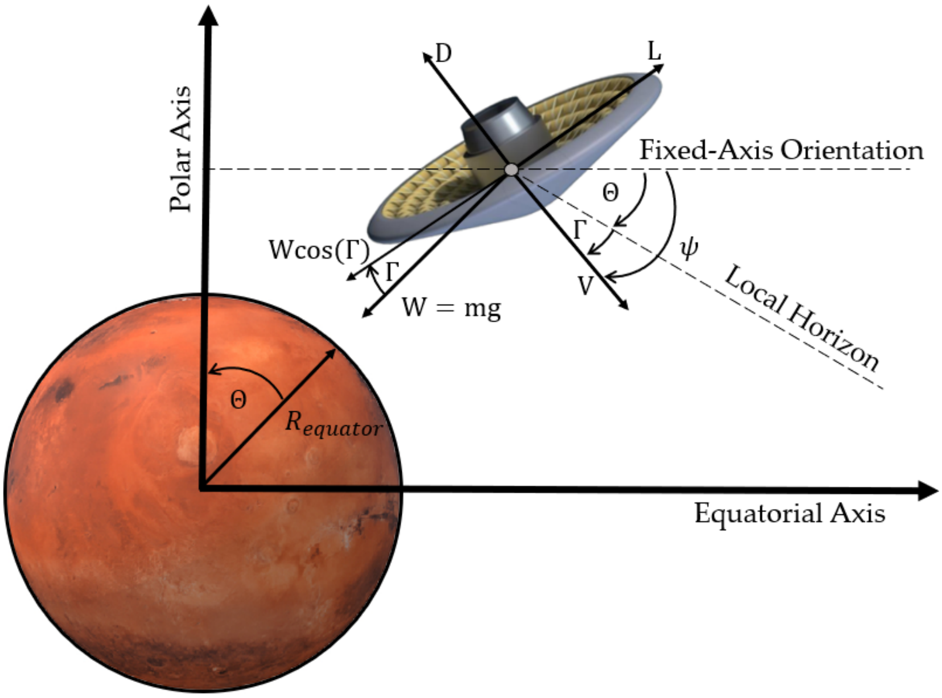

Figure 3.13.: Planar motion of entry trajectory

By applying the definition of the complementary angle with respect to the flight path angle and to the auxiliary angle used to orientate the vehicle in the inertial frame, the relation in Equation 3.24 is defined. This can be substituted in Equation 3.22 by taking the time derivative of the angles, such that the normal acceleration is given in Equation 3.25.

$$\psi = \Gamma + \Theta \rightarrow \frac{d\psi}{dt} = \frac{d\Gamma}{dt} + \frac{d\Theta}{dt} \tag{3.24}$$

$$V\left(\frac{d\Theta}{dt} + \frac{d\Gamma}{dt}\right) = -\frac{L}{m} + g\cos(\Gamma) \tag{3.25}$$

The drag in Equation 3.22 may also be written more conveniently in terms of the ballistic coefficient β in Equation 3.26 as shown in Equation 3.27. The mass can further be parted into the contribution of the payload and that of the IAD.

$$\beta = \frac{mg}{C_D A} = \frac{\left(m_{pay} + m_{IAD}\right) g}{C_D A} \tag{3.26}$$

$$\frac{dV}{dt} = -\frac{\rho g V^2}{2\beta} - g\sin(\Gamma) \tag{3.27}$$

Similarly, the lift coefficient can be expressed in terms of the lift-to-drag ratio as shown in Equation 3.28 which can then be substituted in Equation 3.27 to yield Equation 3.29.

$$C_L = \left(\frac{C_L}{C_D}\right) C_D = \left(\frac{C_L}{C_D}\right) \frac{A\beta}{W} \tag{3.28}$$

$$\frac{d\Gamma}{dt} = -\frac{d\Theta}{dt} - \left(\frac{\rho g}{2\beta}\right) \frac{C_L}{C_D} V + g\frac{\cos(\Gamma)}{V} \tag{3.29}$$

The kinematic equations can be defined from the horizontal and vertical components of the velocity vector by considering the geometry of the constrained motion [157]. Referring to Figure 3.13, the following two differential equations in Equation 3.30 and Equation 3.31 can be derived, where h is the altitude and $R_{equator}$ is the equatorial radius of the planetary body of interest, assumed to be perfectly spherical.

$$\frac{dh}{dt} = -V\sin(\Gamma) \tag{3.30}$$

$$\frac{d\Theta}{dt} = \frac{V\cos(\Gamma)}{R_{equator} + h} \tag{3.31}$$

Equation 3.31 can finally be substituted in Equation 3.29 for a complete description of the flight-path angle Γ as in Equation 3.32.

$$\frac{d\Gamma}{dt} = -\left(\frac{\rho g}{2\beta}\right) V \left(\frac{C_L}{C_D}\right) + \cos(\Gamma)\left[\frac{g}{V} - \frac{V}{R_{equator} + h}\right] \tag{3.32}$$

To model the variation of the gravitational acceleration over the trajectory's path, Equation 3.33 is employed. This removes the assumption of a constant value at sea level g_0 and leads to a slight improvement in accuracy.

$$g = \frac{R^2_{equator} g_0}{(R_{equator} + h)^2} \approx g_0\left[1 - \frac{2h}{R_{equator}}\right] \tag{3.33}$$

The three final equations of the 3-DOF plane motion are thus presented in Equation 3.21, Equation 3.30 and Equation 3.32. These are the equations of motions which are integrated numerically for a fixed-time step using the fourth-order Runge-Kutta method available in Matlab with the ode45 function [158]. This is a common approach taken to solve first-order ordinary differential equations where a small incremental step is implemented [159].

The inputs required for the trajectory motion are summarised as the entry altitude h_E, the entry velocity V_E, the system mass at the entry conditions m and the entry angle Γ_E. Further constraints may be identified for a penetrator mission, involving the desired speed and angle at the impact V_I and Γ_I. A summary of the trajectory parameters of Martian penetrator missions advocating for inflatable IADs is shown in Table B.2.

3.5. Aerodynamic Model

The main function of the method described in this section is that of predicting the aerodynamic loading experienced by the stacked toroid during its EDL phases in the Martian atmosphere. The loading conditions are conventionally reduced to the drag L and lift forces D, previously utilized in section 3.4, which may be defined as follows:

$$\begin{aligned} D &= \frac{1}{2}\rho V^2 A_{ref} C_D \\ L &= \frac{1}{2}\rho V^2 A_{ref} C_L \end{aligned} \tag{3.34}$$

The determination of the aerodynamic coefficients C_D and C_L, however, is rather difficult since it depends on the design of the stacked-toroid and the freestream conditions. Because of the difficulty of replicating representative entry high-speed flows in a laboratory experiment, high-fidelity aerodynamic is primarily derived using well-established computational methods such as Direct Simulation Monte Carlo (DSMC) and CFD. However, both methods are computationally prohibitive for MDAO. Panel methods are most frequently implemented due to their ability to readily model arbitrary geometries at much lower computational costs [160]. Engineering-based aerodynamic analyses are commonly performed using panel methods for spacecraft entering the Martian atmosphere [161, 162], however, these are only limited to the continuum hypersonic regime and do not account for rarefied effects. On the contrary, this work proposed a combination of panel codes applicable both to the continuum and rarefied regimes to extend the range of applicability of such methods. The output of the aerodynamic panel methods implemented can be described by the pair of pressure C_p and shear stress C_τ coefficients, which can be converted into drag C_D and lift C_L coefficients according to Equation 3.35 or vice-versa in Equation 3.36, and then in turn into axial C_A and normal C_N coefficients as in Equation 3.37 or the other way round in Equation 3.38.

$$\begin{bmatrix} C_D & C_L \end{bmatrix} = \begin{bmatrix} C_p & C_\tau \end{bmatrix} \begin{bmatrix} \sin(\theta) & \cos(\theta) \\ \cos(\theta) & \sin(\theta) \end{bmatrix} \tag{3.35}$$

$$\begin{bmatrix} C_p & C_\tau \end{bmatrix} = \begin{bmatrix} C_D & C_L \end{bmatrix} \begin{bmatrix} \sin(\theta) & \cos(\theta) \\ \cos(\theta) & -\sin(\theta) \end{bmatrix} \tag{3.36}$$

$$\begin{aligned} C_L &= C_N \cos(\alpha) + C_D \sin(\alpha) \\ C_D &= C_N \cos(\alpha) + C_A \cos(\alpha) \end{aligned} \tag{3.37}$$

$$\begin{aligned} C_N &= C_L \cos(\alpha) + C_D \sin(\alpha) \\ C_A &= -C_L \cos(\alpha) + C_D \cos(\alpha) \end{aligned} \tag{3.38}$$

The correct conversion from one non-dimensional coefficient to another requires the definition of adequate reference frames. In fact, when the geometry is generated in its file format, the vehicle is created in its geometric reference frame that follows the convention of the planar geometry used to create the surface of revolution. Such a frame must be first converted into a body frame and then related to the local wind direction. The flow is aligned with the IAD's negative x-axis direction in the geometric frame when both the angle of attack α and the sideslip angle β_s are zero. The body frame employed in this work follows the right-hand coordinate frame with the z-axis pointing towards the centre of the planetary body of interest, such as Earth or Mars, as shown in Figure 3.14, where the subscript b refers to the body frame and a to the air or wind frame. To transform the body frame into the geometric one, the transformation matrix in Equation 3.39 is first established, followed by the transformation vector from the wind frame to body frame also in Equation 3.40 for the given angle of attack α and side-slip angle β_s [163].

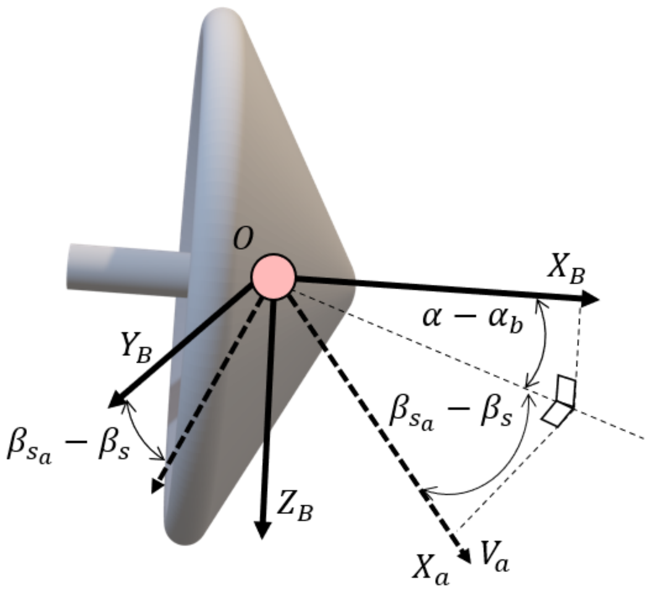

Figure 3.14.: Body-axis and wind-axis reference frames of the stacked-toroid

$$T_{gb} = \begin{bmatrix} 1 & 0 & 0 \\ 0 & -1 & 0 \\ 0 & 0 & -1 \end{bmatrix} \tag{3.39}$$

$$T_{bw} = \begin{bmatrix} \cos(\alpha)\cos(\beta_s) & -\cos(\alpha)\sin(\beta_s) & -\sin(\alpha) \\ \sin(\beta_s) & \cos(\beta_s) & 0 \\ sin(\alpha)\cos(\beta_s) & -\sin(\alpha)\sin(\beta) & \cos(\alpha) \end{bmatrix} \tag{3.40}$$

The transformation from the wind to the geometric frame, needed to transform the aerodynamic quantities of interest to the frame of the file containing the geometry, is therefore given by $T_{gw} = T_{gb}T_{bw}$. By defining the wind frame with the flow always in the same direction as the negative x-axis, the definition of the angle between the oncoming flow and the surface normal vector δ of each panel is given in Equation 3.41, where $\hat{n}_i$ is the normal vector of the panel in consideration of the mesh.

$$\delta_i = \arccos\left(-T_{gw}\begin{bmatrix} -1 \\ 0 \\ 0 \end{bmatrix} \cdot \hat{n}_i\right) \tag{3.41}$$

The parameter δ is the complementary angle to the panel angle θ relative to the freestream vector such that $\theta = \pi/2 - \delta$. Its usage is implemented in this work for clarity in the nomenclature as this is typically adopted in the literature.

The complimentary angle δ, in combination with the pressure and shear stress coefficients of each panel, indicated by the subscript i, can be used to compute the aerodynamic coefficients as in Equation 3.35. Different methods to obtain these coefficients are described in the following subsections. Once these are available, the global force C_f^g and moment C_M^g coefficients in the geometric axis can be computed from Equation 3.42 and Equation 3.43, where r_i is the vector of points from the geometric moment reference to the barycentre of the panel, and the unit vector $\hat{\tau} = \hat{n}_i \times \delta_i$ [163].

$$C_f^g = \begin{bmatrix} C_{f_x} \\ C_{f_y} \\ C_{f_z} \end{bmatrix} = \frac{1}{A_{ref}} \sum_{i=1}^{n} (C_{\tau_i} \hat{\tau}_i - C_{p_i} \hat{n}_i) A_i \tag{3.42}$$

$$C_M^g = \begin{bmatrix} C_{M_x} \\ C_{M_y} \\ C_{M_z} \end{bmatrix} = \frac{1}{A_{ref} L_{ref}} \sum_{i=1}^{n} r_i \times (C_{\tau_i} \hat{\tau}_i - C_{p_i} \hat{n}_i) A_i \tag{3.43}$$

The moment coefficients are first calculated with respect to the origin of the geometric frame, defined in the design object file in the construction phase of the planar outline, but can be later translated to the centre of gravity (CoG) of the body arbitrarily chosen, which may differ with the moment reference centre (MRC):

$$C_M^{CoG} = -r_{CoG} \times C_f + C_M^{MRC} \tag{3.44}$$

At the same time, the force and moment coefficients of the IAD can be computed in the body axis, indicated by the superscript b as C_f^b and C_M^b, using the transformation matrix in Equation 3.39 as shown in Equation 3.45 and Equation 3.46 respectively.

$$C_f^b = T_{gb}^{-1} C_f^g \tag{3.45}$$

$$C_M^g = T_{gb}^{-1} C_M^g \tag{3.46}$$

Following the convention adopted in aerospace vehicle design, the force coefficients are defined as the axial C_A, lateral C_Y and normal C_N force coefficients while the moment coefficients as the roll C_l, pitch C_m, and yaw C_n aerodynamic moment coefficients as shown in Equation 3.47:

$$\begin{aligned} C_f^b &= \{C_A, C_Y, C_N\} \\ C_M^b &= \{C_l, C_m, C_n\} \end{aligned} \tag{3.47}$$

A description of the approach taken to generate the surface mesh on the stacked toroid is therefore outlined in subsection 3.5.1, followed by the discussion on different GSI models that are implemented in this work to determine the aerodynamic coefficients in continuum and rarefied conditions.

3.5.1. Mesh Generation

Any arbitrary body may be divided into a set of discrete panels, each of which can be physically represented as a flat or slightly curved plate with one side exposed to the flow [164] to approximate the local shape of the geometry. The number of panels adopted and their dimensions are dependent on the trade-off made between accuracy and computational resources invested. This can be visualised from the expressions in Equation 3.42 and Equation 3.43 that contain the summation terms across the entire number of panels. In general, decreasing the size of the panels and increasing their number leads to a decrease in the numerical error [165]. It is also important to mention that one of the limitations of panel method codes is that they can only simulate convex shapes [164]. It is therefore possible to adopt the approach for a stacked-toroid since the vehicle would appear concave for $\beta_s = \pi$, which would occur only in unstable conditions that are not treated in this work.

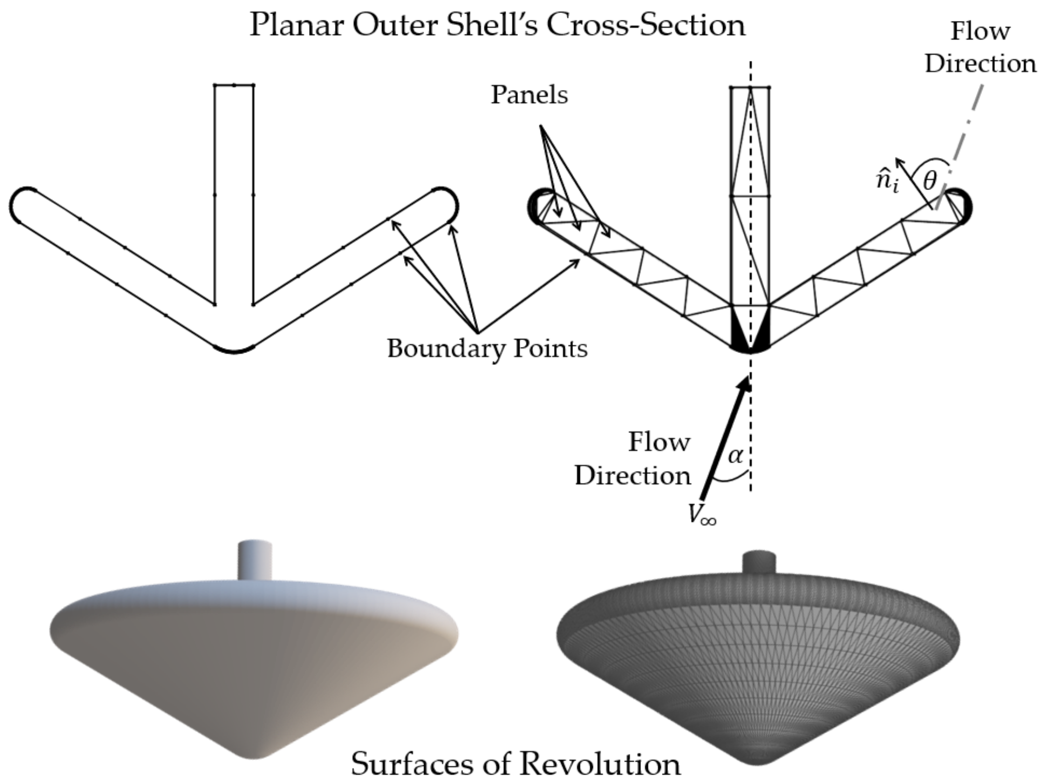

Figure 3.15.: Planar view of the stacked toroid's outer shell (top) and constructed surfaces of revolution (bottom) illustrating the Delaunay triangulation mesh used for the panel method

The initial phase to generate a suitable panel mesh of the stacked toroid is to create a surface of revolution of the planar parametrized geometry defined in section 3.1. This is easily attained by multiplying x Cartesian coordinates of the 2D profile by the cosine of an arbitrary variable ϕ spanning from 0 to 2π with ϕ_n intervals such that the x variables are rotated around the y-axis in the surface of revolution. Then, the y Cartesian coordinates are multiplied by a matrix of $(1 \times \phi_n)$ dimensions to ensure that the y-coordinate remains constant throughout the surface generation. Finally, the x-axis is multiplied by the sine of the same variable ϕ to obtain the z-coordinate values. The new set of three coordinates can be used as inputs to the "surface" function in Matlab to generate a 3D surface of revolution, where the mesh corresponds to the tessellated quad-panels defined by the variable ϕ.

However, since triangulated panels are required for the generation of a stereolithography (STL) file, the Delaunay triangulation function available in Matlab is used to generate triangular elements formed by the connection of points satisfying the Delaunay criterion for which no point lies inside the circumcircle of any triangle [166]. The STL format class is chosen because it captures the mesh information whilst being compatible with a wide range of software and Computer-aided design (CAD) applications. A library of associates functions is also available in Matlab to detect and list improper features in an STL file, such as non-manifold vertices, to ensure the correct generation of the object and mesh. The geometry can therefore be easily used by the other MDAO disciplines or transferred to external users to assure reproducibility and validation of the results attained with relatively compact file sizes. An illustration of the triangulation algorithm applied to a planar stacked toroid's outer shell and to its surface of revolution is shown in Figure 3.15, where it appears evident that the mesh refinement is given by the number and location of the boundary points. In the example illustrated an increased level of refinement is implemented in the shoulders of the outermost torus and in the nose cone.

The local inclination angle is shown in Figure 3.16 in relation to the freestream velocity and outward normal vector for the 3D surface of revolution.

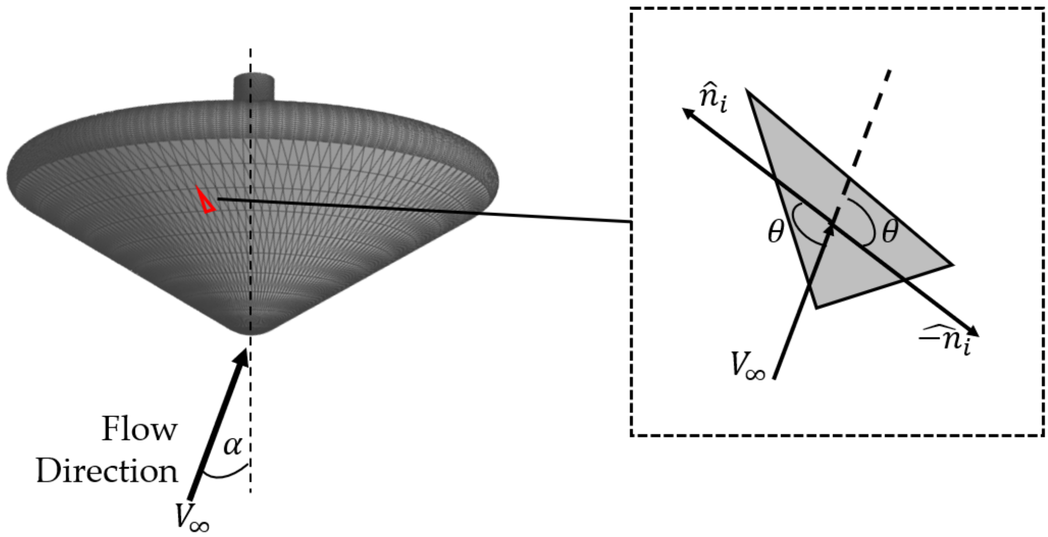

Figure 3.16.: Magnified view of the local inclination angle on a triangulated panel of the 3D stacked toroid's surface

3.5.2. Continuum Regime

To analyze the aerodynamic flow around stacked-toroid configurations in hypersonic conditions, the modified Newtonian flow theory [167] is combined with the panel method. This approach drastically reduces computational requirements compared to Navier-Stokes solvers. Newton's model assumes rectilinear flow motion, treating the fluid as linear particles that lose normal momentum upon contact with a solid body but conserve tangential momentum [165].

The derivation of the modified Newtonian method, which is a modification of the original Newtonian method, is presented in section C.3. The resulting pressure coefficient, as given by Equation 3.48 with Equation 3.49 substituted as the value for $C_{p,max}$, is used to calculate the drag coefficient C_D and lift coefficient C_L in Equation 3.50. In this method, the shear stress coefficient is always assumed to be zero, as shown in Equation 3.48. Anderson [165] emphasizes the suitability of this method for hypersonic flows, as its accuracy improves for high values of the Mach number ($M_\infty \to \infty$) and a specific heat ratio approaching unity ($\gamma \to 1$).

$$C_p = C_{p,max} \sin^2(\theta) \quad C_\tau = 0 \tag{3.48}$$

$$C_{p,max} = \frac{2}{\gamma M_\infty^2} \left\{ \left[\frac{(\gamma+1)^2 M_\infty^2}{4\gamma M_\infty^2 - 2(\gamma-1)} \right]^{\frac{\gamma}{\gamma-1}} \left[\frac{1-\gamma+2\gamma M_\infty^2}{\gamma+1} \right] - 1 \right\} \tag{3.49}$$

$$C_D = C_p \sin(\theta) \quad C_L = C_p \cos(\theta) \tag{3.50}$$

Referring back to the simple 2D discretisation illustrated in Figure 3.15, the modified Newtonian method can be adapted to an arbitrarily shaped 3D body according to Figure 3.17. Given a point P on the body of the stacked-toroid, the vector dot product of the freestream velocity with the unit normal vector to the surface tangent to P is outlined in Equation 3.51, where ϕ is the angle between $\hat{n}$ and V_∞. The plane may also be defined by the panel inclination angle $\theta = \pi/2 - \phi$ as in Equation 3.52 [165].

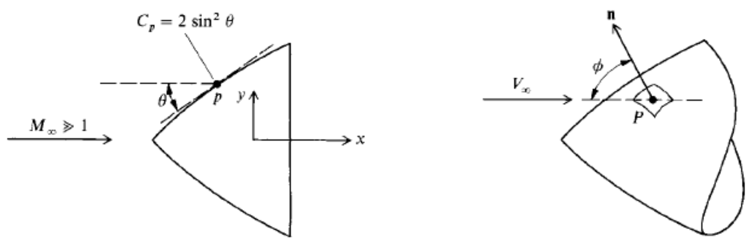

Figure 3.17.: Adaptation of 2D geometry (left) to 3D flow (right) [165]

$$V_\infty \cdot \hat{n} = |V_\infty| \cos(\phi) = |\sin\left(\frac{\pi}{2} - \phi\right)| \tag{3.51}$$

$$V_\infty \cdot \hat{n} = |V_\infty| \sin(\theta) \to \sin(\theta) = \frac{V_\infty}{|V_\infty|} \cdot \hat{n} \tag{3.52}$$

3.5.3. Rarefied Regime

While the modified Newtonian theory is applicable to hypersonic continuum flows, it fails to model rarefied effects. When the Knudsen number $Kn > 10$, the flow shall be regarded as being in FMF, and the aerodynamic interactions are dominated by the collisions of the atmospheric particles with the surface of the stacked toroid, as opposed to intermolecular collisions which are neglected. To capture the physical behaviour of such collisions, different gas-surface interaction (GSI) models are available in the literature with varying interactions and re-emission characteristics [168]. Most of the models implemented in this work and hereby described, rely on the concept of energy accommodation coefficient α_E to relate the GSI model to the material by determining the portion of energy transfer from the gas mixture to the surface of the vehicle [169]. The quantity is defined in Equation 3.53, where E_i is the energy of the incoming flow particles, E_r is the energy of the reflected particles and E_w is the energy that the reflected particles would have had, had they been fully accommodated to the wall temperature.

$$\alpha_E = \frac{E_i - E_r}{E_i - E_w} \tag{3.53}$$

The variation of the aerodynamic coefficients is found to be significantly affected on Mars with respect to the normal and tangential components of the energy and momentum coefficients [170]. Determining its magnitude, therefore, is very important. In the literature, it is well-established that the value would lay somewhere between 0.8 and 1 [170–172]. However, most analyses retrieved in the literature [173] assume energy and momentum accommodation coefficients of 1.0, which is considered a conservative value since it allows to receive the greatest amount of heating and the lowest amount of drag [170]. The choice of the GSI model depends on several factors such as the surrounding flow conditions and the materials used for the outer IAD shell. All five GSI models identified in the literature [174] are hereby presented and implemented for the purposes of verification. The ADBSat code[1] is integrated into the present environment for such models. In Section 4.3, a comparison with high-fidelity data will be conducted to determine the most suitable model for accurately representing the stacked-toroid class of vehicles. The accuracy of each model will be evaluated by calculating the percentage error against higher-fidelity results obtained from independent literature studies. In the case where sufficient information is available for Mars entry, the model exhibiting the lowest percentage error will be selected for integration into the MDAO framework of this research.

Sentman's Model

The first model implemented is the one proposed by Sentman [175] which assumes fully diffusive re-emission of the colliding gas particles from the vehicle's wall whilst accounting for the relative motion of the IAD with respect to the atmosphere. The pressure coefficient estimated using the Sentman model is given in Equation 3.54 while the shear stress contribution is in Equation 3.55. The expressions depend on the angle δ, the speed ratio s, wall temperature T_w, the incident gas temperature T_{in} assumed to be equal to the freestream temperature T_w in FMF [176], the error function $erf(x)$ defined in Equation 3.56 and the accommodation coefficient α_E taken to be equal to unity.

[1] Code retrieved from https://github.com/nhcrisp/ADBSat Date Accessed: 10/05/2023

$$C_p = \left(\cos(\delta)^2 + \frac{1}{2s^2}\right) \cdot (1 + erf(s\cos(\delta)) + \frac{\cos(\delta)}{s\sqrt{\pi}} \exp\left(-s^2\cos(\delta)^2\right)$$
$$+\frac{1}{2}\sqrt{\frac{2}{3}\left(1 + \frac{\alpha_E T_w}{T_{in} - 1}\right)} \left[\sqrt{\pi}\cos(\delta)\left(1 + erf(s\cos(\delta))\right) + \frac{1}{s}\exp\left(-s^2\cos(\delta)^2\right)\right] \tag{3.54}$$

$$C_\tau = \sin(\delta)\cos(\delta)\left(1 + erf(s\cos(\delta))\right) + \frac{\sin(\delta)}{s\sqrt{\pi}} exp(-s^2\cos(\delta)^2) \tag{3.55}$$

$$erf(x) = \frac{2}{\sqrt{\pi}} = \int_0^\pi exp(-t^2)dt \tag{3.56}$$

Schaaf and Chambre's Model

An additional model which is widely used in rarefied conditions is that proposed by Schaaf and Chambre [177]. The mathematical model, described in Equation 3.57 and Equation 3.58 for C_p and C_τ, differs slightly from Sentman's model as it presents two coefficients to model the normal σ_N and tangential σ_T momentum transfer, which allow for a characterisation of the force on the surface attainable experimentally [169]. Besides this fundamental difference, which removes any assumptions on the nature of the collisions, the model similarly depends on the wall temperature T_w, the ambient temperature T_∞, speed ratio s and angle δ.

$$C_p = \frac{1}{s^2}\left[\left(\frac{2-\sigma_N}{\sqrt{\pi}} s\cos(\delta) + \frac{\sigma_N}{2}\sqrt{\frac{T_w}{T_\infty}}\right) exp(-s^2\cos(\delta)^2)\right.$$
$$\left.+\left([2-\sigma_N]\left[s^2\cos(\delta)^2 + \frac{1}{2}\right] + \frac{\sigma_N}{2}\sqrt{\frac{\pi T_w}{T_\infty}} s\cos(\delta)\right)\left(1 + erf(s\cos(\delta))\right)\right] \tag{3.57}$$

$$C_\tau = \frac{\sigma_T \sin(\delta)}{s\sqrt{\pi}}\left[exp(-s^2\cos(\delta)^2) + s\sqrt{\pi}\cos(\delta)(1 + erf(s\cos(\delta)))\right] \tag{3.58}$$

Cercignani-Lampsi-Lord's Model

To remove the assumptions of adsorption and the dependency of the interaction of each gas particle with the surface, the Cercignani-Lampsi-Lord (CLL) [178] offers one of the most successful kernel-based representations of GSI based on experimental results. Its application is primarily directed at DSMC problems, where its closed-form solutions are based on Schaaf and Chambre's model [169]. Differently from the other models, the CLL method takes into account the characteristics of each individual species j present in the atmospheric gas. For a given normal accommodation coefficient α_N and tangential momentum accommodation coefficient σ_T, the pressure coefficient of each species is given in Equation 3.59, which collapses to Equation 3.57 when $\alpha_N = 1$ with α_N being substituted for σ_N, and the shear stress coefficient in Equation 3.60. In addition to the dependency on α_N, the speed ratio s, wall temperature T_w, and freestream temperature T_∞, the model depends on the parameters Y_1 and Y_2 given respectively in Equation 3.61 and Equation 3.62.

$$C_{p,j} = \frac{1}{s^2}\left[(1+\sqrt{1-\alpha_N}\Upsilon_1 + \frac{1}{2}\left(exp(-\iota_j(1-\alpha_N)^{\chi_j}\left(\frac{T_w}{T_\infty}\right)^{\delta_j}\frac{\zeta_j}{s}\right)\left(\sqrt{\frac{T_w}{T_\infty}}\sqrt{\pi}\Upsilon_2\right)\right] \quad (3.59)$$

$$C_{\tau,j} = \frac{\sigma_T \sin(\delta)}{s}\Upsilon_2 \quad (3.60)$$

$$\Upsilon_1 = \frac{1}{\sqrt{\pi}}\left[s\cos(\delta)exp(-s^2\cos(\delta)^2) + \frac{\sqrt{\pi}}{2}\left(1+2s^2\cos(\delta)^2\right)(1+erf(s\cos(\delta)))\right] \quad (3.61)$$

$$\Upsilon_2 = \frac{1}{\sqrt{\pi}}\left[exp(-s^2\cos(\delta)^2) + s\sqrt{\pi}\cos(\delta)(1+erf(s\cos(\delta)))\right] \quad (3.62)$$

The terms ι_j, χ_j, ζ_j and δ_j which also appear in Equation 3.59 are parameters dependent on the species which are obtained by Walker, Metha and Koller [179], as reported in Table B.6, by data-fitting with DSMC results. A strong limitation of these parameters, however, is that they are limited to the gas species present in the Earth's atmosphere and that, therefore, no coefficients for CO_2 have been retrieved from the literature. The total aerodynamic coefficients are computed as weighted sums of each individual gas species' contribution as shown in Equation 3.63, where M_{avg} is the average mass of the mixture, Ξ_j the mole fraction of the species and m_j is the species mass. A similar approach can be established for the shear stress contribution.

$$C_p = \frac{1}{M_{avg}}\sum_{j=1}^{J}\Xi_j m_j C_{p,j} \quad (3.63)$$

Storch's Model

The model proposed by Storch [180] is described by the expression in Equation 3.64 and Equation 3.65, where the dependency of the pressure coefficient and shear stress coefficient coincides with that of the other models, on the angle δ, the coefficient α_E, the wall temperature T_w and the freestream temperature T_∞. In addition, the effect of the incident velocity V_∞ and the average velocity of the molecules diffusely reflected at the wall $V_w = \sqrt{\frac{\pi R T_w}{2}}$ is taken into consideration. Storch's model is based on the assumption of hyperthermal flow [163, 180]. This means that the thermal velocity of the gas is significantly larger than the bulk velocity. From a mathematical standpoint, this occurs when the speed ratio in Equation 3.20 is small. This assumption may not be accurate for a body travelling at large speeds, and its validity must be assessed.

$$C_p = 2\cos(\delta)\left(\sigma_N\frac{V_w}{V} + [2-\sigma_N]\cos(\delta)\right) \quad (3.64)$$

$$C_\tau = 2\sigma_T\sin(\delta)\cos(\delta) \quad (3.65)$$

Cook's Model

The final analytical method investigated is the one proposed by Cook [181] which, similarly to Storch's expression, is only applicable to hyperthermal flows. Cook's expressions for the drag and lift coefficients are given in Equation 3.66 and Equation 3.67, which are derived from Sentman's model in Equation 3.54 and Equation 3.55 for hyperthermal conditions as $s \to 0$. The parameters δ, α_E, T_w and T_∞ are needed to compute the aerodynamic coefficients [163, 164].

$$C_D = 2\cos(\delta)\left(1 + \frac{2}{3}\cos(\delta)\sqrt{1 + \frac{\alpha_E T_w}{T_\infty - 1}}\right) \tag{3.66}$$

$$C_L = \frac{4}{3}\sin(\delta)\cos(\delta)\sqrt{1 + \frac{\alpha_E T_w}{T_\infty - 1}} \tag{3.67}$$

3.5.4. Transitional Regime

Due to the complex nature of the transitional flow regime, it may not be possible to directly determine the aerodynamic loading by means of low-fidelity analytical expressions and it might instead be a necessity to rely on high-fidelity simulations. As an alternative, bridging function relations are frequently employed to provide predictions between FMF and continuum flows. Such functions, however, depend on empirical parameters that must be derived from experimental data, flight measurements and computational results to be specifically tuned to a given class of vehicles. The sine-squared function of Wilmoth [182] in Equation 3.68 is often used for $0 < a_1 + a_2 \log_{10}(Kn) < \frac{1}{2}$, where the parameters a_1 and a_2 are typically fit to the available data.

$$C_x = C_{x,cont} + \left\{(C_{x,fmf} - C_{x,cont})\sin^2\left(\pi[a_1 + a_2\log_{10}(Kn)]\right)\right\} \tag{3.68}$$

It is noted that Equation 3.68 is only valid for the condition satisfied in Equation 3.69 [183].

$$0 \leq a_1 + a_2\log_{10}(Kn) \leq \frac{1}{2} \tag{3.69}$$

Equation 3.68 enables the computation of any aerodynamic quantity in the transitional flow at any given Kn value for one panel based on its continuum and rarefied performance. Nevertheless, the Kn limits in Table 3.4 ($Kn_{cont} \leq Kn \leq Kn_{fmf}$), and associated altitude, for the FMF and continuum regime may be difficult to track, and the choice of Kn_{cont} and Kn_{fmf} is of significant relevance. In the literature, different limits have been employed. The analysis of the Space Shuttle Orbiter's flight data in Earth orbit indicated the utilisation of $Kn_{cont} = 1 \cdot 10^{-3}$ and $Kn_{fmf} = 10$ [184], though Blanchard suggested increasing the FMF limit to $Kn_{fmf} = 100$ for the same vehicle [185]. In the case of the Martian mission Viking I, $Kn_{cont} = 2 \cdot 10^{-3}$ and $Kn_{fmf} = 25$ were used [183], while the continuum bound of $Kn_{cont} = 1 \cdot 10^{-3}$ was estimated for Pathfinder, Mars'01 Orbiter and Microprobe on Mars, in addition to the Stardust reentry mission [183]. Since no definitive bounds can be inferred from the values obtained in the literature, this work adopts the values in Table 3.4.

Once the boundary cases are identified, for the rarefied and continuum regimes respectively, the expression requires careful identification of the parameters a_1 and a_2. These, in fact, should be analytically fit to the high-fidelity data available in the transitional flow specifically for the class of stacked-toroid vehicles. The DSMC data obtained and discussed in [56] is employed in the next chapter to identify such parameters. For this purpose, the non-linear least square-method is employed as a regression model to calculate the coefficients that are most suited to a given set of input data x_{DSMC} and y_{DSMC}. The nonlinear function lsqcurvefit in MATLAB solves the problem in Equation 3.70 to find coefficients a_1, a_2 with the matrices $C_x((a_1, a_2), x_{DSMC})$ being of the same size as y_{DSMC} for an initial estimate of a_1 and a_2.

$$\min_x ||C_x((a_1, a_2), x_{DSMC}) - y_{DSMC}||_2^2 = \min_x \sum_i (C_x((a_1, a_2), x_{DSMC_i} - y_{DSMC_i})^2 \tag{3.70}$$

3.5.5. Shading Algorithm

Determining elemental flow exposure, often known as shading, is a typical issue with discrete element estimation of aerodynamic forces [186]. Because of the rectilinear motion of the flow streamlines, the panel method assumes that the flow does not wrap around the edge of the stacked-toroid to impact its back surface. A shaded region is therefore created behind the frontal region directly in contact with the airstream where no momentum transfer occurs. It follows that the local pressure in the shadowed region can be assumed to be equivalent to the freestream pressure $p = p_\infty$ and that, therefore, the pressure coefficient is equal to zero $C_p = 0$ according to Equation C.32 as depicted in Figure 3.18 for the modified Newtonian method. Equation 3.52 enables the evaluation of the correct inclination angle given a panel and the incoming flow velocity vector. The back-face culling algorithm [187] may then be used to select the flow-facing surfaces on the $i-th$ panel in Equation 3.71.

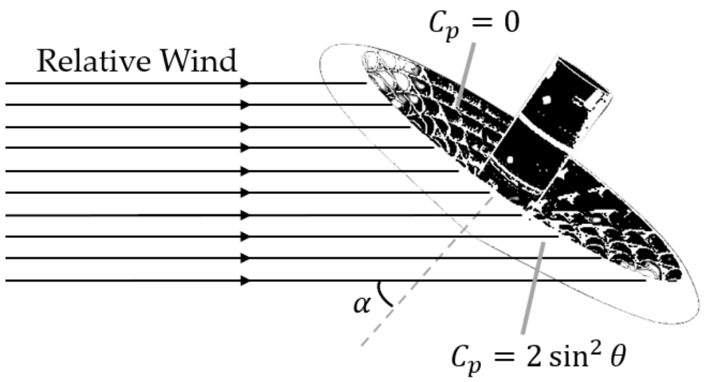

Figure 3.18.: Shadow region according to Newtonian flow theory

$$\frac{V_\infty}{|V_\infty|} \cdot \hat{n}_i \begin{cases} < 0 & \text{flow-facing} \\ \geq 0 & \text{back-facing} \end{cases} \tag{3.71}$$

The simple shading algorithm described in Equation 3.71, however, is only dependent on the orientation of each individual panel with respect to the incoming flow. This means that this method is unable to discern the panels which are shielded from the flow by upstream bodies. In the case of a stacked-toroid, the front aeroshell may completely or partially cover the payload which would not contribute to the aerodynamic analysis. For this study, it is crucial to be able to identify which components are not exposed to the incoming flow, and if done incorrectly, this might slow down processing [186].

The back-face culling algorithm is therefore supported by an additional method developed for the ADBSat code[2] [163, 164, 174], in which only the set of panels that meet the condition $\frac{V_\infty}{|V_\infty|} \cdot \hat{n}_i < 0$, referred to as "group A", can be shadowed and only those panels that meet the condition $\frac{V_\infty}{|V_\infty|} \cdot \hat{n}_i \geq 0$, or "group B" can shadow other panels. The region of interest for a stacked-toroid with zero angle-of-attack is shown in Figure 3.19.

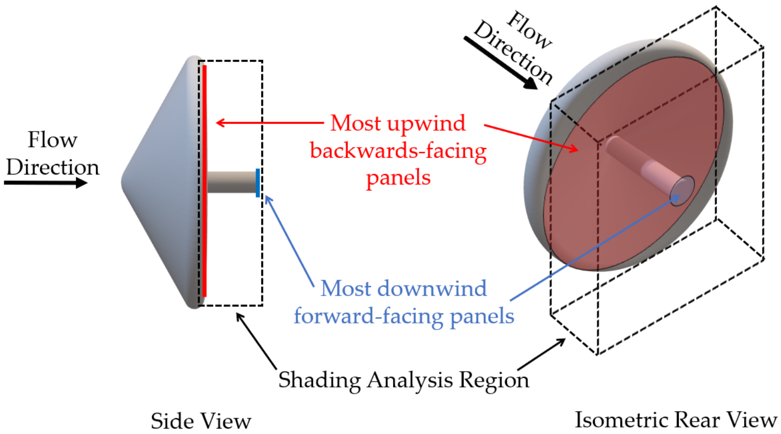

Figure 3.19.: Region of shading analysis for complementary algorithm

The following procedure is thus followed according to the approach described in [163]:

1. The identification of the most downwind panel in set A (Panel Y) and the most upwind panel in set B (Panel Z) is conducted
2. The set A is reduced to A' by realising that only the panels downwind of Z can be shadowed. At the same time, set B is reduced to B' in which only the panels upwind of Y can be used to shadow other panels.
3. Each panel in set A' is checked against B' to identify the upwind panels. The barycentre of this subset is assessed for the 2D projection of each sub-set panel. If the barycentre is within the projection, then it is considered as being shadowed and its aerodynamic contribution is zero, otherwise, the next panel is evaluated.

Sinpetru et al. [163] remark that the algorithm is not a foolproof method of shading determination and may be inaccurate for coarse meshes with large flat sides. While this should not be the case for a stacked-toroid IAD, verification shall be conducted in the next chapter.

[2]Shadow analysis available at https://github.com/nhcrisp/ADBSat/blob/master/toolbox/calc/shadowAnaly.m Date Accessed: 10/05/2023

3.5.6. Aerostability

Equation 3.43 can be used to obtain the C_M about the MRC, taken to be at the origin of the constructed surface of revolution. When the position of the CoG is known, the moment coefficient can also be computed about this point with Equation 3.44. The moment coefficient is of interest to determine the IAD's aerodynamic stability. As discussed by Mostaza-Prietro and Roberts [188] for spacecraft subjected to aerodynamic torques, the derivatives of the pitching moment coefficient with respect to the angle attack $\frac{\partial C_m}{\partial \alpha}$ and the derivative of the yawing moment with respect to the sideslip angle $\frac{\partial C_n}{\partial \beta_s}$ must be negative as shown in Equation 3.72.

$$\frac{\partial C_m}{\partial \alpha} < 0 \quad \frac{\partial C_n}{\partial \beta_s} < 0 \tag{3.72}$$

Additional aerostability parameters can be calculated, but they rely on knowing the moment of inertia and angular velocity of the vehicles, which are often unavailable during the early design stages. Therefore, it is common practice to focus on longitudinal static stability, which is considered sufficient in such cases. To achieve this, the coefficient of pressure (CoP) must be defined. The CoP represents the point where the average pressure force acts. In the body-frame orientation depicted in Figure 3.20, the y-coordinate of the CoP is defined for a continuous body as a function of the pressure distribution $p(y)$ as in Equation 3.73. This is then approximated for a discretised geometry made of panels based on each panel's C_P [189].

$$y_{CoP} = \frac{\int y p(y) dy}{\int p(y) dy} \rightarrow y_{CoP} = \frac{\sum y_i C_{p_i}}{\sum C_{p_i}} \tag{3.73}$$

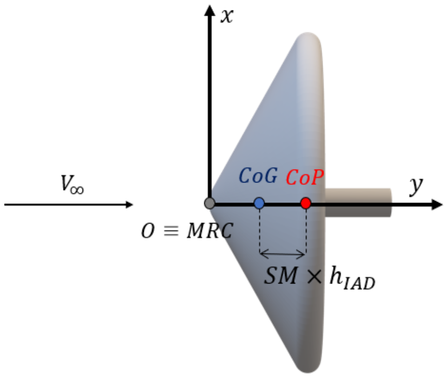

Figure 3.20.: Longitudinal Stability of Stacked-toroid

The longitudinal static stability of the decelerator is attained by ensuring that the CoG is in front of the CoP, as in Figure 3.20. The stability is increased by further shifting the CoG towards the nose cone, thus increasing the distance between the CoP and CoG, defined as static margin SM in Equation 3.74 which is normalised by the decelerator's height. A larger value of SM is desirable for aerostability because it ensures that the vehicle consistently returns to a flow-pointing attitude when subjected to disturbances [165].

$$SM = (y_{CoP} - y_{CoG}) / h_{IAD} \tag{3.74}$$

3.6. Aerothermodynamic Model

The purpose of the aerothermal analysis for an entry vehicle is that of estimating the convective heat loading experienced at the surface of the decelerator itself to quantify then the amount of heat protection required to ensure that the temperature experienced throughout the trajectory is within the requirements. Therefore, the main quantities of interest are the heat flux perceived by the IAD during the EDL phases and the total heat load accumulated throughout the trajectory. The radiative heat contribution is considered of minor importance for low speeds ($V < 10 km/s$ for Earth, $V < 2 km/s$ for Mars) [165, 190, 191], but these are implemented for completeness [190]. Similarly to the aerodynamic model discussed in section 3.5, high-fidelity methods such as CFD and DSMC are prohibitive for an MDAO framework due to their computational cost. It would not be feasible, in fact, to compute the aerothermal loads acting on the vehicle at every point in the trajectory. To readily evaluate such quantities, analytical expressions can be employed at the cost of fidelity and results accuracy which shall be further investigated in the verification and validation stages in section 4.4.

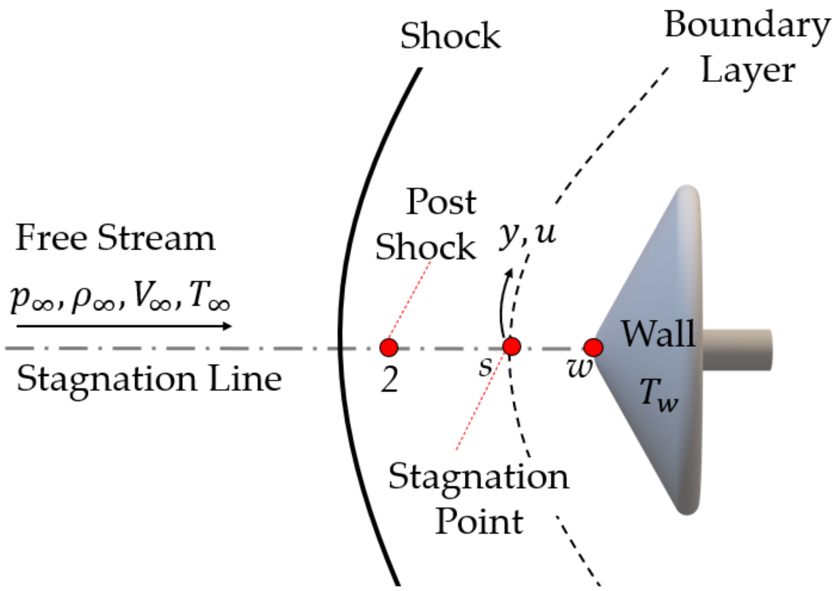

Figure 3.21.: Stagnation point on Stacked-toroid at $\alpha = 0°$ for heat-flux relationships

The stagnation region of an entry vehicle is chosen as the critical point to estimate the aerothermal loads in hypersonics and spacecraft design since it reaches the highest enthalpy levels, being located directly downstream of the shock layer [165] as shown in Figure 3.21. Simple expressions to evaluate the convective heating to the stagnation point of blunt axisymmetric bodies have thus been widely explored in the literature for wide ranges of different thermodynamic conditions. Lees [192] proposed analytical calculations of heat transfer for chemically reactive shock layers. Fay and Riddell [193] later developed a stagnation-heat-flux correlation applicable to dissociated air grounding on the boundary-layer theory for reacting flows. This latter relation was further explored to develop simplified empirical expressions as a function of the freestream density and velocity [194], such as the Kemp and Riddell [195] relation, which is however only applicable to Earth re-entry. A more generalised formulation that was also suitable to different planetary entry scenarios was formulated by Chapman et al. [196], requiring a set of parameters specific to the given atmospheric conditions. An empirical approach was later proposed by Sutton and Graves [197] to neglect the hot-wall correction term in Chapman's model.

To provide a thorough description of the analytical models employed in this work and their underlying assumptions and limitations, the definition of some fundamental aerothermal quantities is required. The first one is the Prandtl number Pr in Equation 3.75, a dimensionless number that represents the ratio of the momentum diffusivity to thermal diffusivity [165], where the viscosity μ can be obtained using Sutherland's model in Equation 3.19 for continuum conditions with μ_s and for rarefied flows with μ_{EC}, and the heat capacity c_p is given in Equation 3.16. The conductivity of the gas can be approximated by the empirical formula in Equation 3.76 for perfect air on Earth [157]. An equivalent expression is given for Mars in Equation 3.77 by fitting the Chapman-Enskog approximation results retrieved from [198] for 50 K $\leq T \leq$400 K.

$$Pr = \frac{c_p \mu}{k} \tag{3.75}$$

$$k_{air} = \frac{2.64638 \cdot 10^{-3} T^{1.5}}{T + 245.4 \cdot 10^{-12T^{-1}}} \tag{3.76}$$

$$k_{mars} = 6 \cdot 10^{-8} T^2 + 8 \cdot 10^{-5} T + 0.0013 \tag{3.77}$$

The dimensionless Lewis number is thus defined in Equation 3.78 as a function of the Prandtl number, the viscosity of the fluid, its density and the mass diffusivity D_m [165] to account for the thickness of a thermal boundary layer.

$$Le = \frac{\mu}{\rho D_m Pr} \tag{3.78}$$

Finally, the heat load experienced by a stacked toroid throughout its trajectory is defined as the total amount of heat flux the vehicle is exposed to throughout its trajectory, resulting in the time-integration of the heat flux as described by Equation 3.79.

$$Q = \int_0^{t_{end}} q(t) dt \tag{3.79}$$

Besides characterising the aerothermal performance of the vehicle, the determination of the heat fluxes perceived by the wall of the decelerator is of high importance to size the F-TPS. By considering energy equilibrium at the surface, Equation 3.80 must be satisfied, where q_{rerad} is the heat re-radiated to the environment and q_{cond} the heat conducted to the payload and other inner sections of the IAD.

$$q_{cond} = q_c + q_r - q_{rerad} \tag{3.80}$$

3.6.1. Convective Heating in Continuum Regime

Numerous convective heating relations have been proposed in the literature for the stagnation point of blunt vehicles. However, the five approaches discussed in the preceding paragraphs have gained significant recognition in (re-)entry applications [199]. While certain models may appear more suitable than others for specific Mars studies, the selection should also consider the entry trajectory of the case study. By investigating and comparing all the models with flight data in section 4.4, a wide range of conditions can be addressed due to the varied applicability and different assumptions inherent in each model. Similar to the approach used in aerodynamic modelling, the selection of the model to be integrated into the present framework among multiple options is based on the available information for Mars entry and the model's lowest positive percentage error in both heat flux and heat load under the most representative aerothermal loading conditions expected for the case study. This ensures that the analytical solution provides a slight overestimation without leading to excessive overdesigns of the F-TPS.

Fay-Riddell

The Fay-Riddell fully-catalytic expression in Equation 3.81 is notoriously employed to theoretically relate the stagnation enthalpy, or total temperature, to the heat flux to the stagnation point for air mixtures. This limits the applicability of Fay-Riddell's model to re-entry simulations. For the specific case in which no chemical reactions are expected, which is reasonable for moderate temperatures, the Lewis number in Equation 3.81 is set equal to unity ($Le = 1$), such that Fay-Riddell's expression is simplified to Equation 3.82 [195].

$$q_s = 0.763 \times Pr^{-0.6} (\rho_w \mu_w)^{0.1} (\rho_s \mu_s)^{0.4} \left[1 + (Le^{0.52} - 1) \left(\frac{h_D}{h_s} \right) \right] (h_s - h_w) \sqrt{\left(\frac{du}{dy} \right)_s} \tag{3.81}$$

$$q_s = 0.763 \times Pr^{-0.6} (\rho_w \mu_w)^{0.1} (\rho_s \mu_s)^{0.4} (h_s - h_w) \sqrt{\left(\frac{du}{dy} \right)_s} \tag{3.82}$$

The estimation of the thermodynamic properties in Equation 3.81 and Equation 3.82 at the stagnation point, indicated by the subscript s, and at the wall, marked by the subscript w according to the nomenclature in Figure 3.21 is addressed in section C.4.

The effectiveness of the model is reduced at large Mach numbers, where the perfect gas assumptions fail due to the presence of real gas effects such as dissociation. The Fay-Riddel model in fact is unable to effectively capture the multi-species dissociation effects of the flow. Moreover, the Fay Riddell relation has a theoretical maximum limit of total enthalpy of 23 MJ/kg for air [200]. As such, the results obtained using Equation 3.82 are taken with caution and verified by comparison with other models.

Detra-Kemp-Riddell

Following Fay and Riddell's model [193], a simplified empirical model was proposed by Detra-Kemp-Riddell [195, 201] grounding on the experimental shock tube data measured by Rose and Stark [202]. The super-catalytic expression, given in Equation 3.83, is only applicable to the Earth's atmosphere and is based upon the heat transfer to a cold-wall sphere, in which a correction coefficient that varies between 0 and 1 is included for a hot-wall approach. This correction, represented by the last fraction term in Equation 3.83 as shown in Equation 3.84, depends on the reference temperature taken as 300 K ($T_{ref} = 300$) and associated heat capacity taken as 1009 $J/K/kg$ for perfect air ($c_{p,ref} = 1009 J/K/kg$) [201] and approximately 857 $J/K/kg$ for Mars' atmosphere.

$$q_s = \frac{110.34 \cdot 10^6}{\sqrt{r_N}} \frac{\rho_\infty}{\rho_0} \left(\frac{V_\infty}{V_c}\right)^{3.15} \frac{h_s - c_p \cdot T_w}{h_s - c_{p,300K} \cdot 300} \tag{3.83}$$

$$\text{hot-wall correction} \begin{cases} \frac{h_s - c_p \cdot T_w}{h_s - T_{ref} c_{p,ref}}, & \text{if} \quad T_{ref} > T_w \\ 1 \quad\quad\quad\quad , & \text{if} \quad T_{ref} \leq T_w \end{cases} \tag{3.84}$$

Equation 3.83 depends on two additional terms, which are the density at sea-level ρ_0 taken as 1.225 kg/m^3 for Earth and 0.020 kg/m^3 for Mars, and the planet's circular velocity given as $V_c = \sqrt{\frac{GM_{planet}}{R_{planet}}}$, with G being the gravitational constant $G = 6.674 \cdot 10^{-11}$ $m^3/kg/s^2$, M_{planet} being the mass of the planet and R_{planet} its average radius assuming a perfectly spherical body. For Earth, the circular velocity is equivalent to 7.9054 km/s, whereas a value of 3.5371 km/s would be used for Mars.

Van Driest

An alternative heat-flux expression for the continuum regime that follows the example of the Fay-Riddell's model in Equation 3.82 has been developed by Van Driest [203] for a non-catalytic wall condition. This means that the expression represents the lower bound for the estimation of aerothermal heating and for this reason, it is typically used to design for demise. Similarly to Equation 3.82, the stagnation and wall enthalpy are given in Equation C.39, the stagnation density in Equation C.37 and the viscosity at the stagnation point in Equation 3.19 with the temperature at the stagnation point described in Equation C.38. The definition of the velocity gradient at the stagnation point is also taken from Equation C.40.

$$q_s = 0.763 \times Pr^{-0.6} (\rho_s \mu_s)^{0.5} (h_s - h_w) \sqrt{\left(\frac{du}{dx}\right)_s} \tag{3.85}$$

Since the method is based on empirical measurements, its accuracy can vary depending on the specific conditions. Similarly to Fay-Riddell's model, Van Driest's expression is primarily applicable to laminar boundary layer flows. Moreover, its validity may decrease for increasing Mach numbers, where the real gas effects are predominant. Furthermore, the isothermal wall assumption [203] of a constant and smooth surface temperature neglects the effect of temperature gradients on the convective heat transfer and the presence of any irregularities or roughness which could alter the thermodynamic properties of the flow.

Chapman

The more generalised form of the heat-flux relations given by Chapman [196, 204] in Equation 3.86 with a combination of parameters that are dependant on the freestream gas composition and flow conditions. For Earth reentry conditions with a laminar boundary layer, the parameters $c_1 = 1.06584 \cdot 10^8 \sqrt{m}$, $n = 0.5$ and $m = 3$ are typically employed [205, 206]. At the same time, the values of $n = 0.5$, $m = 3.04$ and $c_1 = 4.73562 \cdot 10^6 \sqrt{m}$ are inferred from the literature for Mars entry [155]. Despite the simplicity of the aerothermal relation, comparison with higher-fidelity methods revealed that Chapman's model provides sufficient detail for conceptual studies [207]. Equation 3.86 is thus investigated for stacked-toroids.

$$q_s = c_1 r_N^{-n} \left(\frac{\rho}{\rho_0}\right)^{(1-n)} \left(\frac{V_\infty}{V_c}\right)^m \tag{3.86}$$

Sutton and Graves

The final model considered in this work for the continuum regime is that proposed by Sutton and Graves [197]. The expression, also applicable to any planetary atmosphere by varying the value of the only associated coefficient, neglects the hot-wall correction in Equation 3.86 and employs a fully-catalytic cold-wall model which becomes more realistic at surface temperatures with very high flow stagnation enthalpies. Sutton and Graves' empirical relation for the heat-flux at the stagnation point is given in Equation 3.87. The model may be used for an axisymmetric blunt body when the flow is in chemical equilibrium.

$$q_s = c_1 V_\infty^3 \left(\frac{\rho_\infty}{r_N}\right)^{0.5} \tag{3.87}$$

The applicability of the stagnation heat flux correlation was extended by Sutton and Graves [197] to a number of atmospheric gases including nitrogen, oxygen, hydrogen, helium, neon, argon, carbon dioxide, ammonia, methane and 22 gas mixtures entailing the base gases [191]. The validity of the relation has been established between enthalpies of magnitude 2.3 to 116.2 MJ/kg and wall temperatures between 300 and 1111 K [191]. Based on the thermal properties of the gases, the coefficient c_1 is typically taken as being equal to $c_1 = 1.7415 \cdot 10^{-4}$ for Earth reentry [205], while a value of $c_1 = 1.83 \cdot 10^{-4}$ is adopted for a gas mixture of 97% CO_2 and 3% N_2 [190], representative of the Martian environment.

3.6.2. Convective Heating in Rarefied Regime

While several analytical models whose individual validity will be assessed in section 4.4 have been discussed for the continuum regime, the estimation of the aerothermal loading in FMF can be conducted by assuming that the stacked toroid does not affect its surrounding environment, which is the case for $Kn > 10$ as the intermolecular collisions can be neglected. To model the exchange of energy from the incoming flow to the stacked toroid's surface, the molecular diffusive accommodation coefficient can be employed as defined in Equation 3.53 [208], where E_w is the energy related to the molecules re-emitted from the wall with a Maxwellian velocity probability distribution at the corresponding wall temperature T_w.

Based on the diffuse energy accommodation coefficient, Schaaf and Chambre [177] have developed an analytical expression to estimate the heat flux on a flat plate as a function of its inclination angle. The formulation, shown in Equation 3.88, assumes that the number of impinging and re-emitted molecules is the same. This means that the model is most accurate for steady-state conditions. Moreover, Schaaf and Chambre [177] assume that the atmosphere can be described by the ideal gas law.

$$\begin{aligned} q_{fmf} =& \alpha_E p_\infty \sqrt{\frac{RT_\infty}{2\pi}} \left\{ \left[s^2 + \frac{\gamma}{\gamma - 1} - \frac{\gamma + 1}{2(\gamma - 1)} \frac{T_w}{T_\infty} \right] \right. \\ & \left. \cdot \left[e^{-(s\sin\theta)^2} + \sqrt{\pi}\,(s\sin\theta)\,[1 + \mathrm{erf}\,(s\sin\theta)] \right] - \frac{1}{2} e^{-(s\sin\theta)^2} \right\} \end{aligned} \tag{3.88}$$

3.6.3. Convective Heating in Transitional Regime

Analogously to estimating the aerodynamic loading in the transitional regime, the heat transfer in such flow conditions may be characterised via bridging functions [209]. While the implementation of Legge's expression [210] has been advocated by other aerothermal tools such as SCARAB [209] and FOSTRAD [55, 211] due to its simplicity, the model produces a sharp variation of heat transfer for varying flow regimes and would maintain a constant stagnation heat flux throughout the transitional flow conditions. In fact, the model does not exhibit any dependency on Kn as shown in Equation 3.89, where the heat transfer coefficient in the transitional flow $hc_{s,trans}$ is computed based on the continuum $hc_{s,cont}$ and FMF $hc_{s,fmf}$ quantities. The heat transfer coefficient is determined from the stagnation heat transfer in which the freestream density and velocity are used according to Equation 3.90 [212].

$$hc_{s,trans} = \frac{hc_{s,cont}}{\sqrt{1 + \left(hc_{s,cont} / hc_{s,fmf} \right)^2}} \tag{3.89}$$

$$hc_s = \frac{q_s}{\frac{1}{2}\rho_\infty V_\infty^3} \tag{3.90}$$

An enhanced approach is enabled by Wilmoth's [182] bridging function in Equation 3.68 which, conversely from Legge's expression, foresees a smoother transition in rarefied conditions. Equation 3.68 is thus modified to estimate Equation 3.90 instead of the aerodynamic coefficients as shown in Equation 3.91. The condition in Equation 3.69 shall also be satisfied for the results to be meaningful. While the validity of the bridging function shall be further assessed in the next chapter by comparison with higher-fidelity data, the excellent correlation noted for the Orion stagnation point heat transfer coefficients computed with the same analytical methods which are employed in this work for the continuum aerothermal regime in FOSTRAD [211] reveals that these might be sufficient to characterise the transitional regime. Therefore, the next chapter shall assess whether a bridging function is required in the aerothermal regime or whether the analytical models implemented in the continuum flow are capable of adequately predicting the performance under transitional effects.

$$hc_s = hc_{s,fmf} + \left\{ (hc_{s,cont} - hc_{s,fmf}) \sin^2 \left(\pi [a_1 + a_2 \log_{10}(Kn)] \right) \right\} \tag{3.91}$$

Following the approach used for the aerodynamics modelling in Equation 3.70, the non-linear least square method is employed to estimate the coefficients a_1, a_2 that yield the most accurate fitting of Equation 3.91 according to Equation 3.92.

$$\min_x ||hc((a_1, a_2), x_{DSMC}) - y_{DSMC}||_2^2 = \min_x \sum_i (hc((a_1, a_2), x_{DSMC_i} - y_{DSMC_i})^2 \tag{3.92}$$

3.6.4. Radiative Heating

Similarly to the strategy adopted for the modelling of convective heating, the radiative heating is evaluated by means of relatively simple correlations which can be determined through general parameters such as the freestream density, the vehicle's velocity and its nose radius. West and Brandis [190] have developed engineering predictive models using a loosely coupled aerothermodynamics solver bridging onto a second-order upwind code assuming steady-state flow with a two-temperature thermochemical nonequilibrium for Mars. The code takes into consideration the Martian atmosphere with 15 species: $CO_2, CO, N_2, O_2, NO, C, N, O, CN, CO^+, NO^+, C^+, O^+$, N^+, e^-, with reaction finite chemistry models outlined by Johnston and Brandis [213] with a laminar boundary layer and super catalytic wall conditions for the convective flux.

The numerical correlation identified by West and Brandis [190] is given in Equation 3.93, consisting of an exponential fourth-order polynomial of three variables with 35 terms with the coefficients given in Table B.15 and Table B.16 respectively for low- ($2km/s \leq V \leq 6km/s$) and high-speed (6 km/s $< V \leq 8$ km/s) relations. The difference between the sets of fitting variables is due to the activation of the CO $4th$ Positive and CN Violet band systems beyond 6 km/s which alter the heat transfer [190].

$$q_r = e^{f(V_\infty, \rho_\infty, r_N)} \tag{3.93}$$

Analogous models are available for Earth re-entry scenarios in [191] for shock speeds higher than 11 km/s, which is when the flowfield-radiation coupling becomes more pronounced. These, however, are not directly implemented in this work as the purpose is that of modelling Mars missions. Moreover, due to the large shock speed needed, their application is limited to high-speed re-entry cases. The net heat flux perceived by the vehicle's outer shell is thus $q_{total} = q_c + q_r$, assuming that the radiation of the shock and the re-radiation of the F-TPS is negligible.

3.6.5. Heat Distribution

The analytical models presented thus for the aerothermodynamic analysis of stacked toroids are based upon simplified boundary-layer equations which are only applicable to the stagnation point of the vehicle [193]. To extend the theory to the downstream regions from the stagnation point, an additional relation is needed. The problem was first explored for laminar boundary layers by Kemp, Rose and Detra [214] to describe the heat transfer along the nose of cylindrical bodies exposed to dissociating flow under the assumption of local similarity.

However, an improved relation has been utilized in the SCARAB tool [209] for more complex blunt geometries. The relation given in Equation 3.94 is therefore utilized in this work to estimate the heat flux distribution across the surface of a stacked-toroid based on the panels' local inclination angle θ. The same relationship has been adopted by Mehtaa et al. [211] in FOSTRAD to evaluate the heat distribution of satellites in Earth's orbit.

$$q(\theta) = q_s \left(0.1 + 0.9\cos(\theta)\right) \tag{3.94}$$

To further improve the accuracy of the heat distribution away from the hemispherical nose-cone which Equation 3.94 is expected to predict well, Krasnov's model [215] for a conical body is implemented according to Equation 3.95 with the nomenclature defined in Equation 3.96, Equation 3.97 and Equation 3.98.

$$q = q_s \frac{2A_k\bar{x}_c}{\sqrt{B_k + \bar{x}_c^3}} \tag{3.95}$$

$$A_k\left(\theta_c\right) = \frac{\sqrt{3}}{2}\left\{\left[\left(1 - \frac{1}{\gamma_\infty M_\infty^2}\right)\sin(\theta_c) + \frac{1}{\gamma_\infty M_\infty^2}\right]\left(\frac{\pi}{2} - \theta_c\right)\right\}^{\frac{1}{2}} \tag{3.96}$$

$$B_k\left(\theta_c\right) = \frac{(3/16)D_k/\theta_c}{\left(1 - \frac{1}{\gamma_\infty M_\infty^2}\right)\sin^4\theta_c + \frac{\sin^2\theta_c}{\gamma_\infty M_\infty^2}} - \cot^3\theta_c. \tag{3.97}$$

$$\begin{aligned} D_k(\theta_c) = &\left(1 - \frac{1}{\gamma_\infty M_\infty^2}\right)\left(\theta_c^2 - \frac{\theta_c\sin(4\theta_c)}{2} + \frac{1 - cos(4\theta_c)}{8}\right) \\ &+ \frac{4}{\gamma_\infty M_\infty^2}\left(\theta_c^2 - \theta_c\sin(2\theta_c) + \frac{1 - cos(2\theta_c)}{2}\right) \end{aligned} \tag{3.98}$$

where $\bar{x}_c$ is the distance along the surface from the apex of the cone x_c normalised according to the definition in Equation 3.99 [215]. The expression in Equation 3.95 assumes that the inviscid gas parameters are frozen at the end of the spherical nose and do not vary along the conical surface.

$$\frac{\bar{x}_c}{r_N} = cot(\theta_c) + \frac{x_c}{r_N} - \left(\frac{\pi}{2} - \theta_c\right) \tag{3.99}$$

Santos, Hosder and West [216] have also adopted Krasnov's heat flux expression to model the heat distribution across a stacked-toroid's conical surface in conjunction with an additional contribution for the nose-cone. This approach is also established in this work, where Equation 3.94 may be employed for the IAD's nose and shoulder and Equation 3.95 for the vehicle's body as illustrated in Figure 3.22. To ensure a continuous heat flux distribution across the axial profile of the IAD, Santos et al. [216] recommend including an offset to the running length s_c such that Equation 3.99 is re-defined according to Equation 3.100. The offset may be determined using the Levenberg-Marquardt algorithm in MATLAB[3] for nonlinear least-squares to equate the heat flux in the conical and nose-cone regions.

$$\bar{x}_c = \frac{x_c + s_c}{r_N} \tag{3.100}$$

[3]Documentation available at https://it.mathworks.com/help/optim/ug/least-squares-model-fitting-algorithms.html accessed: 18/04/2023

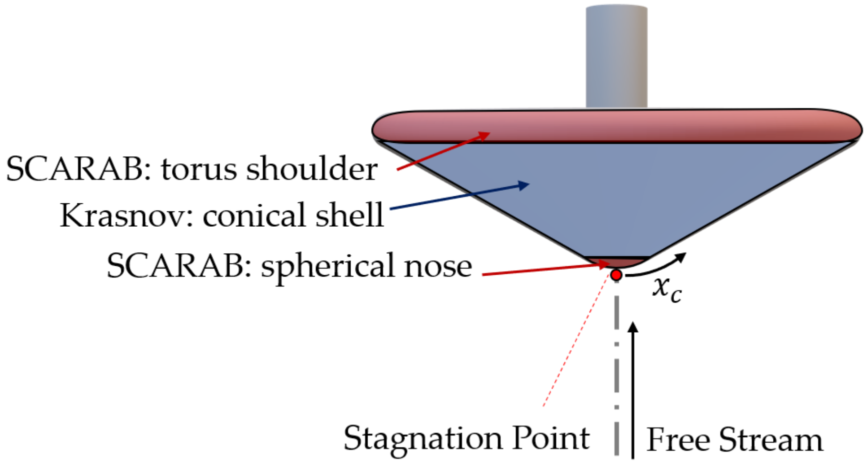

Figure 3.22.: Heat distribution downstream of stagnation point using two analytical methods

The current discussion on heating distribution primarily focuses on the frontal part of the aeroshell, as it experiences the highest heat flux due to flow impingement. However, it is also important to consider the heat contribution to the back faces of the aeroshell. In order to include this aspect, convective heating correlations based on the wind tunnel experimental program of THOR [53] can be utilized. The expressions for the back-shell and payload heat contributions are provided in Equation 3.101 and Equation 3.102, respectively. These expressions depend on the heat transfer film coefficient h_f and the boundary-layer momentum thickness Reynolds number Re_θ. Detailed explanations of these parameters are presented in the subsequent section (see Equation 3.108 and Equation 3.106). It is important to note that the heating levels for the back-shell and payload of a stacked-toroid are expected to be approximately 5% to 6% of the stagnation point on the frontal face [53]. Although the F-TPS thickness could be reduced for the back shells, it is crucial to prioritize the design considerations for the frontal area where the heating conditions are more critical.

$$h_f/h_{f_s} = 1.8225 \cdot 10^{-5}\,(Re_\theta)^{1.7335} \quad \text{back-face} \tag{3.101}$$

$$h_f/h_{f_s} = 5.6145 \cdot 10^{-6}\,(Re_\theta)^{1.8759} \quad \text{payload} \tag{3.102}$$

3.7. Deflection Modelling

A fundamental characteristic of IADs, and in particular of the stacked-toroid configuration, is the deformation of the surface that occurs during entry due to the aerodynamic loading exerted on the flexible TPS material, causing it to deform. The flexible structure is pushed inwards within the region between adjacent toroids, thereby generating a scalloping of the vehicle as illustrated in Figure 3.24. The presence of such phenomena was first observed during the IRVE flights [38], but was ultimately demonstrated by Lichodziejewski et al. [102] in a wind tunnel campaign. The structural deformation of the vehicle results in a modification of the aerodynamic and aerothermal loading experienced by the accelerator. Nevertheless, because of the complex flow behaviour which would require an accurate prediction of turbulence, non-equilibrium thermo-chemistry and radiation heat transfer, high-fidelity modelling would be computationally prohibitive. The present work shall therefore account for the presence of scallops by implementing low-fidelity aerodynamic and aerothermodynamic relations that are capable of estimating the degree of influence that the deformation of the aeroshell has on the aerodynamic coefficients and heat flux distribution.

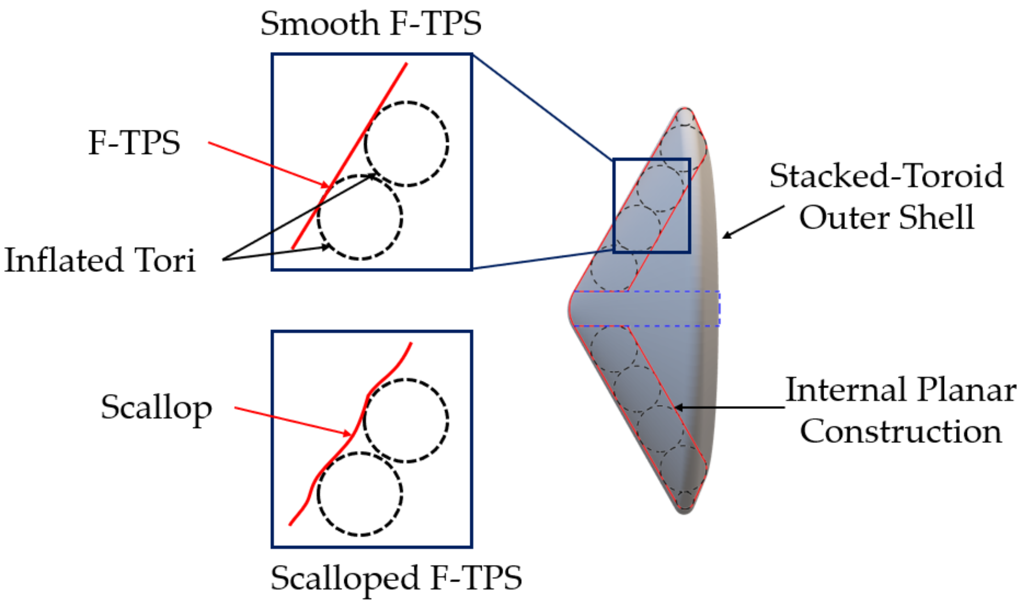

Figure 3.23.: Visualization of scalloping phenomenon on F-TPS of inflated stacked-toroid

Following the nomenclature adopted by Hollis and Hollingsworth [53], the scallop is parametrised as shown in Figure 3.24, where a toroid tangency angle β_{SC} is constructed relative to the normal of the undeformed F-TPS. The radius of the scallop R_{SC} is inscribed in the circle tangent to the neighbouring toroids at the location of the scallop. More importantly, the depth of the scallop k_{SC} is defined as the maximum distance between the scallop itself and the original undeformed configuration of the F-TPS. It is important to note that in a flight the scallop depth would vary with trajectory, environmental conditions and dynamic pressure. Typically, the characterisation of the scalloping topology is referred to by the tangency angle β_{SC} which is defined in Equation 3.103 from trigonometry.

$$\beta_{SC} = \arctan\left(\frac{r_{torus}}{r_{torus} + R_{SC} - k_{SC}}\right) \tag{3.103}$$

The aeroelastic characterisation of a stakced-toroid conducted by Wu et al. in transonic, supersonic [217] and hypersonic [218] regions by means of 3D two-way FSI simulations, revealed that all continuum conditions are exposed to the scalloping phenomenon, with axial and pitching vibration amplitudes comparable between the transonic and hypersonic conditions. Interestingly, Wu et al. [218] also determined that the vibration amplitudes of the toroids remain uniform across the hypersonic region from Mach 5 to Mach 12, with no divergence or instabilities observed. Since the numerical methodology proposed by Wu et al. [217, 218] would be too computationally expensive for the present work, the maximum expected value of scalloping is utilised for a conservative estimation. Since the aeroheating effects are most significant at hypersonic speeds, where the high surface temperature and inflation gas expansion most affect the thermal stress, the effect of scallops is only regarded at $M > 5$ with a non-divergent behaviour for aerothermal performance, whereas it is accounted for all regimes in the aerodynamics analysis.

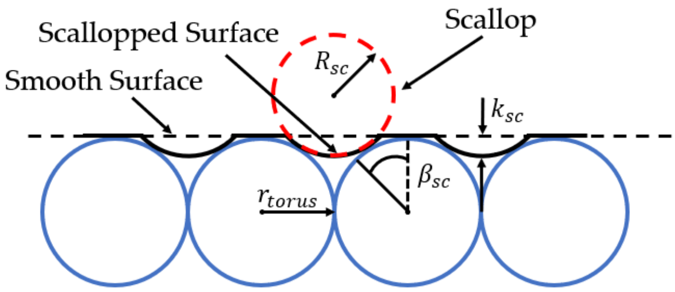

Figure 3.24.: Detail of parametric scalloping phenomenon

3.7.1. Aerodynamics

No analytical correlation of the aerodynamic loading as a function of the deflection has been retrieved from the literature. The numerical study by Guo et al. [29] numerically characterised the hypersonic aerodynamics of deformed aeroshells with $0° \leq \beta_{SC} \leq 25°$ in the continuum and near-continuum regimes. A fitting correlation could therefore be implemented numerically depending on the Knudsen number and degree of deflection. However, the variations noted in the integrated quantities of interest, namely the drag and lift coefficients, yield variations within 2%. The difference given by the effect of scalloped surfaces is lower than the error associated with the simplified scalloping model adopted, which assumes a constant scallop radius at all tori interfaces. On the contrary, a study conducted on static shape deformation by Guo et al [35] shows that the surface deformation increases with the distance from the nose cone. Nevertheless, even this latter study by Guo [35] predicts a variation of drag and lift coefficient less than 4% for the deflected surface investigated at $0° \leq \alpha \leq 70°$.

A more crude but effective solution for the scope of the present work is to implement the correlation adopted in the IRVE-3 flight by Olds et al. [38]. The expression, shown in Equation 3.104 consists of a simple cone-sharpening model used to replicate the predicted gross response of the vehicle under external pressure loading. The equation hereby implemented applies variations in the aerodynamic coefficients ΔC_x to the rigid ideal static coefficients by assuming that the effective forebody structure is deflected under loading. Interestingly, the deltas that are applied to correct for the presence of structural deflection on the surface are a function of dynamic pressure. However, there is a lack of such functions in the existing literature. To address this gap, empirical correlations are proposed in subsection 4.3.5 by fitting a polynomial to the reconstructed trajectory of IRVE-II and validating it using the IRVE-3 flight data. The derived expressions for the axial and normal force coefficients are presented in Equation 4.1 and Equation 4.2, respectively, while the lift and drag coefficients are described by Equation 4.3.

$$C_{(A,N),flexible} = C_{(A,N),Rigid} - \Delta C_{(A,N)}(q_\infty) \tag{3.104}$$

3.7.2. Aerothermodynamics

The experimental study conducted by Hollis and Hollingsworth [53] on a F-TPS applied to a stacked-toroid decelerator determined the aeroheating effects of the surface deformation on its aerothermal performance. Specifically, rigid, nonsmooth aeroshell models were used to simulate and quantify the boundary-layer transition and convective heating levels as a consequence of the surface deformation and associated scalloping phenomenon. Hollis [53] investigated different models of the IRVE vehicle in NASA's Langley Aerothermodynamics Laboratory at Mach numbers between 5.8 and 6.1. The experimental results were then compared to flow field predictions using high-fidelity CFD simulations with a finite-volume 3D solver that accounts for nonequilibrium chemistry. The combination of the experimental data with the numerical results enabled the development of a parametric correlation for the effect of scalloping on heating depending on the scallop height k_{sc}, maximum inflated radius of the decelerator $r_{inflated}$ and laminar boundary layer momentum thickness Reynolds number Re_θ. This latter quantity can be estimated using a simple explicit relation for a flat plate given by Schlichting [219] in Equation 3.106 as a function of the streamwise Reynolds number Re_x in Equation 3.105.

$$Re_x = \frac{\rho_\infty V_\infty r_{inflated}}{\mu_\infty} \tag{3.105}$$

$$Re_\theta = 0.664\sqrt{Re_x} \tag{3.106}$$

Hollis' scalloped augmented heat flux correlation is given in Equation 3.107 as a function of the $\frac{k_{SC}}{r_{inflated}}$ radius where k_{SC} is needed in metres and $r_{inflated}$ in feet. The expression is used to estimate the increase in convective heat transfer due to the transition from laminar to turbulent conditions. The augmented heat transfer coefficient is given in the form of a film coefficient h_f which may be computed according to Equation 3.108 [53] by assuming that the adiabatic wall enthalpy is equal to the freestream total enthalpy H_0, with a wall temperature of 300 K.

$$\left(\frac{h_{f_{turb}}}{h_{f_{lam}}}\right) = 1 + 7.3457\left(\frac{k_{SC}}{r_{inflated}}\right) + 0.006 + 0.049294\left(\frac{k_{SC}}{r_{inflated}}\right)^{0.51841} \cdot Re_\theta \tag{3.107}$$

$$h_f = \frac{q}{H_0 - H_{300K}} \tag{3.108}$$

The increase in convective heat flux due to the deflection of the stacked toroid is therefore predicted by means of Equation 3.107 to determine the heat distribution across the stacked toroid's surface, where the relations described in subsection 3.6.1 can be used to determine the stagnation heat flux.

3.8. Flexible Thermal Protection System

During the EDL sequence that the stacked-toroid must undergo, the inflated outer shell is bound to experience large heat fluxes from its surrounding environment in the form of convection and radiation, which is then transferred to its internal structures and payload via conduction. To ensure that the vehicle survives the severe environmental conditions encountered, the F-TPS must be carefully designed. When compared to traditional TPS designs, its flexible counterpart offers the capability of being packaged into a smaller volume within the rocket fairing and inflated upon entry.

The requirements for the flexible TPS components are that the layers can withstand the highest aerodynamic pressure and shear loads with the associated aeroheating effects. In addition, the flexible structure must be tolerant to the packing and deployment of the system [36]. To meet the specific engineering functional aspects of each mission, a combination of multiple layers of materials is specifically selected as shown in the staggered configuration in Figure 3.25. This concept has been developed by NASA across the various projects mentioned in chapter 2, such as PAIDAE [97], IRVE [44–46, 114], and LOFTID [121–123]. The three functional layers serve the following purposes [220]:

- The outer layers must sustain the incident heat flux, surface pressure and aerodynamic shear force during the EDL phases in the form of convective heating, optical thickness, emissivity and catalycity of the material. These layers must be structurally robust with low catalicity and should also present a high emissivity to re-radiate the heat to the surrounding. Moreover, it is essential for the chosen materials to maintain their performance after handling, shape deformation, compression and packing [30].
- The insulation layers' main function is that of delaying the thermal pulse experienced in the entry trajectory. The delay must be sufficiently extended to keep the underlying structure within the temperature design limits. Although the insulators only experience a small amount of shearing flow, given that they are located behind the outer fabric, it is desirable for the insulating material to be robust and fault tolerant in the event of a failure to the outer layers [30].
- The gas barrier must act as a support for the insulating layers and a surface for fastenings connecting the TPS to the main inflated structure. More importantly, the gas barrier layers prevent the hot gases and decomposition products arising as a result of the heat transfer from damaging the toroidal structures.

An optimal selection of the F-TPS layups shall focus on materials that have low areal weight and low permeability [30]. At the same time, these should also be sufficiently malleable to maintain uniformity and homogeneity after being subject to deformation. Other manufacturing features of the material should also be considered such as the maturity of the manufacturing processes and the ability to constantly reproduce consistent products for testing [30]. Example candidates of the material layups investigated in the literature include Nextel and SiC for the outer fabric, due to their high strength and little shrinkage at high continuous temperatures. Pyrogel, on the other hand, is often chosen as the insulator because of its flexibility and resistance to high temperatures. Kapton is instead employed for the gas barrier as it retains its properties at large temperature differences [30].

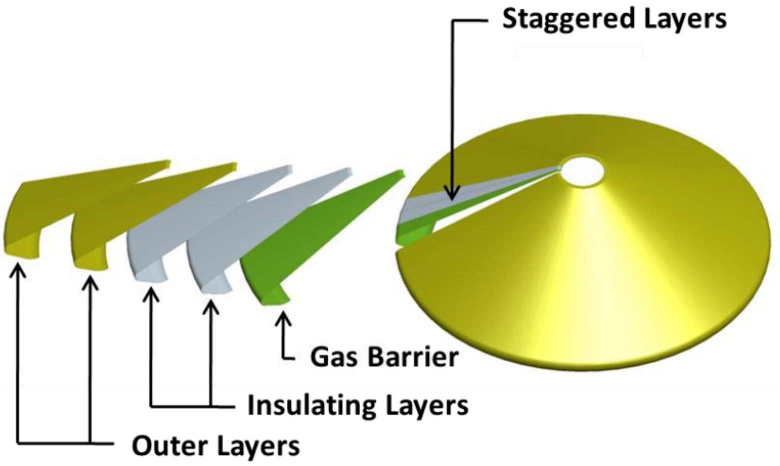

Figure 3.25.: Definition of the F-TPS layers [36]

Although the thermal characterisation of different F-TPS layups is beyond the scope of this work, given that an experimental campaign would be required to define the complex material response [30, 32, 220], the proposed MDAO framework includes the capabilities to estimate the thermal performance of a given layup and to optimise its thickness. Based on the experimental and high-fidelity simulation results presented, Del Corso et al. [30, 32] claims that a 1D analysis comprising convection, radiation and conduction is sufficiently accurate for the through-thickness results. Given the nature of the MDAO process, a 1D heat diffusion model is hereby proposed to estimate the temperature variation across an arbitrary F-TPS layup over the expected trajectory freestream conditions.

The simplified problem for n F-TPS layers, each of thickness L, is shown in Figure 3.26, where the outer fabric layers are exposed to the transient heat flux $q(t)$ in the form of convection q_c, conduction q_{cond} and re-radiation q_{rerad}. The inner layers of the fabric, gas barrier and insulator, on the other hand, are only subject to heat conduction driven by the temperature gradient within the TPS layers. Conversely, the last layer of the gas barrier is in contact with the structural mass of the stacked toroid. Following the example set by Del Corso et al. [30, 32], the heat conduction between the inner layers is treated as a thermal resistance, and heat contact conductance is applied at the interface between each layer. It is noted that this conductance, caused by the presence of a non-ideal contact between two surfaces, is the inverse of the thermal conductivity measured experimentally for any given material [30]. Since the contact conductance $q_{contact}$ at the interface of two materials is dependent on the freestream pressure and temperature, this may also be expressed as $q_{contact} = f(p_\infty, T_\infty)$. However, the rather limited data on contact conductance available in the literature for the materials of interest to a F-TPS may dictate the modelling of $q_{contact}$ as being constant [221].

The problem of predicting the temperature across a compound structure composed of layers with different material thermal properties and each with different thicknesses has been widely addressed in the literature [222]. In particular, the implementation of analytical approaches appears to be dominant due to the computational advantages [223]. However, not are these only mostly applied to steady-state flows but they also present large degrees of error in the solution.

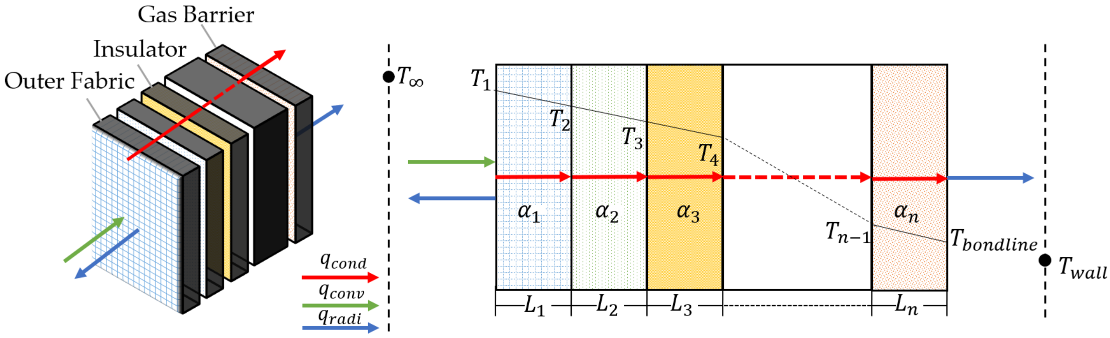

Figure 3.26.: Schematic of generic F-TPS layup (left) and 1D heat diffusion model with boundary conditions (right)

To investigate a transient flow, where the boundary conditions, material properties and heat parameters vary, a numerical approach is preferred. This is the case for the F-TPS of a stacked-toroid, where the freestream temperature changes with altitude, the heat diffusion coefficients vary with temperature [224] and the heat contact conductance is altered by changes in pressure and temperature [32].

Amongst the numerical schemes employed in the literature for solving thermal diffusion equations, the Finite Difference Method (FDM) is the most popular one due to its simplicity. Zhu et al [225] presented the FDM discretisation for the transient thermal analysis of a 2-layer TPS. In this section, the method is expanded to account for multiple layers of varying thickness and material properties. This is a non-trivial modification proposed in this work because the difference in thickness may reach one order of magnitude between the outer fabric and the gas barrier. This would make the solution insensitive to the variation of material properties over the discretised space. An improved approach is hence described for a F-TPS.

The discretisation of the domain illustrated in Figure 3.26 is shown in Figure 3.27, where the first mesh nodes in space and time are $i = 1$ and $m = 1$ respectively to be consistent with the Matlab syntax. The mesh implemented for the heat diffusion uses a semi-infinite compound wall, where the square nodes at $(t = 1, m = \{1, 2, ..n\})$ are known as the initial values $T(o, x) = T_0(x)$. The diamonds, located at $(t = \{1, 2, ..end\}, m = \{1, n\})$ represent the location of the known boundary values. Conversely, the circles are used to indicate the interior points where the finite difference scheme is applied to approximate the solution. In addition, the colour of the nodes is consistent with the respective discretised layer, while black nodes are used at the interfaces between different layers. It is already clear that the mesh implemented is uniform and no variation along any other spatial direction is included. This assumes that the temperature difference only propagates along the x direction such that $\frac{\partial^2 T}{\partial x^2} = 0$.

The right-hand side of the problem is modelled by assuming conservation of heat flux, such that the temperature at the wall end can be set equal to the desired payload temperature, based on the requirements of the mission $T(t, x = n) = T_n(t)$. This assumes that the bondline temperature is equal to the wall temperature $T_{bondline} = T_{wall}$ in Figure 3.26. The left-hand side, on the other hand, is computed from the incoming aerothermal heat flux which varies over time $q(t)$.

The governing equation for the one-dimensional heat diffusion problem is given in Equation 3.109, where the heat diffusivity α_h is expressed as a function of the thermal conductivity k, specific

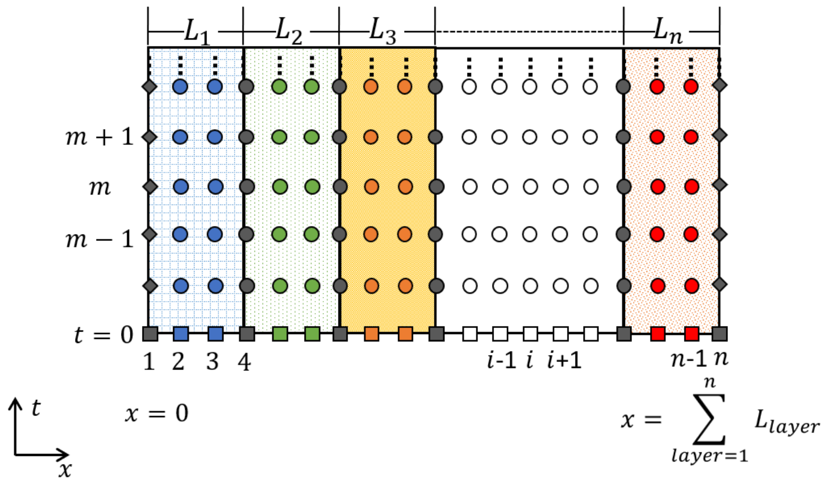

Figure 3.27.: Spatial and Temporal discretisation of the F-TPS domain

heat C_p and density ρ in Equation 3.110. No internal heat source is modelled in the given form of the differential equation.

$$\frac{\partial T}{\partial t} = \alpha_h \frac{\partial^2 T}{\partial x^2} \tag{3.109}$$

$$\alpha_h = \frac{k}{\rho C_p} \tag{3.110}$$

Equation 3.109 can therefore be solved numerically by employing the finite central-difference approximation such that the derivatives are replaced with the corresponding scheme as in Equation 3.111. Given that the purpose of the model described in this section is that of optimising the TPS thickness, the spatial discretisation is performed by maintaining the number of nodes per layer constant. It follows that the distance between two nodes Δx of different layers with different lengths may differ. More computationally efficient approaches may be employed for the problem of layers with variable thickness, such as the implementation of spanning functions used to control the distribution of the mesh nodes and their concentration [226]. However, for the problem hereby considered, the utilization of a constant number of grid points per layer is deemed sufficient when a mesh independence study is performed.

$$\frac{T_i^{t+\Delta t} - T_i^t}{\Delta t} = \alpha_h \frac{T_{i-1}^t - 2T_i^t + T_{i+1}^t}{\Delta x_i^2} \tag{3.111}$$

However, Equation 3.111 is not suitable for the F-TPS problem presented, since the scheme is insensitive to the spatial variability of the material properties [226]. In fact, the heat diffusivity varies along the spatial discretisation as illustrated in Figure 3.26, depending on the specific layer of the F-TPS $\alpha_h = f(x)$. For time-varying properties, the heat diffusion may also vary with temperature, and thus with time $\alpha_h = f(x,t)$. To solve this problem, the solution proposed by Patankar [227] is adopted. This consists of applying a harmonic weighted averaging of the material characteristics. The conductivity at the interface between two adjacent grid points $(i, i+1)$ is given in Equation 3.112, as long as at least two nodes are used to discretise each layer.

$$k_{i+1/2} = \frac{2k_i k_{i+1}}{k_i + k_{i+1}} \tag{3.112}$$

The left-hand side boundary condition is therefore expressed in Equation 3.113, where the indices for the material properties are in agreement with the harmonic average in Equation 3.112 in agreement with the temperature indices. A forward time, centred space approximation is thus applied. The transient heat flux $q(t)$ refers to the aerothermal heating due to convection modelled in section 3.6. From this term, the heat conduction and heat due to re-radiation are subtracted as indicated by the second and third terms in the larger set of brackets such that $q_c = q_{cond} + q_{rerad}$ in W/m^2 for conservation of heat-flux. The emissivity ϵ is dependent on the outer fabric, and σ is the Stefan–Boltzmann constant equal to $5.6704 \cdot 10^-8 W/m^2 K$.

$$T_1^{m+1} = T_1^m + \frac{\Delta t}{\left(\Delta x_1 \rho_1^m C_{p_1}^m\right)} \left(q^m - \frac{k_1^m \left(T_1^m - T_2^m\right)}{\Delta x_1} - \epsilon\sigma \left((T_1^m)^4 - (T_\infty^m)^4 \right) \right) \tag{3.113}$$

The temperature in the interior nodes is then calculated as Equation 3.114, where the last term added to the expression is the heat contact conductance $q_{contact}$ defined in Equation 3.115. It is noted that the contact conductance coefficient h_c is equal to zero for the interior nodes and is only a non-zero quantity at the interface between layers. The interface is illustrated by the black nodes in Figure 3.27.

$$T_i^{m+1} = T_i^m + \frac{2\Delta t}{\Delta x_i \rho_i^m C_{p_i}^m + \Delta x_{i+1} \rho_{i+1}^m C_{p_{i+1}}^m} \cdot \left[\frac{k_{i+1}^m \left(T_{i+1}^m - T_i^m\right)}{\Delta x_{i+1}} - \frac{k_i^m \left(T_i^m - T_{i-1}^m\right)}{\Delta x_i} \right] + q_{contact} \tag{3.114}$$

$$q_{contact} = \begin{cases} {h_c}_i{}^m (T_{i+1}^m - 2T_i^m + T_{i-1}^m), & \text{if} \sum_{i=1}^n x(i) = \sum_{k=1}^n L_k; \\ 0, & \text{otherwhise} \end{cases} \tag{3.115}$$

Finally, the temperature on the right-hand side of the domain in Figure 3.27 is computed by applying conservation of heat flux as a boundary condition. The form of the equation is similar to the one shown in Equation 3.113, but is applied to the last node n where no incident heat flux $q(i)$ is applied as illustrated in Equation 3.116.

$$T_n^{m+1} = T_n^m - \frac{\Delta t}{\Delta x_n \rho_n^m C_{p_n}^m} \cdot \frac{k_n^m \left(T_n^m - T_{n-1}^m\right)}{\Delta x_n} + \epsilon\sigma \left((T_n^m)^4 - T_\infty^4 \right) \tag{3.116}$$

While the spatial discretisation may vary across different layers, the spatial discretisation is maintained constant across the simulation. Since an explicit scheme is implemented, the maximum time step is selected based on the criterion in Equation 3.117. The condition is equivalent to having a Fourier number lower than 0.5, to avoid unstable solutions that may oscillate and diverge if Δt is too large.

$$\Delta t \leq min\left(\frac{\Delta x_i \rho_i^m C_{p_i}^m}{2k_i^m}\right) \tag{3.117}$$

A further note on the selected time-step must be made concerning the applicability to the first and last nodes, where the heat transfer by radiation is included. In fact, because of the more restrictive boundary, the condition in Equation 3.118 is applied if Equation 3.117 generates unstable solutions [228], where T_{max} is the maximum temperature allowed in the corresponding F-TPS layer before failure.

$$\Delta t = min\left(\frac{\Delta x_1^2}{2\alpha_{h1}^{\ m}(1+\frac{\sigma\epsilon\Delta x_1}{k_1^m}T_{max}^3)}, \frac{\Delta x_n^2}{2\alpha_{hn}{}^m(1+\frac{\sigma\epsilon\Delta x_n}{k_n^m}T_{max}^3)}\right) \tag{3.118}$$

The ultimate goal of the present method is that of providing the optimal design of a F-TPS in terms of its thickness, whilst ensuring that a sufficiently low temperature is attained at the bondline interface. The aerial mass in kg/m^2 can be identified by multiplying the density of each layer with its thickness $\rho \cdot L$. As a constraint to the problem, the maximum temperature attained in each layer must be lower than the maximum allowed limit to ensure the survivability of the system. The optimisation problem is described by Equation 3.119.

$$min(\sum_{k=1}^{n} L_k \cdot \rho_k) \text{ such that } max(T_k) \leq T_{max,k} \tag{3.119}$$

The utilization of the nonlinear gradient-based optimiser function in Matlab, referred to as fmincon [229], can be exploited with constraints to search for the minimum F-TPS mass that satisfies the temperature constraints. The application of this function has already been advocated by Zhu et al. [225] to optimise a 2-layer TPS.

The proposed methodology can be applied to virtually any F-TPS configuration with an arbitrary number of layers. However, the IRVE-3 programme qualified its baseline F-TPS layup consisting of Nextel BF-20, Pyrogel 3350 and Kapton BF-20 [102]. Though the IRVE-3 flight experienced a peak heating of 14 W/cm^2 [102], the design was tested for fluxes up to 24 W/cm^2 [30]. More recent advances by NASA developed the second generation of F-TPS, in which Nicalon SiC material is employed to replace Nextel for the outer layers, making the system resistant to fluxes as high as 50 W/cm^2 [30]. With research aiming for 75-100 W/cm2, F-TPS will continue to advance as 3D woven fabric manufacturing methods and material technology advance [31]. For the purpose of this study, the utilization of the second-generation SiC material with the configuration illustrated in Figure B.9 is recommended. The material properties needed for the thermal model for the three material layers are reported both in Table B.17 and in Figure B.10 as a function of temperature.

3.9. Outlook

The breakdown of the inputs and outputs which are exchanged between the different disciplines of the proposed framework is shown in Figure 3.28. The design parameters are represented by the green icon labelled as "inputs". In the upcoming case study discussed in chapter 5, only four parameters are included in the design space. However, this can be expanded to include additional parameters such as payload radius and height, as shown in Table 3.1. Each combination of parameters corresponds to a fully-defined stacked-toroid geometry, which can be converted into a surface mesh for use by the individual disciplines. The latter, are coloured in light blue in Figure 3.28 and are equivalent to the disciplines highlighted in Figure 2.5.

The variables stored for each trajectory iteration include freestream atmospheric parameters such as pressure p_∞, temperature T_∞, density ρ_∞, atmospheric composition n_∞, and Knudsen number Kn. These variables, along with the entry trajectory parameters (entry speed V_E, angle Γ_E, and altitude h), are transferred to each discipline. The angle of attack α and angle of sideslip β_s are also defined at the beginning of each trajectory.

The aerodynamic discipline, in conjunction with the planar trajectory, calculates the shear C_τ and pressure C_P coefficients. These coefficients are then converted into normal C_N and axial C_A coefficients to account for both continuum and rarefied conditions. Finally, they are transformed into drag and lift coefficients for each time increment along the trajectory Δt. The equations of motion utilize these coefficients to calculate the velocity V, Reynolds number Re_x, Mach number M, speed ratio s, and transport properties of the air at different altitudes, which are recursively fed back to the aerodynamic module. The moment coefficient C_M is also determined to ensure longitudinal static aerostability.

A similar approach is taken in the aerothermodynamics module, which does not directly impact the flight equations of motion. The heat transfer coefficients h_f are computed along the trajectory to bridge the gap between continuum and rarefied conditions in the transitional regime. These coefficients are then converted back into heat fluxes at the stagnation point q_s using local velocity and density values. The heat load Q across the entire trajectory can be calculated. By defining a scalloping angle β_{SC}, the corresponding deflection corrections to the aerodynamic coefficients ΔC_x and heat flux distribution q_{SC} can be determined.

The structural mass m_{IAD} is derived from the geometric parameters, design inputs on the materials used, and general configuration of the stacked-toroid structural components. Environmental conditions, such as maximum dynamic pressure $q_{\infty,max}$, maximum g-load and maximum experienced drag D, drive the determination of the minimum inflation pressure p_{min}. When deployment occurs, the structural mass is subtracted from the ballistic coefficient β of the second stage to correct the equations of motion.

Two levels of optimization are employed in the framework. The inner optimizer is solely utilized to minimize the thickness, and therefore mass (given a uniform aerial density), of the F-TPS layers. The approach is well established in TPS design and requires the transient heat flux at the stagnation point $q_s(t)$, taking into account both convective and radiative contributions. The sizing of the F-TPS involves ensuring that the maximum temperature, T_{max}, is not surpassed in each layer and that the bondline temperature remains below the desired threshold. On the other hand, the outer optimizer can be customized to address specific optimization problems related to the mission at hand. Each mission may have unique requirements and objectives. For instance, in the application presented in chapter 5, the outer optimization focuses on minimizing the IAD mass in accordance with the MiniPINS requirements.

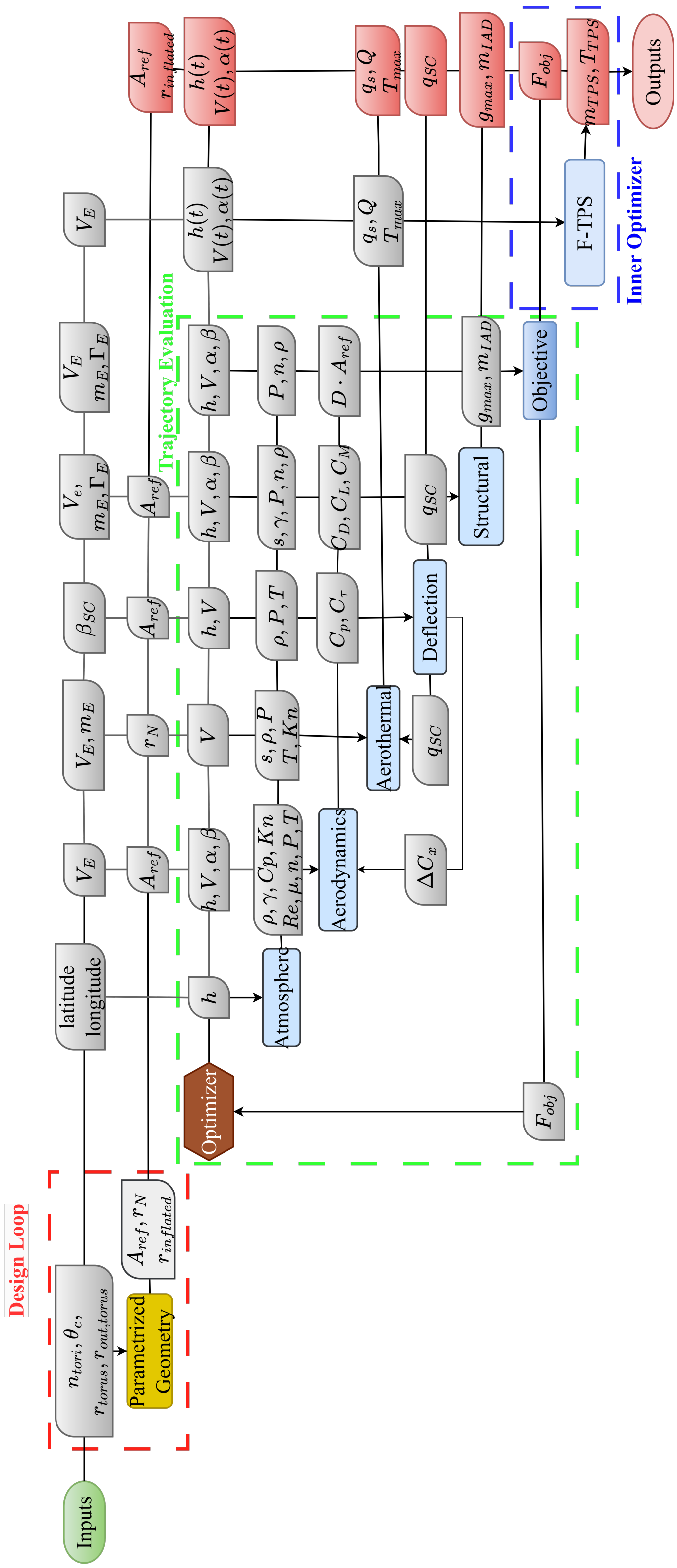

Figure 3.28.: MDAO framework

4. Verification & Validation

This chapter serves the dual purpose of ensuring the correct implementation of the methodology, through verification, and establishing its degree of accuracy and reliability through validation. To clearly distinguish between the various Verification & Validation (V&V) strategies employed in the subsequent sections, the section titles specify which aspect is addressed.

4.1. Parameterization: Verification

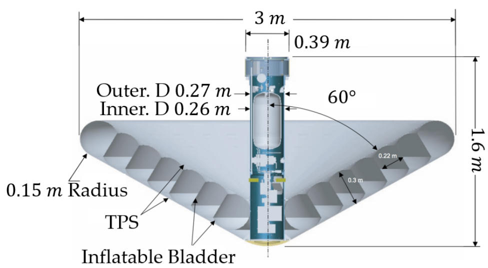

(a) Planar Design; adapted from [39]

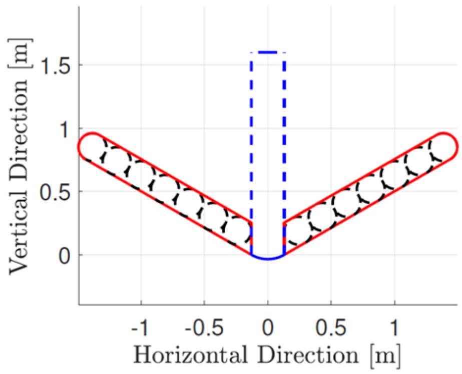

(b) Constructed Parametric Design

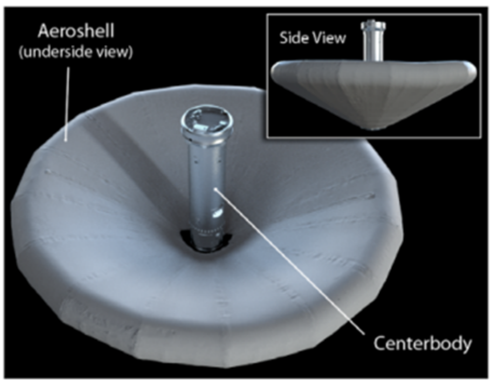

(c) Three-dimensional Design; adapted from [230]

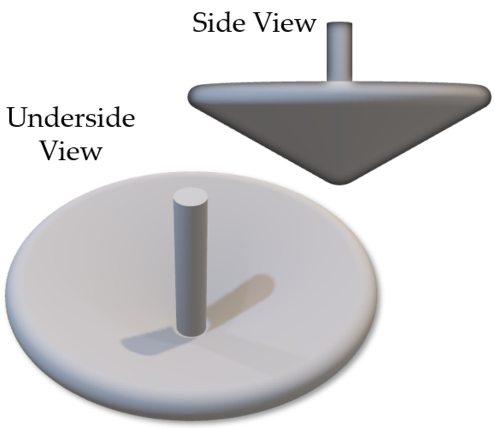

(d) Surface of Revolution of Parametric Design

Figure 4.1.: Construction of Parametric IRVE-II Flight Vehicle

In order to verify the correct construction of a parametrised stacked-toroid geometry, the mathematical framework proposed in section 3.1 is compared to technologically advanced systems. Specifically, the IRVE-II, IRVE-3 and HEART flight vehicles are used as references with the design space in Table 4.1. The choice of these three configurations is well suited to the verification process of this work since the various designs not only differ in component dimensions but also present a different arrangement of the shoulder outer torus and payloads.

Firstly, the planar cross-section of IRVE-II in Figure 4.1(a) illustrates the key dimensions used in the mathematical model in section 3.1 which result in the definition of the outer constructed profile in (b). The colour red is used to highlight the outer shell, whereas black is used for the inner tori and blue for the payload and nose cone. Despite the inner tori not being perfectly circular in the IRVE-II vehicle, and the payload being approximated as a cylinder, it is visually evident that the reproduced geometry matches the outer topology of the flight vehicle.

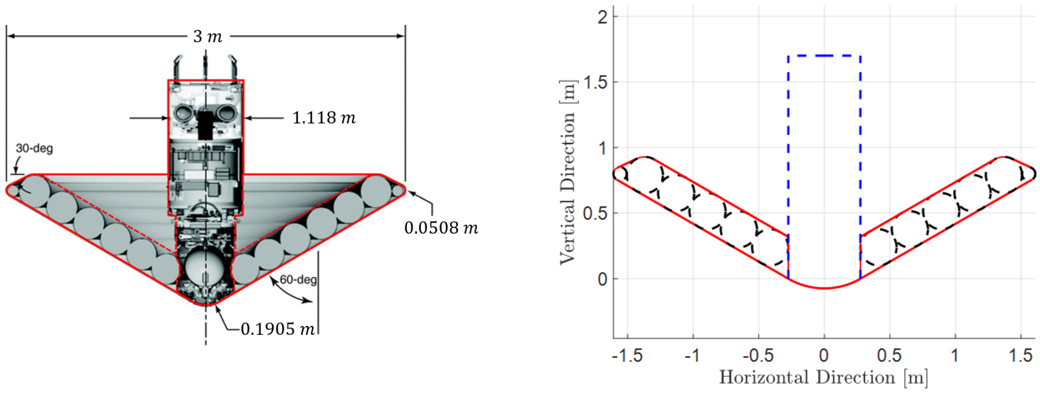

(a) Planar Design; adapted from [231] (b) Constructed Parametric Design

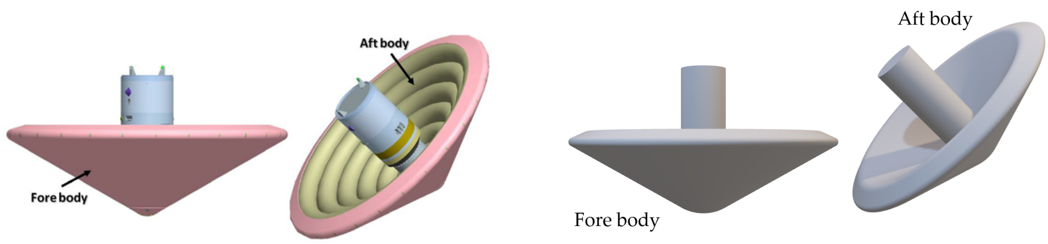

(c) Three-dimensional Design; adapted from [30] (d) Surface of Revolution of Parametric Design

Figure 4.2.: Construction of Parametric IRVE-3 Flight Vehicle

The three-dimensional visualization of the vehicle, both in its frontal and rear views in (c), is also reproduced by creating a surface of revolution according to the procedure described in subsection 3.5.1. The design in (b) is therefore converted into the 3D STL file shown in (d), where the topology is qualitatively similar to that of the flight vehicle. A slight difference is noted in the outer shell roughness since the IRVE-II flight vehicle is manufactured from a series of gores which are instead absent on the surface of revolution. The difference between the two geometries is expected to be marginal and, therefore, its effect is not investigated in this work.

The parameterization of IRVE-3 is proposed in Figure 4.2. Differently from IRVE-2, it presents a smaller torus on the shoulder of the outermost torus, which is an additional component that is included in the methodology outlined in section 3.1. The shoulder torus is correctly modelled as visible in the comparison between (a) and (b). The additional volume generated by this component is also noticeable in the 3D surface of revolution in (d) which, when compared to (c), reveals agreement with the aft-body's outer shell.

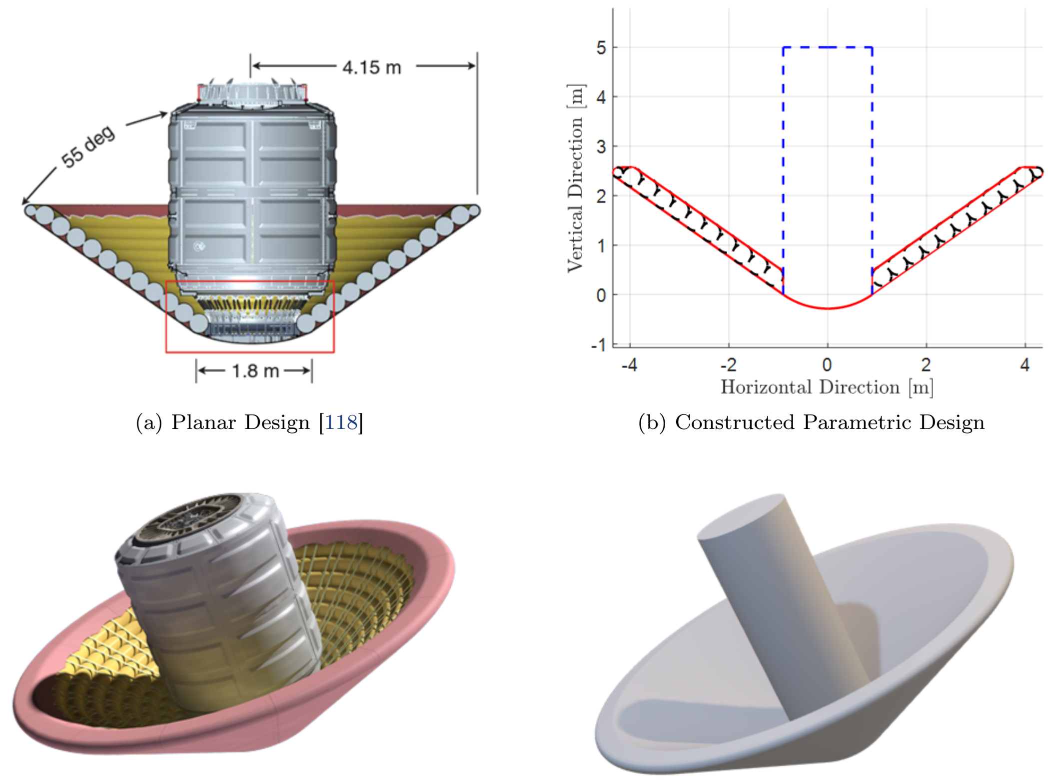

(a) Planar Design [118]

(b) Constructed Parametric Design

(c) Three-dimensional Design; adapted from [115]

(d) Surface of Revolution of Parametric Design

Figure 4.3.: Construction of Parametric HEART Flight Vehicle

Given the comparable dimensions of the IRVE-II and IRVE-3 designs, a third vehicle is employed to complete the verification of the parametric method. A comparison of the HEART design is thus illustrated in Figure 4.3. The planar design in (a) reveals the larger payload design and the number of tori, with the presence of an outer torus. The comparison of (b) with (a) for the planar profile and (d) with (c) for the 3D surface of revolution reveals the applicability of the proposed approach to vehicles with varying dimensions within the design space.

Vehicle	θ_c $[deg]$	N $[-]$	r_{torus} $[m]$	$r_{out,torus}$ $[m]$	h_{pay} $[m]$	r_{pay} $[m]$
IRVE-II	60	7	0.1100	-	1.6	0.195
IRVE-3	60	6	0.1350	0.0508	1.7	0.275
HEART	55	11	0.1945	0.1016	5	0.9

Table 4.1.: Parametric Design of IRVE-II, IRVE-3 and HEART Vehicles

While a visual examination of the parametrized geometries provides a qualitative evaluation, a quantitative analysis is required for verification purposes. To enable this analysis, the original design contour of each vehicle is extracted and digitalized. This allows for direct plotting of the planar design coordinates onto the constructed parametric design, facilitating the measurement of any discrepancies, as depicted in Figure 4.4. Since all 3D vehicles are symmetric surfaces of revolution, only the 2D planar profile is considered. Additionally, it is sufficient to evaluate only half of the 2D profile given its symmetry about the vertical axis.

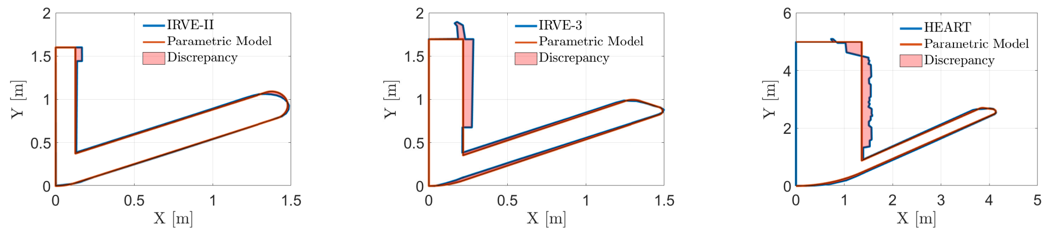

(a) IRVE-II (b) IRVE-3 (c) HEART

Figure 4.4.: Discrepancy between parametric and original planar design of stacked toroids

The red shaded region in Figure 4.4 represents the difference between the original and constructed parametric profiles. The percentage of the shaded discrepancy area relative to the original design is evaluated and summarized in Table 4.2 to determine the deviation of the constructed geometry with respect to the original one. IRVE-II exhibits an error below 4%, indicating a close agreement, while IRVE-3 and HEART have a slightly larger error of around 7.7% due to additional uneven components on the payload surface. The major deviations occur in those areas, with some minor errors in the nose-cone and outer shoulder regions due to digitalization inaccuracies in the original geometry.

The assessment reveals that a potential source of error arises from the simplified payload shape, which assumes a constant cylinder shape defined by the nose-cone radius throughout the profile. However, this source of error, amounting to less than 7.7%, is considered negligible for expected flight conditions at low angles of attack. This is due to the fact that the payload will be predominantly covered by the frontal aeroshell, minimizing its aerodynamic influence. Incorporating a more accurate payload geometry would not yield significant benefits to the simplified aerothermal, F-TPS, and mass models integrated within the current MDAO framework. The proposed parametric approach is therefore considered successfully integrated and suitable to model rigid stacked toroid IADs.

Vehicle	Original Area [m^2]	Shaded Area [m^2]	Discrepancy [%]
IRVE-II	0.6746	0.0265	3.93
IRVE-3	0.7746	0.0603	7.78
HEART	8.3231	0.6346	7.62

Table 4.2.: Discrepancy between constructed and original stacked-toroid geometry

4.2. Planar Motion Trajectory: Verification

Planar motion is widely applied to entry trajectories and its validity is already well established. However, to verify the correct implementation of the planar equations of motion described in section 3.4 and their suitability in simulating the entry trajectory of a stacked-toroid, a comparison between the numerical results and the actual flight trajectory of the IRVE-II vehicle is hereby conducted. The overview of the mission concept of operations is given in Figure 4.5, showing that the trajectory data is measured between 80 km, used as the reference entry, and 40 km for approximately 30 seconds [230]. Given that the atmospheric model described in section 3.3 is only applicable to the Martian atmosphere, the aerodynamic database and environmental conditions, namely the entry velocity, density and speed of sound, are extrapolated from the reconstructed flight trajectory [100] as inputs for the planar equations of motion.

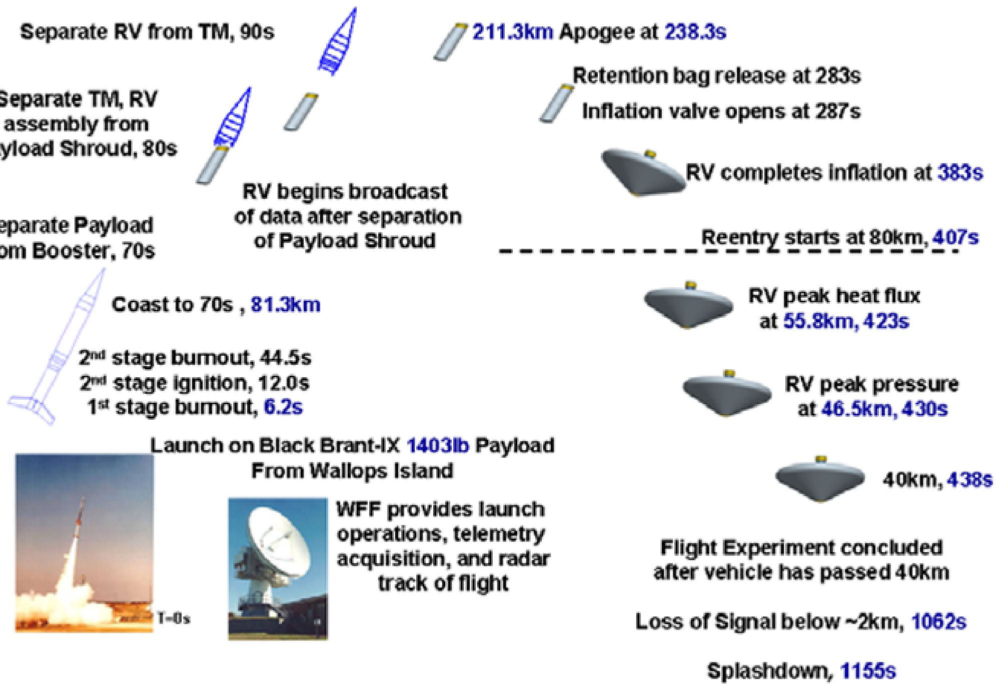

Figure 4.5.: IRVE-II Mission Overview [230]

The comparison of the actual flight trajectory of IRVE-II and the simulation results is shown in Figure 4.6 for the altitude-Mach number curve, deceleration load against altitude, dynamic pressure against altitude and, finally, for the downrange profile over the time of flight. All the results presented show an excellent agreement with the flight data, presenting R^2 correlations larger than 0.98 in all cases. It is noted that the reconstructed trajectory data of IRVE-II was obtained using the Program to Optimize Simulated Trajectories II [100], accounting for each trajectory stage. However, of interest to this section is the re-entry phase between 40 km and 80 km of altitude. The reference data adopted in this work for comparison also falls within the pre-flight simulation Monte Carlo results conducted by O'Keefe et al. [100], confirming the validity of the data.

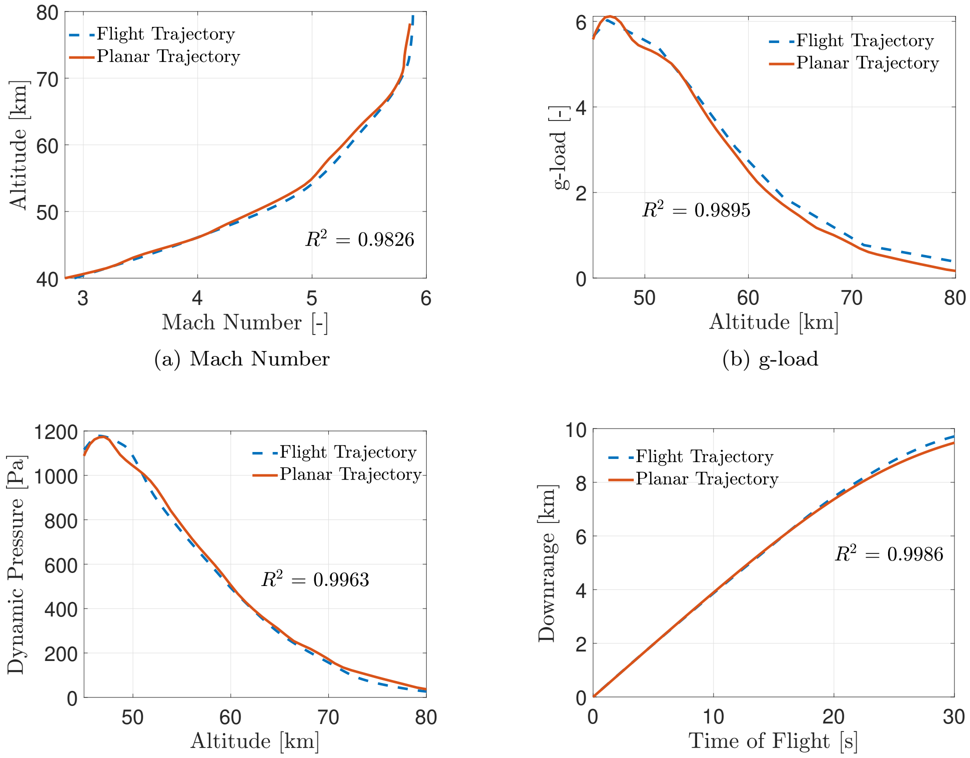

(a) Mach Number

(b) g-load

(c) Dynamic Pressure

(d) Downrange

Figure 4.6.: Comparison of Reconstructed IRVE-II Trajectory with Planar Motion

The mean percentage errors are shown in Table 4.3, where errors between $1-7$ % are obtained across the plots. The excellent agreement, due to the minimised source of uncertainty in aerodynamic coefficients and atmospheric parameters given that these have been extrapolated from the actual flight, confirms the suitability of the planar model to evaluate trajectories in early design stages.

Although the errors resulting from the assumptions made in the definition of the planar equations are generally small, it is important to acknowledge their presence. One such assumption is the absence of lateral wind speeds, which was instead measured in the case of IRVE-II [100, 230]. However, for the purposes of this work, these errors are considered to be negligible. The effect of wind on the entry trajectory is further discussed in section B.7.

$h-M$ Figure 4.6(a)	$g-h$ Figure 4.6(b)	$q-h$ Figure 4.6(c)	$R-t$ Figure 4.6(d)
1.978%	7.097%	3.696%	1.074%

Table 4.3.: Average Percentage Error $|\delta_{\%,avg}|$ of IRVE-II Trajectory Model

4.3. Aerodynamics

4.3.1. Mesh Independence: Verification

Prior to establishing the validity of the aerodynamics method described in section 3.5, it is crucial to verify that the results obtained with the panel methods for a stacked-toroid are independent of the vehicle's spatial discretisation. The IRVE-II design is constructed as shown in Figure 4.1 and nine meshes are generated with an increasing level of refinement in Table 4.4. The increasing level of refinement in the meshes is visually displayed in Figure 4.8 to show that while the number of panels is increased, the topology of the baseline geometry in each mesh is conserved. The mesh independence hereby verified is also valid for the integration of the panel method with the aerothermal models later analysed for the heat distribution.

Number of Triangles	1694	4152	5220	5562	10656	11784	26078	54446
Number of Nodes	849	2076	2612	2783	5330	5894	13041	27225

Table 4.4.: Mesh independence study for aerodynamics panel method

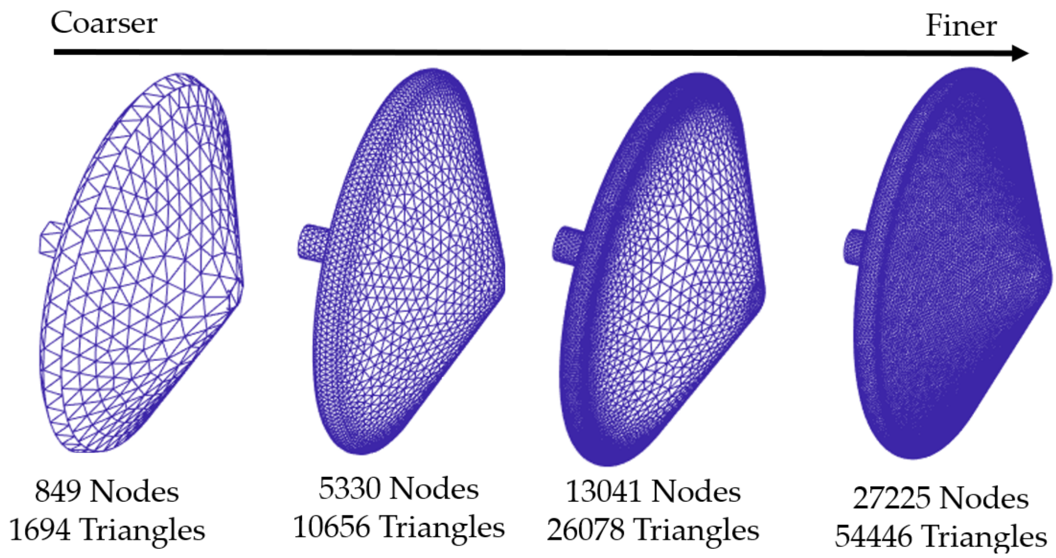

Figure 4.7.: Refinement of the number of panels generated for the IRVE design

The modified Newtonian panel code is thus run for the investigated meshes and the drag coefficient is measured for the scenario in which $M = 5$ and $\gamma = 1.4$. The computational time and normalized drag coefficient are shown in Figure 4.7. It is observed that no change in drag coefficient is observed beyond 30,000 mesh triangles and that only 1% of variation is measured after 5,000 triangles. The convergence of the resulting normalised drag coefficient is also associated with the logarithmic reduction of the average panel area in proportion to the total surface area of the stacked toroid. A value lower than $4 \cdot 10^{-4}$ is recommended based on the percentage change of C_D.The lower surface area should especially be employed in the rounded features of the geometry, such as the nose cone and the outer torus' shoulder. The increased mesh refinement comes at the expense of an increased computational time, though this varies from 0.2 seconds for approximately 1000 elements to 0.6 seconds for $4.5 \cdot 10^4$ elements. Therefore, the slight increase in computational time is justified by the enhanced accuracy of the numerical model. Given that the computational time is only a fraction of a second, though it will be largely amplified by the number of iterations required in the MDAO framework, a minimum number of $3 \cdot 10^4$ mesh triangles is ensured in the following simulations.

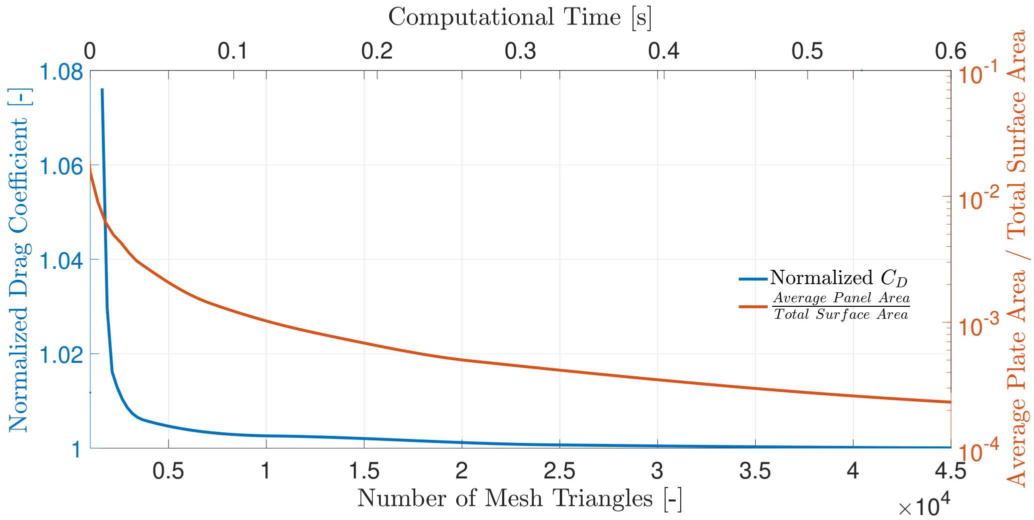

Figure 4.8.: Aerodynamic Mesh Independence Analysis for the number of panels generated

4.3.2. Shading Algorithm: Verification

To illustrate the effective functionality of the shading algorithm implemented from the ADBSat tool [174], in addition to the back-culling method, two scenarios are hereby presented as in Figure 4.9. The first one, referred to as "Scenario A", entails a stacked toroid perceiving a stream of air on its port side at an angle of attack of zero degrees and a side-slip angle of 90°. On the other hand, "Scenario B", is subject to a freestream flow from its rear side at a slant angle of 45° to inspect the variation of the payload on the rear surface of the outer shell.

The difference in the panels which are captured by the algorithm as being exposed to the flow and those which are regarded as being shaded is shown in Figure 4.10 for scenario A, where the top views are obtained with the complete shading algorithm and the bottom views are obtained only with the back-culling algorithm. While no significant difference is noted in the front, port and starboard views, the effect of the shading algorithm is most noticeable in the rearview. In fact, the starboard section of the rear view appears to be exposed to the flow due to the inclination of the panels with respect to the flow and completely neglecting the presence of a forebody which is instead impeding the flow from impinging onto the rear section. Qualitatively, this results in approximately half of the rear section being included in the aerodynamic calculation that should instead be neglected. The entire payload also appears to be interfacing with the incoming flow when only the back-culling is used, whereas only half the top section of the cylindrical body is included with the shading algorithm.

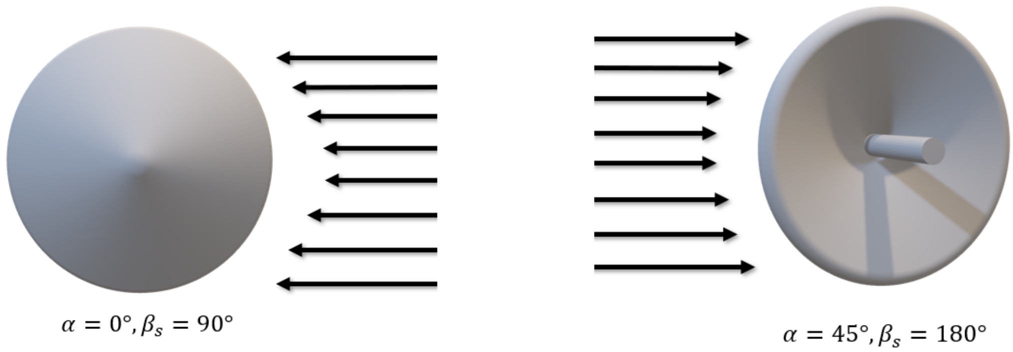

(a) Scenario A

(b) Scenario B

Figure 4.9.: Different stacked toroid's orientations to illustrate the shading algorithm

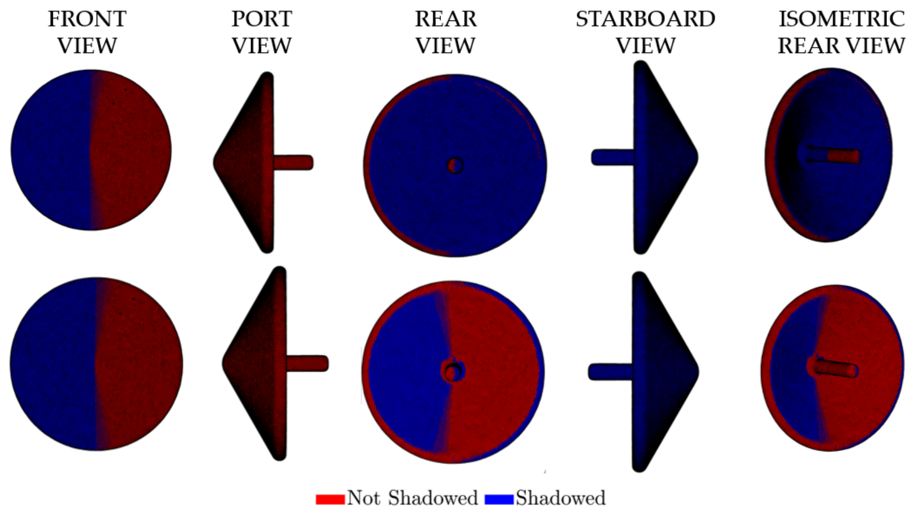

Figure 4.10.: Complete shading algorithm (top) and only back-culling (bottom) of "Scenario A"

Similarly, the shading algorithm is applied to scenario B in Figure 4.11, where the most remarkable observation is made on the shadow that the payload generates on the rear section of the outer shell. In fact, the algorithm correctly recognises that the payload is blocking part of the flow, and is projecting the 2D image onto the 3D curved profile. While this improved topology of the shadow, when compared to the back-culling method, contributes to a smaller portion of the IAD as opposed to the difference shown in Figure 4.10, it does reveal the correct implementation of the shading algorithm.

To quantify the error that the back-culling alone would cause, without the complete algorithm to account for the shading caused by forebodies, the percentage error of the aerodynamic coefficients obtained using the modified Newtonian panel method, with and without the shading algorithm, are plotted in Figure 4.12 across a range of sideslip angles between 0° and 180°. As expected, the

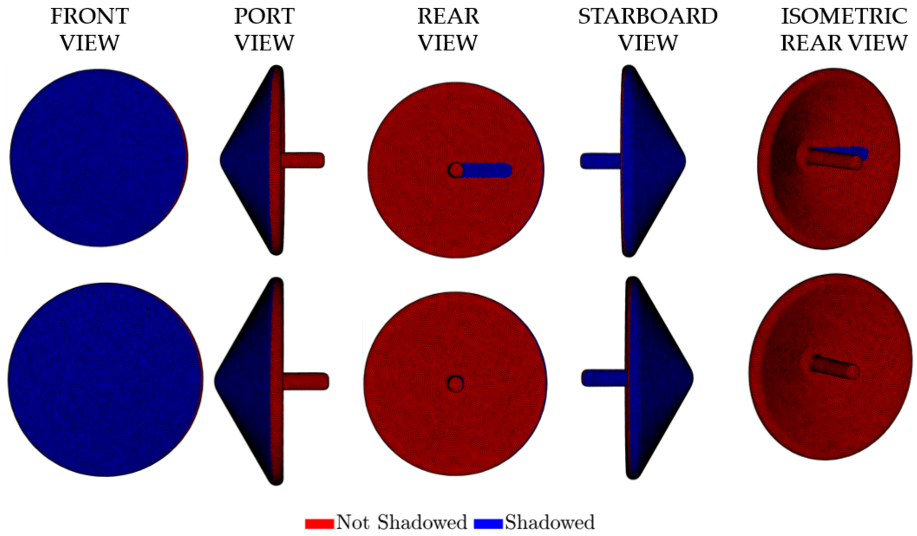

Figure 4.11.: Complete shading algorithm (top) and only back-culling (bottom) of "Scenario B"

error for both the drag and lift coefficient is below 5% for values of β_s below 45°. On the contrary, as $45° \leq \beta_w \leq 90°$, the error peaks for both the aerodynamic coefficients, reaching errors as high as 60% for C_D and 100% for C_L. It is noted that the shadowing algorithm predicts a higher drag and, consequently a lower lift, than without. The As $\beta_s \geq 90°$, the error trends are specularly repeated as between $0° \leq \beta_w \leq 90°$ given the axisymmetric nature of the stacked-toroid used. The correct implementation of the shading algorithm is thus verified and its application has been shown to reduce the error by values as large as 100% for large side slip angles. It is also noted that the algorithm may be turned off if needed for $\beta_w \sim 0$ and $\alpha \sim 0°$

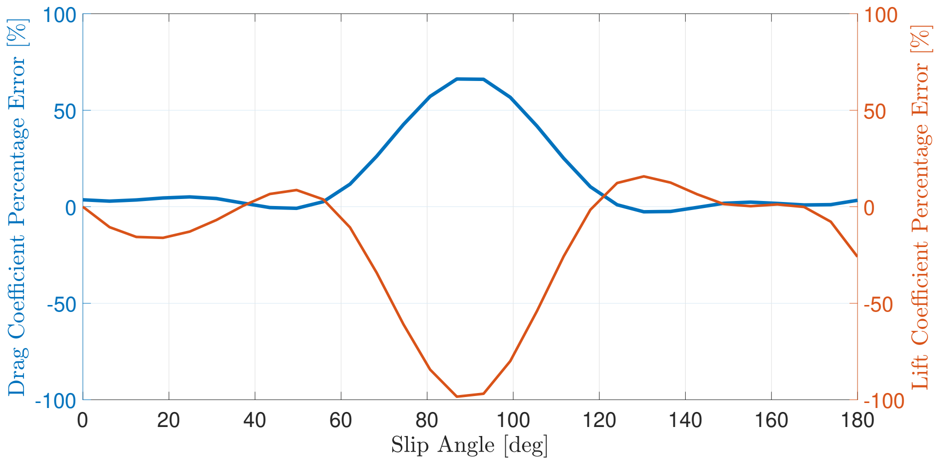

Figure 4.12.: Percentage Error of Panel Method without shading algorithm on C_D and C_L

4.3.3. Continuum Regime: Verification

To verify the correct implementation of the modified Newtonian method in conjunction with the local inclination panel method applied to a stacked-torus vehicle, the high-fidelity numerical data obtained by Xiaoshun and Xue [232] using the ICEM and FASTRAN CFD solvers is retrieved for the continuum regime. It is important to note that a rather imprecise mesh independence study was performed in the study, with only four grids of increasing refinement between 1 and 3.5 million elements, and a lack of description of the boundary layer modelling. In fact, the article only reports a first layer thickness of 0.015 mm but does not specify the number of layers, the expansion of these layers and the y^+ value. Thus, a 25% of error is estimated by the author of this work in the CFD data to account for the uncertainty concerning the mesh generation and boundary layer modelling.

Xiaoshun and Xue [232] performed viscous and inviscid simulations using the environmental conditions shown in Table 4.5 for supersonic and hypersonic speeds by varying the inlet Mach number between 1 and 7. A direct comparison of the simulations with the modified Newtonian method is shown in Figure 4.13, where the 25% uncertainty is shown with the error bars. The difference between the viscous and inviscid models is immediately noticeable for $M_\infty \leq 4$, whereas a convergence is noted as $M_\infty > 5$. As expected, the modified Newtonian method appears to be nearly within the uncertainty bounds imposed for $M_\infty \to \infty$ and shows the most amount of uncertainty in the low-speed regime particularly with respect to the inviscid model. The viscous model is thus used for reference. The contour plot of Mach number is shown in Figure B.3.

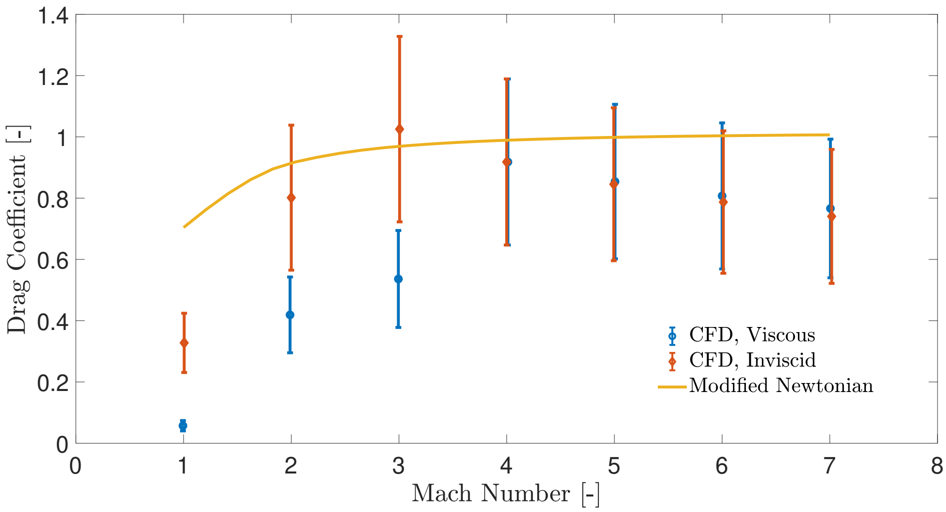

Figure 4.13.: Comparison of modified Newtonian method with viscous and inviscid CFD data by Xiaoshun and Xue [232]

Altitude $[km]$	Temperature $[K]$	Pressure $[Pa]$	Density $[kg/m^3]$	Kinematic Viscosity $[m^2/s]$	Mach Number $[-]$
50	270.65	75.77	$771.027 \cdot 10^{-4}$	$1.659 \cdot 10^{-2}$	1-7

Table 4.5.: CFD Environmental Data for IRVE-3 analysis by Xiaoshun and Xue [232]

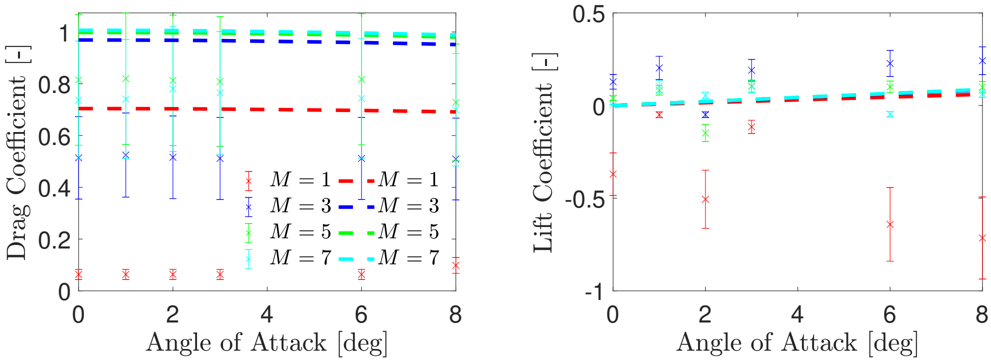

(a) Drag Coefficient

(b) Lift Coefficient

Figure 4.14.: Comparison of Viscous CFD simulation by Xiaoshun and Xue [232] at varying angles of attack and Mach numbers with modified Newtonian method

The comparison between the modified Newtonian method and the CFD data at various angles of attack is presented in Figure 4.14 for the viscous case. To account for uncertainty, a margin of 25% has been applied to the discrete data points. It can be observed that both numerical methods exhibit a similar rate of variation in the aerodynamic coefficient with respect to α. This suggests that the panel code is capable of accurately predicting angle of attack variations, particularly for α values below $8°$. The panel method code shows improved agreement with higher-fidelity simulations as the Mach number increases. While this observation holds true for the drag coefficient, the CFD lift coefficient appears to exhibit more fluctuations. However, considering the oscillating negative values and the non-zero magnitude at $\alpha = 0°$, it can be inferred that either the geometry used for the CFD data is not perfectly axi-symmetric or the numerical error is larger than the observed quantity. Therefore, this comparison primarily serves to highlight the correct trends predicted by the panel method.

Further comparison with independent studies retrieved from the literature is presented to expand the verification process to different geometries under different flow conditions. The CFD aerodynamic analysis conducted by Wang et al [89] addressed the IRDT-like system and investigated different half-cone angles. The cases for $\theta_c = 50° - 60°$ are reported. Wang specifies that the use of the $k - \omega$ turbulence model is implemented with a structured boundary layer, and ensures that a sufficient number of iterations is chosen to allow numerical convergence of the residuals. No error bars are thus applied. The drag coefficient measured for $0.2 \leq M \leq 15$ is plotted in Figure 4.15 against the panel method with the modified Newtonian method. The results show a strong agreement between the higher-fidelity simulation and the method adopted in this work under continuum flow conditions. The drag coefficient of the stacked toroid is correctly identified in the hypersonic regime, with the highest discrepancy registered at lower speeds, as expected.

The difference between the two methods approaches zero for $\theta_c = 50°$, whereas an error offset is measured for the $\theta_c = 60°$ configuration, hinting that the solution may be more accurate for shallower angles of the stacked toroid. This is not surprising since the modified Newtonian method assumes a linear variation of flow quantities across each panel which holds when the panels are shallow. Nevertheless, the mean percentage error is 2.54% for the first instance and 6.87% for the second one, meaning that a sufficiently high degree of agreement for conceptual studies is yielded. The error at each Mach number is given in Table B.9.

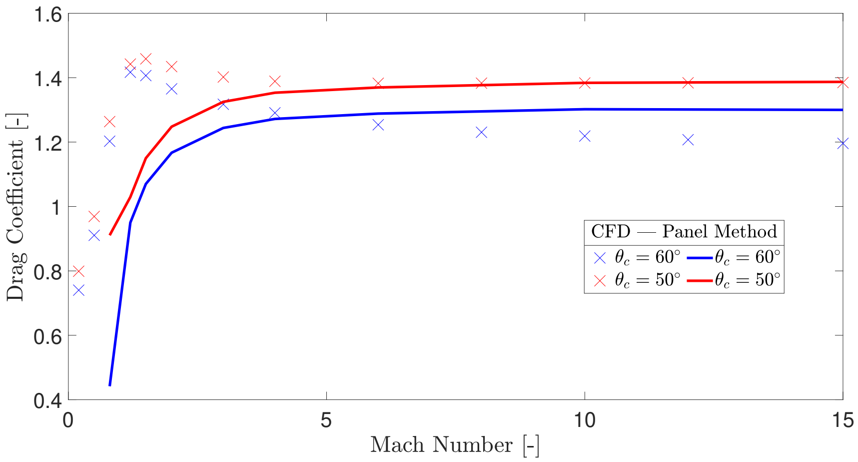

Figure 4.15.: Variation of Drag coefficient for modified IRDT vehicle against CFD data [89]

A final qualitative comparison is presented in Figure 4.16, where the pressure coefficient distribution is plotted for the modified Newtonian method and the CFD of the IRDT-2 vehicle. The qualitative juxtaposition shows that, although the original vehicle presents a mechanical discontinuity between the first and second IAD stages which is not accounted for by the simplified geometry parametrised, the panel method correctly identifies the region of highest pressure on the stacked toroid's surface and also models the pressure differential due to the presence of a non-zero angle of attack. This suggests the correct utilization of the reference frames for the flow direction.

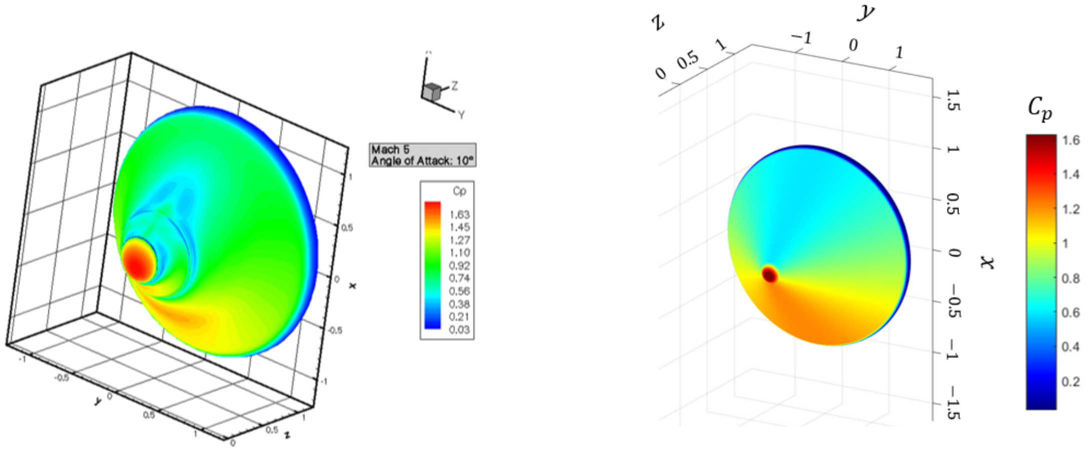

(a) CFD Surface plot [233]

(b) modified Newtonian panel method

Figure 4.16.: Comparison of surface plot of pressure coefficient C_p for the IRDT-2 fully inflated vehicle at $M = 5$ and $\alpha = 10°$

4.3.4. Continuum Regime: Validation

In addition to verifying the correct integration of the local inclination method with the modified Newtonian method, as established from the comparison with high fidelity data, its accuracy and degree of applicability is validated from a comparison with the flight data of IRVE-II and IRVE-3. In fact, while IRVE-I experienced a launch failure during the separation sequence, IRVE-II's successful flight provided invaluable aerodynamic data that is employed for validation purposes in the continuum regime since the data was collected between 80km and 40km on Earth ($Kn << 0.1$). The telemetry was post-processed at NASA's Wallops Flight Facility and later published by O'Keefe and Bose [100]. Interestingly, the data reconstruction displays a set of data that is reconstructed from a pre-flight aerodynamic database as a function of the environmental characteristics and the attitude of the vehicle, and a set of post-flight aerodynamic data attained to accurately match the telemetry measurements as shown in Figure B.4. While both sets of data are here presented, O'Keefe [100] attributes the cause of the oscillations between 430 and 445 seconds ($M \geq 6$) to the flexibility of the inflatable during the pressure pulse. This can be interpreted as either a reduction in effective cone angle or as an increase in effective total angle of attack $0° \leq \alpha \leq 10°$. Further discussion on the difference between the two databases is presented in subsection 4.3.5 to validate the deflection model.

By retrieving the aerodynamic coefficient, angle of attack, Mach number and dynamic pressure as a function of the flight time in [100], the flight data is manipulated to allow a fair comparison with the modified Newtonian method. The axial and normal coefficients are plotted in Figure 4.17 as a function of Mach number, where the corresponding angle of attack is also indicated on the right y-axis. While the average values μ of the aerodynamic coefficients are used for comparison with the panel method implemented in this work, the 2-standard deviation interval 2σ are also indicated to show the confidence of the data.

The applicability of the modified Newtonian method to the IRVE-II vehicle is validated by comparing both the pre- and post-flight C_A and C_N to the corresponding quantities obtained using the panel method as listed in Table B.7 and plotted in Figure 4.17. As one would expect, the axial force coefficient appears to be more accurate in the hypersonic regime, whereas a large discrepancy of up to 21.83% is measured at supersonic speeds. Interestingly, the underestimation of the axial coefficient obtained with the modified Newtonian method increases the accuracy when compared to the post-flight data as opposed to the rigid-model aerodynamic database. To quantify the agreement, the mean percentage error at the points sampled according to Table B.7 is 11.56% for the pre-flight data and 14.65% for the post-flight data. In fact, it is clear that the numerical data is almost within the 2σ confidence interval for the supersonic regime, but is well within the bounds for $M > 5$.

On the contrary, the normal force coefficient appears to be within the bounds of both the pre-flight and post-flight data. While it is important to realize that the magnitude of the coefficient is close to zero, and that a percentage error may not be appropriate as a comparison, the discrepancy may be quantified by means of the root-mean-square deviation (RMSE). A value of 0.0159 is yielded for the rigid database, with a standard deviation of 0.0168 meaning that a good agreement, whereas a RMSE of 0.105 with a standard deviation of 0.0504 is obtained for the post-flight data, revealing a poorer agreement as in Table 4.6. This reveals that the proposed local inclination method is suitable for predicting the aerodynamic performance of rigid models, particularly in the higher Mach regime, but performs slightly worse for flexible vehicles.

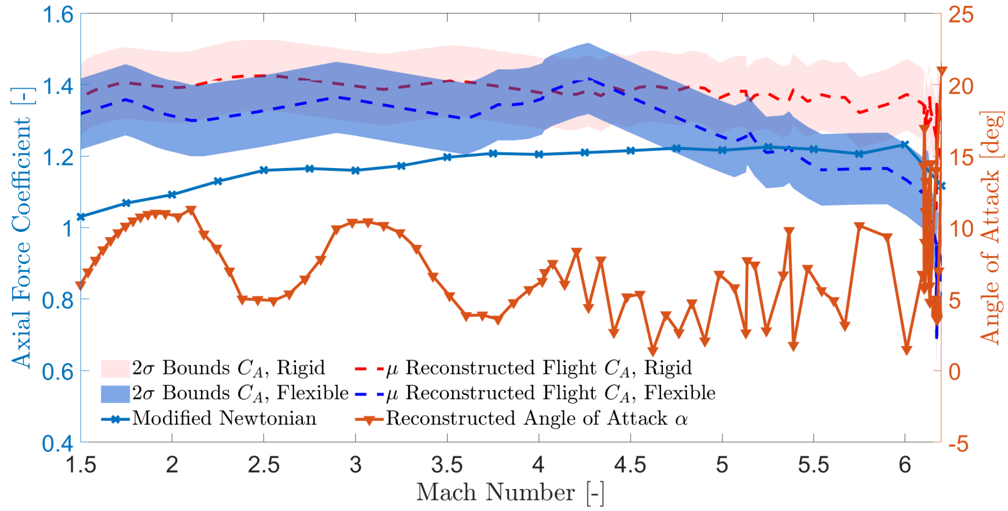

(a) Axial Force Coefficient

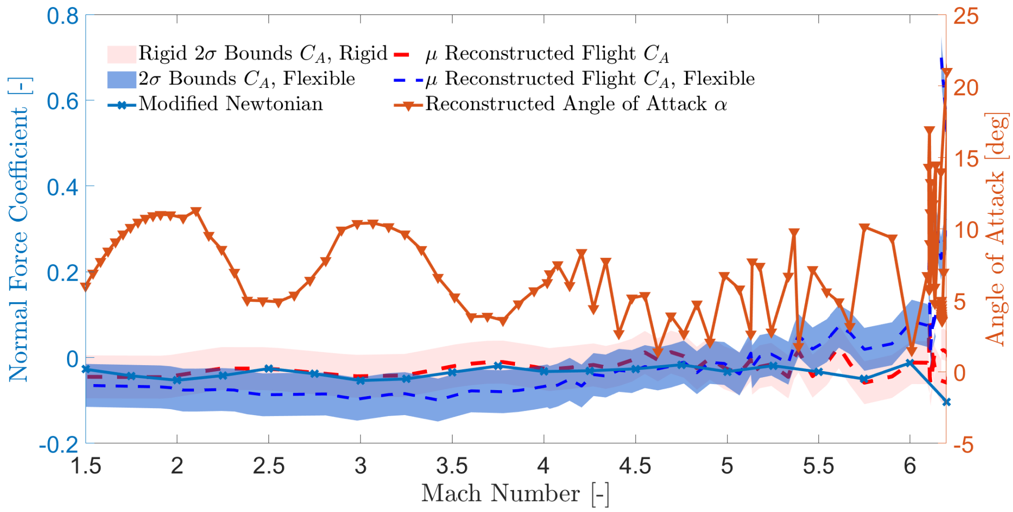

(b) Normal Force Coefficient

Figure 4.17.: Comparison of IRVE-II data [100] with modified Newtonian method

Data	C_A		C_N	
Agreement	Pre-Flight	Post-Flight	Pre-Flight	Post-Flight
RMSE	0.2150	0.1668	0.0159	0.1054
Standard Deviation	0.0504	0.1148	0.0168	0.0955
Data Range	0.2389	0.5056	0.0633	0.4208

Table 4.6.: IRVE-II aerodynamic data agreement with modified Newtonian method

To further validate the applicability of the modified Newtonian method to a stacked-toroid when subjected to a broader Mach regime and harsher entry conditions which are more representative of a future Mars mission, the flight data of IRVE-3, launched July 23rd 2012 on a suborbital trajectory and reconstructed by Olds et al. [38] is employed for comparison. The aerodynamic forces and attitude of the vehicle during the EDL phases shown in Figure B.5 are used to obtain the mean values of the curves such that the fluctuating quantities are disregarded. In particular, the combination of the angle of attack with the Mach number is used to obtain the aerodynamic coefficients as predicted by the 3D modified Newtonian panel method. The comparison of the flight data with the numerical results is shown in Figure 4.18, which shows the plot of the data listed in Table B.8.

Similarly to the comparison with the CFD data for verification purposes, it is observed that the agreement between the panel method code and the flight data increases with the Mach number. The initial error, at subsonic speeds, is in the range of 18-28% for the aerodynamic coefficients investigated, which decreases to 0.06-3.44% in the hypersonic regime. Overall, the consistent agreement in aerodynamic performance reveals a mean percentage error of 7.04% for the drag coefficient and 10.52% for the lift coefficient. Besides the numerical error and limitations of the code, the difference is also attributed to two major factors. The first one is the averaging of the otherwise fluctuating quantities measured in flight as noted in Figure B.5. The second, and most important, consideration is that the aerodynamic flight performance deviates from the ballistic range database utilized by Olds [38] at Mach speeds lower than 3.5 due to the deflection of the inflatable body estimated to reduce the half-cone angle by approximately 2.6°, thereby reducing the effective forebody cone angle and thus varying the pressure distribution. This is addressed in further detail in subsection 4.3.5 to validate the analytical relation suggested in [38] to improve the aerodynamic prediction.

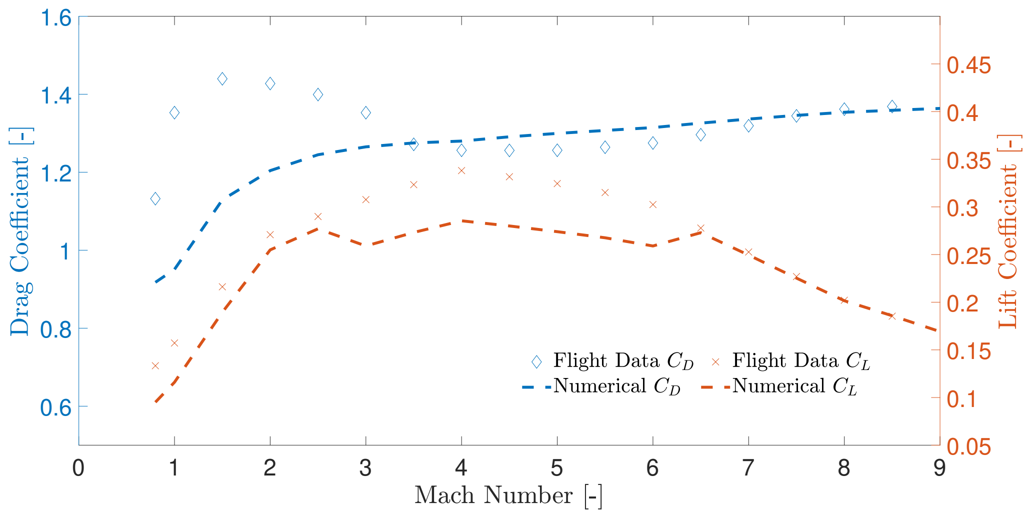

Figure 4.18.: Comparison of aerodynamic coefficients as predicted by the modified Newtonian method with reconstructed IRVE-3 flight data

4.3.5. Aerodynamic Correction due to Inflatable Deflection: Verification

To verify the suitability of Equation 3.104 in considering the F-TPS deflection, the dynamic pressure profile along the IRVE-II trajectory is first retrieved from [100] as the independent variable. The delta required in Equation 3.104, denoted as ΔC_A, for the axial force coefficient is then computed at each point in the IRVE-II trajectory. This is accomplished by calculating the difference between the pre-flight aerodynamic database, which assumes rigid models, and the post-flight telemetry. Therefore, ΔC_A is defined as $C_{A,\text{flight}} - C_{A,\text{rigid}}$. The calculated deltas serve as the dependent variable, and the individual data points are plotted in Figure 4.19. An exponential expression is fitted to the data points to establish the delta-correlations. The equation, displayed in Figure 4.19 is presented in Equation 4.1. Good agreement, quantified by $R^2 \sim 0.79$, is obtained despite encountering a significant amount of uncertainty at low dynamic pressures ($q \to 0$), where the model fails since no significant aeroshell deflection is expected. The same procedure is followed for the normal force coefficient C_N such that $\Delta C_N = C_{N,flight} - C_{N,rigid}$, where the fitted exponential function plotted in Figure 4.20 with an agreement of $R^2 \sim 0.96$, thus revealing an excellent correlation with the flight data deltas.

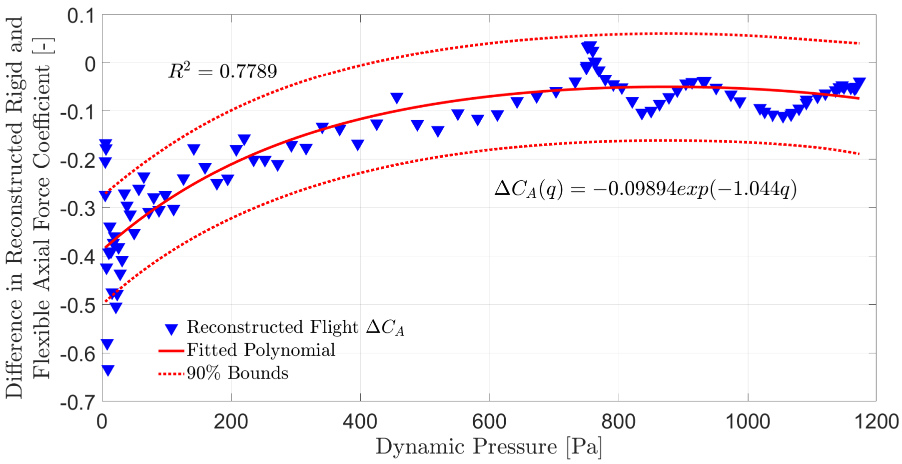

Figure 4.19.: Fitting Correction Function for IRVE-II's flight [100] Axial Force Coefficient

$$\Delta C_A(q) = -0.09894exp(-1.044q) \tag{4.1}$$

$$\Delta C_N(q) = 0.8205exp(-0.01955q) \tag{4.2}$$

The correlation in Equation 4.1 is utilized to calculate the corrected values of C_A. The outcomes are listed in Table B.10. In the comparison of the modified Newtonian method with the pre- and post-flight databases, denoted by the legend labels "rigid" and "flexible" respectively, the correction terms ΔC_A are considered for both pre- and post-flight data. The findings indicate a noticeable decrease in percentage error ranging from 2% to 10% for both datasets up to $M = 5$. However, for $M > 5.5$, a higher error is observed due to the decrease in density and subsequent reduction in dynamic pressure at higher altitudes. This issue aligns with the previously discussed error at $q \to 0$.

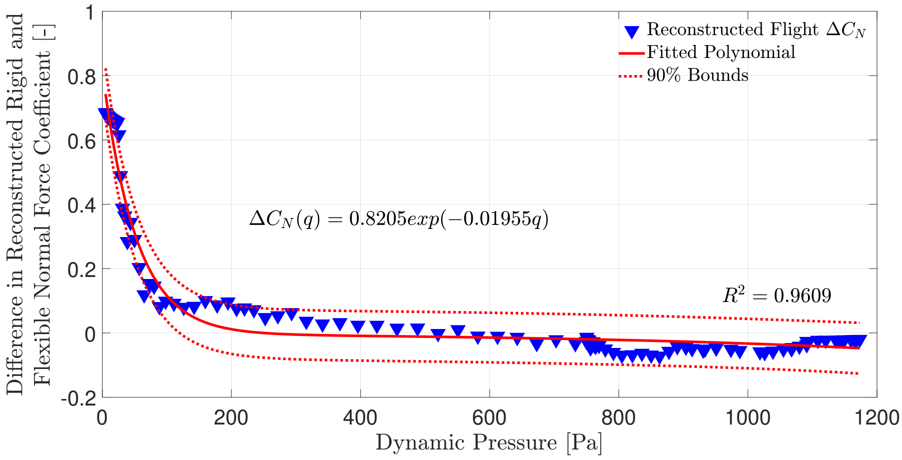

Figure 4.20.: Fitting Correction Function for IRVE-II's flight [100] Normal Force Coefficient

As for the axial force coefficient, the identified deltas for the normal force coefficient as a function of dynamic pressure are substituted in Equation 3.104 to yield the results tabulated in Table B.11. While the correlation shows negligible changes in ΔC_N for $M < 5$ due to the low fitted coefficient in the exponential term which makes $exp(-\infty) \to 0$, the variation becomes more pronounced in the hypersonic region, where the dynamic pressure is lower due to the lower atmospheric density. The absolute percentage error plotted in Figure 4.21 reveals the reduction in percentage errors of the modified Newtonian method when compared to both the pre- and post-flight database. It is noted that the figure is plotted in a semi-log axis due to the large degree of the errors because the C_N coefficients are low in magnitude as the vehicle flies at low α.

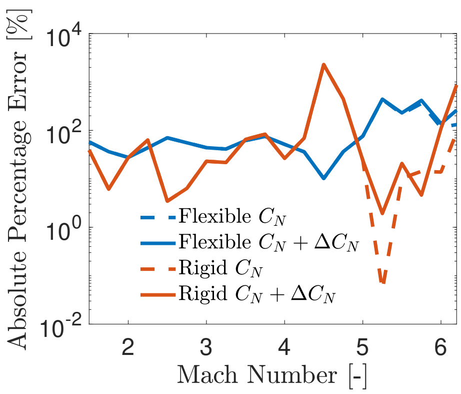

(a) Normal Force Coefficient

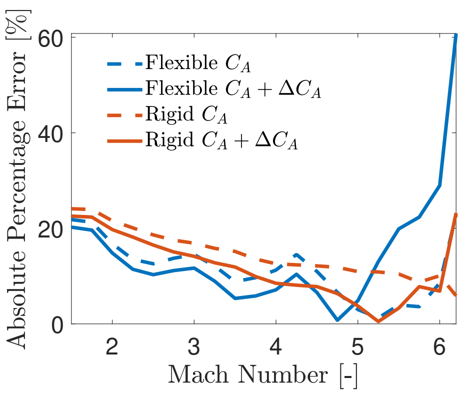

(b) Axial Force Coefficient

Figure 4.21.: Absolute Percentage Error of Modified Newtonian method with Correction for Deflection of IRVE-II Flight

4.3.6. Aerodynamic Correction due to Inflatable Deflection: Validation

Having verified the adequate functionality of the empirical correlations derived from the IRVE-II flight data, their applicability to stacked toroids is validated by utilizing both Equation 4.1 and Equation 4.2 to an independent mission: the IRVE-3 flight data [38] in Figure 4.18 is used as a benchmark. The modified Newtonian method is therefore adjusted to include the deltas applied to the drag and lift coefficients according to Equation 4.3.

$$\Delta C_D = \Delta C_N \sin\alpha + \Delta C_A \cos\alpha; \qquad \Delta C_L = \Delta C_N \cos\alpha - \Delta C_A \sin\alpha; \tag{4.3}$$

The resulting percentage errors are plotted in Figure 4.22. First, it is remarked that the peak dynamic pressure in IRVE-3 is much larger than in IRVE-II, having increased from 1.2 kPa to approximately 6 kPa. Nevertheless, both Equation 4.1 and Equation 4.2 yield zero as $q \to \infty$. It is, in fact, clear that the deltas are significant only at low and high Mach numbers, where the dynamic pressure is close to 0. Interestingly, the percentage error is reduced noticeably from 30% to 12% at $M = 1$ for C_L. A slight reduction in percentage error is also present at $M \sim 9$ for the C_D. However, a sudden and undesired increase in error is present in the higher hypersonic region for C_L. This is attributed to the C_L flight data having a small value and the delta correction increasing as the dynamic pressure reduces. Moreover, the much larger dynamic pressure levels attained by IRVE-3 lead to an extrapolation of the functions, which is likely to be the case for future Mars missions. Even in the IRVE-3 flight, however, the variation of aerodynamic loading as a consequence of deflection is marginal with variations within 2-4%. The applicability of the proposed functions is therefore preliminary validated for the cases in which the dynamic pressure is much larger than zero. It is recommended to bound the expression when the absolute corrections in aerodynamic coefficients exceed 30% as it is likely that the model is overshooting.

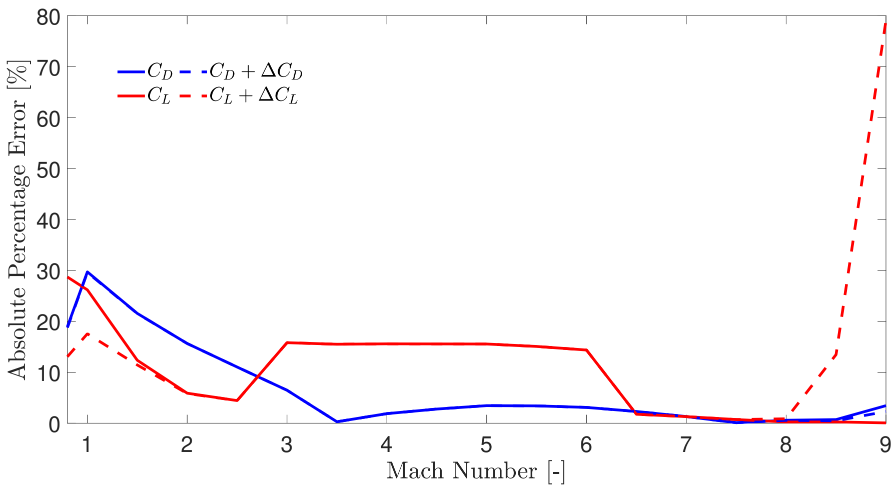

Figure 4.22.: C_D and C_L Absolute Percentage Error of Modified Newtonian method with Correction for Deflection of IRVE-3 Flight

4.3.7. Rarefied Regime: Verification

Given the absence of flight or experimental aerodynamic data of stacked-toroid IADs in rarefied conditions, high-fidelity data is employed to verify the integration of the rarefied aerodynamic models with the local inclination panel method. Moss et al. [56] has carried out numerical simulations with DSMC by applying well-established 3D codes to the IRVE vehicle across a range of different trajectory conditions. The free molecular flow results at an altitude of 150 km with $Kn = 10.05$ are hereby employed for comparison with the aerodynamic analytical formulae adapted to the local panel method. The normal and axial force coefficients are plotted in Figure 4.23 for $0° \leq \alpha \leq 180°$ and listed for completeness in Table B.14 and Table B.13 respectively,

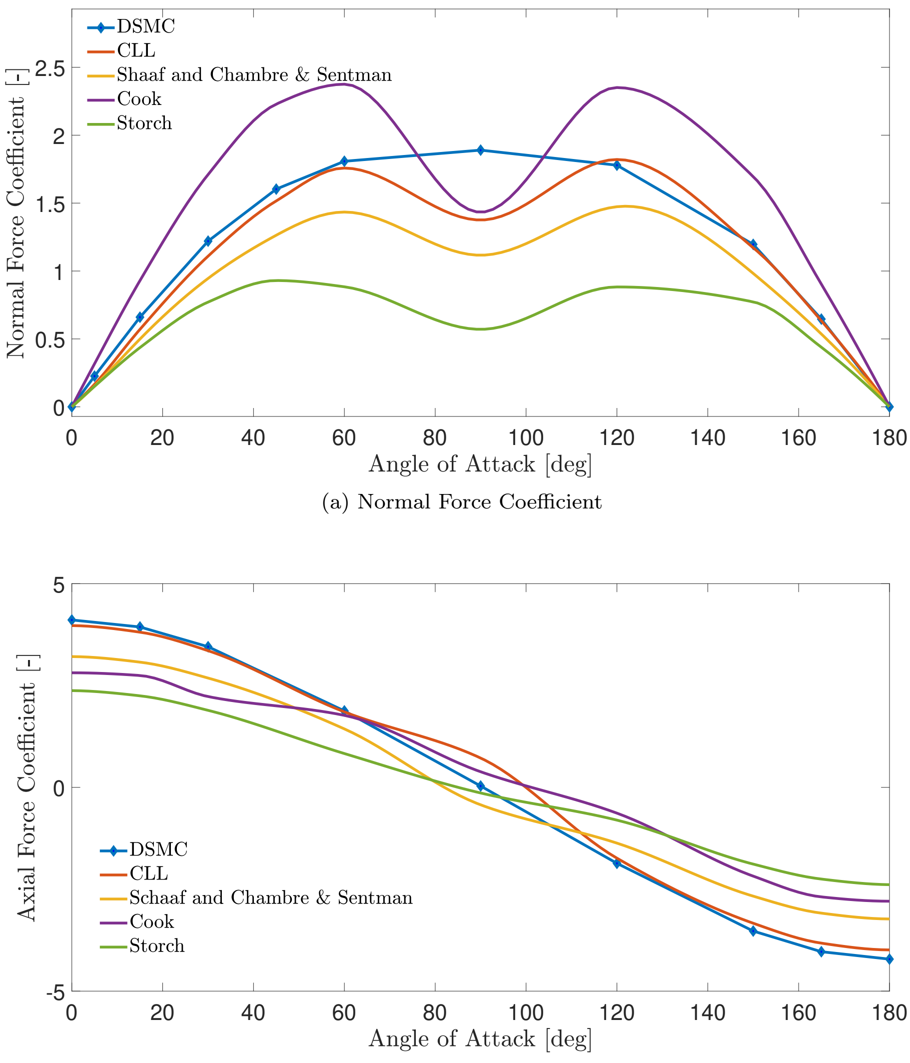

(a) Normal Force Coefficient

(b) Axial Force Coefficient

Figure 4.23.: Comparison of rarefied panel method with Moss' [56] DSMC data

The results comparison strongly indicates that the analytical models successfully capture the general trends of increasing and decreasing aerodynamic loading as the angle of attack varies. Among the models tested, the CLL method demonstrates the highest level of accuracy, as evidenced by mean percentage errors of 3.73% and 9.58% for the normal and axial coefficients, respectively. However, it is important to note that the CLL method relies on the coefficients listed in Table B.6, which are specific to species present in Earth's atmosphere. Consequently, the CLL method cannot be directly applied to Mars due to the unavailability of coefficients for CO_2 and CO. The agreement between the CLL equation and DSMC solutions justifies the close match in results. Nevertheless, since the required coefficients for CO_2 and CO are lacking, the CLL model cannot be utilized for Mars-related analysis.

Alternatively, the Schaaf and Chambre method, which is equivalent to Sentman's equation when $\sigma_T = \sigma_N = 1$, produces results applicable to both Mars and Earth. However, the accuracy diminishes, with mean errors around 23% for both axial and normal force coefficients. Cook's approach yields similar outcomes, also exhibiting a decrease in accuracy. In contrast, Storch's formulation is the least accurate, displaying errors exceeding 40%. This inaccuracy can be attributed to the hyperthermal assumption, which is invalid for entry applications. In conclusion, considering the unavailability of CLL coefficients for CO_2 and CO, the Schaaf and Chambre method emerges as the preferred choice for analyzing aerodynamic loading during Mars entry and will therefore be integrated in the present MDAO framework.

In addition, it is worth highlighting that all the analytical models exhibit limitations when it comes to the normal force coefficient at $\alpha = 90°$, as depicted in Figure 4.23. However, it is important to consider that this angle is beyond the range of interest for a stacked toroid, as such a design would typically be intended to operate at low or moderate angles of attack. Furthermore, when examining the errors within the relevant range of α, as illustrated in Figure 4.24, it becomes evident that the percentage errors remain relatively stable and do not display significant deviations within a range of approximately ±10% around the mean value. The correct implementation of the methods is verified and their suitability is established under different conditions. The Schaaf and Chambre method prevails as the chosen one for implementation for the analysis of future Mars missions.

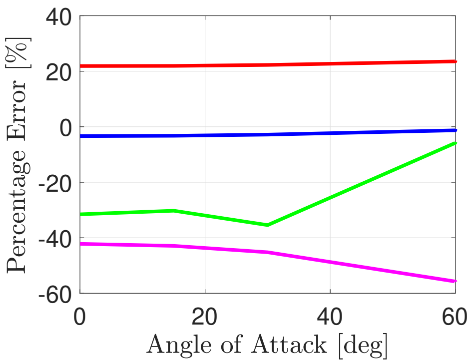

(a) Percentage error of Normal Force Coefficient

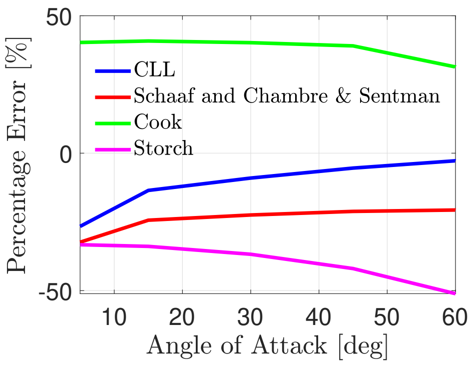

(b) Percentage error of Axial Force Coefficient

Figure 4.24.: Percentage Error of Rarefied Panel Codes with Moss' [56]

4.3.8. Transitional Regime: Verification

The low-density aerodynamic data obtained by Moss et al. [56] using high-fidelity CFD for near-continuum and continuum flow regimes and DSMC for FMF covers the Knudsen range of $1.49 \cdot 10^{-5} \leq Kn \leq 10.05$ at different angles of attack. To obtain the bridging parameters suitable to the class of vehicles representative of stacked-toroids, the FMF limit is taken as $Kn = 10$ and the continuum one at Kn=$1 \cdot 10^{-3}$. The fitting of Wilmoth's function to the axial and normal aerodynamic coefficients is shown in Figure 4.25 for $\alpha = 0°$. The fitting of both C_A and C_N is done first with the parameters retrieved from the literature for standard 70-degree re-entry capsules, and then using the least-square method in Equation 3.70. The R^2 obtained using the two methods is listed in Table 4.7 for both coefficients.

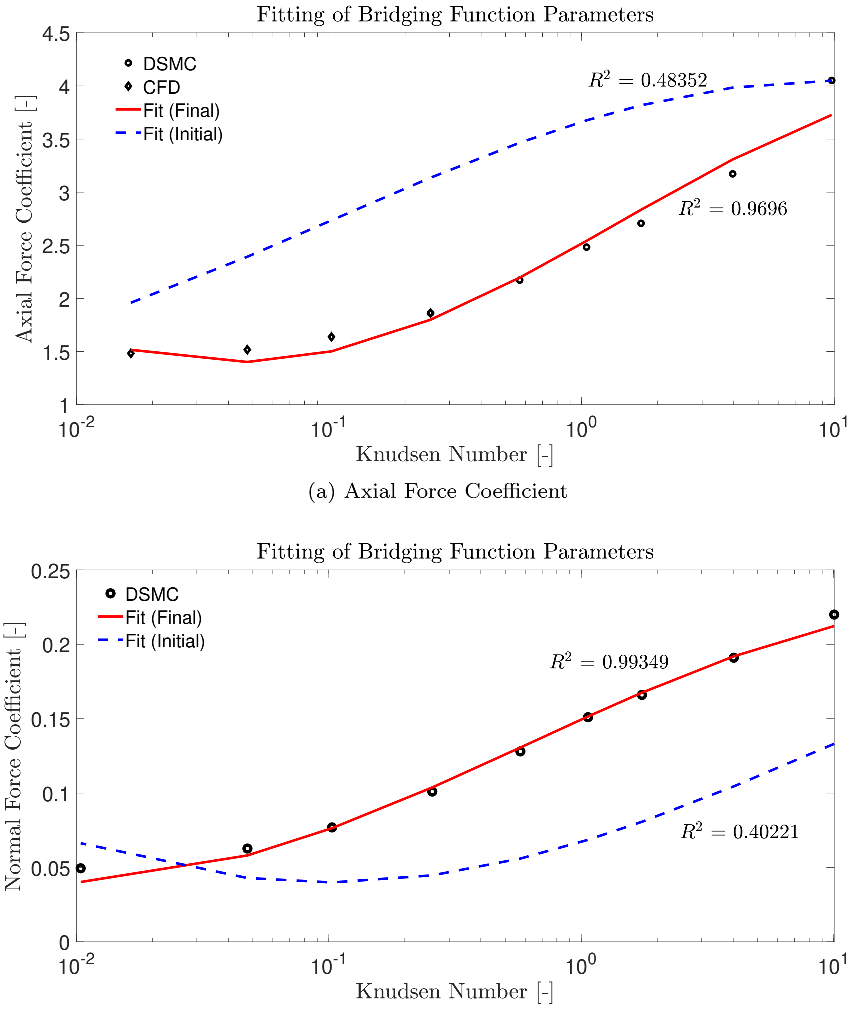

(a) Axial Force Coefficient

(b) Normal Force Coefficient

Figure 4.25.: Fitting of Wimoth's function in transitional regime with Moss' [56] DSMC data

The implementation of parameter fitting techniques in Wilmoth's function has yielded highly significant enhancements in the agreement between the high-fidelity data and the analytical model. The resulting improvements are significant: the R^2 value for the normal force coefficient increased from 0.48 to 0.97, while the axial force coefficient has seen a jump from 0.40 to 0.99. These substantial improvements indicate that the fitted parameters, namely a_1 and a_2, are far more suitable for accurately predicting the aerodynamic coefficients of stacked-toroids in the transitional regime, compared to the original values advocated in the existing literature.

Coefficient	Fitting	a_1	a_2	R^2
C_N	Literature	0.3750	0.3333	0.4835
	Least-Square Method	0.2247	0.1635	0.9696
C_A	Literature	0.3750	-0.3333	0.4022
	Least-Square Method	0.7227	-0.1516	0.9935

Table 4.7.: Fitted Bridging Coefficients for Aerodynamic force coefficients

Since the fitting parameters a_1 and a_2 are obtained from the simulation data that Moss [56] generated for IRVE-II at zero angle of attack, it is necessary to further assess the suitability of such parameters for a non-zero α. This is particularly useful for gliding flight and skipping entry trajectories or vehicles that have an offset to the centre of gravity to generate a lift component, such as IRVE-3. Therefore, the angle of attack needs to be taken into consideration when verifying the model proposed. Moreover, the application of the fitted coefficients to independent sets of data verifies the suitability of the proposed method for future studies. For this purpose, the additional high-fidelity data presented in [56] for $0° \leq \alpha \leq 180°$ in terms of C_A and C_N are taken for reference. Wilmoth's function is thus utilized with the coefficients in Table 4.7 and the analytical predictions are compared to the DSMC and CFD results. The agreement obtained for each fitting is plotted in Figure 4.26 in terms of R^2 as a function of α. The numeric R^2 values are also listed along with the RMSE in Table B.12.

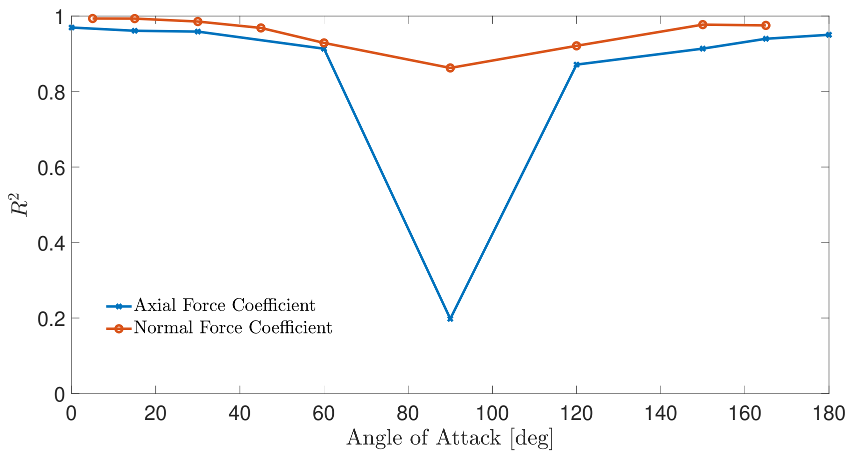

Figure 4.26.: C_A and C_N Wimoth's function agreement in transitional regime for $\alpha \neq 0°$

The results demonstrate that the fitted parameters exhibit outstanding and consistent agreement with the high-fidelity aerodynamic data, particularly at larger angles of attack. While a minor decrease in the coefficient of determination (R^2) is observed in the vicinity of $\alpha = 90°$, it remains comfortably within the order of 0.9 or higher for $\alpha < 90°$, and around 0.86 for $\alpha > 90°$. A notable exception arises precisely at $\alpha = 90°$, where the model's accuracy experiences a significant reduction for both aerodynamic coefficients. Although the R^2 value for C_A remains relatively high at 0.8626, the estimation for C_N is less accurate, as indicated by a substantially lower R^2 value of 0.1979. Nonetheless, it is important to recognize that designing a stacked-toroid decelerator to operate at such elevated angles of attack ($\alpha = 90°$) is extremely unlikely and generally undesirable. The observed inaccuracy of the model in this specific scenario has been previously identified in the FMF aerodynamic model (see Figure 4.23). However, for the range of intended applications addressed by this study, this limitation is deemed of minimal significance and does not undermine the overall validity of the findings.

4.3.9. Aerostability: Verification

The verification of the expressions presented in Equation 3.43 and Equation 3.44 for the moment coefficients and Equation 3.73 for the CoP of a discretised stacked-toroid is established by comparison of the numerical results obtained in the present work with the high-fidelity CFD data obtained by Moss [56]. Moss [56] presents a configuration of the IRVE vehicle in which the CoG is located $y_{CoG} = 0.74\ m$ aft of the nose-cone. The same mass distribution is thus reproduced in this work, motivated by the absence of further information in the literature, for the trajectory point at an altitude of 95 km and the comparison of moment coefficients is presented in Figure 4.27 for two reference locations, namely the nose-cone and the CoG. Given that $Kn = 0.0168$ for the reference trajectory altitude, the modified Newtonian method is used to generate the aerodynamic moment coefficients. However, comparable results would be attained with the other analytical models in FMF.

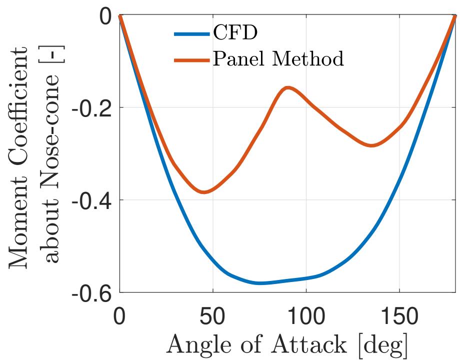

(a) C_M about Nose-cone

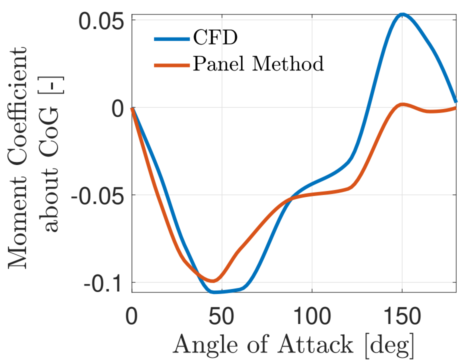

(b) C_M about CoG

Figure 4.27.: Comparison of C_M vs α between panel method and Moss' [56] CFD results

The moments about the nose-cone are found to yield a good agreement with the higher fidelity data up to $\alpha = 30°$. The vehicle is trimmed at low to medium angles of attack, as $\frac{C_m}{\alpha} < 0°$. Due to the inaccuracy of the panel method that has already been addressed in this work in the vicinity of $\alpha = 90°$ the model starts to decrease in accuracy beyond $\alpha \sim 35-40°$ until $\alpha \sim 135°$ to then exhibit a consistent agreement until $\alpha = 180°$. A similar discussion can be made concerning the moment shifted to the CoG, in Figure 4.27 where the panel method adequately captures the decreasing and increasing trends of the moment over different angles of attack. Interestingly, it recognises the trim point at which the moment coefficient reaches zero but neglects the consequent increase in C_M. This is further supported by the comparison of percentage errors in Figure 4.28.

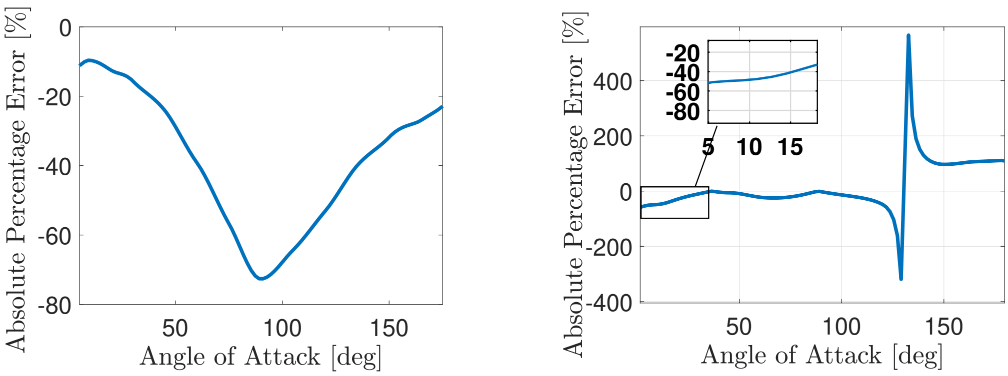

(a) C_M about Nose-cone

(b) C_M about CoG

Figure 4.28.: Percentage error of panel method moment coefficient and Moss' [56] CFD results

With the exception of $\alpha = 0°$ and $\alpha = 180°$, where the coefficients are approximately 0 and the percentage error may yield large values, the error at low angles of attack is approximately 15-20%. On the contrary, slightly larger errors of approximately 30-40% are seen at the moment about the CoG. This is to be expected as, based on Equation 3.44, an additional source of error arising from the aerodynamic coefficients is included besides the error of the nose-cone moment. The general agreement at low angles of attack is satisfactory for estimating the static longitudinal stability of the decelerator. A larger static margin can be imposed as a conservative approach.

While a comprehensive analysis of the CoP variation under nominal flight conditions is unavailable in the literature, Moss [56] demonstrates the sensitivity of the CoP location with rarefaction. The approximation presented in Equation 3.73 is limited by the pressure distribution modelled using analytical methods. Notably, no variation as a function of Mach number is predicted [165], as the C_P distribution maintains its shape under different environmental conditions. However, the values obtained using low-fidelity aerodynamic models are listed in Table 4.8, indicating that the modified Newtonian method yields the most conservative estimation with the forwardmost predicted CoP value. Therefore, the modified Newtonian method provides the least positive or largest negative SM.

These results qualitatively agree with those discussed by Moss [56], as the CoG is located behind the CoP for the proposed configuration. Moss [56] also acknowledges that y_{CoP} moves forward with decreasing rarefaction, which aligns with the results presented in Table 4.8, where the analytical methods used for the FMF regime exhibit larger values of y_{CoP}. Additionally, Moss [56] reports a negative SM, considering an incidence angle larger than 0° in the EDL phases, which was deemed acceptable. The absence of more detailed information in the literature concerning the actual location of the CoG for the IRVE vehicles does not allow further comparison.

Static Stability	Modified Newtonian Method	Schaaf and Chambre	CLL	Storch	Cook	Sentman
y_{CoP} $[m]$	0.5328	0.6889	0.5818	0.5359	0.5476	0.6943
SM [%]	-11.51	-2.84	-8.79	-11.34	-10.69	-2.54

Table 4.8.: CoP location along IRVE vehicle for $\alpha = 0°$ and associated SM for $y_{CoG} = 0.74m$

4.4. Aerothermodynamics

4.4.1. Continuum Regime: Validation

The suitability of the analytical models described in section 3.6 in continuum flow conditions is hereby validated by comparison with the heat flux flight profile of IRVE-II reconstructed by O'Keefe et al. [100] and outlined by Dillman et al. [39]. The data used for comparison was tracked in flight by multiple ground radars, while onboard sensors also provided acceleration and roll rates [39]. Though a pre-flight nominal peak heating of 1.97 W/cm^2 was predicted, a peak heat flux of 2.20 W/cm^2 was obtained due to the launcher exceeding the expected apogee [39].

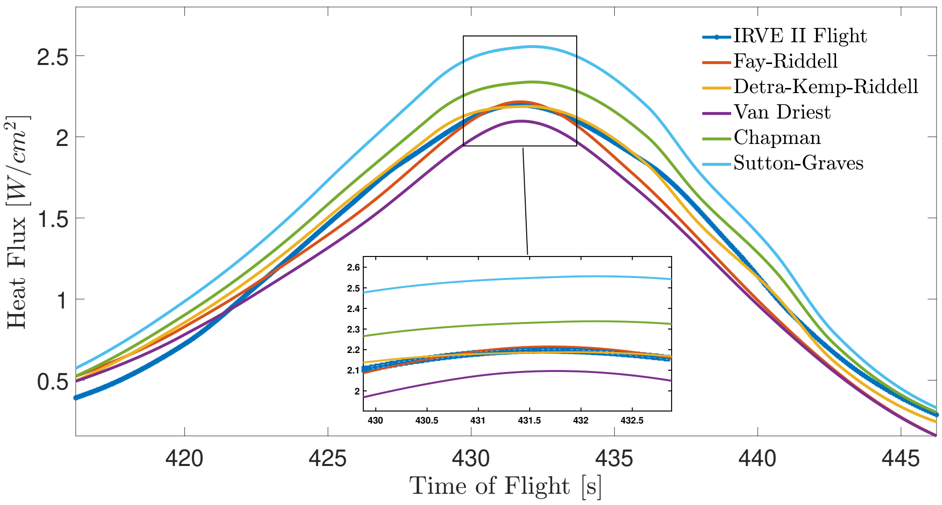

Figure 4.29.: Comparison of stagnation-heating Aerothermal analytical models with IRVE-II

The IRVE-II heat flux profile at the stagnation point is plotted in Figure 4.29 along with the analytical predictions of the different methods implemented. It is immediately evident that all the models effectively capture the correct behaviour of the curve. The increasing gradients of the curve before the peak heat flux is attained, as well as the decreasing gradients in the following section, are correctly matched by all models. Moreover, the peak heat flux is modelled at approximately the same flight location by all the expressions, in agreement with the flight data. Interestingly, both Fay-Riddell and Detra-Kemp Riddell's models appear to best correlate to IRVE-II's measured heat flux profile, while Sutton-Graves's method overestimates the heat experienced by the vehicle throughout the whole trajectory and, on the contrary, Van Driest's method slightly underestimates it over the flight due to its non-catalytic wall assumption.

To quantify the agreement between the different models, the RMSE of each analytical expression is provided with respect to the IRVE-II flight data in Table 4.9 along with the ratio of the RMSE to the standard deviation (SD) to provide a clearer indication of the metric's adequacy. All RMSE values appear to be significantly smaller than the data deviation, thus signifying the presence of a good agreement between the numerical and flight data. The larger $RMSE/SD$ value yielded by Sutton-Graves, however, remarks its greater discrepancy when compared to the alternative methods. This is confirmed by the R^2 values obtained, also illustrated in Table 4.9, with all models having $0.94 \leq R^2 \leq 0.98$ except from Sutton-Graves, which again shows a lower quantity of $R^2 \approx 0.78$ and a mean absolute percentage error of 23% across the measured flight locations. Nevertheless, the discrepancy of this latter method is not to be necessarily interpreted as an inadequate model, but rather as a more conservative approach to estimating the heat flux of the trajectory. The absolute percentage error is also plotted in Figure 4.30 for all the methods, showing a consistent agreement throughout the flight. Slightly larger errors are yielded where the measured heat flux is at a minimum due to small values being at the denominator of the fraction. The relatively low percentage of errors yielded by the models confirm the application of such formulations for early design stages.

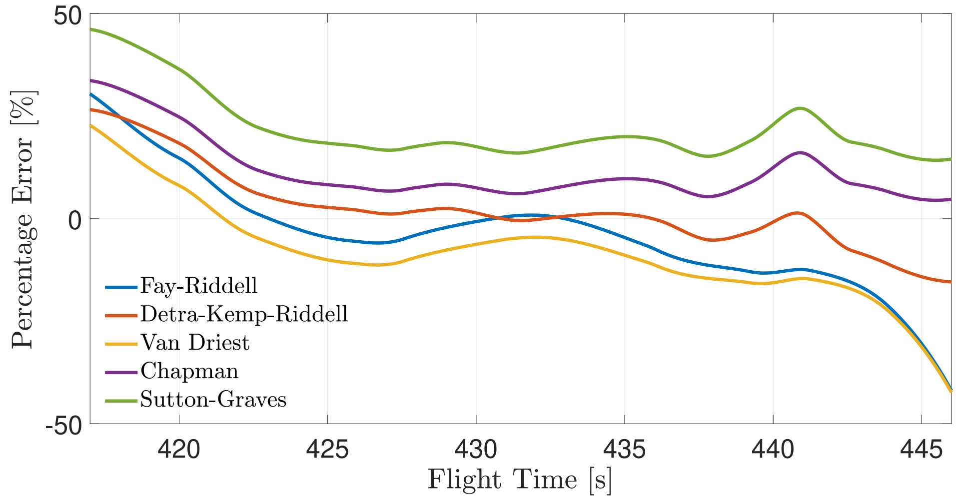

Figure 4.30.: Percentage error of stagnation-heating Aerothermal analytical models with IRVE-II

The maximum heat flux is accurately predicted by Fay-Riddell, Detra-Kemp-Riddell, Van-Driest and Chapman's methods, with errors in the order of 0.8-6.4%. On the other hand, Sutton-Grave's formula overestimates the maximum heat flux by 16%, thus proving to be more conservative. In addition to the maximum heat flux measured, it is important to correctly capture the time at which the peak occurs. Interestingly, this is consistently predicted with high accuracy by all models, with errors below 0.2%. The heat load is also calculated by integrating the heat flux over the flight time, according to Equation 3.79; a heat load of 39.2 J/cm^2 is obtained for IRVE-II, in line with the findings of Dillman [39]. While Fay-Riddell and Van Driest respectively underpredict the total heat load by 3.43% and 8.15%, Detra-Kemp-Riddell, Chapman and Sutton-Graves overestimate the total heat load, thus appearing more suitable for conceptual design stages. All methods are however capable of predicting the correct heat flux behaviour in continuum flight.

While the heat flux measured by IRVE-II is correctly modelled with the proposed low-fidelity approach, the heat levels perceived by the vehicle were rather low due to the low-energy trajectory. To improve the V&V strategy of this chapter with experimental data, the IRVE-3 program is taken into consideration as it was exposed to higher entry heat rates and larger scales which would be more representative of an actual re-entry or Mars mission. The mission, in fact, aimed at demonstrating the survavibility of a stacked-toroid of at least 12 W/cm^2 cold wall heat flux [38]. The trajectory of IRVE-3 [38], is thus utilized to retrieve the environmental properties required by the aerothermal models in section 3.6.

Aerothermal Model	$q(t)$ RMSE	$q(t)$ RMSE/SD	$q(t)$ R^2	$q(t)$ $\lvert\bar{\delta}_{\%}\rvert$	q_{max} $[W/cm^2]$	q_{max} $\bar{\delta}_{\%}$	$t(q_{max})$ [s]	$t(q_{max})$ $\bar{\delta}_{\%}$	Q_{max} $[J/cm^2]$	Q_{max} $\lvert\bar{\delta}_{\%}\rvert$
IRVE-II Flight [100]	-	-	-	-	2.1966	-	431.63	-	39.1978	-
Fay-Riddell	0.0991	0.1611	0.9740	10.09	2.2154	+0.86	431.68	+0.013	37.8537	-3.43
Detra-Kemp-Riddell	0.0691	0.1124	0.9874	7.29	2.1878	+0.40	431.96	+0.078	39.8840	+1.75
Van Driest	0.1387	0.2256	0.9490	11.58	2.0964	-4.56	431.74	+0.026	36.0028	-8.15
Chapman	0.1420	0.2309	0.9466	12.76	2.3378	+6.43	432.13	+0.118	43.0945	+9.94
Sutton-Graves	0.2860	0.4652	0.7832	23.30	2.5562	+16.37	432.14	+0.118	47.1203	+20.21

Table 4.9.: Aerothermal modelling in continuum regime compared to IRVE-II

Similarly to the approach taken for IRVE-II, the heat flux measured in IRVE-3 by means of 5 surface heat flux gauges coupled with pressure transducers [38] is plotted in Figure 4.31 against the heat profile predicted with Fay-Riddell, Detra-Kemp-Riddell, Van Driest, Chapman and Sutton-Graves' methods. The results are in agreement with the discussion of Figure 4.29 for IRVE-II. The analytical estimates correctly model the heat flux measured by the heat flux sensors. Chapman, Detra-Kemp-Riddell and Fay-Riddell produce the curves with the highest agreement to the IRVE-3 data, whereas Sutton-Graves provides an overestimation and Van-Driest an underestimation of the curve.

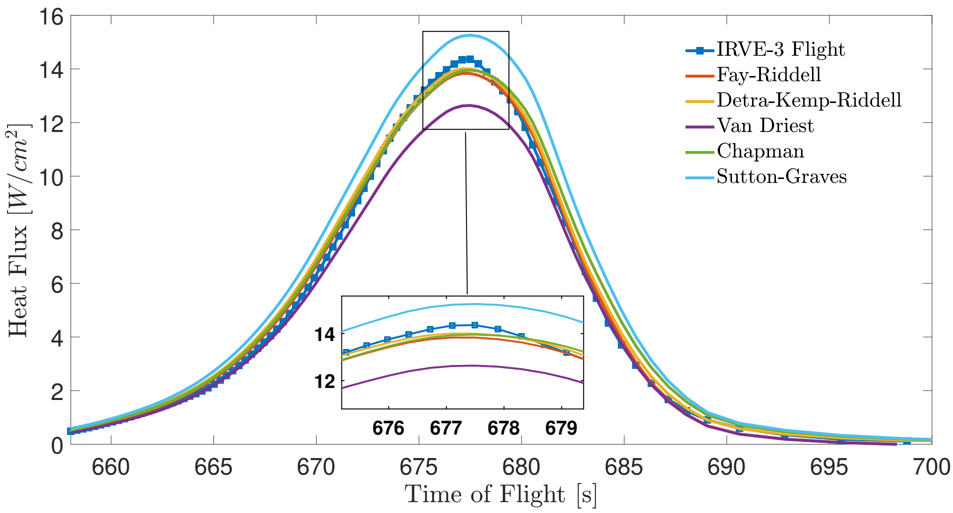

Figure 4.31.: Comparison of stagnation-heating Aerothermal analytical models with IRVE-3

The agreement between the experimental and analytical data is quantified in Table 4.10, where all models yield a good correlation with the flight data, with Sutton-Graves generating the worst agreement as for IRVE-II. An improved behaviour is nevertheless observed, with an R^2 value increasing to 0.96 for this latter approach. All analytical models show excellent correlations with $0.960 \leq R^2 \leq 0.998$. The maximum level of heat flux along the trajectory is also captured correctly, with an exception for the Van-Driest equation that underpredicts the value by a mean percentage error of 12% with respect to the flight data, thus revealing to be the least desired method to design an entry vehicle. As for the IRVE-II mission, the time of maximum heat flux is modelled with exceptional accuracy by all models, with percentage errors ranging between 0 and 0.06%. The percentage errors across the flight trajectory are plotted in Figure 4.32 for all methods, which appear to be consistently below the 10-20% mark across the trajectory. The figures increase slightly towards the end of the flight as a numerical result of the percentage error since the flight data at the denominator approaches zero.

Finally, the computed heat load is also computed and outlined in Table 4.10. All models but Van Driest result in an overestimation of the total heat load, which is desirable for the conservative design of the F-TPS. The application of Fay-Riddel, Detra-Kemp-Riddell, Chapman and Sutton-Graves' methods is thus found to be consistent across different heat regimes and appropriate for the design stage. While Van-Driest's method may be desirable to design for demise, it is not the preferred option for this work as it leads to an underestimation of the heat loads experienced by the vehicle. On the contrary, based on the criterion of lowest positive percentage error in both heat flux and heat load, Sutton-Graves is the only model that overpredicts both quantities for both IRVE-II and IRVE-3. While Van-Driest underpredicts both the maximum heat flux and heat load, Chapman, Fay-Riddell and Detra-Kemp-Riddell slightly underpredict the peak heat flux for IRVE-3. Sutton-Graves is therefore integrated into the present MDAO framework for early design stages as it is the most conservative method.

Aerothermal Model	$q(t)$ RMSE	$q(t)$ RMSE/SD	$q(t)$ R^2	$q(t)$ $\lvert\bar{\delta}_{\%}\rvert$	q_{max} $[W/cm^2]$	q_{max} $\delta_{\%}$	$t(q_{max})$ $[s]$	$t(q_{max})$ $\delta_{\%}$	Q_{max} $[J/cm^2]$	Q_{max} $\delta_{\%}$
IRVE-3 Flight [38]	-	-	-	-	14.3610	-	677.49	-	195.0577	-
Fay-Riddell	0.2209	0.0460	0.9979	6.47	13.8313	-3.69	677.10	-0.06	195.1673	+0.06
Detra-Kemp-Riddell	0.3257	0.0678	0.9953	7.19	14.0032	-2.49	677.10	-0.06	202.4430	+3.79
Van Driest	0.6886	0.1434	0.9792	9.25	12.6375	-12.00	677.49	0	179.2793	-8.09
Chapman	0.3903	0.0813	0.9933	9.00	13.9558	-2.82	677.49	0	204.8201	+5.00
Sutton-Graves	0.9512	0.1981	0.9603	18.58	15.2595	+6.26	677.49	0	223.9542	+14.81

Table 4.10.: Aerothermal modelling in continuum regime compared to IRVE-3 Flight Data

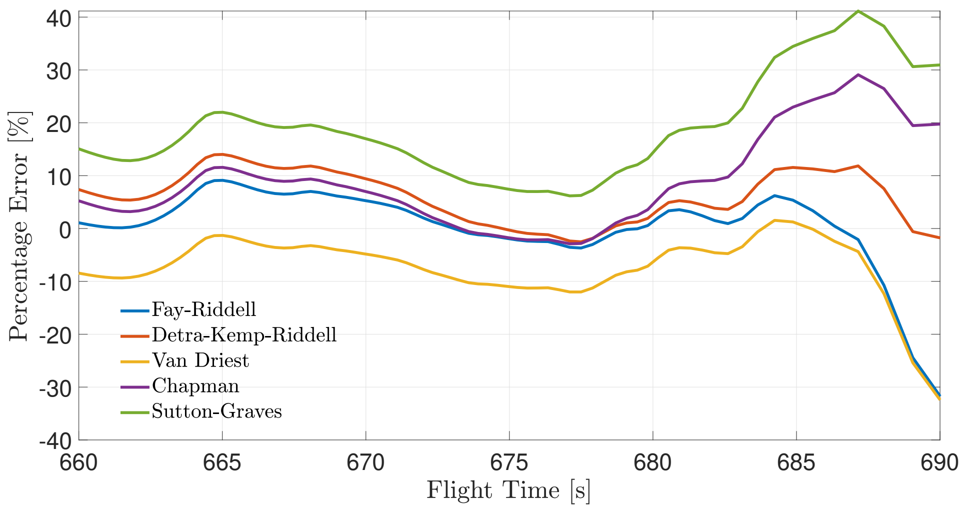

Figure 4.32.: Percentage error of stagnation-heating Aerothermal analytical models with IRVE-3

4.4.2. Heat Distribution: Verification

The verification of the heat flux distribution across the stacked toroid's surface is first investigated by application of the SCARAB's expression as in Equation 3.94. A qualitative comparison between the high-fidelity heat distribution obtained by Moss et al. [56] for the IRVE-II vehicle at an altitude of 95 km is shown in Figure 4.33 with a stagnation heat flux of 0.0396 W/cm^2. It is clear that while the SCARAB method, coupled with the shadowing algorithm at $\alpha = 75°$ correctly reproduces the fading of the heat flux along the faces which are not directly exposed to the incoming flow, the simplistic model fails to estimate the much wider region of high-heat flux. The region directly exposed to the flow does reveal an augmented presence of heat, but this does not match the levels observed in the CFD solution.

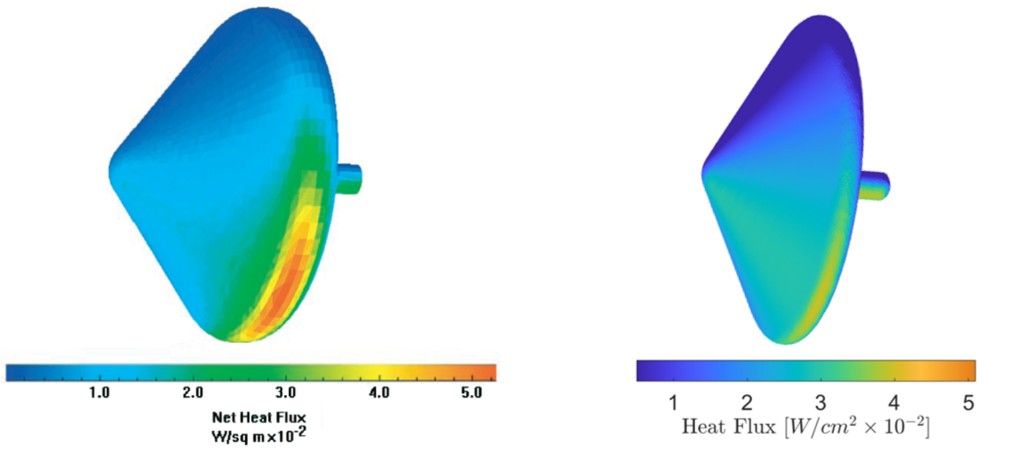

(a) CFD DS3V [56]

(b) Local Inclination SCARAB Method

Figure 4.33.: IRVE-II Surface Heating rate at 95 km and $\alpha = 75°$

A more quantitative visualization of the solution is shown in Figure 4.34, where the same CFD data gathered by Moss [56] is plotted along the vehicle's normalized radius for different altitudes. While the SCARAB method correctly identifies the initial heat flux distribution in the vicinity of the stagnation point, it severely overestimates the heat levels along the conical section to then suddenly drop at the shoulder of the vehicle. The behaviour observed is approximately analogous to all altitudes, with mean percentage errors oscillating between 71-83%.

The alternative method implemented in this work, following the approach adopted by Santos et al. [216], combines the SCARAB method with Krasnov's formulation for conical bodies. The results obtained with this work correlate much better with the high-fidelity data retrieved from Moss [56]. For comparison, the same 56 km and 95 km altitude cases in Figure 4.34 are reproduced with SCARAB being applied to the nosecone and to the shoulder, whilst Krasnov is utilized along the conical aeroshell. The resulting heat flux distributions are plotted in Figure 4.36, where the percentage error is reduced from 83% to 12.15% at 56 km and further down to 7.65% at 95 km. Equivalent distribution profiles are observed at different altitudes.

As opposed to the behaviour noted in Figure 4.34, where the heat flux remained approximately constant along the conical surface of the body, the heat flux curve resembles that of the CFD data, showing a rapid decrease downstream of the stagnation point, with a spike at the shoulder,

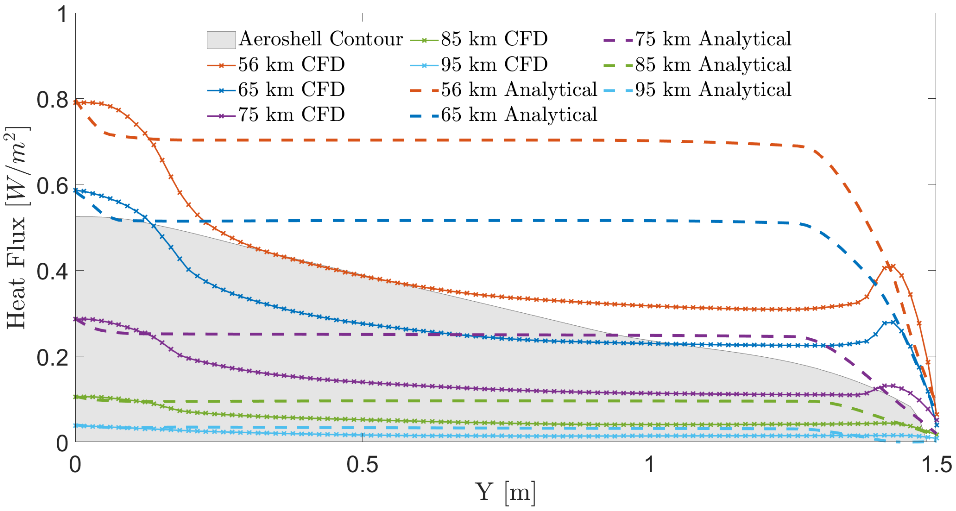

Figure 4.34.: Comparison of heating rate distribution as a function of altitude between the local inclination SCARAB method and the higher-fidelity results in [56]

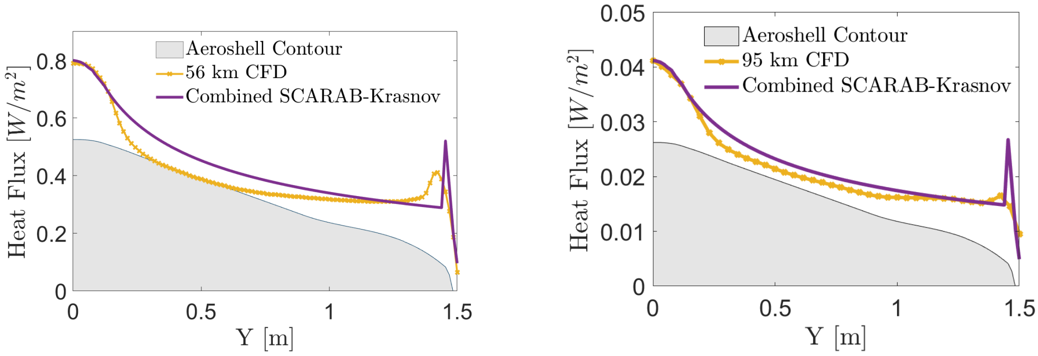

(a) 56 km

(b) 95 km

Figure 4.35.: Comparison of heating rate distribution between the local inclination analytical method and the higher-fidelity results in [56] for the joint Krasnov-SCARAB method

where SCARAB is applied again. The resulting heat flux distribution is visually presented in Figure 4.36, in which the variation of heat flux is much more evident. The heat levels at the nosecone are equivalent in both plots as SCARAB is similarly applied to both locations. It is concluded that the combination of the Krasnov-SCARAB method is an enhanced version of the SCARAB formulation alone which is deemed more appropriate for accurate design studies.

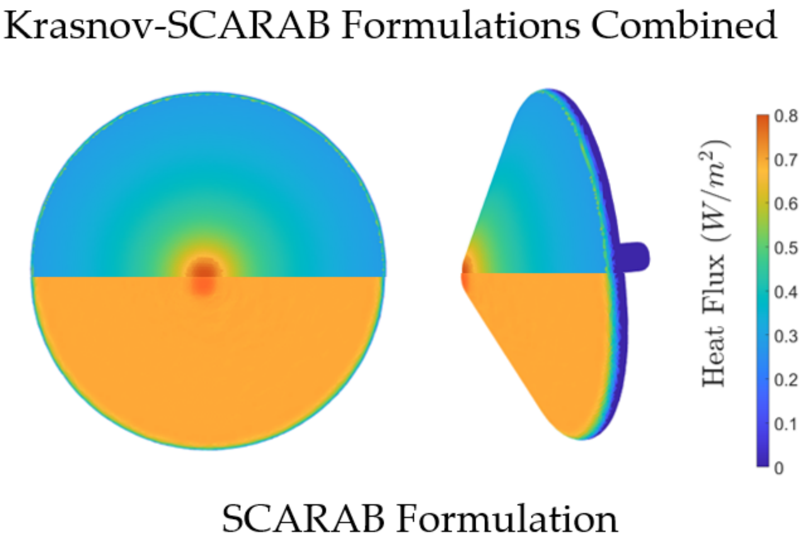

Figure 4.36.: Comparison of IRVE-II surface heating at 56 km with SCARAB and joint SCARAB-Krasnov local inclination analytical methods

4.4.3. Aerothermodynamic Correction due to Inflatable Deflection: Verification

The verification of the heat distribution method proposed in the present work was based on a rigid stacked-toroid model in which the F-TPS is assumed not to deflect. However, it is clear that this assumption does not hold true for the surface of an IAD. To account for the effect of surface scalloping on the accelerator, Hollis' heat augmentation correlation is hereby implemented as described in subsection 3.7.2 against the analytical methods implemented for a rigid model.

To verify the adequacy of the parametric correlation at replicating high-fidelity results, three models are implemented following Hollis' work [53]. Namely, the heat flux along the smooth baseline model is simulated along with a Scallop-10 model, towards the higher end of the deflection spectrum representative of flight conditions, and Scallop-20 with heights that are much larger than any practical flight vehicle design would be subject to [53]. The dimensions used for each model are indicated in Table 4.11 and illustrated in Figure 4.37. For the three considered models in the present work, the runs 20,30 and 84 of the wind tunnel campaign conducted in [53] are utilized, with a Mach number of 6.03, zero-angle-of-attack, freestream temperature of 58.6 K, velocity of 918.1 m/s and a density of 0.125 kg/m^3. A film coefficient of 0.964 kg/m^2s, obtained analytically by means of the Fay-Riddel formulation $h_{f_{FR}}$, is used to normalise the data.

The CFD high-fidelity solution obtained by Hollis [53] is thus compared to the analytical SCARAB formulation for a spherical body, previously shown to overpredict the heat flux along the conical rigid section of a stacked-toroid, the combined SCARAB-Krasnov laminar formulation, expected to yield more accurate results than SCARAB, and the Hollis augmented heat flux relation applied to the SCARAB-Krasnov strategy. It is specified that the Krasnov method in Equation 3.95 is

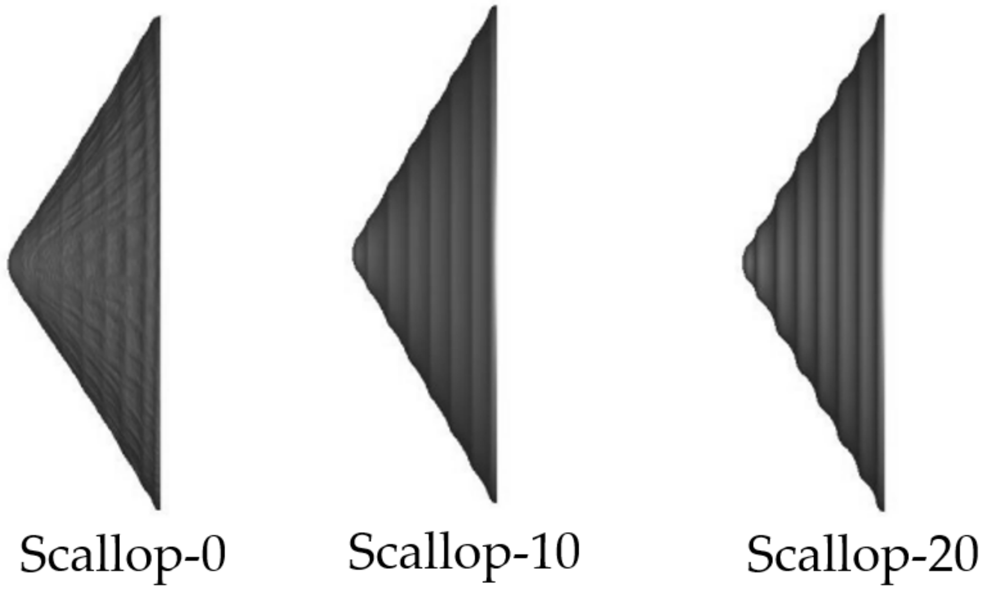

Figure 4.37.: IRVE Parametric Scallop Model Surfaces; Adapted from [53]

Model	r_N $[m]$	$r_{inflated}$ $[m]$	r_{torus} $[m]$	$r_{out,torus}$ $[m]$	β_{SC} $[deg]$	k_{SC} $[mm]$
IRVE Scallop-0	0.3810	0.0762	0.00635	0.0025832	0	0
IRVE Scallop-10	0.3750	0.0762	0.00635	0.0023813	10	21.87217
IRVE Scallop-20	0.3750	0.0762	0.00635	0.0023813	20	44.08175

Table 4.11.: IRVE Parametric Scallop Models

only applied when $\bar{x}_c > cotan(\theta_c)$ and $h_{f_{Krasnov}} \leq h_{f_{SCARAB}}$ along the axial direction. The results are plotted in Figure 4.39 and the errors quantified in Table 4.12.

An analysis comparing different low-fidelity models against the CFD solution highlights several noteworthy observations. Firstly, the laminar SCARAB-Krasnov solution consistently aligns with different scalloping models, indicating its robustness and reliability. Conversely, the inclusion of the Hollis augmented heat correlation diminishes the accuracy of the heat-distribution model in the absence of scallops. However, as the level of scalloping increases, the model's accuracy improves significantly. This trend is exemplified by the data presented in Table 4.12, where the percentage error of the SCARAB-Krasnov model decreases from 46.65% to 18.63% upon implementing the Hollis correlation. Furthermore, it is observed that the SCARAB formulation yields the highest degree of errors when deflections are absent. Nevertheless, it demonstrates suitability for cases involving substantial scallop heights, as it maintains a conservative approach. To assess the cumulative error along the axial distance denoted as Y, the integral of the quantity $h_f/h_{f_{FR}}$ is computed.

The percentage error analysis listed in Table 4.12 provides additional confirmation of the effectiveness of Hollis' augmented relation in improving the laminar solution. Notably, the augmented relation consistently leads to an overprediction of the integrated quantity, in contrast to the laminar equivalent which consistently underpredicts by 26% and 40% for the 10- and 20-Scallop models, respectively. It is worth noting that SCARAB consistently generates significantly larger predictions than the higher-fidelity model, resulting in a more conservative approach overall.

This discussion is further supported by the insights provided in Figure 4.38, which clearly demonstrates a higher level of agreement between the SCARAB model and the CFD solutions in the presence of large scallop depths. Considering the absence of CFD data for obtaining a more precise Re_θ and FSI simulations for the k_{SC} values, the utilization of SCARAB is recommended for the present work instead of the Hollis augmented relationship. The rationale behind this recommendation stems from the fact that SCARAB consistently yields larger predictions, thereby adopting a more cautious and conservative approach. Given the limitations and uncertainties associated with obtaining more accurate data for certain parameters, the SCARAB model offers a practical and reliable alternative in the absence of comprehensive CFD and FSI information.

Model	$\frac{h_f}{h_{f_{FR}}}(Y)\ \hat{\delta}_{\%}$			$\int \frac{h_f}{h_{f_{FR}}}(Y)dY\ \delta_{\%}$		
	SCARAB-Krasanov	SCARAB-Krasanov Hollis Augmented	SCARAB	SCARAB-Krasanov	SCARAB-Krasanov Hollis Augmented	SCARAB
IRVE Scallop-0	43.51	122.75	192.7	+31.17	+97.59	+149.94
IRVE Scallop-10	53.98	43.81	52.31	-26.56	+30.65	+43.75
IRVE Scallop-20	46.65	186.3	20.01	-39.76	+11.66	+17.39

Table 4.12.: Percentage Errors of IRVE Parametric Scallop Models

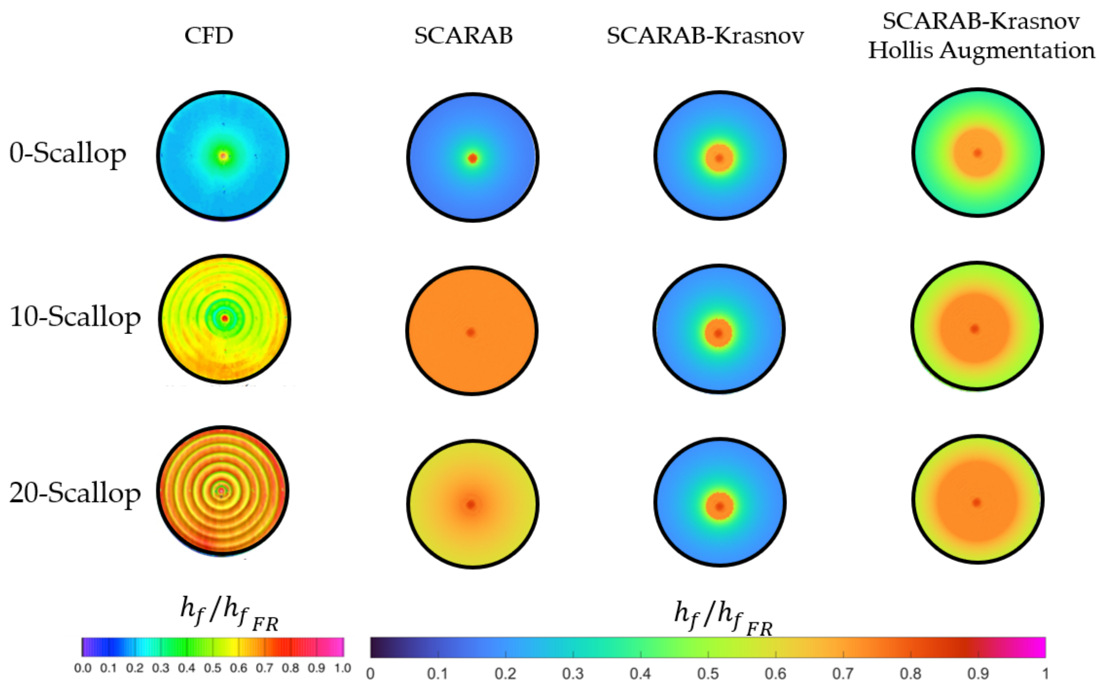

Figure 4.38.: Surface contour plot of film heat transfer ratios for scallop models. CFD solutions retrieved from [53]

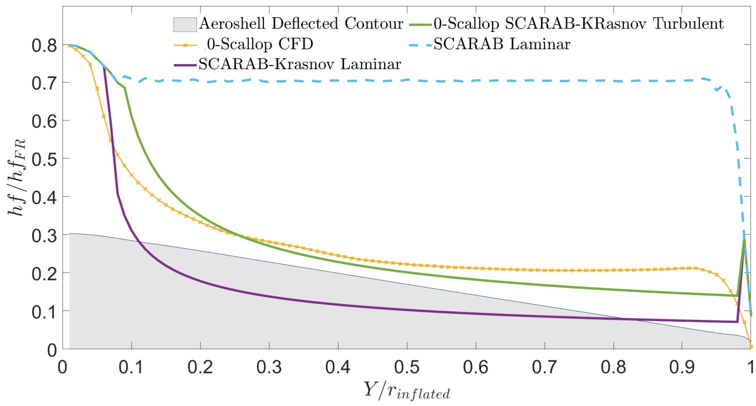

(a) Scallop-0

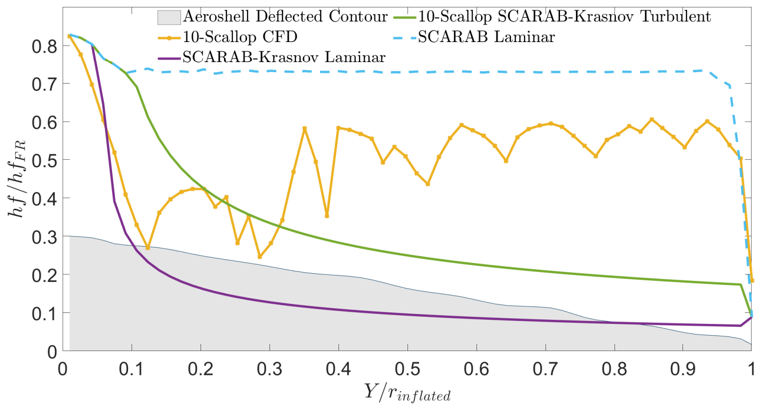

(b) Scallop-10

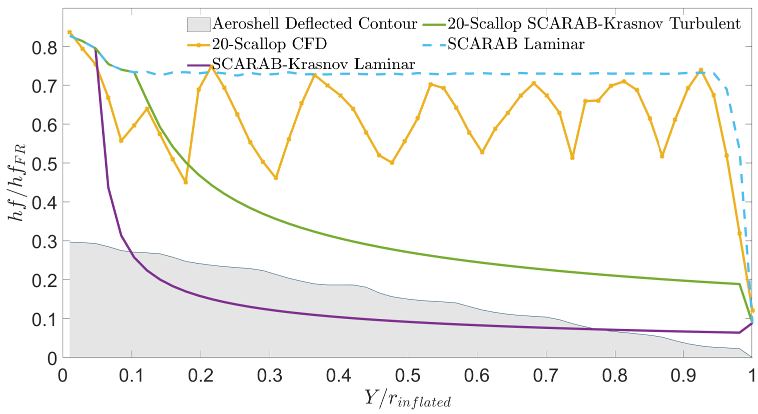

(c) Scallop-20

Figure 4.39.: Comparison of turbulent heat-augmentation correlation against high-fidelity CFD data retrieved from [53].

4.4.4. Rarefied Regime: Verification

The rather scarce, when available at all, aerothermal data of stacked-toroids in FMF makes the V&V strategy adopted in this section challenging. The flight data available from IRVE-II, IRVE-3 and IRDT is primarily post-processed in continuum regimes and while LOFTID might be the exception, the data has yet not been published at the time of writing. Furthermore, while aerodynamic DSMC data in rarefied conditions were retrieved in [56], Moss et al. considered the aeroheating in FMF to be negligible compared to peak heating and thus only provided data for the transitional regime. Given the absence of such data in the literature, this section only serves the purpose of conducting a preliminary verification as an initial step towards validating the model proposed in section 3.6 in the context of stacked-toroids.

The DSMC simulations performed by Moss et al. [56] for the IRVE vehicle provide the stagnation-heat values using different numerical solvers from an initial altitude of 110 km down to 46 km such that the Knudsen number ranges from $1.49{\cdot}10^{-5}$ to 0.257. The continuum and transitional regimes are addressed, but the aerothermal performance in the rarefied regime is not directly quantified. A sixth-order polynomial is hence fitted to the available DSMC data, which is found to yield the best agreement with the data as shown in Figure 4.40 by the R^2 value approaching unity. The equation of the best-fit polynomial, also shown in Figure 4.40, is therefore used to extrapolate the stagnation-heat flux values at the remaining altitudes explored by Moss [56]. The trajectory flight time, environmental information to obtain the heat transfer coefficient, Knudsen number and stagnation heat flux at the extrapolated altitude locations are reported in Table 4.13, still yielding a $R^2 \sim 0.999$ with respect to the fitted polynomial. Moreover, the extrapolated data appears to be within the 90% confidence bounds in Figure 4.40. The heat flux coefficient hc is also computed according to Equation 3.90. The reasonable trends of the flat curve in the extrapolated segment are demonstrated by inspection of other DSMC simulations of blunt bodies for Mars entries retrieved for the literature [234]. In particular, Mars Pathfinder and Mars Microprobe Capsules not only yield similar heat-flux curves against altitude but also present comparable stagnation heat flux quantities for both reacting and non-reacting gas conditions.

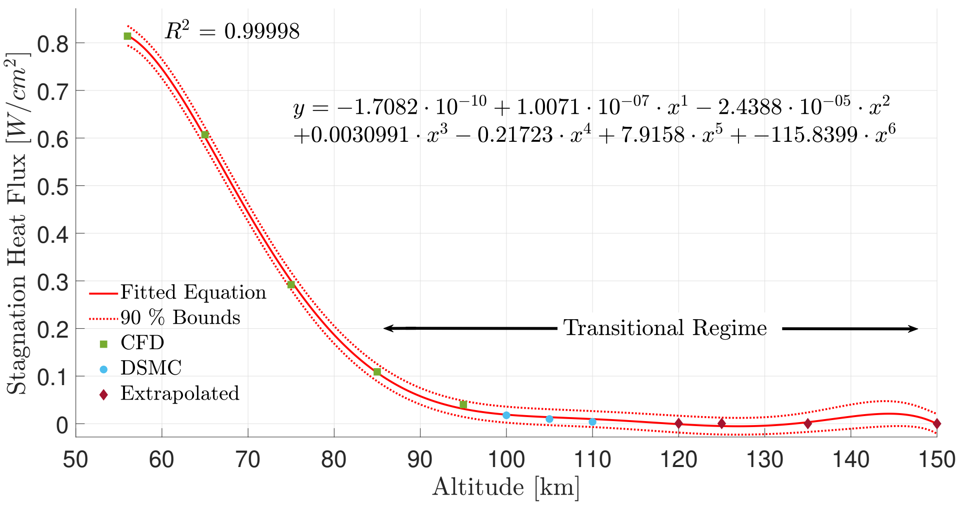

Figure 4.40.: Polynomial fitted to DSMC data in [56] to extrapolate heat flux in FMF

Altitude $[km]$	Flight Time $[s]$	Knudsen Number $[-]$	Stagnation Heat Flux $[W/m^2]$	$\frac{1}{2}\rho_\infty V_\infty^3$ $[kg/m/s^2]$	hc $[-]$
150	269.2	10.05	0.277	0.28	0.9893
135	290.2	4.02	1.375	1.56	0.8814
125	302	1.74	4.195	5.31	0.7901
120	307	1.064	7.495	10.16	0.7377

Table 4.13.: Reference trajectory conditions for aerothermal analysis in transitional flow regime

From the extrapolated data in Table 4.13, it is clear that only a single data point is available in FMF, corresponding to flight condition at 150 km with $Kn = 10.05$. The magnitude of the stagnation heat flux at this point is used for verification purposes of the Schaaf and Chambre's method in Equation 3.88. For completeness, the heat flux at the near-FMF conditions is also evaluated to further investigate the limits of the analytical method employed. The inputs required by Equation 3.88 are reported in Table 4.14 at each trajectory point for the extrapolated conditions. The resulting heat flux at the stagnation point calculated using the analytical model is also shown in Table 4.14 along with the extrapolated DSMC quantities. As expected, the low-fidelity model's accuracy increases with Knudsen number, reaching a discrepancy of only 11.2% in FMF. While it is likely that the error would further decrease at larger Kn values, the measured error is deemed acceptable for early design stages. Further validation would be required with experimental data which is currently not available in the literature.

h $[km]$	Kn $[-]$	s $[-]$	T_∞ $[K]$	p_∞ $[Pa]$	R $[J/kg/K]$	q_{DSMC} $[W/cm^2]$	q_{Schaaf} $[W/cm^2]$	$\lvert\delta_\infty\rvert$ $[\%]$
150	10.05	$1.5 \cdot 10^{-3}$	633	$4.562 \cdot 10^{-4}$	342.60	0.2770	0.2460	11.19
135	4.02	$2.4 \cdot 10^{-3}$	517	$9.320 \cdot 10^{-4}$	330.95	1.3750	0.3569	74.04
125	1.74	$3.5 \cdot 10^{-3}$	417	$1.700 \cdot 10^{-3}$	322.54	4.2110	0.3957	90.60
120	1.06	$4.3 \cdot 10^{-3}$	363	$2.500 \cdot 10^{-3}$	317.90	7.5100	0.3236	95.69

Table 4.14.: FMF and near-FMF comparison of analytical method with extrapolated DSMC data for IRVE heat flux

A final observation concerning the utilization of Schaaf and Chambre's model for the estimation of the aerothermal heat flux in FMF must be made. In fact, Equation 3.88 shows a dependency on the local inclination angle with respect to the incoming flow θ, such that a heat flux distribution along the surface of the stacked-toroid may be attained. This is shown in Figure B.6, where the distribution of heat flux is plotted across the vehicle's surface and along its axial y direction. From a qualitative standpoint, the model correctly identifies the approximate decreasing trends away from the stagnation point, with a sudden decrease in the spherical nose cone and a further sharp drop in the outer shoulder of the vehicle. However, similarly to the model adopted for the continuum distribution in Equation 3.94 as plotted in Figure 4.34, a uniform distribution is incorrectly maintained across the majority of the axial distance. Moreover, the rather constrained range of heat flux values shows the limited variation of heat flux modelled by Equation 3.88. Due to the excessively simplistic nature of the formulation, the complex distribution for a stacked-toroid is not correctly identified. Nevertheless, the heat flux at the stagnation point, which corresponds to the critical condition, is captured with sufficient accuracy.

4.4.5. Transitional Regime: Verification

To verify the accuracy of Wilmoth' bridging function in Equation 3.91, the non-linear square method in Equation 3.92 is employed with the CFD and DSMC data retrieved from [56] along with the extrapolated data according to Figure 4.40 and Table 4.13 in terms heat flux coefficient. The resulting fitted curve is plotted in Figure 4.41, and the corresponding best-fit coefficients a_1 and a_2 are reported in Table 4.15. The agreement between the high-fidelity heat flux coefficient and Wilmoth's bridging function yields a value of $R^2 = 0.99138$ which reveals an excellent correlation. Wilmoth's model is capable of correctly capturing the hc behaviour in the near-continuum, transitional and near-FMF regime. It is noticed that the model appears to be slightly more inaccurate as $Kn > 0$ which is where Schaaf and Chambre's model should instead be employed.

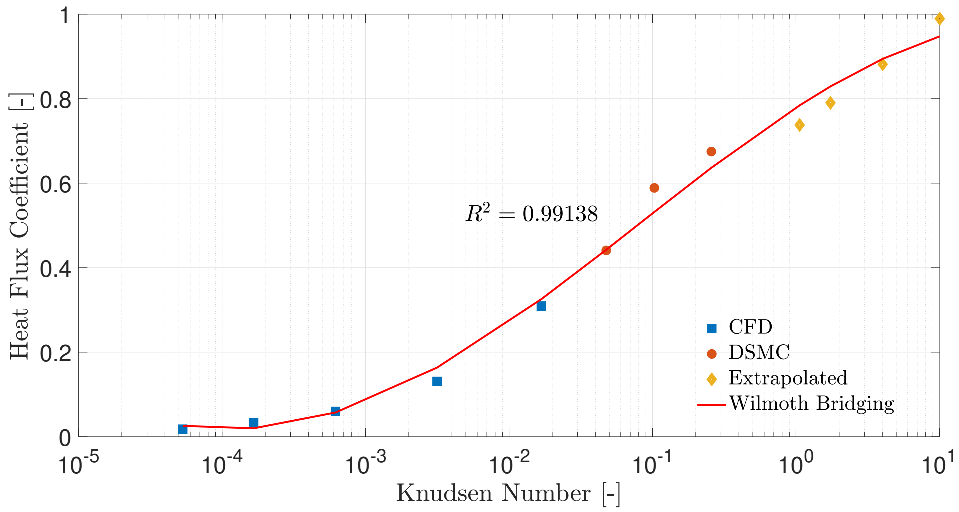

Figure 4.41.: Wilmoth Bridging function fitted to IRVE-II extrapolated DSMC data

Fitting	a_1	a_2	R^2
Least-Square Method	-0.1542	0.0876	0.9792

Table 4.15.: Fitted Coefficients for Aerothermal Bridging Function in Transitional Flow

In order to provide a broader overview of the suitability of the low-fidelity analytical models implemented in this work for both the continuum and FMF regime when applied to the transitional regime, the heat flux coefficient hc is plotted in Figure 4.42 as a function of the Knudsen number for all the described models. Interestingly, the models developed by Fay-Riddell, Detra-Kemp-Riddell, Van-Driest, Chapman and Sutton-Graves are more accurate than Wilmoth's function in the continuum regime but appear to increasingly diverge from the correct solution at $Kn > 10^{-2}$, in the transitional flow, yielding larger discrepancies as Kn is further increased. On the contrary, Schaaf and Chambre's model presents nonphysical solutions for $Kn < 1$, highly inaccurate hc values for $1 < Kn < 10$ and reasonably accurate hc results for $Kn \geq 10$. At the same time, Wilmoth's function is capable of correctly predicting the variation throughout the transitional flow. This highlights the usage of different analytical models for different flow regimes.

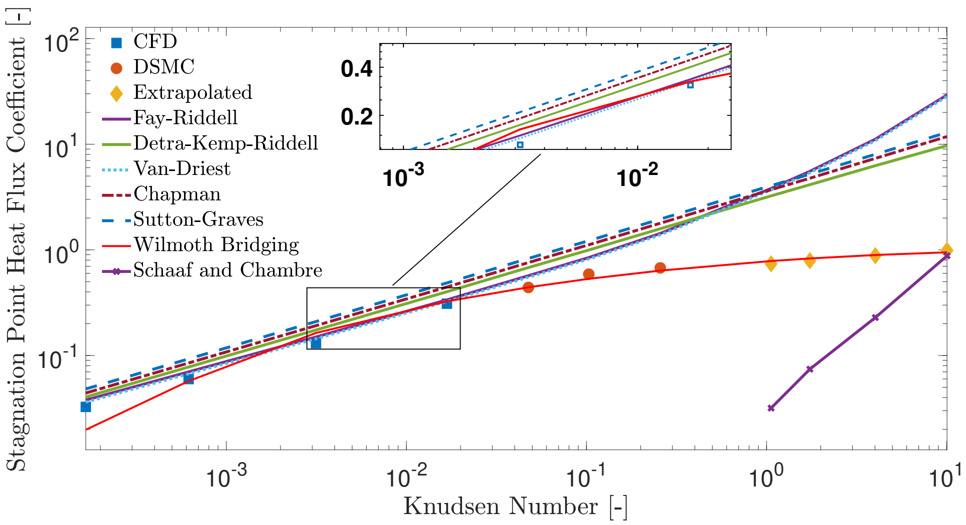

Figure 4.42.: Comparison of Analytical Methods for transitional flow regime with IRVE-II extrapolated DSMC data

To complement the discussion of the adequacy of different models in different flow regimes stemming from Figure 4.42, the percentage error of each model with respect to the high-fidelity data is plotted in Figure 4.43. While Wilmoth's Bridging function yields low errors consistently throughout the Knudsen range addressed, the models implemented in the continuum range quickly diverge in the rarefied flows and the FMF model quickly converges as $Kn \rightarrow 10$. Hence, in the transitional aerothermal regime, Wilmoth's function is chosen for implementation, as it demonstrates reduced errors when compared to the analytical relations utilized in the continuum regime.

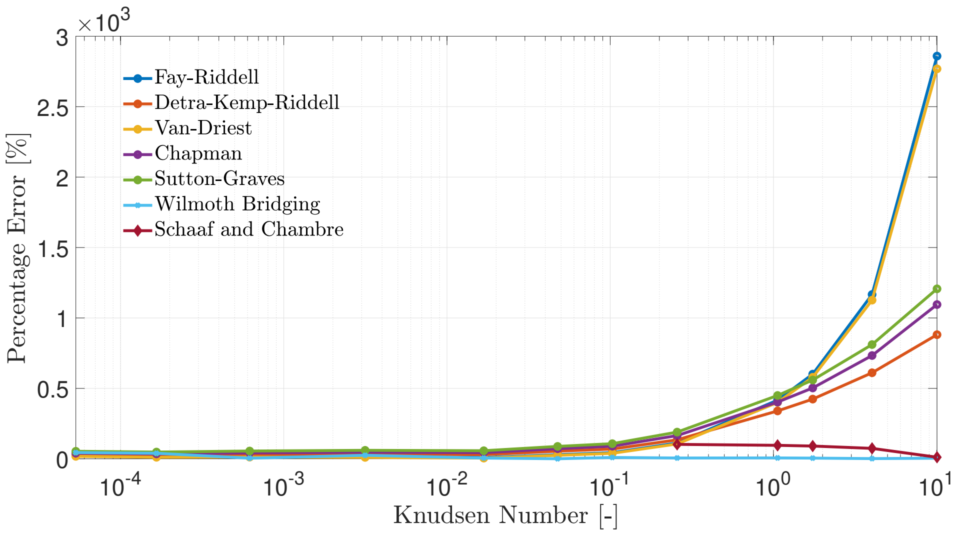

Figure 4.43.: Percentage error of analytical stagnation heat flux with respect to high-fidelity data

4.4.6. Radiative Heating: Verification

The updated radiative heating correlations provided by West and Brandis [190] and implemented in this work have been derived by parametric fitting with numerical data in which the results reveal a discrepancy below 25% with high-fidelity solutions with some outliers around 50%. Using the latter figure as a design margin for the radiative heating is in line with the approach identified in literature application studies [235]. However, for the purpose of verification, the results yielded by the method adopted in the present work are compared to the scarce available data in the literature for stacked-toroid vehicles in the Mars atmosphere. The effect of turbulence on the flow conditions is ignored since this is found to be negligible on radiative heating in the event of little or no ablation of the F-TPS [236]. Three individual data points are retrieved and considered for comparison. The environmental and design conditions of these cases are compliant with the domain of interest simulated by West and Brandis [190] as indicated in Table 4.16 along with the radiative heating.

For the data points ID 01 and ID 02, retrieved from [237], a range of solutions is given as two different high-fidelity methods were employed with Mars' 16-species atmosphere model and a flow temperature of 150 K. Namely, the tangent-slab method and the back-ray tracing algorithm. Interestingly, the low-fidelity solution lies within the higher fidelity bounds, with percentage errors spanning from +3.9% to 12.8%. While the low-fidelity method adopted in the present work does not vary with the vehicles' diameter, the high-fidelity data only shows a variation lower than 5%, due to the radiation of the intensity not being absorbed by the shock layer [237], thus confirming the dependency on the variables of Equation 3.93. On the other hand, comparison with ID 03 [238] shows a much larger percentage error of 43.8%, mainly due to the lower magnitude of the heat flux, which is still within the 50% uncertainty bounds of the method. Thus, the verification of the correlation's implementation is deemed successful.

Reference	ID	V_∞ $[km/s]$	ρ_∞ $[kg/m^3]$	r_N $[m]$	$2r_{inflated}$ $[m]$	θ_c $[deg]$	q_r $[W/cm^2]$		$\delta_{\%}$ [%]
							High-Fidelity	Present Work	
[237]	01	7	$1{\cdot}10^{-4}$	3.75	15	70	17.1-20.1	19.3	+3.9 \-12.8
[237]	02	7	$1{\cdot}10^{-4}$	3.75	1.5	70	18.2-21.2	19.3	+6.04 \-8.53
[238]	03	6.25	$1{\cdot}10^{-4}$	4	16	70	2.1	3.02	+43.8

Table 4.16.: Comparison of Radiative Heating at stagnation point for Mars environment

4.5. Flexible Thermal Protection System

The method outlined in section 3.8 consists of a 1D heat diffusion model for a multi-layer body. The approach was established following Del Corso's [30] claim that this approximation would be sufficient to model the temperature across the thickness of each layer. However, the claim is hereby investigated to both verify the correct implementation of the model against other numerical tools and to ensure the validity of the results against experimental data. The advanced high-temperature F-TPS developed by the Aeronautical Research Mission Directorate Hypersonic project at NASA is taken as the reference model, previously described in Figure B.9. The candidate materials have been tested in the Laser-Hardened Materials Evaluation Laboratory (LHMEL) [239], a facility comprising a vacuum chamber at a pressure level of $1 \cdot 10^{-5}$ torr in which a continuous discharge of CO_2 occurs at 15 kW to impinge on the test material. The 76cm-vacuum-chamber, at the end of the laser beam shown in Figure 4.44 contains a holder frame that allows a square F-TPS sample with a cross-sectional area of 103 cm^2 to be tested. The outer surface temperature is measured with a multicolour pyrometer and internal temperature is recorded with thermocouples [30].

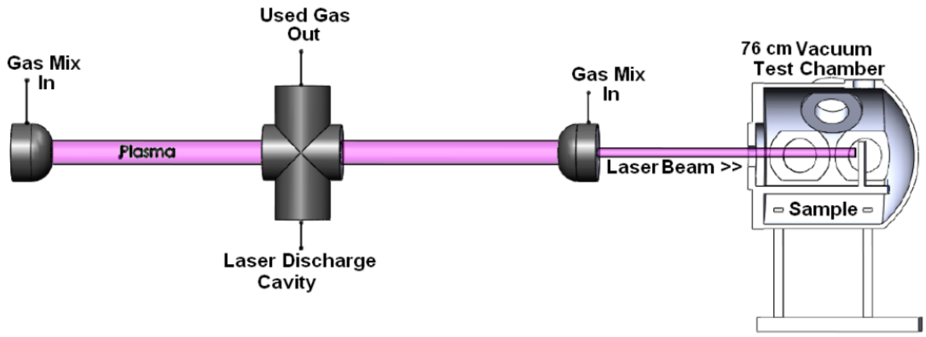

Figure 4.44.: Schematic of the LHMEL Test facility [30]

The F-TPS in Figure B.9 has been tested at conditions representative of Mars entry as given in Table 4.17. The Silicon carbide layup, adopted in this work, was successfully found to survive 100 W/cm^2 heat flux [30], with the temperature data shown in Figure B.8. Given the presence of an anomalous measurement at approximately 50 seconds in the first thermocouple in Figure B.8, the data from the test at 50 W/cm^2 is used for verification and validation. This represents a more conservative approach for the peak heat flux experienced by the F-TPS, whilst also offering a larger heat load given the longer duration of the test.

Material	Thickness L $[cm]$	Aerial Weight m/A $[g/cm^2]$	Test Duration t $[s]$	Test Heat Flux $q(t)$ $[W/cm^2]$	Heat Load Q $[J/cm^2]$
Nicalon SiC	0.0506	0.0425	90-200	50-100	$9 - 10 \cdot 10^3$
Pyrogel 3350	0.3047	0.0518	90-200	50-100	$9 - 10 \cdot 10^3$
Kapton	0.0025	0.0037	90-200	50-100	$9 - 10 \cdot 10^3$

Table 4.17.: F-TPS configuration for LHMEL test [30]

4.5.1. F-TPS: Numerical Verification

First, a higher-fidelity heat diffusion model is set up in Ansys within the transient thermal module. This is widely applied in the literature to address complex thermal problems, such as the TPS of a spacecraft [240] in which radiation, convection and conduction can be readily modelled. The F-TPS thermal model, simplified in Figure 4.45 is modelled such that radiation is applied on the first and last layer according to the emissivity values in Table 4.17 with a uniform freestream temperature fixed at 273 K. The location of the thermocouples used to gather the experimental data in Figure B.8 TC is also indicated [30].

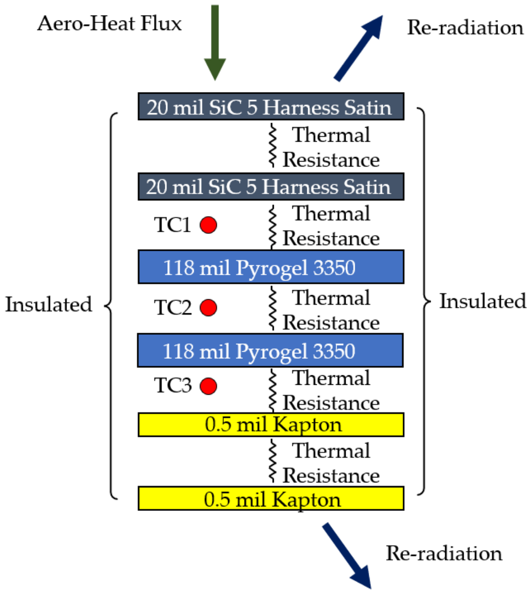

Figure 4.45.: Thermal model of the F-TPS layup

The heat flux is then applied according to Equation 4.4 with a temporal discretisation of $\Delta t = 0.5s$ for a total time of 300 s. A total number of 600 points is thus used for the time description. Spatial discretisation is performed for different meshes with an increasing number of elements and nodes. Four of such meshes are shown in Figure 4.46. The side of each F-TPS layer has a width of 10.148 cm in order for the total cross-sectional area to be 103 cm^2 in accordance with the original test conducted by Del Corso et al. [30].

$$q(t) = \begin{cases} 50 \quad W/cm^2, & \text{if} \quad 0 \leq t \leq 200s \\ 0 \quad W/cm^2, & \text{if} \quad t > 200s \end{cases} \tag{4.4}$$

The numerical results of the temperature distribution over time are recorded for the locations in correspondence to the surface and the thermocouples, referred to as $TC1$, $TC2$ and $TC3$ respectively, following the nomenclature in Figure B.8. Specifically, $TC1$ is measured at the interface between the second layer of SiC and the first layer of Pyrogel. Conversely, $TC2$ is located between the two Pyrogel layers and, finally, $TC3$ is between the second Pyrogel layer and the first Kapton layer. The average absolute difference in temperature for each mesh with respect to the finest mesh in Figure 4.46, measured for each of the aforementioned identifiers,

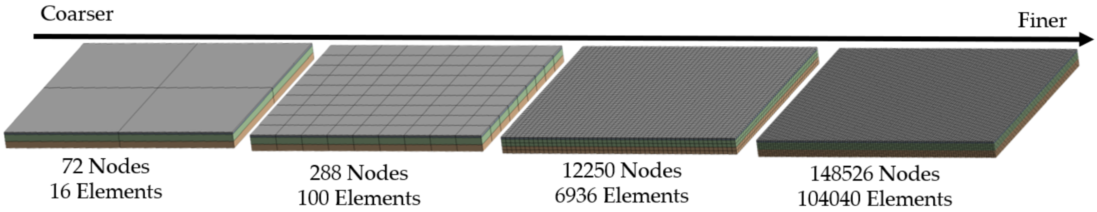

Figure 4.46.: Mesh refinement for F-TPS in Ansys

is then computed. The results are plotted in a semilogarithmic base in Figure 4.47, where the error is found to exponentially decrease with the number of mesh elements. An error below 1 K is considered acceptable to deem the mesh as being sufficiently accurate for the simulation, attained at approximately $1.2 \cdot 10^4$ number of mesh elements.

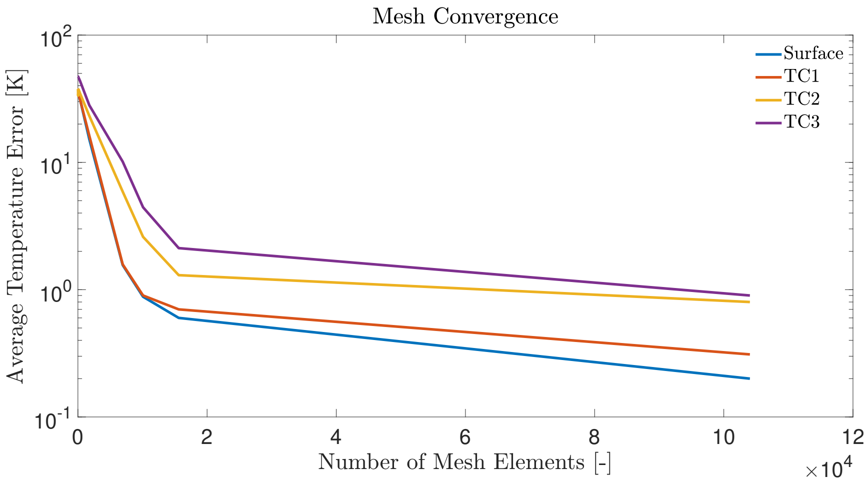

Figure 4.47.: Mesh Convergence Study for Thermal study

4.5.2. F-TPS: Experimental Validation

Once convergence has been established, the computed temperature of the accepted mesh is utilized to compare the numerical results to the experimental ones in Figure B.8 for the 50 W/cm^2 case. To address the lack of experimental data on thermal contact conductance for the materials of interest, a parametric study was conducted in Ansys. The objective was to minimize the disparity between the numerical and experimental temperatures in steady-state. The selected contact conductance values, in accordance with Betsy et al. [241], are provided in Table 4.18.

The results with and without the contact conductance are plotted in Figure 4.48, from which it is possible to note that the temperature levels in steady-state are correctly identified with the presence of the thermal contact conductance. Table 4.19 highlights the much lower average absolute error between the experimental and numerical data for the steady phase of the test (50-200 s) when the contact conductance is included. When the temperatures are subject to significant variations, in the transient phases of the test ($t \leq 50\ s$ & $t > 200\ s$), the increasing and

Contact Surfaces	Thermal Contact Conductance h_c $[W/m^2/K]$
SiC-SiC	100
SiC-Pyrogel	100
Pyrogel-Pyrogel	30
Pyrogel-Kapton	200
Kapton-Kapton	1000

Table 4.18.: Thermal Contact Conductance in F-TPS Layers

decreasing trends are correctly modelled in both cases. A significant error is however present, due to the simplicity of the model adopted which lacks an accurate description of real-gas effects such as decomposition, charring, outgassing and ablation. Moreover, it is also important to recognise the presence of uncertainty in the experimental data due to the presence of thermocouples at the interfaces between the materials.

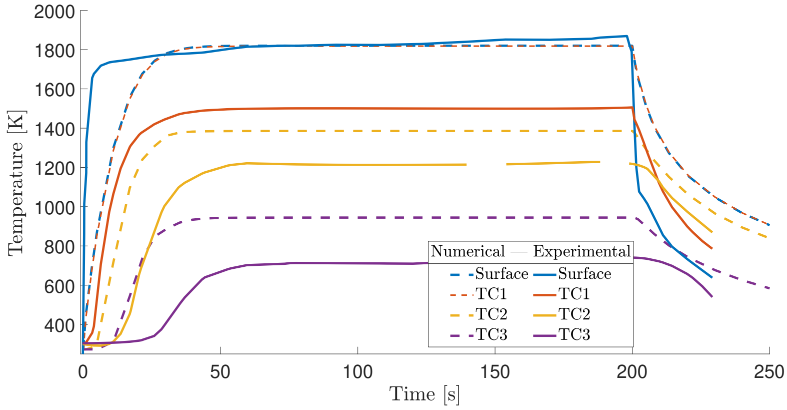

(a) Without contact conductance

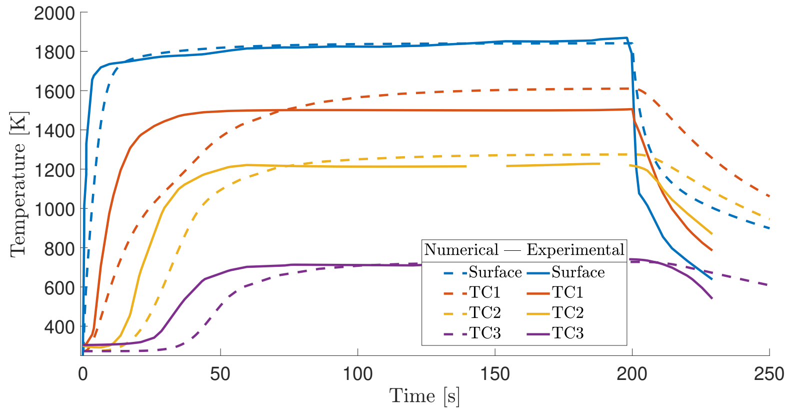

(b) With contact conductance

Figure 4.48.: Comparison of Ansys transient thermal results with experimental data

F-TPS	δ_{avg} [%]			
	Surface	TC1	TC2	TC3
Without Contact Conductance	1.09	21.13	14.18	32.85
With Contact Conductance	0.79	6.80	4.35	0.68

Table 4.19.: Absolute Percentage Error of Ansys with experimental data, with and without contact conductance in steady-state (50-200 s)

Improved results for the transient phases of the heat transfer may be obtained by modelling the contact conductance as a function of the temperature and pressure [30]. The identification of the correct thermal contact conductance, however, should be an experimental problem rather than a parametric fit. For this reason, while a novel feasible solution to improve the correlation between experimental and numerical data is provided in subsection B.5.2, the constant values in Table 4.18 are considered sufficient for this work. Once the contact conductance is established and the benchmark high-fidelity simulation results are obtained for comparison, the 1D heat diffusion model described in section 3.8 is implemented. As for the high-fidelity simulation, a mesh independence study is conducted in which the number of nodes per layer is increased and the average absolute percentage change in temperature for the surface, $TC1$, $TC2$, and $TC3$ locations are recorded.

The resulting trends are shown in Figure 4.49 from which some major observations can be made. Firstly, as expected, the percentage change rapidly decreases with the spatial discretisation. This is a direct consequence of the finite difference approximation which generates a numerical error proportional to the squared distance between two adjacent nodes. At the same time, the computational cost exponentially increases with the number of nodes per layer, increasing from 0.47 seconds for 2 nodes in each layer to 77.66 seconds when the value is increased to 20. A trade-off must be made between the degree of numeric error that is considered acceptable and the computational time required to perform the simulation. While one extra minute may be a reasonable time for one simulation, in fact, it would become prohibitively expensive when contextualised in the MDAO framework that this work aims to develop since thousands of simulations would be required to compute the optimal F-TPS configuration for each trajectory and vehicle. Keeping in mind this balanced choice of computational accuracy and time, 12 nodes per layer are chosen for the baseline geometry since the percentage error is already lower than 1% and the resulting discretisation is summarised in Table 4.20.

Layers	Thickness L $[cm]$	Nodes per Layer $[-]$	Spatial Discretisation Δx $[mm]$	Temporal Discretisation Δt $[ms]$
SiC ×2	0.0506	12	0.0423	0.0274
Pyrogel ×2	0.3047	12	0.2539	0.0274
Kapton ×2	0.0025	12	0.0021	0.0274

Table 4.20.: Baseline Discretisation for Thermal Analysis

The temperature distribution resulting from the baseline discretisation of the 1D heat diffusion model as outlined in Table 4.20 is plotted in Figure 4.50 against both the experimental data and the numerical data obtained using Ansys. The agreement with the experimental data is pronounced in the steady-state region, with more significant discrepancy observed in the initial

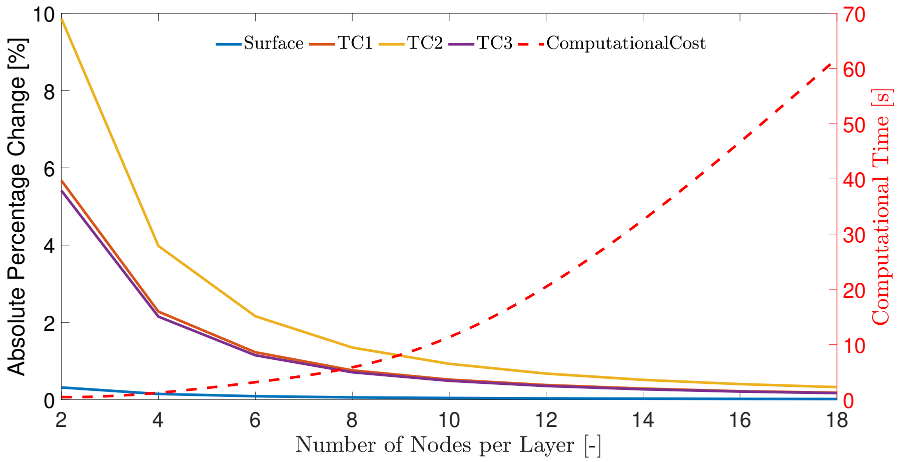

Figure 4.49.: Temperature change convergence and computational cost with number of nodes

Comparison of Thermal Diffusion FDM	δ_{avg} Surface	TC1	TC2	TC3
Experiment [30]	1.66	3.023	7.96	9.037
Ansys	5.88	14.60	18.12	19.97

Table 4.21.: Percentage Error of 1D FDM with Experimental and Simulation data

transient phase. However, it is noted that the discrepancy always overpredicts the temperature predicted by the numerical model, resulting in a slightly more conservative design. A similar observation is made with respect to the results obtained in Ansys, as confirmed by the error distribution over time plotted in Figure 4.51 in which the location of the error coincides for both sources of data, verifying that the method has been correctly implemented and that the numerical error is due to the oversimplification of the problem in which real gas effects, such as decomposition, outgassing, internal re-radiation between layers and charring, are neglected. These, in fact, would result in excessively expensive computations for a MDAO approach.

It is useful to note the presence of large uncertainty in the initial transient, which is compensated by a reasonable level of error in the final transient. While the larger percentage error is partly due to the temperature values being lower than in the final transient, meaning that the smaller values at the denominator would amplify the error value, it may also be attributed to the initial accuracy of determining the sudden rise in temperature. When applied to an entry trajectory it is expected that the peak heat flux, which is the most critical point for the design of the F-TPS, would be predicted more accurately since it would follow the sudden initial peak in temperature, based on the trends observed in Figure 4.50 and Figure 4.51.

The averaged percentage error of the heat diffusion model is finally given in Table 4.21 with respect to the experimental and Ansys data for each measurement location. Given that an average error between $1-9\%$ is computed across the test duration, the model in its simplicity is considered valid for early design stages and preliminary estimations of the F-TPS.

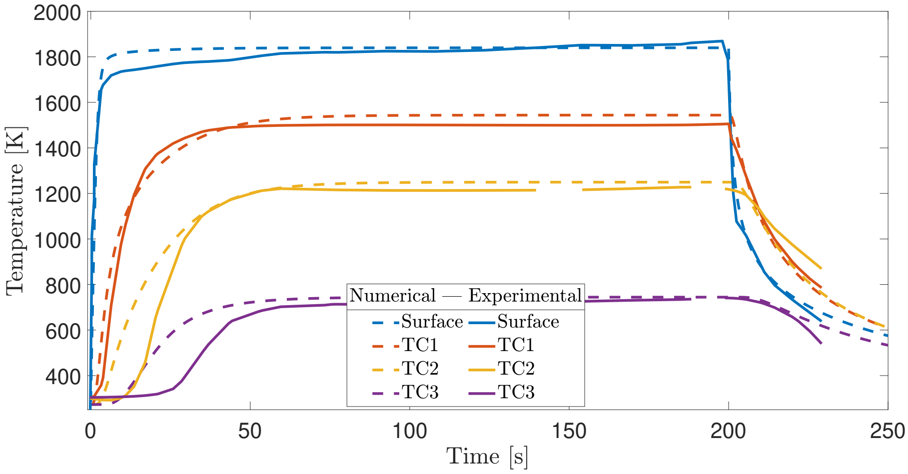

(a) Comparison with Experimental data

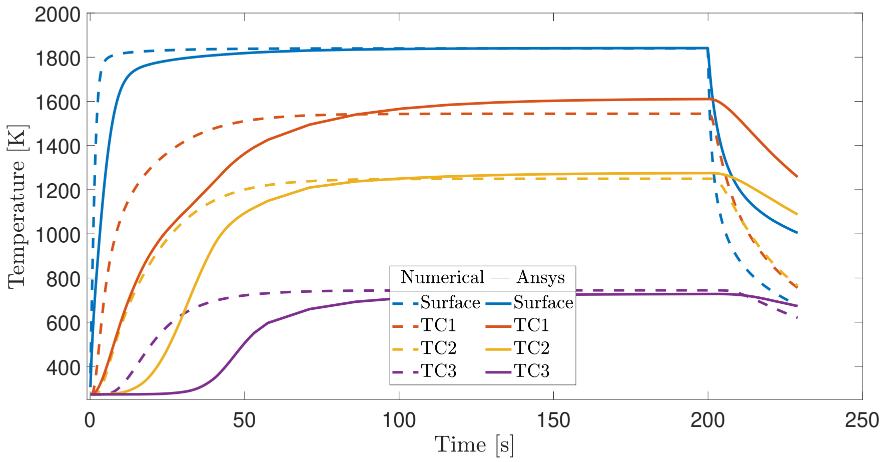

(b) Comparison with Ansys data

Figure 4.50.: Temperature distribution of 1D FDM Heat Diffusion model

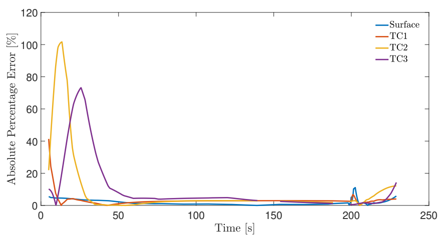

(a) Comparison with Experimental Data

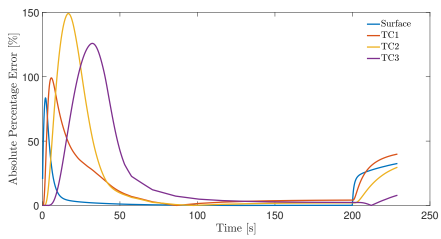

(b) Comparison with Ansys data

Figure 4.51.: Error distribution of 1D FDM Heat Diffusion model

5. Case Study: MiniPINS

Penetrators have been proposed for planetary exploration, building upon military developments for scientific purposes. Lorenz [242] provides a historical review of penetrator origins, and [243] offers a recent Russian perspective. Amongst the EDL concepts retrieved, including parachutes [244–246] and unconventional alternatives like unfolding umbrellas [247] and telescoping cylinders [244], the use of stacked toroids for penetrators has not been addressed. Table B.3 presents an overview of mechanical characteristics encountered in penetrator missions.

The developed computational framework enables mission studies on stacked-toroid configurations for various applications. A case study focuses on a penetrator mission to Mars, specifically the MiniPINS mission in its early design stages. The EDL sequence is extrapolated from the previous mission, MetNet. This work provides an overview of the EDL process and a detailed analysis of the MiniPINS mission. To showcase the developed environment, a case study focusing on a penetrator mission to Mars is proposed. The choice of Mars stems from the growing interest in penetrating missions, including those by ESA, governmental agencies, academic institutions, and industries. The case study specifically examines the MiniPINS mission, which is currently in its early design stages after completing its design phase B. The EDL sequence for the MiniPINS mission is extrapolated from the previous mission: MetNet.

5.1. MetNET: The Predecessor

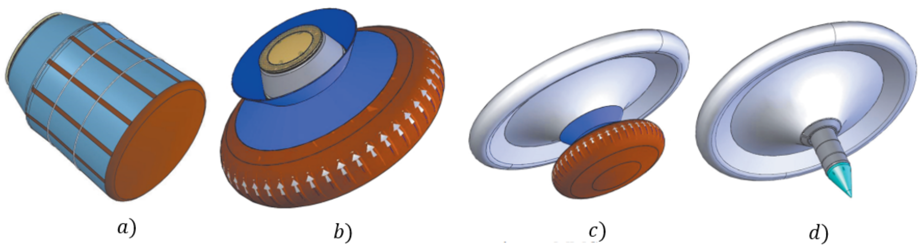

Figure 5.1.: MetNet a) in its stowed configuration b) with the first stage IAD deployed c) second-stage tension cone deployment and d) landing configuration with penetrator [79]

The Mars Network Lander (MetNET) is a recent study of a small semi-hard penetrator design with a preliminary analysis of the innovative EDL system based on inflatable structures, led by the Finnish Meteorological Institute (MTI) in cooperation with the Lavochkin Association and Russian Space Research Institute [248]. The design stage of the EDL system, which took place over a period of 7 years, was initiated by a series of comparative analyses between initial concepts, amongst which three candidates relying on inflatable technologies were considered ranging from shock absorbers to tension cones. Following a series of qualitative trade-offs, an inflatable heat shield was chosen for the entry phase and a tension cone for the descent. The EDL system's design, shown in Figure 5.1, incorporates an inflatable heat shield with a 1 m diameter. It consists of a 2.31 kg rigid aerodynamic shielding, a flexible thermal protection system, and a 1.17 kg inflation system. The inflatable structure comprises 12 tubular segments, each 250 mm in diameter. A tension cone with a 1.8 m inflated diameter allows for a landing speed of 47-55 m/s. The landing system, including a gas generator, surface module, and equipment compartment, has a total mass of 1.06 kg.

The EDL sequence, depicted in Figure 5.2, initiates with the separation phase. During this phase, the carrier spacecraft ejects the capsule containing the penetrator, which then enters the Martian atmosphere at interplanetary transfer trajectory speeds slightly exceeding 6 km/s. As the vehicle lacks active attitude control, the carrier spacecraft performs attitude manoeuvres to release the capsule under the desired entry conditions. For MetNet, the optimal entry conditions were determined to involve an entry angle ranging between -14° and -20°.

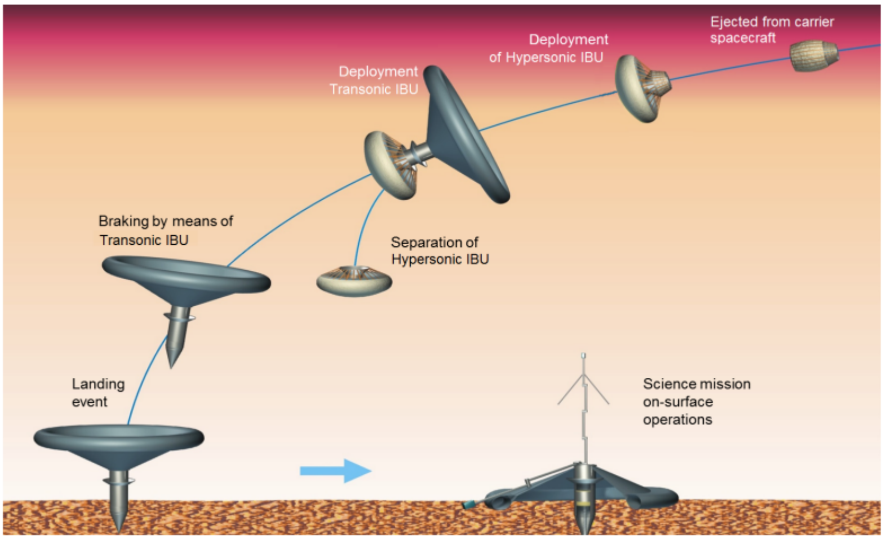

Figure 5.2.: MetNet EDL Concept of Operations [248]

Following the separation and entry stages, the hypersonic inflatable braking unit is deployed. This unit comprises an inflatable heat shield designed to ensure thermal protection during the hypersonic phase of the entry trajectory. Its primary objective is to decelerate the vehicle to a speed slightly below Mach one. The tension cone is deployed in the transonic regime, while the inflatable heat shield is discarded 10 seconds later to facilitate vehicle stabilization. Once stability is achieved, the penetrator is deployed and securely locked with the tension cone. This arrangement enables the penetrator to gradually decelerate to subsonic speeds and achieve a controlled landing with an impact velocity of 50 m/s.

Given that the design of the MiniPINS EDL sequence has a significant heritage from MetNet's one, Figure 5.2 assumes a particularly important connotation as it defines the baseline for the design of the case study that shall be investigated in this work. The decision of reutilizing the same concept is due to the selection of a reliable and simple technology which has already been partially developed [248]. However, stacked-toroid are mission-enabling alternatives that may not only enhance the performance of the system but also allow for harsher entry trajectories.

5.2. MiniPINS Design

Building upon the MetNet lander's heritage, the Mars In-Situ Sensors (MINS) of the MiniPINS mission involved the deployment of four penetrating probes weighing 25 kg each onto the surface of Mars. The two major mechanical subsystems which are of interest to this work are the penetrator, regarded as the payload of the vehicle, and the EDL system. Concerning the former, extensive analysis has been conducted to first prove the feasibility and consequently develop the technologies required for a penetrating probe to withstand the shock, survive the environmental conditions on Mars and collect measurements of the Martian subsoil. As illustrated in Figure 5.3, the physical architecture of the MINS payload is complete. It consists of an external structure needed to shield the internal electronics and sensors, which are powered by in-built solar panels. The dimensions of the penetrator, which are needed to constrain the design space exploration, are conservatively estimated to be 300 mm in diameter and approximately 780 mm in length [249]. In its stowed configuration, the assumption of regarding the penetrator as a cylindrical body for the cylindrical centrebody is reasonable.

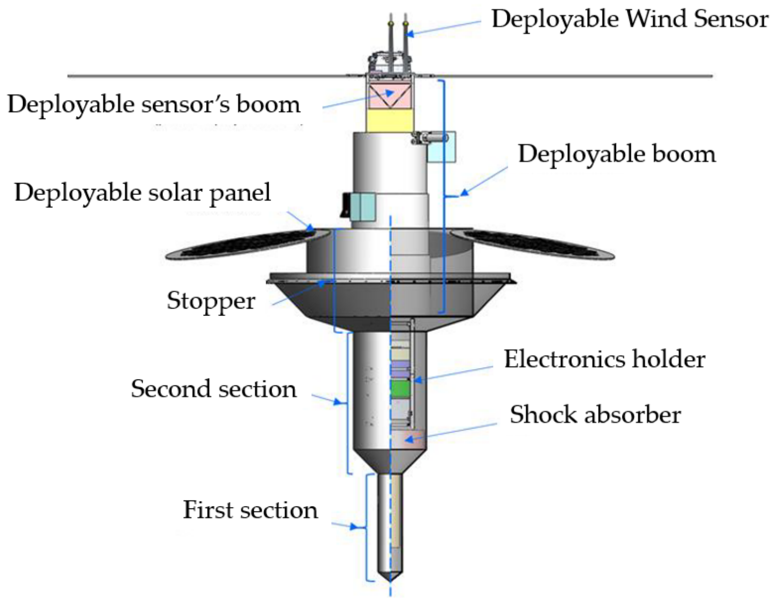

Figure 5.3.: MiniPINS Penetrator Design [250]

Similarly to the configurations adopted by MetNet shown in Figure 5.2, MiniPINS comprises a EDL system with two stages. The first one is a capsule stowed in a conical attachment configuration equivalent to that of the MetNet mission, with a volume of approximately 0.3 m^3 and a maximum outer diameter of 691.1 mm. The decision of maintaining the same stowed configuration was attributed to the desire to re-utilizing the deployment mechanism and mechanical interface with the carrier spacecraft as the one previously developed for the MetNet mission. In its deployed configuration, however, the capsule has been slightly modified to contain a rounder edge, where flow separation would be expected to occur, with a smaller radius. A shoulder radius of 44.6 mm is used with a nose cone radius of 1407 mm. Moreover, the rear section of the vehicle has been maintained with a simple conical shape as visible in Figure 5.4. An internal middle section of 150 mm is required to accommodate a 2U CubeSat structure [251], while a larger penetrator diameter of 300 mm is yielded in the upper section. An inflated diameter of approximately 1526 mm is attained by the first stage, increasing the volume to 0.68 m^3 [249].

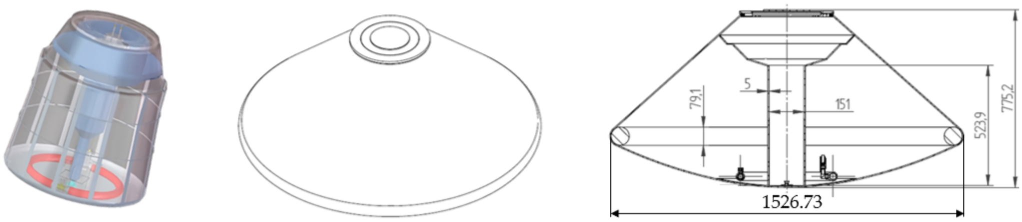

Figure 5.4.: First stage of the preliminary MiniPINS EDL system in its stowed configuration [1] (left) and deployed configuration [252] (centre) with dimensions in mm (right)

The second stage, shown in Figure 5.5 follows the same example set by MetNet as it provides a decelerating stage for the transonic and subsonic regimes by means of a tension cone. This stage is attached to the internal edges of the capsule to maintain the decelerator inside the vehicle, shielded from the environment throughout the harsher trajectory conditions. The deployed second stage has a larger diameter than the first one by approximately 27%. This difference in diameter, and thus area, is needed to generate a dynamic pressure difference to separate the two stages at the desired speeds. This aspect is of crucial importance to consider whilst exploring the design of an alternative EDL system as it may constrain the range of feasible inflated diameters. The penetrator, in fact, is emplaced in the Martian soil by means of the second stage which needs to be fully separated from the first one.

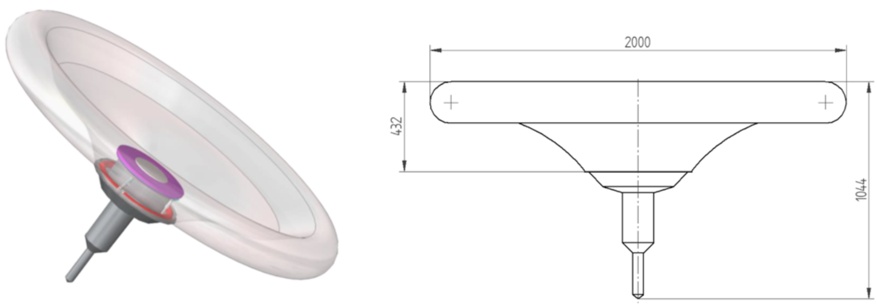

Figure 5.5.: Second stage of the preliminary MiniPINS EDL system in its deployed configuration (left) with dimensions in mm (right) [250]

The preliminary mass budget of the MiniPINS mission to Mars is shown in Table 5.1, where the auxiliary subsystems include the thermal, power, command and data handling as well as electrical subsystems. The mass of the penetrator is slightly under 4 kg, but the mass required for the additional mechanical interfaces and components is accounted for. Conversely, the first EDL stage takes up 40% of the total system mass. An additional 20% of mass margin is included given the early design stages of the mission. The total system mass of 21.3 kg is thus increased to approximately 25 kg, in line with the goal of the mission.

Element	Mass [kg]	With 20% margin [kg]
Penetrator + Sensors	3.7 + 1.75	6.54
Auxiliary Subsystems	5	6
EDL First Stage	8.4	10.08
EDL Second Stage	2	2.4

Table 5.1.: Mass budget of MINS with margins; Adapted from [251]

5.3. Penetrator Mission Overview

The landing of Martian penetrators involves two main methods. The first method consists of the mother ship entering orbit around Mars and then releasing the probes at a specific orbital position to reach the desired landing site on the surface. This effectively results in a parabolic entry. The second method involves releasing the probes from the mother ship before it enters Mars orbit, thereby attaining hyperbolic entry conditions. Both methods achieve an accurate landing, but the first method is preferred from an aerothermal perspective as it reduces the entry velocity. An illustration of the different mission stages is provided in Figure 5.6, where the following phases are identified:

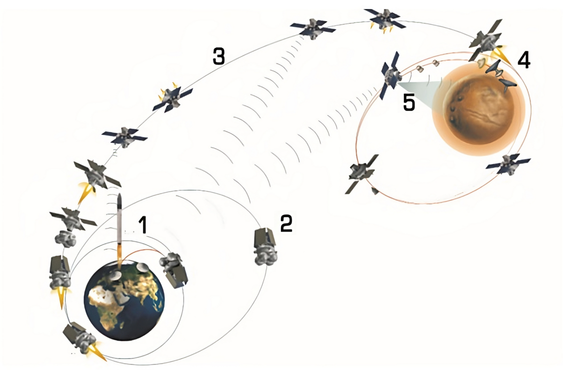

Figure 5.6.: Stages of the penetrator mission [253]

1. Integration and launch of the penetrator mission into Earth's orbit
2. Settling into the Earth-Mars trajectory
3. Cruise phase in which the penetrator is maintained in its stowed configuration
4. Arrival at Mars' orbit and preparation of the penetrator vehicle for landing. The first EDL stage is deployed and inflated exoatmospherically
5. Following entry at 120 km above the surface, landing and scientific operations are performed. The second stage is deployed in transonic conditions. The first stage is jettisoned such that the second stage reaches its landing configuration.

5.4. EDL System Requirements

Having defined the design and mission of MINS, the requirements have to be explicitly stated. While an extensive list of functional, interface, environmental and physical requirements is not relevant to the present work, it is necessary to define the specifications of the requirements that directly affect the EDL decision-making. The concise list in Table 5.2 is not intended for verification and validation purposes, but to primarily delineate the case study of this work as well as to provide constraints for the design space exploration.

ID	Description
R-01	The vehicle shall enter the Martian atmosphere at 5 km/s at an altitude of 120 km
R-02	The vehicle shall enter the Martian atmosphere at a nominal entry angle of -11 degrees
R-03	The penetrator impact speed shall be between 60-80 m/s
R-04	The EDL system shall perform aerodynamic breaking to attain the desired impact speed
R-05	The EDL second stage shall be inflated at Mach 0.8
R-06	The EDL phases shall be executed autonomously after deployment from the orbiter
R-07	The EDL first stage shall be inflated before entering the Martian atmosphere
R-08	The vehicle shall include the penetrator and inflatable EDL system after separation from the orbiter

Table 5.2.: System requirements of MiniPINS mission

5.5. Modified Mission with Stacked-Toroid

The preliminary EDL trajectory is reconstructed for MiniPINS in Figure 5.7, based on the MetNet mission with the input parameters tabulated in Table B.2. This is the baseline mission profile of MiniPINS in which the first stage is an entry capsule and the second stage is a tension cone. However, given that the EDL design was extrapolated from the MetNet mission for simplicity, in conjunction with the excessive mass required by the first stage of the EDL system, the exploration of an alternative solution is hereby investigated.

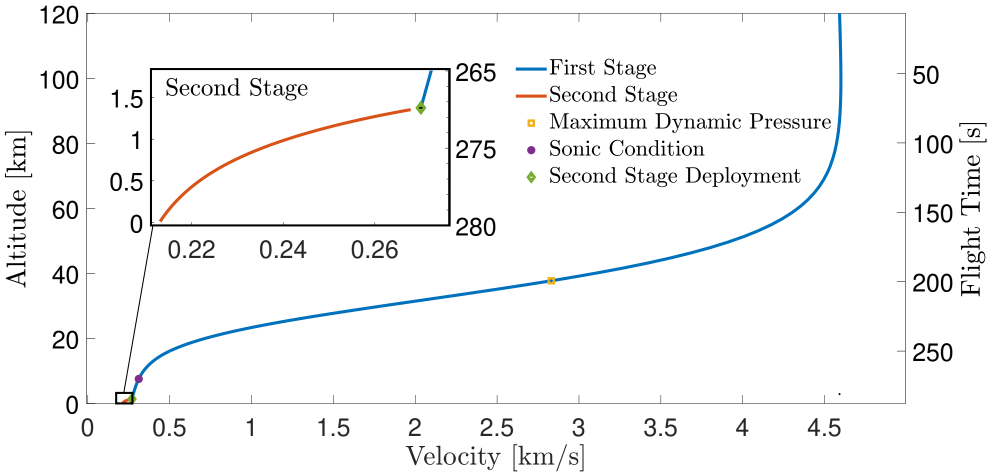

Figure 5.7.: MiniPINS baseline trajectory from MetNet heritage

The proposed alternative mission that may enhance the performance of the penetrator mission by replacing the entry capsule in the first stage with a stacked toroid IAD during the entry and descent phases is illustrated in Figure 5.8. While the second stage of the mission remains unchanged due to the mechanical interfaces associated with the penetrator and its emplacement process, the first stage undergoes modifications to explore the potential benefits of using a stacked toroid. MiniPINS did not consider this alternative architecture, as the primary focus of the mission was on the penetrator design. To avoid the need for additional testing and qualifications of new technologies and interfaces, MiniPINS extrapolated the Metnet EDL architecture. Conversely, MetNet, which was initially developed in the early 2000s and completed all qualification activities by 2013, did not incorporate the stacked-toroid configuration. At that time, stacked toroids had not yet emerged as a mature technology. However, in recent years, advancements such as IRVE-II, IRVE-3, and LOFTID have demonstrated the technological maturity of the stacked-toroid configuration.

Currently, the entry capsule occupies 40% of the system mass, which limits the amount of scientific research that can be conducted during the mission. By reducing the mass of the first stage, either the overall system mass can be decreased to ease the EDL stages or the weight savings can be compensated by additional payload mass for further experiments. Incorporating a stacked toroid offers the potential for increased scientific output and opens up numerous opportunities for advanced research. At the same time, the alternative mission offers an opportunity to demonstrate the practical application of the optimization environment developed in the thesis for mission-level design. By implementing the proposed modifications and evaluating their impact on the overall mission performance, the effectiveness and versatility of the optimization framework can be validated.

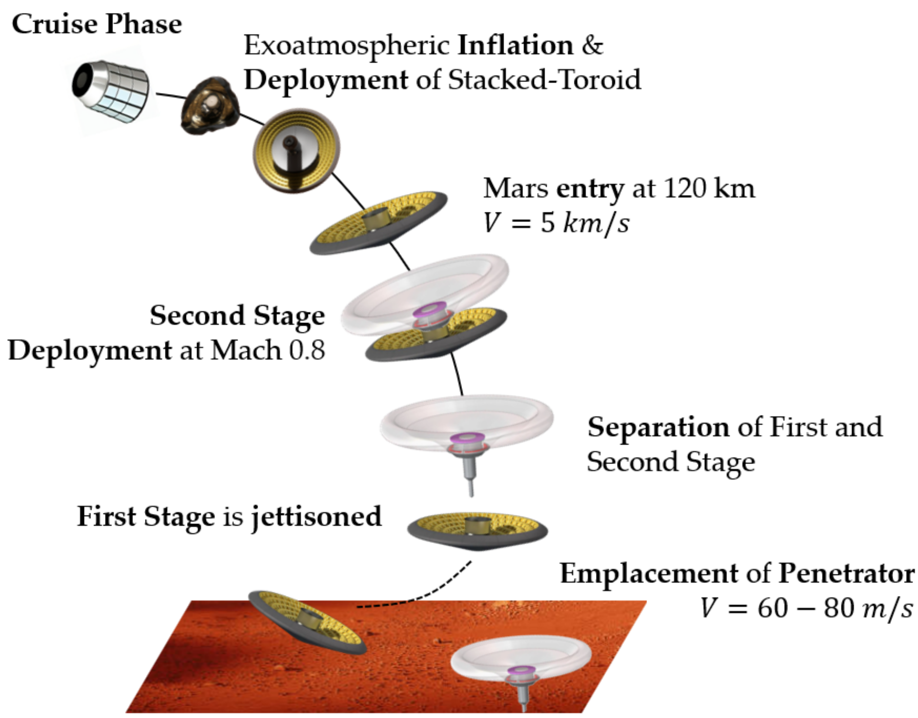

Figure 5.8.: Modified mission stages for case study with stacked-toroid IAD

An alternative mission profile to the one presented in Figure 5.8 was initially considered, comprising a single stage stacked-toroid in which the penetrator would already be deployed at the nose cone since its entry configuration. This would avoid the complexity and increased mass associated with the second stage. However, it would also expose the outer surface of the decelerator to heat augmentation due to shock impingement which would require further work on the TPS and material side [254]. An alternative could be to maintain the penetrator stowed behind the decelerator for the hypersonic entry phase to then deploy it in subsonic conditions. Nevertheless, a suitable mechanism to deploy the penetrator would need to be devised.

Given that the adopted mission presents two stages, the aerodynamic and aerothermodynamic performance of the stacked toroid is addressed by the framework developed in the present research. However, to characterise the aerodynamic performance of the second stage, as to ensure the desired landing velocity in compliance with R-03 and R-04 in Table 5.2, the wind tunnel aerodynamic data measured for the MetNet penetrator in Table 5.3 is used. For the case of $\alpha = 0°$, the fitted polynomial in Equation 5.1 yields a perfect agreement with the data ($R^2 = 1$).

$$C_D = 0.6841 M_\infty^3 - 0.6473 M_\infty^2 + 0.4560 M_\infty + 0.8392 \tag{5.1}$$

M_∞	$\alpha = 0°$	$\alpha = 10°$	$\alpha = 20°$	$\alpha = 30°$	$\alpha = 40°$
0.20	0.91	0.99	1.02	1.015	1.01
0.43	0.97	1.02	1.035	1.025	1.02
0.65	1.05	1.08	1.085	1.08	1.075
0.80	1.14	1.17	1.17	1.16	1.15

Table 5.3.: Aerodynamic drag coefficient of EDL deployed second-stage with penetrator [96]

5.6. Optimisation Problem

The general description of the optimisation problem that this work aims to address revolves around the process of finding the best solution to an objective function $f(\vec{x})$ that is subject to equality and inequality constraints [47]. Given an input to the objective function $\vec{x} = (\theta_c, N, r_{torus}, r_{out,torus})$, the mathematical representation of the problem is defined as follows:

$$\begin{array}{ll} \text{minimise} & f(\vec{x}) \\ & x_{k,LB} \leq x_k \leq x_{k,UB} (k = 1, \ldots, n) \\ \text{subject to} & c_i^{eq}(\vec{x}) = A_i \\ & c_j^{\text{ineq}}(\vec{x}) \geq B_j \end{array}$$

where the limits of each input element are given by the lower $x_{k,LB}$ and upper bounds $x_{k,UB}$ according to the values given in Table 5.4. It is clear that the design space is effectively reduced to four input parameters since the payload height and payload radius are both given by the design of the penetrator, which is 0.3 m in diameter at its largest point and approximately 0.8 m in height. A fixed system mass of 25 kg is also assumed, in accordance with the total mass budget with 20% margins in Table 5.1, such that a decrease in the mass of the EDL system is assumed to be accommodated by an increase in payload mass for further scientific experiments.

The lower and upper bounds of each parameter are identified based on the current manufacturing limitations identified in the literature review in chapter 2. The minimum half-cone angle of 45° has already been utilized in the IRDT programme. On the other hand, the maximum half-cone angle proposed in the literature is 70° for the HEART design. A maximum value of 80° is given to investigate whether a higher half-cone angle may be advantageous. The number of tori N is also varied between 1 and 9, though the value must be maintained as an integer. The upper limit of 9 fully encompasses the representative missions for medium-sized payloads such as the penetrator. The radius of the inner tori is allowed to vary from 10 mm, assumed to be the minimum size for manufacturing the bladder, to 0.5 m to avoid having excessively large toroids be pressurised by the feed system. Finally, the shoulder torus is varied from 0, such that no shoulder torus is included, to a value less than or equal to the maximum value of the inner torus radii.

Parameter	Minimum	Maximum
Half-cone Angle θ_c	40°	80°
Number of Tori N	1	9
Radius of Inner Tori r_{torus}	0.01 m	0.5 m
Radius of Outer Torus $r_{out,torus}$	0 r_{torus}	1 r_{torus}
Payload Height h_{pay}	0.8 m	0.8 m
Payload Radius r_{pay}	0.15 m	0.15 m

Table 5.4.: Design variables used for MiniPINS Penetrator mission Optimisation

It is noted that the trajectory input parameters consisting of the entry angle Γ_E, the entry velocity V_E and entry altitude h_E are fixed according to R-01 and R-02 such that $\Gamma_E = -11°$, $V_E = 5$ km/s and $h_E = 120$ km. Furthermore, the input parameters to the parametric mass model are given in Table 5.5 according to the original inputs used by Samareh [105, 255] for the verification of the model. The materials included are representatives of those utilized in the development of IRVE, HEART and LOFTID by NASA, such as Kevlar 29 and Kevlar 49 for the outer structures and Kuraray Vectran for the synthetic fibres. The toroidal structure based on Brown's design [256] which uses a fiber-reinforced film to minimise the weight. The same parameters have also been utilized for the EDL system analysis study by NASA [7, 8], supporting their suitability for this work. Moreover, since the scope of the optimisation is also that of comparing the relative variation in different design configurations to provide insight into their operations, the absolute values are of reduced importance.

Material Properties			Safety Factors		
Parameter	Unit	Value	Parameter	Unit	Value
Radial Straps Yield Strength	$[GPa]$	9	Gores Seams Margin	$[-]$	1.05
Radial Straps Material Density	$[kg/m^3]$	1440	Safety Factor Gores	$[-]$	4
Toroid Fiber Reinforced Bias Angle	$[deg]$	75	Safety Factor Toroid Fiber	$[-]$	4
Toroid Gas Barrier Material Yield	$[GPa]$	0.5	Safety Factor Toroid Gas Barrier	$[-]$	4
Toroid Gas Barrier Material Density	$[kg/m^3]$	1470	Safety Factor Toroid Axial Straps	$[-]$	4
Toroid Axial Straps Material Yield	$[GPa]$	3	Inflation Gas Pressure Margin	$[-]$	1.25
Toroid Axial Straps Material Density	$[kg/m^3]$	1440	Inflation Gas Mass Margin	$[-]$	1.25
Gores Material Yield Strength	$[GPa]$	0.5	Safety Factor Radial Straps	$[-]$	4
Gores Material Density	$[kg/m^3]$	1470	Toroid Fiber Gap Ratio	$[-]$	0.05
Number of Radial Straps	$[-]$	18	Toroid Fiber Adhesive Mass Fraction	$[-]$	0.5
Inflation Gas Molecular Weight	$[g/mol]$	22	Inflation System Mass Fraction	$[-]$	0.3

Table 5.5.: Input parameters to parametric IAD mass model [105, 255]

For the purpose of conservative aeroheating and aerodynamic corrections, a scallop radius of $\beta_{SC} = 20°$ is assumed. Additionally, the entry velocity is considered to remain constant prior to entering the atmosphere. This assumption is reasonable due to the highly rarefied nature of the atmosphere and the resulting reduced drag. Although it is an approximation, it provides a suitable velocity for the bridging parameters in the FMF for Wilmoth's function. In the continuum regime, the bridging aerodynamic coefficients are obtained by exploiting the Mach independence characteristic, where negligible differences are observed in the Newtonian method for $M > 10$. This assumption is required as no knowledge of the velocity at the continuum and FMF boundaries is available prior to performing the trajectory simulation. Furthermore, a wall temperature of 300 Kelvin is utilized for the analytical aerothermal models and used as the bondline temperature constraint for the F-TPS. R-07 justifies the treatment of the stacked-toroid as being fully inflated throughout the trajectory, as the inflation is assumed to have occurred extoatmospherically prior to reaching the 120 km entry threshold.

The nomenclature c_i^{eq} and c_j^{ineq} in the definition of the optimisation problem is used to represent the equalities i and inequalities j of the optimisation problem. While the former ones are more difficult to satisfy, requiring one satisfactory value, the latter accept a broader range of solutions. For the case study of the present work, the following constraints are identified.

Constraints

The initial constraint applied to the problem deals with the heat flux and heat load experienced throughout the trajectory. The inner optimizer, relying on gradient-based optimization, aims to minimize the mass of the F-TPS. This necessitates a sufficiently thick heat shield capable of withstanding aeroheating loading. Assuming the F-TPS is applied across the outer shell and the nose-cone instead of using a heavier rigid TPS, the input transient heat flux profile, denoted as $q(t)$, determines the required thickness and associated mass of the heat shield. However, if the heat flux surpasses the heat shield's capacity to endure, the constraint will not be satisfied. From a mathematical standpoint, this is easily represented by the flag outputted in the Matlab environment from the fmincon optimization function. The following equality constraint is imposed, where a flag value of -2 or 0 indicates that the constraints were not satisfied or the optimization could not be solved, while a value of 1 signifies a successful optimization.

$$FLAG_{F-TPS} = 1 \tag{5.2}$$

The second constraint applied is concerned with the effective deployment of the second EDL stage. According to requirement R-05, a Mach number of 0.8 must be reached in the trajectory. This means that the iterated value at each trajectory point must reach $M = 0.8$ for the condition to be satisfied. This event is captured in the code by a second flag, such that:

$$FLAG_{stage-deployment} = 1 \tag{5.3}$$

Following the deployment of the second stage, it is also required as per R-03 for the penetrator to attain a final landing speed between 60 and 80 m/s. This takes the form of the inequality constraints which can readily be expressed below:

$$60m/s \leq V(t_{end}) \leq 80m/s \tag{5.4}$$

The inflated decelerator necessitates a storage tank containing the pressurised gas for the inflation process. As discussed in chapter 3 this is assumed to be spherical, such that the radius of the tank shall not exceed that of the payload radius, which defines the dimensions of the frontal shell. The following inequality is given:

$$r_{tank} \leq r_{pay} \tag{5.5}$$

Using a similar strategy, the loads experienced by the fabric in the toroidal, spar and restraint wrap sections must be below the yield strength used in the materials. The following three structural constraints are defined:

$$\sigma_{toroid,max} < \sigma_y \tag{5.6}$$

$$\sigma_{spar,max} < \sigma_y \tag{5.7}$$

$$\sigma_{wrap,max} < \sigma_y \tag{5.8}$$

As a consequence of the definition of the parameter $r_{out,torus}$, a geometric constraint is applied to the design space search to relate the maximum allowable radius of the outer torus to the equivalent parameter used for the inner tori. In fact, it is necessary for the radius of the outer shoulder torus to be smaller than the inner tori. An equivalent value between the two $r_{out,torus} = r_{torus}$ would signify an increase in the number of tori N by one. To avoid this particular case, a constraint is applied to the input design space with the following mathematical relation:

$$r_{torus} > r_{out,torus} \tag{5.9}$$

Though not explicitly denoted by the requirements, the aerobraking function mentioned in R04 denotes the need for a stable vehicle. The static aerostability of the decelerator should thus be imposed as a constraint. According to the discussion in subsection 3.5.6, the location of the CoG needs to be defined. Based on the penetrator design in Figure 5.3, it is likely that this is located between the second section and the top part of the vehicle's centrebody. However, given that no information is available in the literature, any assumption would be unjustified. Hence, only the derivative of the moment coefficients about the nose cone are implemented in this optimisation problem, but the SM constraint is displayed for completeness and further investigated for the final optimised configuration. A typical value of 15% should be ensured for such applications [165].

$$\frac{\partial C_m}{\partial \alpha} < 0 \tag{5.10}$$

$$\frac{\partial C_n}{\partial \beta_s} < 0 \tag{5.11}$$

$$SM \geq 15 \tag{5.12}$$

Three more constraints can then be defined for the dimensions of the stacked-toroid. The first one is concerned with the packing efficiency of the accelerator, which according to Table 3.3 reaches values of $\frac{r_{inflated}}{r_{pay}} \sim 7$. However, for the current case study in which $r_{pay} = 0.15$ m is defined, the maximum inflated radius would be 1.05 m, which is rather prohibitive for the design space exploration. In fact, the r_{pay} of the vehicles used for the comparison present values larger than 33% to 726 %. It is thus decided not to include this constraint for this study, but to keep it in consideration when analysing the results. Then, the fairing dimensions can be used to constrain the maximum payload radius and height. However, given the miniaturized nature of MINS, the values are well within the reference bounds indicated in Table 3.2. For the sake of completeness, these three constraints are represented mathematically.

$$r_{inflated} \leq 7r_{pay} \tag{5.13}$$

$$r_{pay} \leq r_{fairing} \tag{5.14}$$

$$h_{pay} + 2r_{tank} + h_{stowed} \leq h_{max,fairing} \tag{5.15}$$

Objective Function

Having defined the equality and inequality constraints of the problem, it is crucial to define the objective function of the optimisation around which the case study revolves. This is used to establish the optimised design space and its characteristics are dependant on the problem as defined by the user. No specific requirements are specified on its nature, such as continuity or differentiability. Many realistic problems could require multiple objectives to capture the system behaviour within its limitations, needing trade-offs between the different solutions. Nevertheless, more complex objective functions may result in challenging optimisation processes [47].

Potential optimization functions for the EDL system can involve individual or combined technical factors. These factors include minimizing the impact velocity, ballistic coefficient, peak heat flux, stowed volume, and total mass. On the other hand, maximizing the static margin, payload mass, and drag area can also be considered. Alternatively, parameters such as cost, reliability and complexity could be quantified and taken into consideration for each design choice. In more advanced design stages, multi-objective functions can be utilized, which allow for holistic mission-level optimization. For example, maximizing flight time to gather telemetry during descent or maintaining communication with the mothership by achieving specific orientations, or minimizing the deployment altitude of the second stage. However, for this study, considering the preliminary nature of the MINS mission, the limited available EDL requirements, and the demonstration purpose of the proposed environment, a single objective function is adopted. Given the limitation identified in the first stage of the original MiniPINS EDL architecture in terms of mass, adding up to 40% of the total system mass, the optimisation function is set to minimise the mass of the novel EDL architecture comprising of the structural mass and the F-TPS mass:

$$f(\vec{x}) = m_{F-TPS} + m_{IAD} \tag{5.16}$$

5.6.1. Optimisation Algorithm

The choice of the optimisation method to adopt is not trivial. While this is specific to the optimisation problem at hand, it is also of interest to provide a baseline optimiser that can be applied to the exploration of stacked-toroid space design with different objective functions and constraints. In general, two main optimisation methods are identified: gradient-based methods and meta-heuristics [189]. The former follows a downhill search direction that is computed from the gradient of the objective function at the input conditions. In other words, the algorithm chooses the direction of the negative gradient vector given in Equation 5.17 in the attempt of reaching a point where no improvement in the objective function is reached, given that the constraints are not violated.

$$\nabla_x f(x) = \begin{bmatrix} \frac{\partial f}{\partial x_1} \\ \frac{\partial f}{\partial x_2} \\ \cdots \\ \frac{\partial f}{\partial x_n} \end{bmatrix} \tag{5.17}$$

Although it can be computationally expensive to compute the gradient of a highly complex objective function, gradient-based methods offer stable convergence for convex search spaces in which only one optimal solution is present. Nevertheless, for non-complex spaces, saddle points may appear to be local minima and erroneously interpreted as global solutions [189]. The fmincon gradient-based algorithm employed in MATLAB for the inner optimisation loop, aiming at minimising the mass of the F-TPS, is appropriate given the simpler optimisation problem. However, its suitability for the more complex objective function of the MiniPINS mass minimisation problem is not certain. For this reason, the fmincon function is also applied to the outer optimisation loop based on the results obtained with a meta-heuristic optimiser.

These types of optimisation methods do not require any information on the gradient of the objective function. On the contrary, they rely upon efficient search strategies based on natural processes [257]. An optimal or even stable solution is not guaranteed, as the algorithm attempts to find an improved solution within the optimisation bounds such that the solution could be near-optimal [258]. Amongst the different types of meta-heuristic methods, such as ant colony optimisation [259], harmony search [260], artificial bee colony [261] and particle swarm optimisation [262], the genetic algorithm (GA) is utilized in this work. In fact, since the No Free Lunch theorem postulated by Wolpert and Macready [263] states that no one metaheuristic search is generally superior over any other on average, the decision of which algorithm to choose is made on more practical considerations. Firstly, the implementation of the GA is readily available in the MATLAB environment within the Global Optimization Toolbox[1]. The GA function also includes the capability to account for multiple objectives for more complex types of objective functions in the context of stacked-toroid design and operations. Furthermore, the GA algorithm has been proven to be effective for a wide range of similar applications [189, 264]. It is also unlikely to identify a local optimum as the solution to the global optimisation [265].

As suggested by the name, the GA algorithm is inspired by the mechanism of gene transformation for biological reproduction according to which a decision variable, referred to as gene, is passed on to the next generation, or improved design space when it is altered by three main methods. Namely mutation, crossover and elitism [266]. However, most of the algorithm efficiency depends

[1] Documentation available at https://mathworks.com/help/gads/ga.html Date accessed: 22/05/2023

on the crossover method [266]. While a number of crossover strategies are available in MATLAB, as discussed by Sinpetru [189], the only one available for a combination of integer and non-integer input variables is the "crossoverlaplace" which creates a weighted average of the two parents p_1 and p_2. One of the two formulae in Equation 5.18 is randomly chosen, where bl is a random number generated from a Laplace distribution [267].

$$\text{child} = \begin{cases} p_1 + bl \times |(p_2 - p_1)| \\ p_2 + bl \times |(p_2 - p_1)| \end{cases} \tag{5.18}$$

The choice of the most suitable children for a given set of parents stems from the natural mechanism of increasing the average fitness of the next generation to maintain genetic diversity with the goal of identifying the optimum candidates [189]. The selection of the parents from which to develop the following generation, on the other hand, is done by what is referred to as tournament selection. Each parent is chosen by choosing a random number of candidates and then picking the best individuals from the set. To further increase genetic diversity in the candidates and enable the algorithm to explore a broader search space, the default mutation function "mutationpower" [267] for integer constraints is adopted. The function artificially introduces stochastic variations in the process to prevent stagnation and premature convergence of the solution [189, 268]. Elitism could also be included to ensure that a given percentage of the previous population is not affected by mutation or crossover. However, this is not included to maintain genetic diversity and to reduce the sensitivity to the initial conditions.

The initial generation of candidate solutions, which is then used as parents for the first generation, can either be created randomly with a uniform distribution to increase diversity, or an input starting population can be defined by the user. This function is advantageous for attaining a quicker convergence when the knowledge of engineers can already make calculated decisions on the potential solutions to the problem. To investigate the robustness of the code, however, a random initial population of 50 candidates is chosen. The solution from the GA optimiser is thus used as an input to a second outer optimisation loop reliant on the fmincon function, to identify the global optimum as illustrated in Figure 5.9.

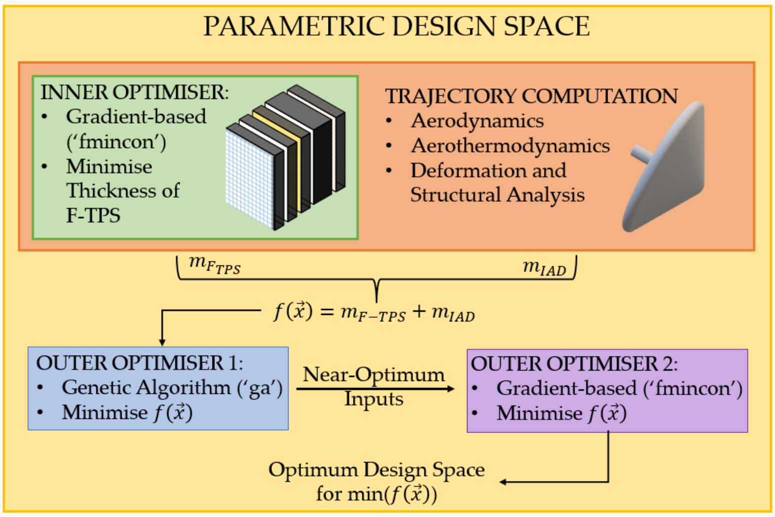

Figure 5.9.: Optimisation strategy adopted for MiniPINS Case Study

6. Results & Discussion

6.1. Outer Optimisation: Stacked-Toroid

Genetic Algorithm

The GA solver, chosen for its ability to simultaneously adapt to discrete- and continuous-variable problems, is selected as the first outer optimisation algorithm. As previously discussed, the ability of the algorithm to find a global minimum is more suited than gradient-based schemes which could end up trapped in local minima [269]. The effective convergence of the algorithm during the optimisation search is represented by the fitness values reached in each generation. Given a random initial population of 50 design configurations which are identified as generation number 0, the state of each design is measured and stored throughout the generations. For the objective function defined in the case of MiniPINS, the total mass for each configuration is computed and the mean mass value across the 50 samples is evaluated along with the best value, or the one with the lowest mass.

The resulting convergence profile is shown in Figure 6.1, where the mean total mass of each generation and associated lowest total mass are plotted throughout the algorithm process. It is noted that the total number of generations required for the final convergence is 15. This means that a total of 750 configurations are examined by the algorithm to identify the one that yields the lowest total mass. The lowest mass in each population is reduced from 7.98 kg to 4.10 kg.

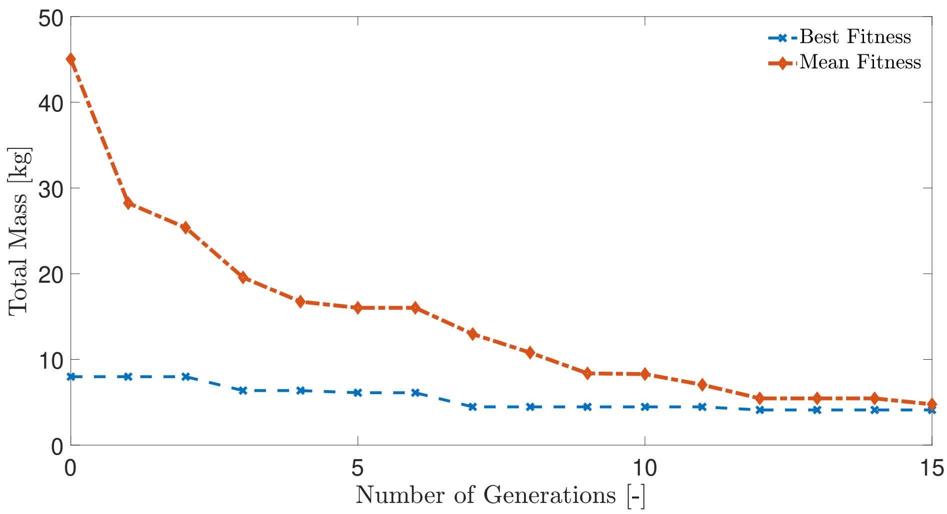

Figure 6.1.: Mean and Best Fitness convergence as a function of GA generations

To demonstrate the identification of the most suitable combination of design parameters, the algorithm explores various design inputs across all generations and presents them in histograms, as shown in Figure 6.2. The results reveal two key observations. Firstly, the algorithm effectively searches the entire design space defined by the upper and lower bounds outlined in Table 5.4. In other words, no design input value has been left unexplored. This comprehensive search is a demonstration of the strength of the optimization search, which rapidly investigates the optimization problem globally. The second observation is that specific values of the design inputs appear more frequently in subsequent generations. For example, the number of tori is predominantly found at integer values of 7, followed by 6 and then 3. Additionally, the radius of the inner tori tends to be concentrated in the lower quartile, with a majority of solutions falling below 0.1 m. Similarly, the radius of the outer torus is frequently proposed at the lower end of the design spectrum. On the other hand, the half-cone angle exhibits greater variability, oscillating between 60° and 75°.

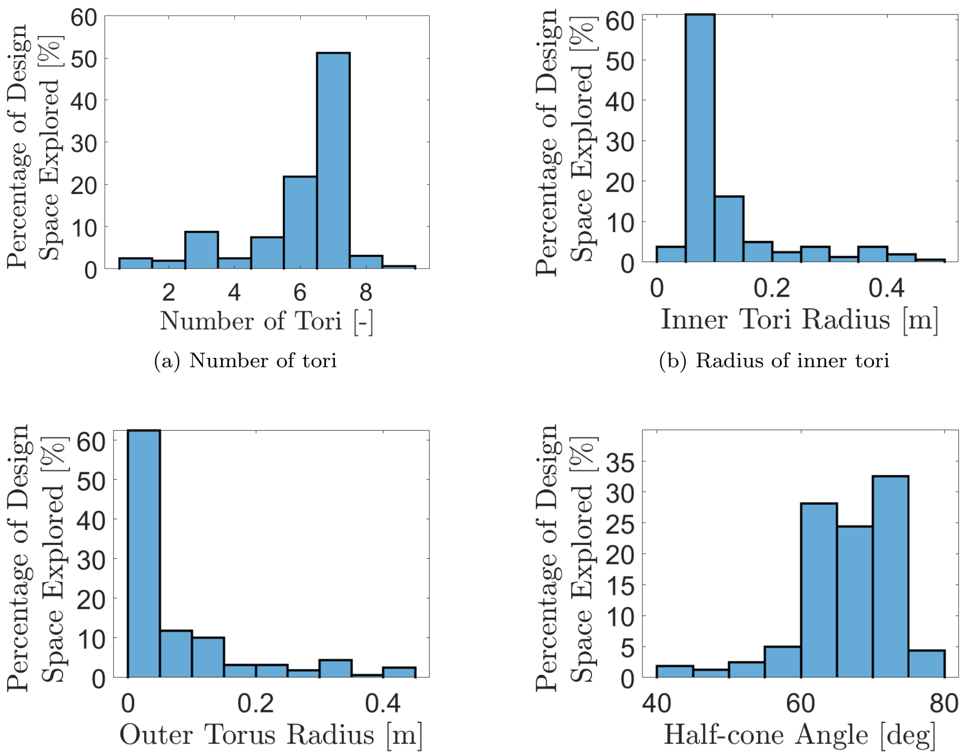

(a) Number of tori

(b) Radius of inner tori

(c) Radius of outer torus

(d) Half-cone angle

Figure 6.2.: Histogram of the input design space explored by the GA solver

The crossover feature of the GA selects values that are most suitable for the optimization problem, leading to a higher abundance of these solutions, which tend to yield the lowest total mass. While mutation introduces diversity, its impact is less significant compared to crossover. This is evident in the graph shown in Figure 6.3, where the range of values decreases over generations, indicating the narrowing down of potential solutions. The last generation represents the optimized scenario with the smallest range of values identified by crossover. The ST and mean values also converge towards the optimal value, highlighting the effectiveness of the GA.

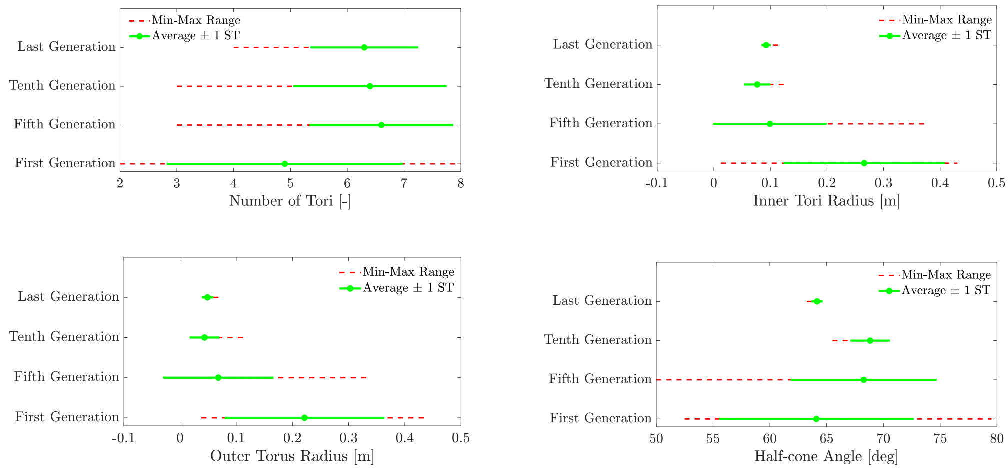

Figure 6.3.: Objective design inputs for initial population, fifth, tenth and last generations

The specific configuration of design inputs that yield the best fitness (or lowest total mass) in each of the 15 generations with a population of 50 each that are explored to attain convergence are tabulated in Table 6.1. As the generations progress, the impact of crossover becomes increasingly apparent as specific design features become more prominent. For instance, the initial number of tori undergoes a gradual decrease in the early generations, but it stabilizes after the 6th generation, indicating that this value is the optimal choice. A similar pattern can be observed with the other design variables, where they remain relatively constant for several consecutive generations before experiencing significant variation. Notably, most of the changes in design variables occur between the 4th and 6th generation. After 12 generations, the solution is nearly converged, with only minor adjustments to the magnitude of the variables. This observation suggests that the algorithm has effectively identified a configuration that yields a highly optimized design, as further changes are minimal beyond this point.

A visual representation of the evolutionary process for the design inputs that yield the lowest system mass is depicted in Figure 6.4, considering a uniformly distributed number of generations. It is noted that the generations depicted in the figure correspond to the values presented in Table 6.1. The most evident observation is the qualitative variation in the design of the stacked-toroid vehicle. The optimization process of the initial population leads to a bulky vehicle, but as the generations progress, its dimensions are gradually reduced. To better understand the relative changes, the centerbody serves as a reference point since it remains unchanged throughout the optimization. First, the maximum height of the shell decreases, followed by a rounding of the outer shoulder radius. In the 6th generation, the decision is made to use fewer but wider tori instead of thinner but more numerous ones. However, this choice is reversed by the 9th generation, which favours more tori of smaller dimensions. No vehicles presenting extreme dimensions are generated by the algorithm, such as a stacked-toroid with only a small torus, since this would not satisfy the constraints of the optimisation problem. Ultimately, the optimal solution appears significantly slimmer compared to that optimised from the initial population. This outcome aligns with the objective function of the study, which aims to minimize the total system mass. Geometrically, the dimensions of the vehicle play a crucial role in this objective, at least in a first-order analysis.

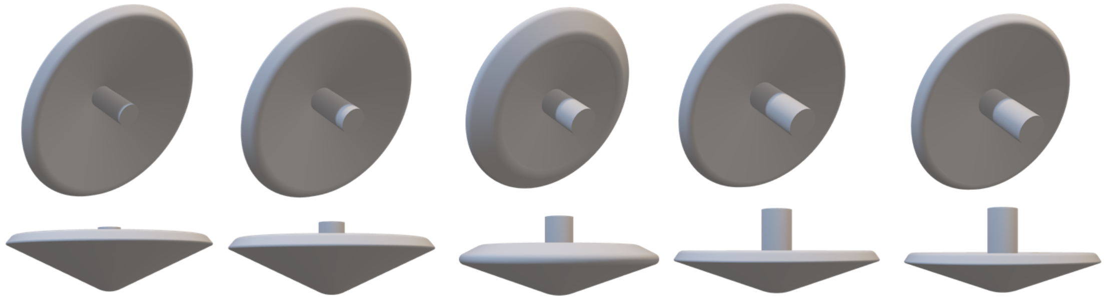

(a) Generation 0 (b) Generation 3 (c) Generation 6 (d) Generation 9 (e) Generation 12

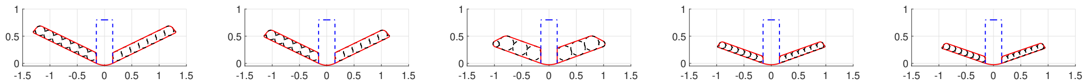

(f) Generation 0 (g) Generation 3 (h) Generation 6 (i) Generation 9 (j) Generation 12

Figure 6.4.: Isometric rear view and frontal view (top) and planar design (bottom) of the evolution of the optimised design space with number of GA generations

Generation Number	N $[-]$	r_{torus} $[m]$	$r_{out,torus}$ $[m]$	θ_c $[deg]$
# 0	7	0.0873	0.0204	63.980
# 1	7	0.0873	0.0204	63.980
# 2	6	0.0873	0.0204	63.980
# 3	6	0.0873	0.0204	63.980
# 4	3	0.0873	0.0204	63.980
# 5	3	0.1325	0.0563	70.000
# 6	7	0.1325	0.0563	70.000
# 7	7	0.0608	0.0146	70.222
# 8	7	0.0608	0.0146	70.230
# 9	7	0.0608	0.0146	70.230
# 10	7	0.0608	0.0146	70.230
# 11	7	0.0608	0.0146	70.230
# 12	7	0.0577	0.0137	70.815
# 13	7	0.0577	0.0137	70.815
# 14	7	0.0577	0.0137	70.815
# 15	7	0.0577	0.0137	70.815

Table 6.1.: Design space with the best fitness for each GA generation

Upon reviewing Table 6.1, it is evident that certain populations maintain a constant best fitness design space for varying numbers of generations (i.e. generations 8-11). This phenomenon, commonly known as "stalling," occurs when the algorithm fails to identify an improved design compared to the previous generation. Although this may initially appear as a limitation of the optimization algorithm, several factors indicate that progress is being made in refining the design space. Firstly, the observed decrease in mean fitness value depicted in Figure 6.1 suggests that the algorithm is exploring and refining the entire design space of the each population. This, coupled with the findings from Figure 6.2 and reduced statistical deviation in Figure 6.3, indicate that the algorithm has identified recurring ranges of design space inputs that lead to improved fitness values within each population. Nevertheless, the occurrence of the stalling phenomenon implies a reduced degree of genetic diversity among the populations, as the best fitness converges towards a local minimum. While the algorithm is capable of moving away from such stalling phases in the present case, it is advisable to employ a larger population size to minimize the number of stalling generations. Additionally, increasing the mutation rate can enhance genetic diversity and potentially aid in overcoming stalling periods.

Gradient-Based Algorithm

Once the GA solver has performed the global search and identified the optimum solution, it is likely that the output design space is near-optimal. To ensure that the parametric vehicle does correspond to the desired configuration that yields the lowest system mass, a secondary outer optimisation is performed. This time, however, the gradient-based fmincon solver is used. The solution of the generation #15 in Table 6.1 is used as the initial guess for the gradient-based search and the optimisation convergence is shown in Figure 6.5. Interestingly, the solution generated by the first outer optimization process was a near-optimum design, as the gradient-based search identifies solutions with lower total mass. Nevertheless, while the decrease in objective function was 48.62% across 15 generations for the GA solver, the percentage decrease is lowered to 9.27% in 30 iterations of the fmincon function. A total mass of 3.72 kg is in fact yielded. This shows that most of the optimisation search had already been carried out by the GA function and that only slight improvements are made by the second outer optimizer.

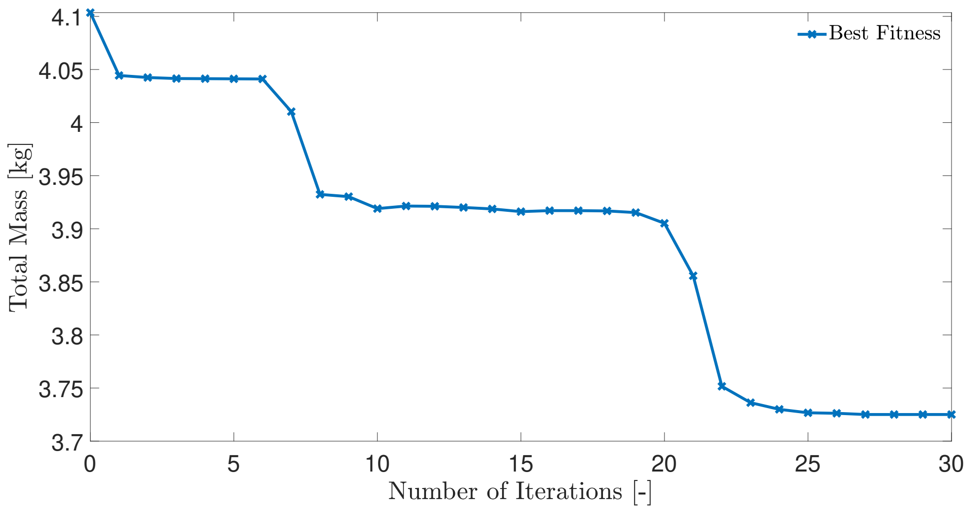

Figure 6.5.: Gradient-based search convergence of fmincon optimisation

Differently from the GA search, where diverse and broad ranges of design inputs are investigated in each population, the gradient-based optimization is much more gradual and continuous. The design inputs reported in Table 6.2 for every other fmincon iteration illustrate the much lower degree of variation in design variables. The payload height and payload radius remain fixed throughout the optimization as dictated by the MiniPINS penetrator design.

The number of tori, which has a reduced degree of freedom in the design space as it can only take the form of an integer number, remains constant throughout the number of iterations signifying that the GA had correctly identified the correct value. On the other hand, the half-cone angle is first maintained constant to then increase by less than 2° after the 6th iteration. This is again maintained at approximately 72.53° to finally decrease to an intermediate solution between the two constant stages. Such slight variations are also noted for the radius of the inner tori, which first show a gradual increase between the 1st and 8th iterations to then maintain a constant value and ultimately reduce to the final value. More interestingly, however, the radius of the outer torus is consistently lowered throughout the iterations until values in the order of $1 \cdot 10^{-6} - 1 \cdot 10^{-5}$ are reached. From a practical standpoint, the outer torus radius is therefore neglected as the magnitude of its radius is negligible with respect to the other dimensions. The value, in fact, is comparable to the tolerance of the optimization algorithm.

Generation Number	N $[-]$	r_{torus} $[m]$	$r_{out,torus}$ $[m]$	θ_c $[deg]$
# 0	7	0.0577	0.0137	70.815
# 2	7	0.0572	0.0137	70.815
# 4	7	0.0572	0.0137	70.816
# 6	7	0.0572	0.0137	70.816
# 8	7	0.0573	0.0111	71.143
# 10	7	0.0578	$3.14 \cdot 10^{-4}$	72.499
# 12	7	0.0577	$3.60 \cdot 10^{-5}$	72.533
# 14	7	0.0577	$2.78 \cdot 10^{-5}$	72.534
# 16	7	0.0577	$1.40 \cdot 10^{-5}$	72.535
# 18	7	0.0577	$5.31 \cdot 10^{-6}$	72.536
# 20	7	0.0577	$1.34 \cdot 10^{-5}$	72.537
# 22	7	0.0576	$6.76 \cdot 10^{-6}$	72.485
# 24	7	0.0565	$1.40 \cdot 10^{-5}$	71.764
# 26	7	0.0563	$1.40 \cdot 10^{-5}$	71.664
# 28	7	0.0563	$1.36 \cdot 10^{-5}$	71.648
# 30	7	0.0563	$1.19 \cdot 10^{-5}$	71.641

Table 6.2.: Design space with the best fitness for each fmincon iteration

The evolution of the stacked-toroid design throughout the optimization process is shown in Figure 6.6, where a comparison between the initial and final designs is illustrated. This also corresponds to the solution of the GA optimization, on the left, and the one generated by fmincon, on the right. Qualitatively, the major difference is related to the outer shoulder being more rounded for the latter, due to the absence of an outer shoulder radius.

A comparison is presented in Table 6.3 between the optimized mass of the stacked-toroid and the preliminary MiniPINS 1st EDL stage mass. It is important to acknowledge that this comparison may not be entirely fair due to differences in design factors such as materials, TPS, mechanisms, interfaces, and structural properties. However, both optimizers show a significant reduction in mass, indicating the potential advantages of using a stacked-toroid design. The decreased mass of the EDL system with the optimized stacked-toroid design offers various benefits. It could

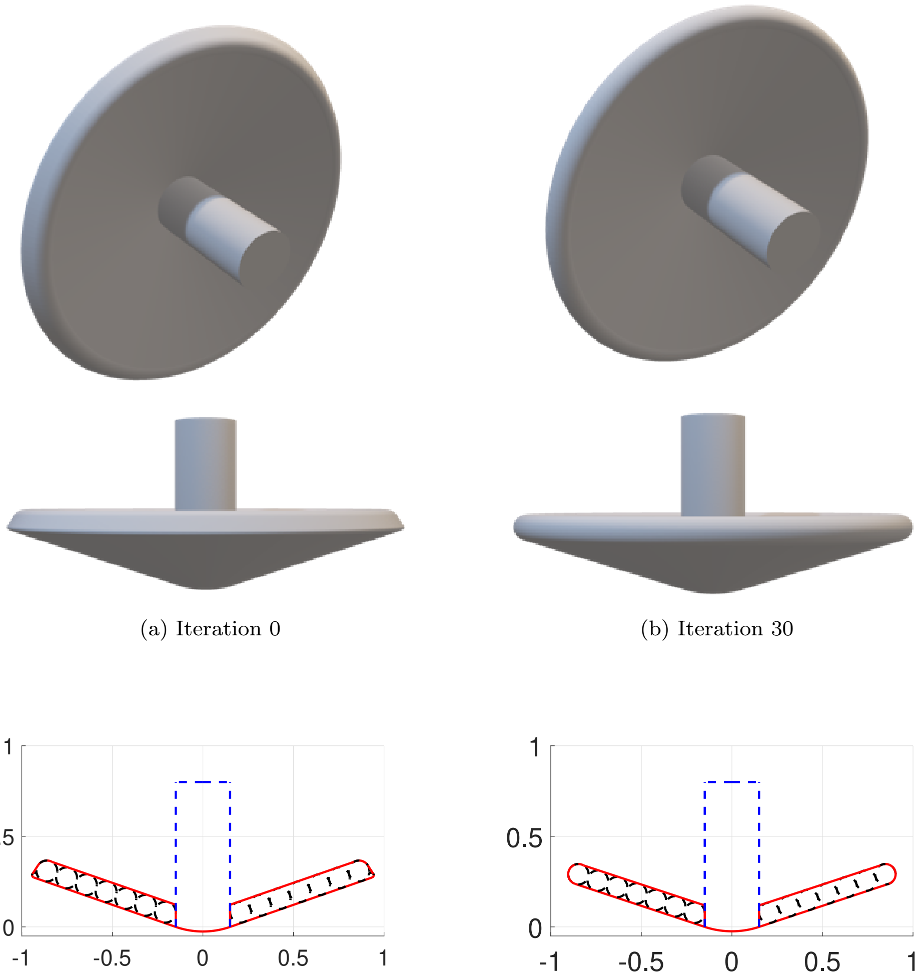

(a) Iteration 0

(b) Iteration 30

(c) Iteration 0

(d) Iteration 30

Figure 6.6.: Isometric rear view and frontal view (top) and planar design (bottom) with the comparison of initial and final "fmincon" optimisation inflatable

allow for additional payload mass, facilitating more scientific experiments. Alternatively, it can alleviate the requirements of the EDL stage by reducing the overall system mass.

The optimized parametric design space generated through the fmincon function (iteration #30) is presented in Table 6.4 and an engineering drawing of the optimum stacked toroid is illustrated in Figure 6.7. In this iteration, the design parameters achieved the lowest possible mass while adhering to the constraints outlined in the optimization problem. More importantly, the optimized variables fall within the bounds of the design space and not at either end as constrained simulations would appear, revealing the suitability of the chosen limits. The inflated diameter of 1.8076 m is lower than the tension cone's inflated diameter of 2 m, ensuring the presence of a difference in dynamic pressure for EDL stage separation.

MiniPINS Capsule Mass $[kg]$	GA Optimizer Stacked-Toroid Mass $[kg]$	fmincon Optimizer Stacked-Toroid Mass $[kg]$	GA Optimizer Mass Reduction [%]	fmincon Optimizer Mass Reduction [%]
8.85	4.10	3.72	53.67	57.97

Table 6.3.: Comparison of optimized stacked-toroid mass with MiniPINS preliminary capsule

θ_c $[deg]$	N $[-]$	r_{torus} $[m]$	$r_{out,torus}$ $[m]$	h_{pay} $[m]$	r_{pay} $[m]$
71.64	7	0.0563	0	0.8	0.15

Table 6.4.: Optimised parametric Stacked-toroid Design Inputs for MiniPINS Case Study

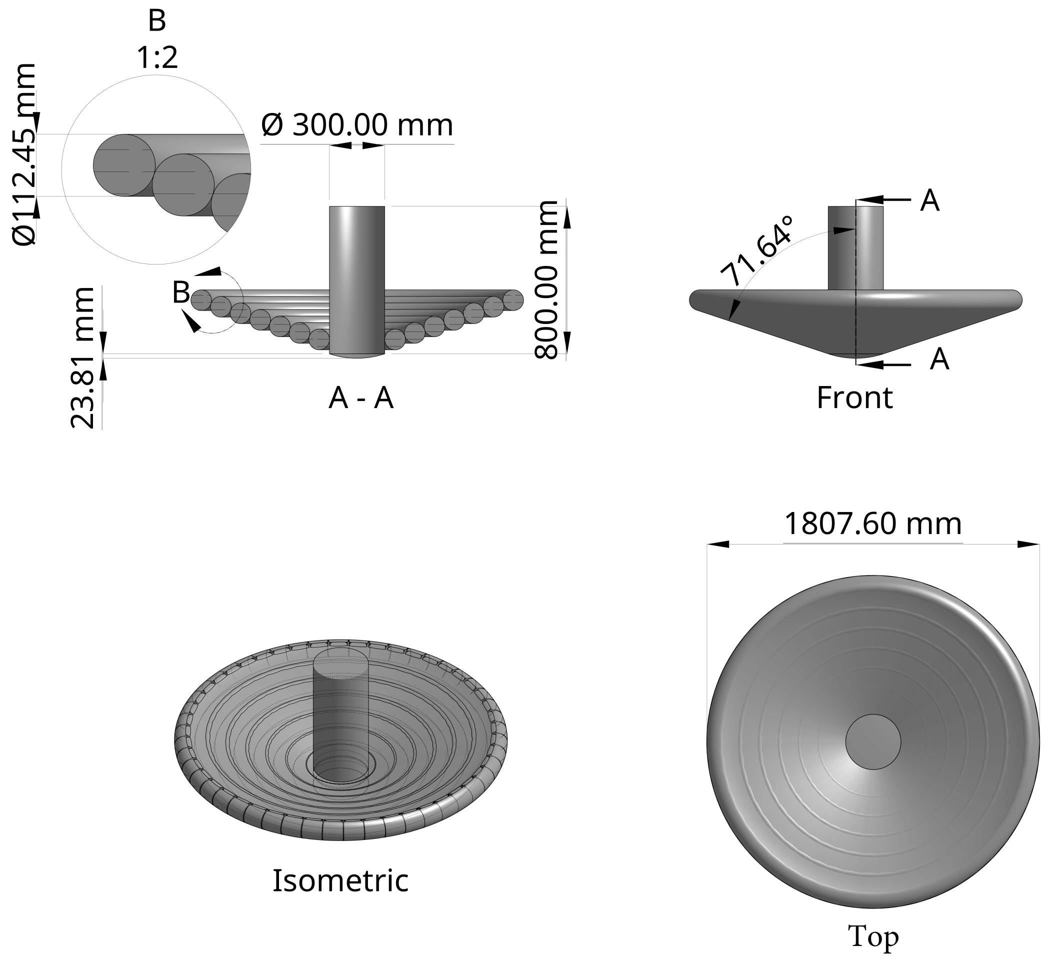

Figure 6.7.: Engineering drawing of the optimum stacked-toroid design

6.1.1. Inner Optimisation: F-TPS

The results presented thus far address the solutions generated by the outer optimizers. However, an inner optimizer is utilized within each trajectory simulation to yield the minimum amount of F-TPS aerial density for a given heat flux transient profile. The convergence of the inner optimizer for the trajectory of the optimized case with design inputs in Table 6.4 is shown in Figure 6.8. The solver quickly converges to the optimum solution, starting from an aerial density of 1.96 kg/m^2 and decreasing to the final value of 0.98 kg/m^2 in just 6 iterations.

However, the F-TPS algorithm may fail to achieve convergence to a viable design configuration when the heat flux reaches excessive levels. This limitation was previously denoted by the symbol $FLAG_{F-TPS}$ in Equation 5.2. An example of a failed optimization, unable to converge, is also depicted in Figure 6.8. In this case, the solution rapidly diverges towards higher values of the objective function compared to the initial starting point. This behaviour arises from the algorithm's attempt to compensate for the elevated heat flux and heat load by increasing the thickness and aerial density of the F-TPS layers. It is worth noting that, as a frame of reference, 10 iterations roughly correspond to 120 function evaluations. Therefore, the optimization process can become computationally expensive, particularly when fmincon fails to discover a feasible solution. To expedite the computation, it is advisable to introduce a maximum iteration limit.

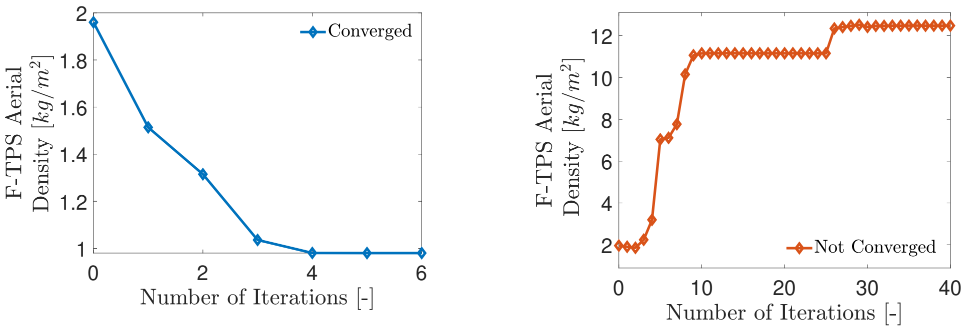

(a) Converged F-TPS optimization (b) Not Converged F-TPS optimization

Figure 6.8.: Variation of F-TPS aerial density with number of fmincon iterations

The thickness resulting from the converged F-TPS problem in Figure 6.8 is given in Table 6.5 along with the maximum temperatures reached by each layer. As desired, the input thicknesses are minimised within the bounds while still satisfying the constraints of the maximum allowable material temperature set in section 3.8. It is also interesting to note that a rather small temperature difference exists between the maximum experienced by the first and second layer, as well as the fourth and fifth. This is mainly a consequence of the large difference in thickness in Table 6.5. While the pyrogel layers appear to absorb most of the heat, the outer layers are responsible for the re-radiation and the innermost ones for delaying the heat soak.

The temperature distribution experienced by each layer is plotted in Figure 6.9 across the entire simulated trajectory. From the coloured area beneath each curve, it is evident that the first and second layers almost experience the same temperature, as previously identified in Table 6.5. A similar conclusion can be made on the fifth layer, which only represents a slight portion of the graph above the 6th layer. All the layers follow the same overall trends associated with the heat flux curve. A peak is measured slightly before 100 seconds, although this is first manifested on

F-TPS Layers	1: SiC	2: SiC	3: Pyrogel	4: Pyrogel	5: Kapton	6: Kapton
$L[mm]$	0.25	0.25	1.52	1.52	0.01	0.01
T_{max} $[K]$	1321.8	1321.4	1064.3	939.9	733.9	732.1

Table 6.5.: Thickness and maximum temperature of optimized F-TPS layers

the outermost layers and then slightly delayed for the inner ones. The design of the F-TPS is thus suitable for the intended purposes and satisfies the temperature requirements for the onboard electronics and payload as the temperature does not exceed 300 K for the bondline layer and all layers are within their maximum margins.

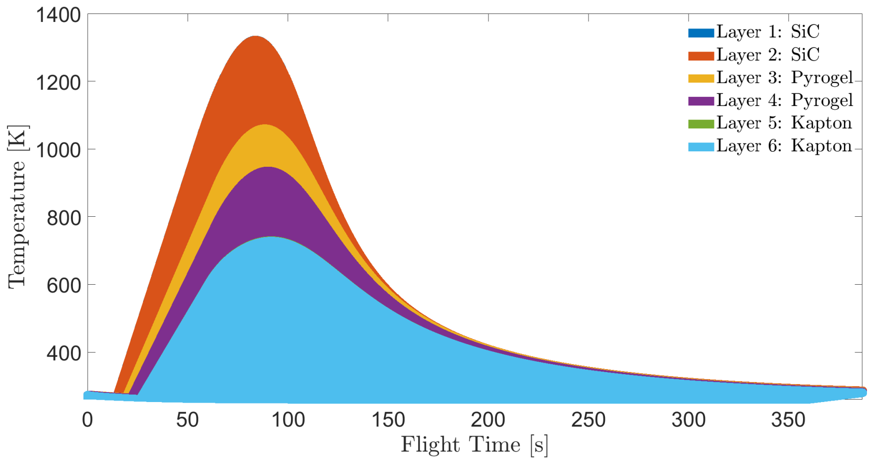

Figure 6.9.: Temperature profile across F-TPS layers throughout entry trajectory

6.2. Trajectory of Optimised Stacked-Toroid

The entry trajectory of the modified MiniPINS mission with the optimised stacked-toroid design in Figure 6.7 is plotted in Figure 6.10. For reference, the baseline trajectory with the capsule plotted in Figure 5.7 based on the MetNet heritage is also shown in Figure 6.10, with a lower entry velocity due to the MetNet mission requirements. For a fairer comparison, both trajectories are ballistic in nature, as $\alpha = 0°$, thereby not generating any lift.

The comparison reveals that despite the harsher entry requirements, the stacked toroid reaches a maximum dynamic pressure at higher altitudes and decelerates the vehicle more effectively. The increased aerodynamic braking, responsible for the deployment at higher altitudes is due to increase in inflated diameter by 80% when compared to the 1 m MetNet capsule. In fact, the MetNet capsule has comparable drag coefficients (0.96-1.14 in subsonic and 1.39-1.41 in supersonic [96]) to those discussed in Figure 6.13. The deployment of the second stage occurs at approximately 14 km from the datum sea level altitude when $M_\infty = 0.8$. This compensates for the reduced dynamic pressure differential between the two EDL stages compared to MetNet. Increasing the deployment altitude by over 10 km as a result of the stacked toroid's higher drag levels during descent, brings advantages such as the ability to select landing sites at higher altitudes, improved communication with the mothership during descent and landing and increased margin for redirection in case of anomalies. More importantly, accurate terrain mapping can be conducted prior to emplacing the penetrating probe. One important consideration for the higher altitude deployment is the potential decrease in freestream temperature, which could be as much as 20 K lower according to Figure 3.9. Therefore, it is needed to conduct a heat management analysis for the onboard electronics to ensure their proper functioning and avoid any adverse effects. A final landing speed of 80 m/s is attained, which corresponds to the upper bound of the desired landing speed in order for the penetrator to reach the desired penetration depth. Therefore, the trajectory of the optimised design already appears to satisfy the constraints imposed, thereby affirming the validity of the proposed solution.

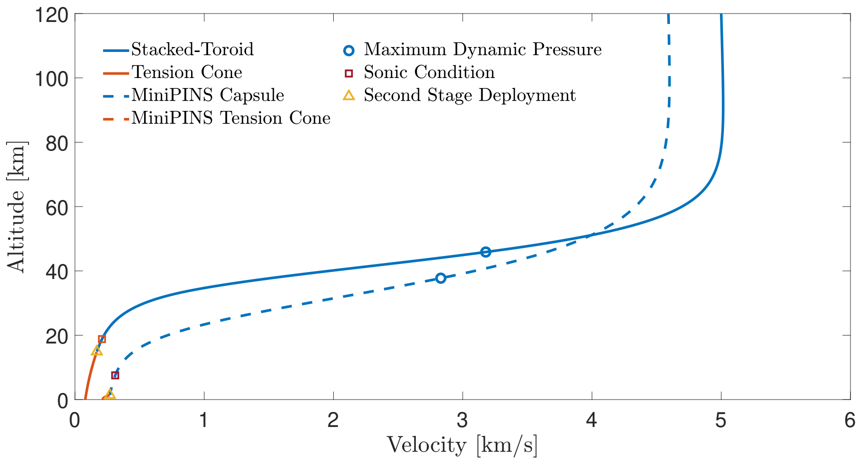

Figure 6.10.: Comparison of modified MiniPINS EDL trajectory with its baseline profile

The correct deployment of the second stage is also depicted in the supplementary trajectory plots in Figure 6.21. The Mach number profile, shown as a function of altitude, shows that the vehicle enters the Martian atmosphere at hypersonic speeds, with $M_\infty = 25$. The value slightly increases to $M_\infty = 27$ within the first 30 km as a consequence of the decrease in temperature and thus the speed of sound. Most of the aerodynamic braking occurs in the descent phase between 60 km and 30 km, where the Mach number is reduced from 24 to 3. The supersonic phase ($1 < M < 5$) is initiated at approximately 35 km, whereas $M = 1$ is reached at about 19 km.

Deployment of the second stage occurs at 14.4 km when the Mach number reaches a value of 0.8. The deployment altitude is considered sufficiently large for the tension cone to stabilise itself and ensure complete separation from the stacked-toroid. Furthermore, the higher deployment altitude than the initial MiniPINS preliminary EDL design allows for landing at higher sites, should the datum sea level altitude be increased by a few kilometres. The suitability of the deployment is also clear from the plot of the flight path angle, showing that the penetrator attains a value of $-90°$ at the datum sea level altitude when it collides with the ground.

Moreover, from the plot of the downrange in Figure 6.21, the stacked-toroid is observed to travel a total of 558 km in downrange, whereas the tension cone contributes to a further 2 km. This further highlights that sufficient ground distance exists between the two EDL stages to allow for a complete separation. Finally, the g-load is also plotted in Figure 6.21, reaching a peak of 21.7.

Given that the mission is unmanned, the value is considered acceptable, especially as no direct requirements were given on this parameter.

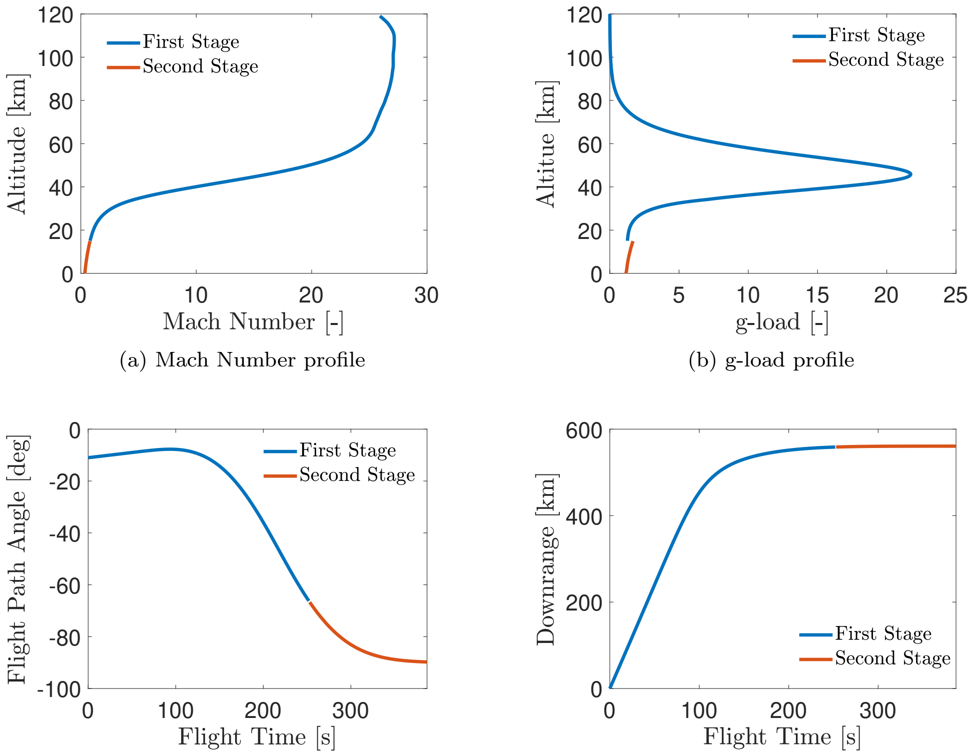

(a) Mach Number profile

(b) g-load profile

(c) Path Angle profile

(d) Downrange profile

Figure 6.11.: Optimised Stacked-Toroid Flight Dynamics EDL Trajectory

The three structural models used as constraints in Equation 5.6-5.8 to ensure the adequacy of the chosen materials are plotted for the whole trajectory in Figure 6.12, and the peak values are listed in Table 6.6. The toroid and spar fabric loads follow the profile of the aerodynamic drag, given the dependency on inflation pressure required to counteract the aerodynamic loading, whereas the restraint wrap load is a function of the g-load in Figure 6.21. The spar fabric loads are the largest ones, followed by the restraint wrap and finally, the toroid fabric. This suggests that most attention should be given to the design and manufacturing of the spar fabric.

$\sigma_{toroid,max}$ $[Pa]$	$\sigma_{spar,max}$ $[kPa]$	$\sigma_{wrap,max}$ $[kPa]$	σ_y $[GPa]$
377.5	1.869	1.073	3.0

Table 6.6.: Maximum aerodynamic stress on optimised Stacked-toroid structures

Nevertheless, the chosen material has a yelid strength of 3 GPa: 3-4 orders of magnitude higher than the maximum stresses predicted. This ensures the vehicle's safe loading, although the simplified expressions may underestimate the loads. In both cases, the optimization successfully met the constraints.

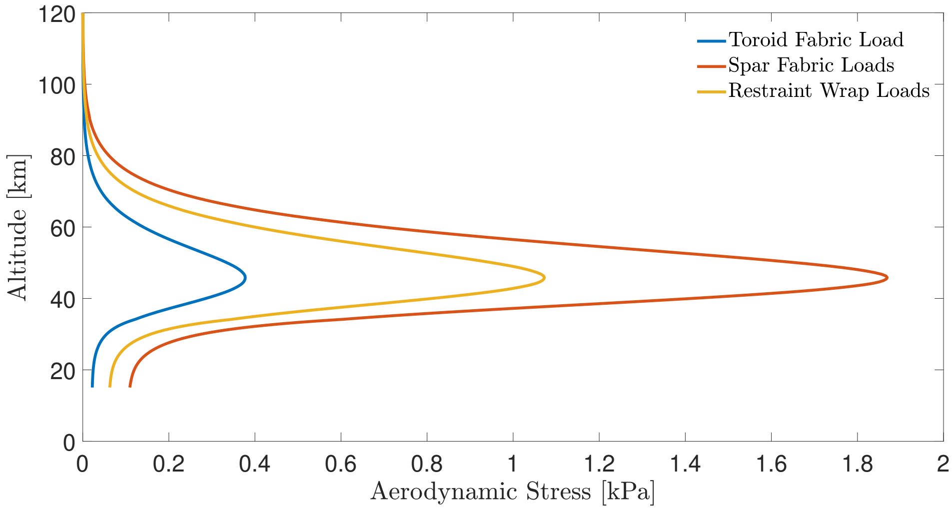

Figure 6.12.: Structural stress perceived by the Stacked-toroid throughout the Mars entry trajectory as a consequence of aerodynamic loading

An overview of the optimised vehicle's trajectory parameters is presented in Table 6.7. It is interesting no note that the pressurant tank, with a diameter of 0.11 m, is smaller than the payload diameter, defined by the penetrator as 0.3 m. Thus, the constraint in Equation 3.2 is satisfied by the optimizer and sufficient marings are available for structural elements.

Trajectory Parameter	Symbol	Value	Unit
Flight Time	t	387	$[s]$
Downrange	R	560.6	$[km]$
Max Dynamic Pressure	q_{max}	622.8	$[Pa]$
Deployment Altitude	$h_{deployment}$	14.4	$[km]$
Max g-load	$\bar{g}$	21.7	$[-]$
Continuum Regime Boundary	h_{cont}	90.6	$[km]$
FMF Regime Boundary	h_{fmf}	128.9	$[km]$
Max Inflation Pressure	$p_{inflation}$	6.4	$[kPa]$
Tank Radius	r_{tank}	56.8	$[mm]$

Table 6.7.: Overview of trajectory parameters for optimised stacked-toroid

6.2.1. Aerodynamic Performance

The aerodynamic performance of the optimised parametric stacked-toroid throughout its entry and descent phases is characterised by the drag force, having regarded the MiniPINS trajectory as being ballistic. The drag coefficient is therefore plotted in Figure 6.13.As expected, a larger drag coefficient is attained in the transitional regime, which is bridged from the FMF one. The assumption of regarding the velocity in the FMF regime as being constant prior to entering the atmosphere, and thus $V_{\infty,FMF} = V_e = 5\ km/s$ leads to a drag coefficient of 1.7, while the bridging predicts a value of 1.66.

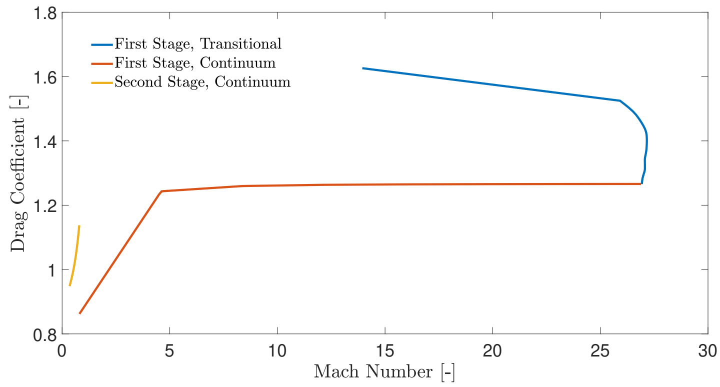

(a) Drag coefficient of both EDL stages

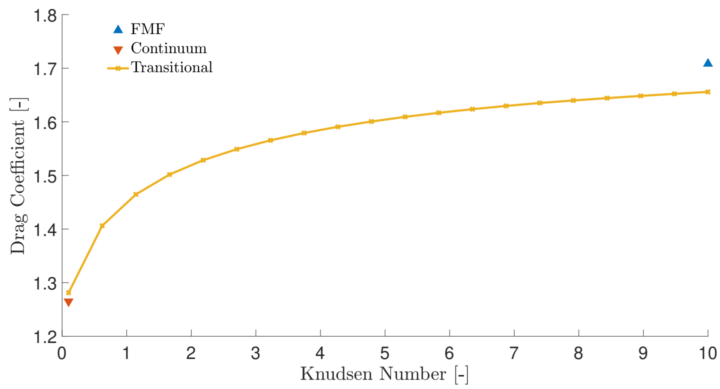

(b) Aerodynamic bridging of stacked-toroid

Figure 6.13.: Aerodynamic performance of optimised parametric stacked-toroid

The fitted curve in the transitional regime, however, appears to be suitable for predicting the aerodynamic forces in this regime. The drag coefficient in the continuum regime, on the other hand, is found by leveraging on the mach independence of the modified Newtonian method at speeds larger than Mach 10. By assuming any Mach value for which $M > 10$ prior to running the trajectory simulation, the bridging in the continuum regime is established. A bridged drag coefficient of 1.28 is given, while the modified Newtonian method predicts 1.26. The mach independence is visible in the continuum regime, where a curve with an approximately constant $C_D = 1.26$ is found between $10 \leq M \leq 27$, though only a very slight decrease is noted until $M = 5$. Conversely, a sharp decrease in C_D is computed in the supersonic and subsonic regime until the second stage is deployed, following the drag profile in Equation 5.1. A comparable pressure distribution over the IAD is attained at differed altitude (see Figure B.13).

The quantification of the drag contribution arising from the flexible deflection of the decelerator's surface is evaluated in Figure 6.14, where the ΔC_D is plotted as a function of Mach number. Interestingly, the contribution is most significant towards the higher end of the hypersonic spectrum, approximately at Mach 26-27. Contrary to previous expectations, the deflection is modelled to be most influential in the rarefied regime, where the dynamic pressure is lowest, also shown in Figure 6.14. A maximum contribution of about 5% is yielded in this region, whereas contribu-

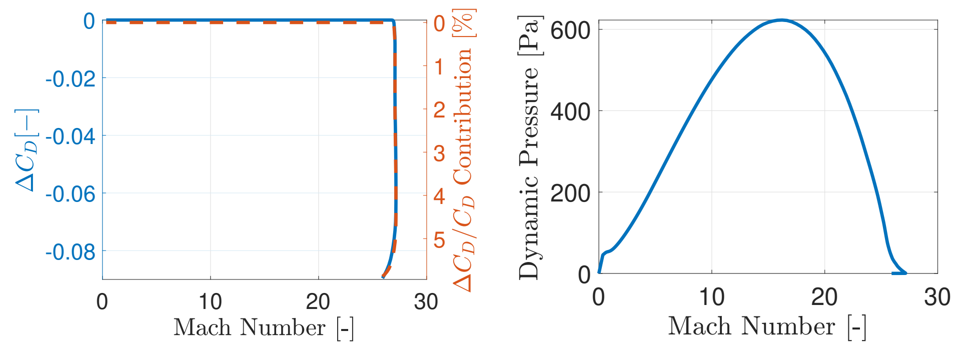

(a) Drag coefficient contribution due to decelerator deflection

(b) Dynamic pressure profile

Figure 6.14.: Aerodynamic performance due to flexibility of aeroshell

tions approaching 0% are identified for the rest of the trajectory. While the reduced percentage contribution is reasonable, the presence of a significant ΔC_D only at Mach 26-27 may suggest that further modelling is required to accurately capture the behaviour of the aeroshell deflection and its implications on the aerodynamic performance.

To estimate the CoP of the decelerator, the modified Newtonian method is used in conjunction with Equation 3.73 at $\alpha = 0°$. Given the absence of a CoG in the available configuration of MINS, the resulting CoP of $y_{CoP} = 0.1731\ m$ from the nose-cone is used to provide a feasibility region of the CoG. Figure 6.2.1 illustrates possible design configurations of the CoG and the corresponding SM values. A maximum SM of 21.63% is attainable in the best-case scenario, assuming that the CoG is located at the nose-cone, which is rather impractical. However, a standard SM of 15% is viable by assuming a CoG location of approximately 0.05 m along the penetrator's principal axis. Such a configuration is illustrated in Figure 6.2.1.

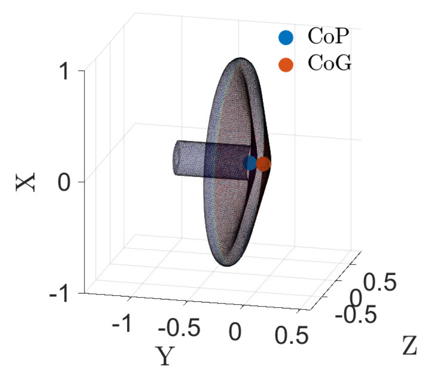

Figure 6.15.: CoG position for $SM = 15\%$

y_{CoP} $[m]$	y_{CoG} $[m]$	SM $[\%]$
0.1731	0.1331	5
0.1731	0.0931	10
0.1731	0.0531	15
0.1731	0.0131	20
0.1731	0	21.63

Table 6.8.: MINS CoG location for positive SM

The roll, pitch and yaw moment coefficients about the nose-cone are plotted in Figure 6.16(a) as a function of altitude. As expected, the coefficients are rather small as the stacked-toroid is symmetric about the XY plane and because of the point about which the moments are taken. Furthermore, the pitch and yaw moments appear to produce almost identical results due to the symmetry of the vehicle at $\alpha = 0°$. On the other hand, the roll coefficient appears to be significantly larger than the other two. By assuming the position of the CoG as depicted in Figure 6.2.1, the roll coefficient about the CoG is plotted in Figure 6.16(b), where the magnitude has increased significantly due to the second term in Equation 3.44. In fact, the profile of C_l as a function of altitude is comparable to the drag coefficient variation in Figure 6.13.

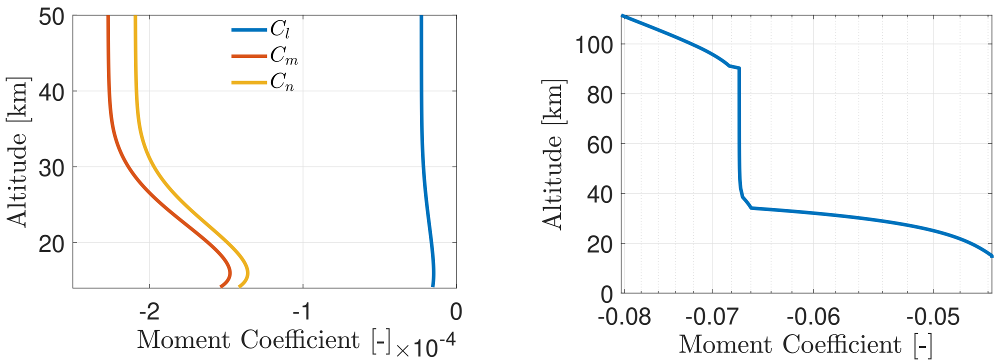

(a) Moment coefficients about Nose-cone

(b) C_l about CoG ($y_{CoG} = 0.0531\ m$)

Figure 6.16.: Moment coefficients throughout the trajectory

The variation of the moment coefficients for the proposed CoG location is plotted in Figure 6.17 at two different altitudes, namely 30 and 50 km. However, the moment coefficients are almost identical at different trajectory locations. While the magnitude of the yawing coefficient C_n increases with variations in α, though rather small in magnitude, both the roll and pitch coefficients show a decrease with an increase in α. This signifies that the pitch coefficient is longitudinally statically stable as $\frac{\partial C_m}{\partial \alpha} < 0$. At the same time, the variation of sideslip is investigated. The roll coefficient shows the same behaviour as with the variation for α given the symmetric planform of the IAD. At the same time, the C_n and C_m exhibit the same characteristics in Δ_s as for $\Delta\alpha$ but inverted for the very same reason. It is observed that also $\frac{\partial C_n}{\partial_s} < 0$, confirming the longitudinally static stability of the yawing moment.

6.2.2. Aerothermodynamic Performance

The aerothermal performance analysis of the optimized stacked-toroid configuration focuses on the transient heat flux experienced by the vehicle and its integrated heat load along the trajectory. The heat flux profile at the stagnation point of the decelerator is depicted in Figure 6.18, illustrating the transitional and continuum flow regimes. The highest heat flux peak is observed at an altitude of 53.9 km above sea level, occurring 82 seconds into the descent, precisely within the continuum regime, which necessitates appropriately sizing the F-TPS. This peak heat flux corresponds to a convective heat flux value of approximately 142 kW/m^2.

In contrast, the peak radiative heat flux is observed approximately 18 seconds later, with a magnitude of only $5.7kW/m^2$, as indicated in Table 6.9. This signifies that the radiative heat's impact is relatively minor, accounting for roughly 4% of the peak convective heating. Furthermore, due to the time difference between the two peak heating events, the total heat flux does not equal the sum of the individual peaks; instead, it reaches approximately 144 kW/m^2. The total heat load is also given in Table 6.9, which is fed to the F-TPS inner optimizer to yield the

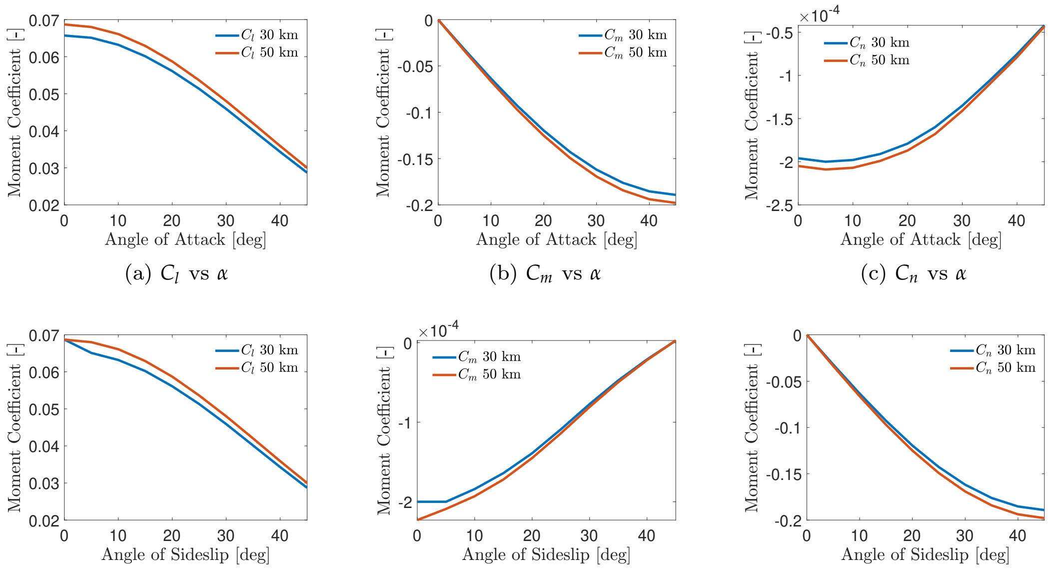

(a) C_l vs α (b) C_m vs α (c) C_n vs α

(d) C_l vs β_s (e) C_m vs β_s (f) C_n vs β_s

Figure 6.17.: Variation of moment coefficients about the CoG ($y_{CoG} = 0.0531\ m$) with α and β_s

temperature profile plotted in Figure 6.9. The feasibility identified by fmincon is thus justified, since the F-TPS has been tested for heat fluxes up to 500 kW/m^2 [30].

The heat flux in the transient regime in Figure 6.18 appears to be modelled correctly, though an offset exists at both the FMF and continuum points. With a convective heat transfer coefficient of 0.9877 in FMF and 0.0045 in the continuum regime, the heat flux is found to be 0.4 and 28 kW/m^2 respectively. However, due to the offset, a uniform profile is maintained at the 25th second of flight, which corresponds to the interface between the transitional and continuum regimes. The discrepancy is attributed to the assumption of having assumed Mach independence for the bridging parameter in the continuum regime. Nevertheless, this deviation is considered insignificant since it occurs far from the peak heat location.

$q_{c_{max}}$ $[kW/m^2]$	$q_{r_{max}}$ $[kW/m^2]$	$q_{tot_{max}}$ $[kW/m^2]$	$Q_{c_{max}}$ $[MJ]$	$Q_{r_{max}}$ $[kJ]$	$Q_{tot_{max}}$ $[MJ]$
142.013	5.701	144.132	7.4281	220.60	7.6487

Table 6.9.: Convective, radiative and total heat flux and heat load perceived by EDL system

The distribution of the heat flux across the surface of the optimised stacked-toroid IAD is plotted in Figure 6.19 with and without the correction arising from the onset of turbulence caused by the deflected aeroshell. The radial distribution is also presented in Figure B.7 for the environmental conditions marked in Figure 6.18 as the interface between the transitional and continuum regimes. The stagnation heat flux of 0.28 W/cm^2 at Mach 27 is most conservatively distributed across the aeroshell by the SCARAB formulation. The capability of modelling the laminar and turbulent flow due to the deflection of the conical aeroshell result in lower heat fluxes across the F-TPS. Moreover, the laminar SCARAB-Krasnov solution shows an abrupt change at the

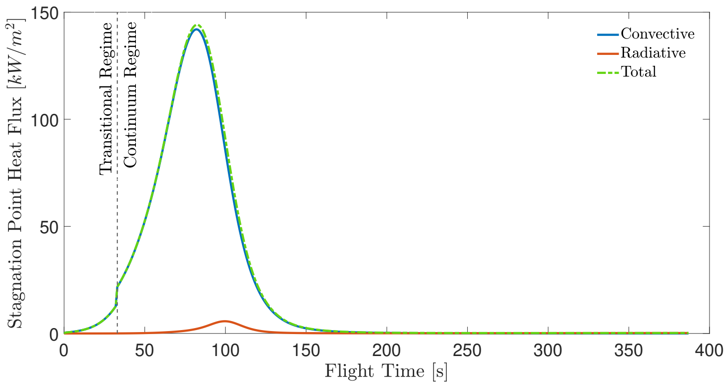

(a) Convective, radiative and total transient heat flux profile

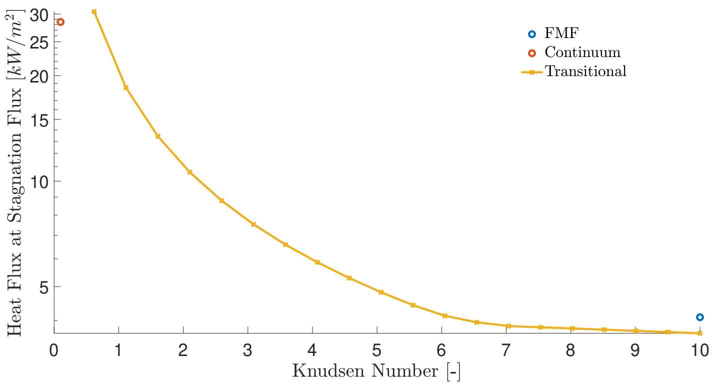

(b) Aerothermal bridging of stacked-toroid

Figure 6.18.: Heat flux profile perceived at the stagnation point of the stacked toroid

interface between the nosecone and the conical aeroshell due to the Levenberg-Marquardt algorithm used to merge the data. The turbulent correction, on the contrary, provides a smoother transition along the aeroshell.

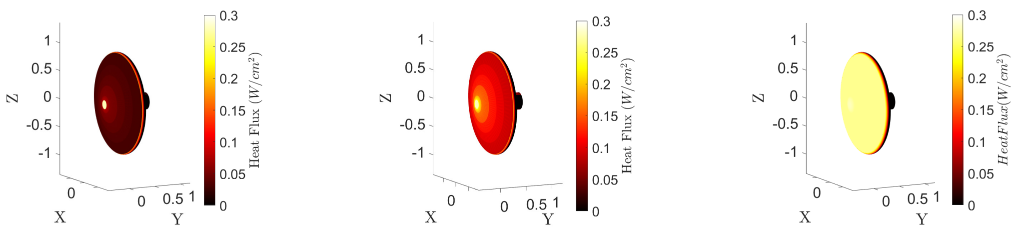

(a) SCARAB-Krasnov Laminar

(b) SCARAB-Krasnov Turbulent ($\beta_{sc} = 20°$)

(c) SCARAB

Figure 6.19.: Heat flux contour plot distribution across optimised stacked-toroid

6.3. Sensitivity Analysis

The optimisation results presented thus far are very much dependent on the optimisation problem described in section 5.6. Specifically, the design space is influenced by the entry conditions defined by the transfer trajectory to Mars, by the attitude of the vehicle and by the environmental characteristics of the atmosphere. To investigate the robustness of the proposed stacked-toroid design with respect to such parameters, a sensitivity study is conducted in which the reference parameters, namely the entry velocity V_E, entry angle Γ_E and atmospheric density, are varied between $\pm$ 20%. The trim angle of attack α is also varied between 0° and 20°.

6.3.1. Entry Conditions

Entry Velocity

Table 5.2 delineates the entry speed requirements for a parabolic entry trajectory under R-01. A nominal entry speed of 5 km/s is, in fact, defined. However, in addition to uncertainties or potential anomalies that could alter the probe speed following separation from the mothership, it may also be preferred to undergo a hyperbolic trajectory in which the entry velocity would be in the orders of $V_E \sim 6\ km/s$. Such considerations are hereby addressed by investigating the trajectory and performance variation of the optimised IAD in Figure 6.7 when $4\ km/s \leq V_E \leq 6\ km/s$ as depicted in Figure 6.20.

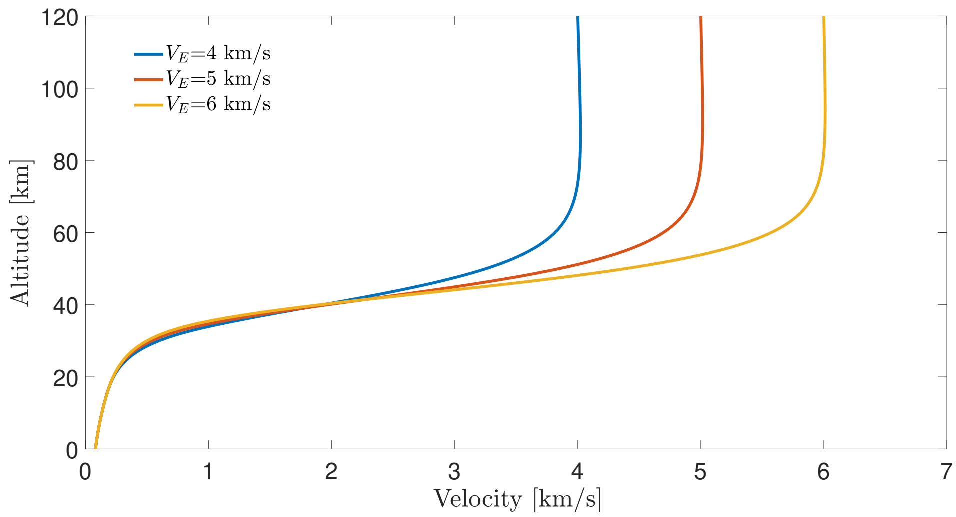

Figure 6.20.: Plot of entry trajectory with different entry velocities

The resulting entry trajectory clearly reveals the difference in velocity at high altitudes, where the atmosphere is more rarefied and aerobreaking occurs at a much lower rate than at lower altitudes. The difference between the trajectories with different speeds, however, becomes less pronounced as the vehicle starts to decelerate and becomes negligible below an altitude of approximately 40 km. Remarkably, the stacked-toroid is capable of compensating for the larger or lower entry speed by withstanding the corresponding larger or lower decelerations. In fact, both the impact speed of the penetrator and the deployment altitude of the second stage remain unchanged across the three trajectories. The increase or decrease in g-load, on the other hand, is substantial with respect to the reference case with $V_E = 5\ km/s$, with increases of 21.2% for the high-speed case and a decrease of 19.86% in the low-speed scenario, showing a direct dependency between the maximum g-load and entry speed.

The variation in g-load is plotted in Figure 6.21 for the three trajectories, along with the heat-flux, dynamic pressure and downrange profiles. In the case of the g-load, heat-flux and dynamic pressure, the curves follow a similar profile with respect to altitude. The increase or decrease of entry speed is directly linked to the increase or decrease of such quantities. However, the difference is not only in maximum magnitude, but also in the time of occurrence. In fact, the higher speeds cause the vehicle to be subjected to the peak dynamic pressure, heat flux and g-load at higher altitudes.

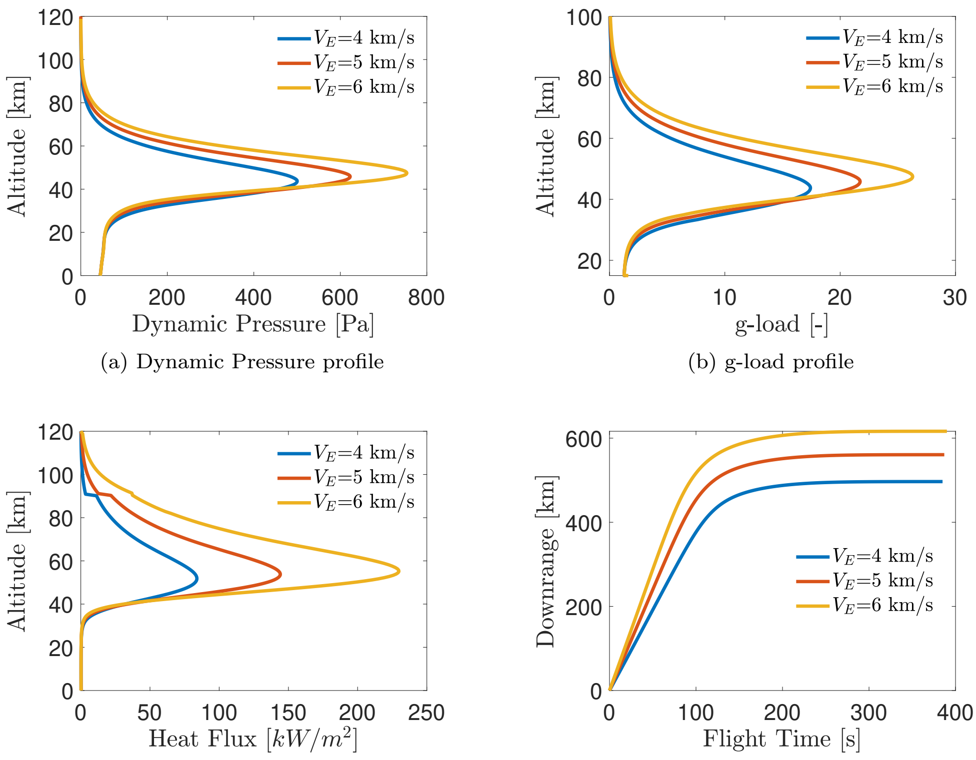

(a) Dynamic Pressure profile

(b) g-load profile

(c) Heat Flux Profile

(d) Downrange profile

Figure 6.21.: Sensitivity analysis of entry velocity on trajectory plots

While the percentage variation in g-load is linear with speed, similarly to the dynamic pressure that changes from -19.61 % to +21.05 % with $V_E = 4\ km/s$ and $V_E = 6\ km/s$, the change in heat flux is non-linear. In fact, an increase in heat flux by 59.4% is recorded for an increase in entry speed of 20% which then results in a heat load increase of 53.13%. On the contrary, a reduction in entry speed by 20% is associated with a reduction in heat flux by 64% and heat load by 40%. Although less affected by the entry speed, changes in downrange in the order of -16% and +10% are shown, whilst the total flight times only vary by a couple of seconds.

The results from the sensitivity analysis reveal that the optimised stacked-toroid design is effective in compensating for different entry speeds and that no major geometrical design variations are needed. Based on the assumption that stacked-toroids can withstand higher dynamic pressures and heat fluxes, the vehicle is suitable for hyperbolic entries or low-speed entries. However, the F-TPS and structural design would need to be further analysed for increased or decreased loading conditions, which would result in a variation in system mass. This may involve incorporating stronger structural elements or employing active systems for load management in case of excessive heat fluxes. However, the F-TPS employed should be capable of withstanding up to 50 W/cm^2.

Since no requirements on the downrange were retrieved for the MINS mission, the downrange is not considered of high importance for the current case study. Nevertheless, for missions where the landing location is indicated as a requirement, the variation of downrange as a consequence of the entry speed could be accounted for by implementing appropriate guidance and control systems to ensure accurate targeting and landing. Though the flight time increment is of a few seconds, it is essential to ensure that the IAD's power systems and critical subsystems are capable of operating reliability for the extended duration of time observed.

Entry Angle

In addition to investigating variations in entry velocity, changes of ±20% the nominal entry angle defined in Table 5.2 (R-02) are hereby addressed. This is useful in evaluating the robustness of the trajectory and the viability of the optimised design under different entry conditions. Angles of $\Gamma_E = -8.8°$ and $\Gamma_E = -13.2°$ are used to complement the reference $\Gamma_E = -11°$. The typical altitude-velocity curve is plotted in Figure 6.22 with varying entry angles.

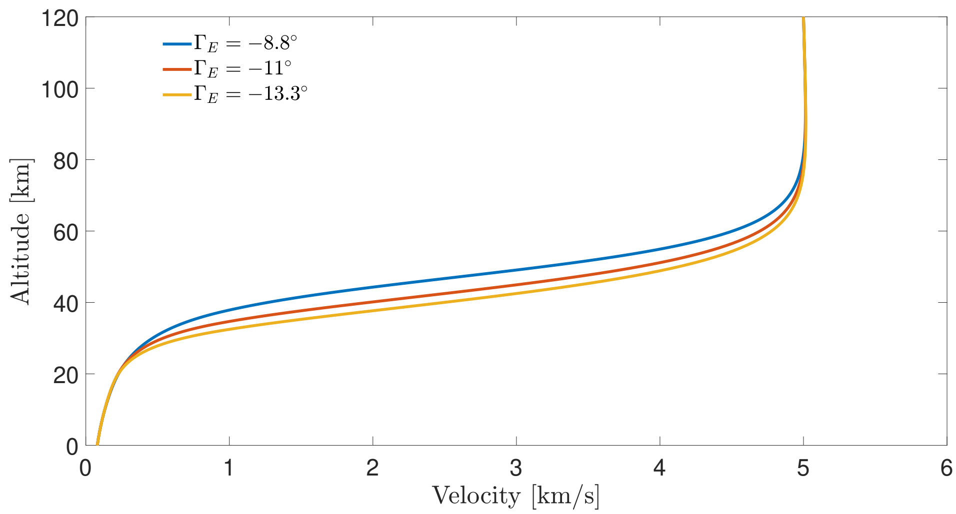

Figure 6.22.: Plot of entry trajectory with different entry angles

The most evident variation occurs in the descent phase between 80 and 30 km, where most of the aerobraking occurs. In fact, the trajectory with a steeper angle slows down at lower altitudes than the one with a shallower angle. Interestingly, all curves reach the same landing speeds and landing configurations. The effects of the entry angle are more noticeable on the curves plotted in

Figure 6.23. When the magnitude of the negative entry angle is decreased by 20% to $\Gamma_E = -8.8°$, the maximum heat flux is decreased by about 20% whilst the flight time is increased by 19%. The two counteracting effects result in an increase in heat load by 22%, since the flight time increase is more dominant than the decrease in maximum heat flux. This is also due to the significant increase in downrange by 40%, showing that further distance is covered by the reduction in Γ_E. Conversely, the g-load experiences a decrease of roughly 40% which is a substantial benefit for the mechanical subsystem. Differently from the variation in entry velocity, the time of occurrence of the peak dynamic pressure, heat flux and g-load occurs at lower altitudes with increasingly negative entry angles.

At the same time, when the magnitude of the entry angle is increased to $\Gamma_E = -13.2°$, the increase in g-load is still observed, but only by 32%, in alignment with the increase in dynamic pressure. The other quantities show a reduced amount of variation, with the downrange decreasing by 20% and flight time and heat load by 10-12%. This reveals that a reduction in magnitude in Γ_E causes a greater variation in the performance parameters of the vehicle. The increased heat load for the reduction in Γ_E may require a thicker F-TPS and a larger structural contribution to withstand the aerothermodynamic environment. Overall, the optimised vehicle satisfied the requirements in Table 5.2 for increasing or decreasing entry angles, but necessitates further analysis once a trajectory is fully defined.

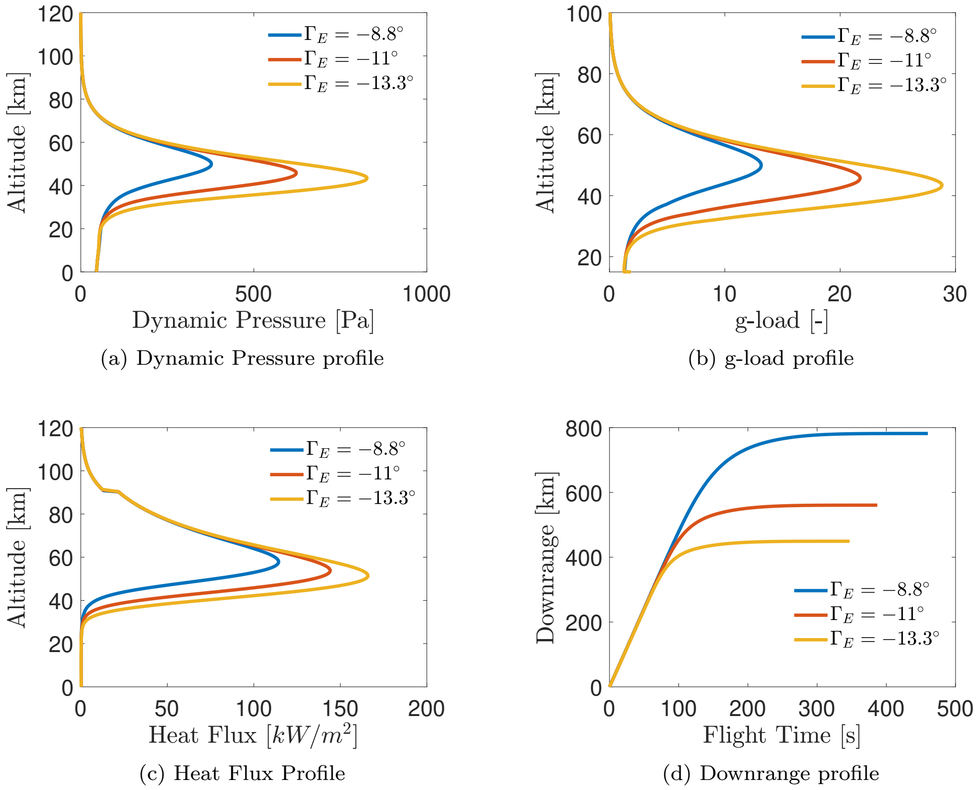

(a) Dynamic Pressure profile

(b) g-load profile

(c) Heat Flux Profile

(d) Downrange profile

Figure 6.23.: Sensitivity analysis of entry angle on trajectory plots

Trim Angle of Attack

The trajectory optimization for the stacked-toroid applied to the MINS penetrator initially assumed a flight without any angle of attack. However, it is important to acknowledge that the presence of an incidence angle with the flow can have tangible effects, whether intended or not. In the latter case, flow disturbances may influence the trajectory, while in the former case, an intentional CoG offset is employed to generate lift and enhance the vehicle's controllability for precise landing at a targeted location. Successful implementation of this approach has been demonstrated by IRVE-3 [102], and it is further advocated by the planned mission IRVE-4 which was never flown [270].

Moreover, the deflection of the aeroshell has been found to generate lateral CoG offsets that resulted in an increase in the trim angle of attack [102]. Instead of varying the reference parameter by ±20% as for the previous instances, the intervals of $\alpha = 5°, 10°, 20°$ are investigated. This is firstly done because the reference angle is $\alpha = 0°$, but also because a negative angle would generate the same results given the symmetry of the decelerator. The interval is chosen based on IRVE-3's flight, which varied its configuration from a trim angle of attack of 8° up to 16°. The entry trajectory, shown in Figure 6.24, is hence varied from ballistic to gliding entry. The variation in the altitude-velocity profile, however, appears to be almost negligible.

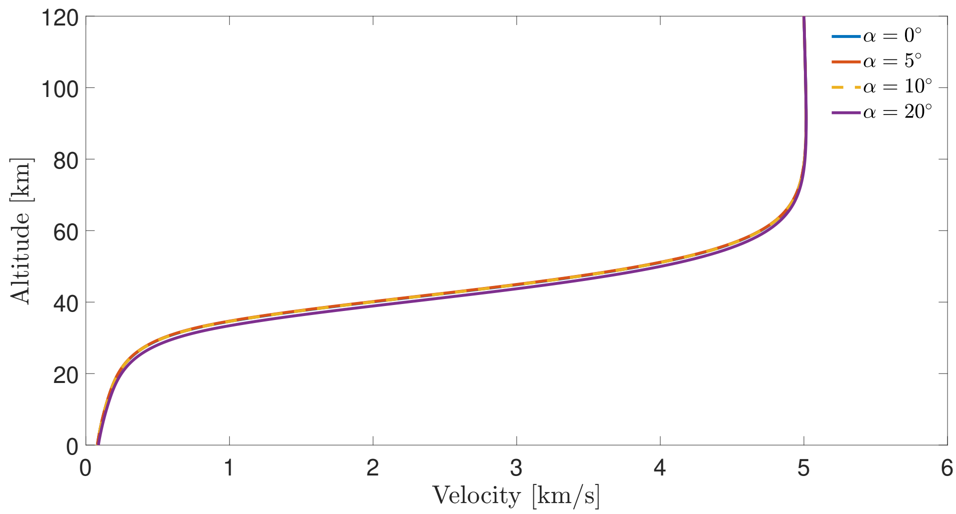

Figure 6.24.: Plot of entry trajectory with different trim angles of attack

An interesting exception arises regarding the deployment altitude of the second stage, which exhibits a decrease with angle of attack, reaching as low as 13.4 km for $\alpha = 20°$. Correspondingly, the associated impact speed shows an increase to 81.7 m/s for $\alpha = 10°$ and 87.1 m/s for $\alpha = 20°$. However, it is worth noting that these values do not align with the requirement R-03, which necessitates an impact speed below 80 m/s. Furthermore, the elevated shock impact resulting from higher impact velocities could potentially jeopardize the integrity of the penetrator. To address this concern, the optimization process should take into account the presence of a non-zero trim angle of attack. This consideration is likely to yield a larger IAD, leading to a decrease in the impact velocity. Alternatively, it may be necessary to employ a stronger penetrator to withstand the increased impact forces.

The effects of the trim angle of attack become more pronounced in the trajectory plots in Figure 6.25 for $\alpha = 20°$ in dynamic pressure, heat flux and heat load. In fact, while the downrange, g-load and flight time show differences below 5%, the maximum dynamic pressure increases by 15% and the heat flux and heat load by about 8%. The small variations reveal that the vehicle maintains an approximately uniform performance at low angles of attack ($\alpha < 10°$). The increasing structural and thermal loadings should be within the design margins but could be further mitigated by implementing stronger materials and a thicker F-TPS. Given the relatively low variations observed in trajectory performance, in conjunction with the increased benefit of precise landing introduced by a non-zero trim angle of attack, the current design appears feasible. However, the variations in impact speed should be addressed to ensure the survivability of the penetrator.

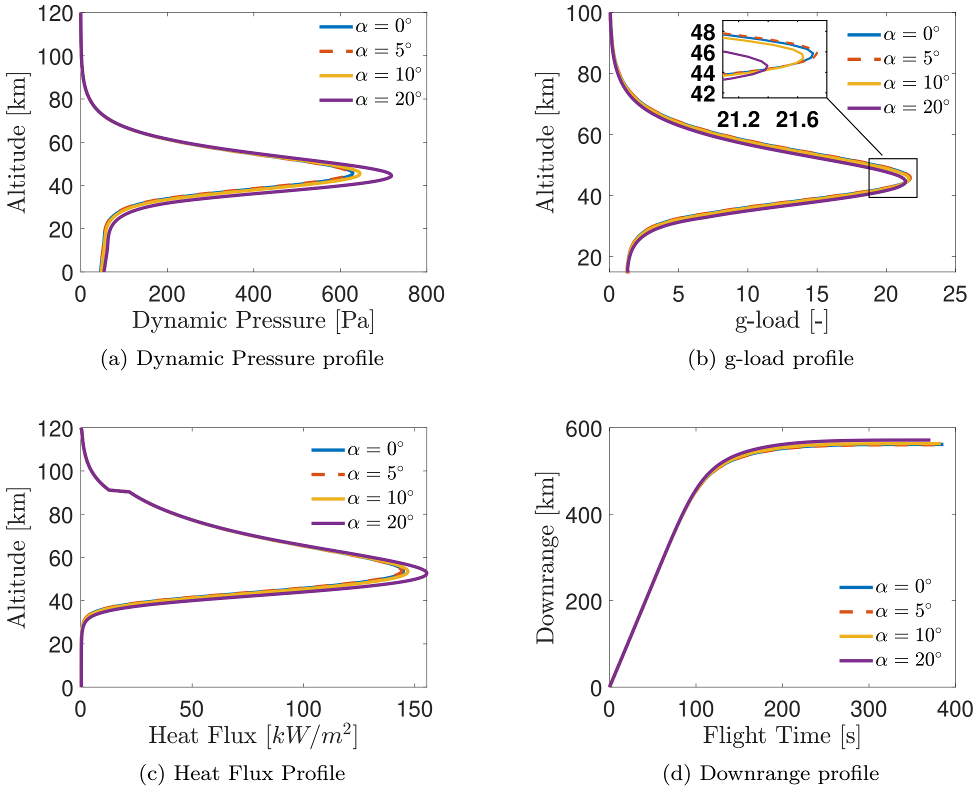

(a) Dynamic Pressure profile

(b) g-load profile

(c) Heat Flux Profile

(d) Downrange profile

Figure 6.25.: Sensitivity analysis of trim angle of attack on trajectory plots

6.3.2. Atmospheric Variation

The last quantity investigated to assess the robustness of the optimised solution in the proposed environment is the atmospheric density. As identified by Brune et al. [238], the freestream density is amongst the most significant parameters affecting the flow over stacked-toroids for Mars entry. The importance of atmospheric density uncertainty was also highlighted by Dillman [39] in the deviations of IRVE-II flight reconstruction profile compared to its planned trajectory.

The atmospheric model used for the baseline optimisation was based on the averaged atmosphere across longitudes and latitudes for an entry date of 01-01-2028 with local time of 12:00 UTC. However, given the preliminary phase of the mission, the mission date is still undefined. Therefore, it is likely that the IAD will experience varying atmospheric conditions. This is even more pronounced with the variation of the solar cycle, which can result in increasing or decreasing atmospheric density, and dust storms that can increase the density. A ±20% change in freestream density from the nominal mission is applied as shown in Figure 6.26.

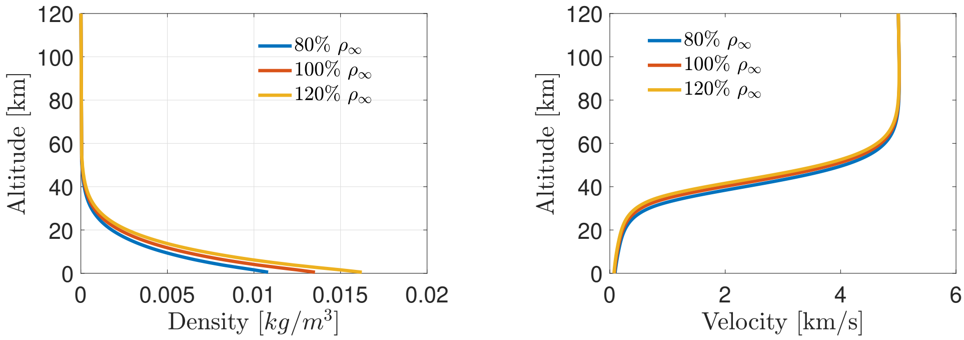

(a) Density profile

(b) Entry trajectory

Figure 6.26.: Plot of entry trajectory for different density profiles

The various curves seem to be shifted based on changes in density. As expected, the entry phases are least affected by variations due to the low density at high altitudes. However, the differences become more pronounced as the altitude decreases and the density increases. This is especially evident in the deployment altitude of the second stages, which changes from 12.9 km for reduced density to 16.5 km for higher density. It demonstrates that the optimized stacked-toroid design allows for higher deployment altitudes in the case of lower densities.

However, the impact velocities are 90.5 m/s and 72.6 m/s for lower and higher densities, respectively. According to R-01 in Table 5.2, the higher-density case complies with the desired landing speed within the specified limits. Conversely, the low-density case results in an impact speed that exceeds the MINS requirements. This suggests that the optimized design is robust against increased density levels but vulnerable to low densities. To address this, an improved version could establish the objective landing speed at 70 m/s, allowing for a greater margin on the upper bound at the expense of the lower bound. A careful trade-off must be made in conjunction with a more accurate estimation of the atmospheric profile once the interplanetary trajectory and mission date are fully defined. Further insight into the density variations is drawn from Figure 6.27, where it is visible that the trajectories maintain their original profile and only exhibit variations lower than 3-6%.

The results of the sensitivity analysis, listed in Table 6.10, provide valuable insights into the performance of the optimized stacked toroid under different scenarios. Overall, the analysis indicates that the design is robust and capable of accommodating variations in entry conditions and atmospheric density. The majority of the investigated cases demonstrate the suitability of the optimized stacked toroid for a wide range of mission characteristics. It successfully adapts to varying entry conditions and maintains desired performance levels. However, it is worth noting that a few cases exhibit impact speeds that exceed the permissible limits set by the MINS

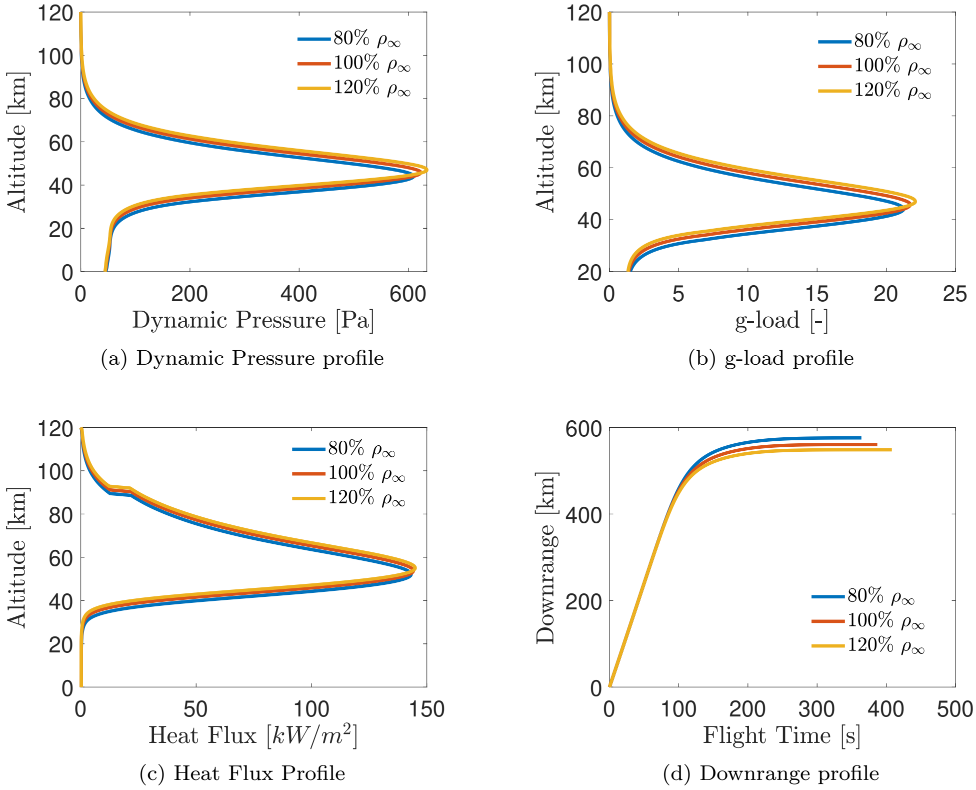

(a) Dynamic Pressure profile

(b) g-load profile

(c) Heat Flux Profile

(d) Downrange profile

Figure 6.27.: Sensitivity analysis of atmospheric density trajectory plots

penetrator. While these instances indicate the design's limitations in specific scenarios, they do not undermine its overall viability. With careful trade-offs and detailed design refinement, these cases can be addressed to ensure the optimized stacked toroid meets the necessary requirements for a variety of missions. The robustness of the design serves as a testament to its effectiveness in withstanding variations in entry conditions and atmospheric density. This resilience showcases the advantages of stacked-toroid IADs when compared to more conventional EDL technologies that would be subject to further constraints concerning the deployment conditions, maximum dynamic pressure and heat loads experienced.

Parameter	Reference	$V_E = 6\ km/s$	$V_E = 4\ km/s$	$\Gamma_E = -13.2°$	$\Gamma_E = -8.8°$	$\alpha = 5°$	$\alpha = 10°$	$\alpha = 20°$	$0.8 \times \rho_\infty$	$1.2 \times \rho_\infty$
$V_I\ [m/s]$	80	80.0	80.0	80.0	80.1	80.4	81.7	87.1	72.6	90.5
$h_{deployed}\ [km]$	14.4	14.9	14.9	15.0	14.7	14.8	14.5	13.4	16.5	12.9
$R\ [km]$	560.6	616.4	496.7	449.4	781.8	561.4	563.4	571.5	584.5	576.0
$\bar{a}_{max}\ [-]$	21.7	26.3	17.4	28.7	12.3	21.7	21.6	21.4	22.1	21.2
$q_\infty\ [Pa]$	622.8	753.8	500.4	827.0	377.3	628.8	645.5	718.3	633.9	610.0
$q_{tot,max}\ [kW/m^3]$	144.132	229.7	51.4	166.0	114.3	144.9	146.8	155.3	144.5	143.2
$Q\ [MJ/m^2]$	7.64	11.7	4.54	6.72	9.31	7.65	7.78	8.31	7.57	7.67
$t\ [s]$	387	390.0	385.0	347.0	460.0	386.0	383.0	371.0	408.0	364.0

Table 6.10.: Overview of Sensitivity Analysis Results

6.4. Design Space Exploration

The benefit of the novel environment proposed in the present work is not only limited to optimising a stacked-toroid based on a series of requirements and constraints but can also enable the exploration of the design space. To demonstrate this functionality, a Monte Carlo analysis is performed in which the four input parameters that constitute the design space (N, θ_c, r_{torus}, $r_{out,torus}$) are randomly generated between the upper and lower bounds defined in Table 5.4 and the associated performance parameters are recorded and stored. A total of 8034 simulations are performed across the entire design space with the distribution in Figure 6.28 and the responses are evaluated for each combination of inputs. The resulting data points are plotted in Figure 6.29 against the objective function and constraints of the optimisation problem, namely the total mass, IAD mass, F-TPS mass, heat load, maximum heat flux, g-load, dynamic pressure, impact velocity, second-stage deployment altitude, tank radius and loads exerted on the toroids, restraint wrap and spar. While not all the one-to-one correspondences between the design inputs and the model responses display a defined correlation, some combinations do unveil relationships that can provide useful insight into the development of future stacked-toroid IADs.

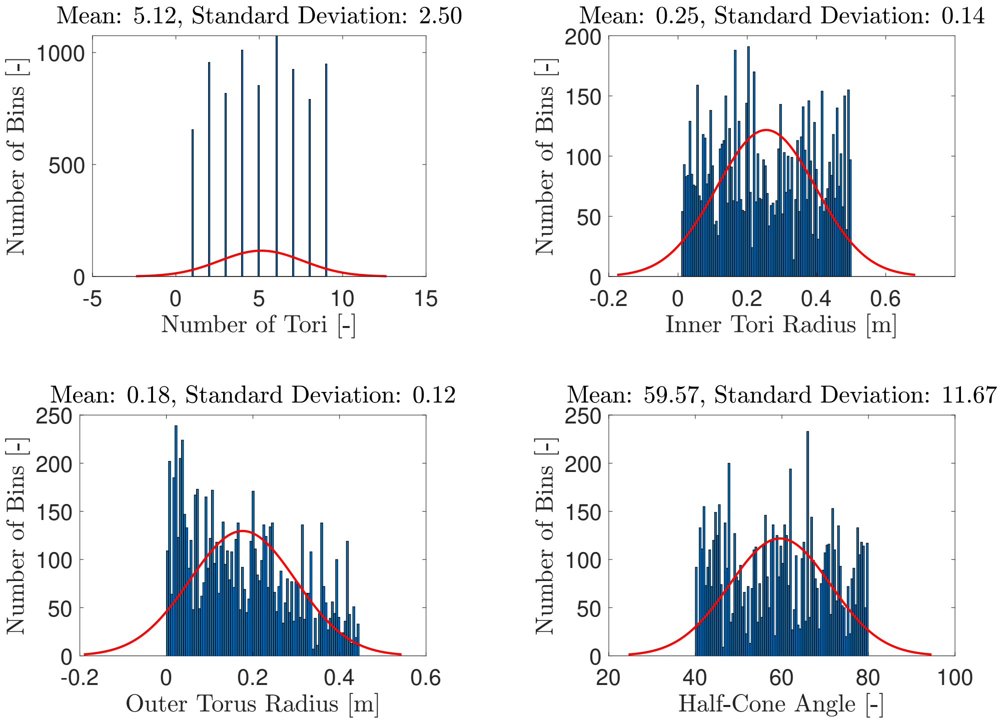

Figure 6.28.: Statistical distribution of input design space

The number of tori exhibits significant variability in all associated responses. It is evident that the number of tori alone is insufficient to determine the performance of the vehicle. However, it is clear that in order to reach the extreme range of total mass, IAD, and F-TPS mass, a larger number of tori is required. In other words, not all designs with a high number of tori result in greater mass, but heavier designs are unlikely to have a low number of tori. A similar observation

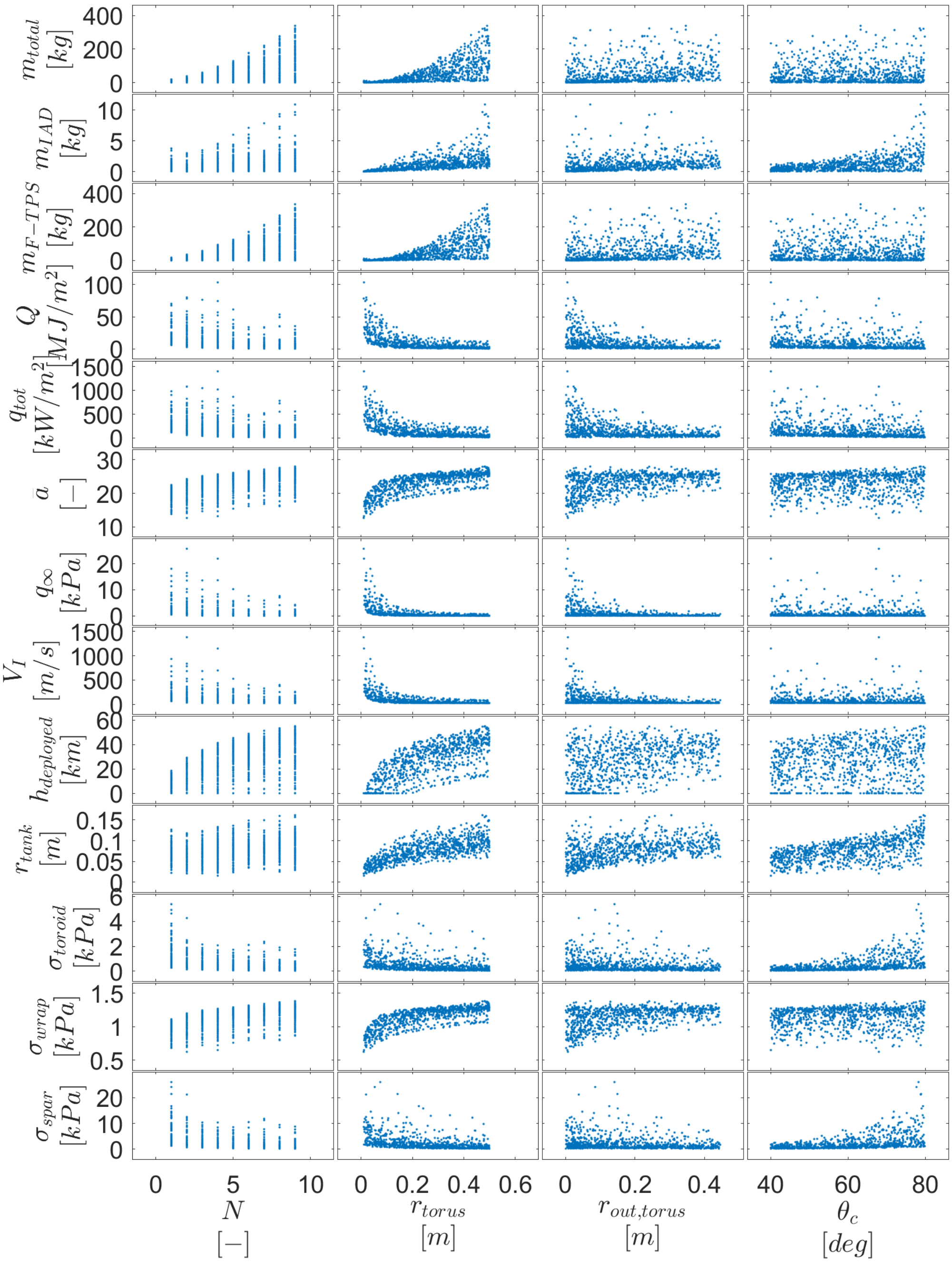

Figure 6.29.: Matrix Plot of Stacked-Toroid Design Space

can be made regarding the deployment altitude of the second stage. As more tori are utilized, the likelihood of higher deployment altitudes increases. This is because a greater number of tori contribute to a larger frontal area, assuming other design inputs remain constant, leading to increased drag. Consequently, more aerobraking manoeuvres are required, necessitating deployment at higher altitudes. While the initial constraint for second-stage deployment was focused on deployment speed, future missions may impose additional requirements on deployment altitude, further constraining the design possibilities. The increased drag is also evident from the impact speed, which tends to reach unfeasible values with fewer tori but becomes reasonable with a larger number of tori. Furthermore, the structural stress on the toroid and spar is greatest with fewer tori, while the constraint wrap is greatest with more tori. This suggests the need for a trade-off analysis among the various structural components.

The radius of the inner tori exhibits stronger correlations with the model responses, although some variables follow similar trends to the number of tori. The total mass and subsystem mass contributions show the same results as the number of tori, indicating an intrinsic duality between these two input parameters that warrants further investigation. In contrast, the thermal loads are clearly influenced by the variation in the radius of the tori. Specifically, as the radius is reduced, the heat flux and heat load tend to increase exponentially. This outcome is expected since smaller tori are associated with a reduced drag area, resulting in less aerobraking. Consequently, faster entry into the Martian atmosphere leads to increased heat loads, which may become unmanageable for very small radii. Similar trends are observed for peak dynamic pressure and impact speed. Based on the previous discussion, smaller tori correspond to higher descent speeds. However, smaller radii also result in reduced g-loads and structural loads. Therefore, it is desirable to choose the radius of the inner tori to be small enough to avoid excessive deceleration but large enough to prevent exponentially increasing heat loads. The optimum value for the present work is identified as approaching the lower end of the design space, while maintaining a sufficiently large radius to mitigate the effects of increasing heat load and dynamic pressure.

The influence of the outer shoulder radius on the model responses is an intriguing aspect that has not been thoroughly explored in the existing literature. While it is challenging to determine specific relationships between the individual effect of the outer shoulder radius and variables such as deployment altitude, tank radius, and system mass, $r_{out,radius}$ exhibits comparable trends to the inner tori radius concerning heat loads, dynamic pressure, and impact speed. Increasing the outer torus radius leads to a reduction in thermal loads and dynamic pressure. This effect is attributed to the increased drag area created by the additional torus. These findings can also be interpreted as an increase in the effective number of tori, albeit with smaller radii. However, the advantages of the outer shoulder radius over an additional torus are not entirely clear. The preliminary analysis conducted by the present model lacks the capability to capture the intricate and interconnected relationships between structural benefits and aerodynamic factors. As a result, the optimization analysis identifies the absence of the outer torus as the ideal configuration. It is important to note that this conclusion is derived from a top-level analysis performed within the MDAO framework.

Interestingly, the half-cone angle does not exhibit any significant correlations with the model responses. The only observable trends that can be extrapolated relate to an increase in IAD mass with higher angles, which also corresponds to a rise in toroidal load. However, for the remaining model responses, no specific trends can be discerned. This suggests that the angle itself should be considered in conjunction with other design inputs to accurately infer the model's response and enhance decision-making during the early stages of design. The absence of clear trends also underscores the purpose of the present environment, which analyzes different configurations by simultaneously varying multiple design inputs. Rather than focusing solely on individual changes, this approach allows for a comprehensive exploration of the design space. By considering the half-cone angle alongside other parameters, designers can gain a holistic understanding of how various factors interact and influence the overall IAD system performance.

To evaluate the joint effect of two design inputs on one or more model responses, the same dataset consisting of over 8000 random data points can be utilized. Reference surface plots are shown in subsection B.6.2. Recognizing the significance of considering the combined influence of multiple input variables, the parameter $r_{inflated}$, as defined in Equation 3.3, is utilized. This parameter encompasses all the variables employed within the current design space. The obtained results are truly remarkable. The matrix scatter plot displayed in Figure 6.30 unveils a one-to-one correlation between the design variable, derived from the simulated design space, and all the considered performance parameters. This finding carries great significance as it suggests the potential utilization of a single variable for rapid estimations of the performance variables.

Although a notable amount of dispersion is evident within the data, particularly as the inflated radius increases, the distribution and scatter of the data points remain sufficiently condensed to enable informed decision-making regarding the performance effects. For instance, a low inflated radius is desired to minimize the total mass, peak g-load, and second-stage deployment altitude. However, it should be noted that a low inflated radius also corresponds to higher heat fluxes, elevated levels of peak dynamic pressure, and increased impact speeds in the second stage. These findings highlight the practical utility of the $r_{inflated}$ parameter for predicting and assessing the performance variables. Such insights enable the optimization of the vehicle's performance characteristics based on the desired outcomes and trade-offs.

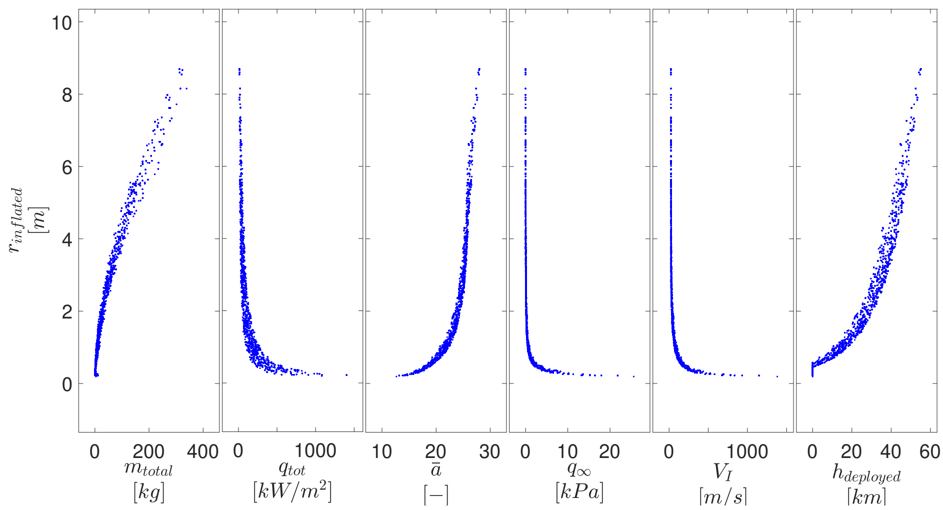

Figure 6.30.: Effect of IAD Inflated Radius on Trajectory Parameters

Given the strong correlations observed with the inflated radius, it is reasonable to consider treating this parameter as a global variable. This raises the question of whether the entire design space can be effectively represented by a single variable. To address this question, the optimization procedure with the GA solver is repeated with a single input: the inflated radius ($r_{inflated}$). Since the remaining design inputs are necessary for all other disciplines, they are randomly generated, with the only requirement being that they satisfy the constraint defined by

Equation 3.3. To find a combination of random design inputs that align with the desired input for the inflated radius, a random search is performed within the bounds defined in Table 5.4. The optimization convergence is illustrated in Figure 6.31, showing that the solver struggles to identify the genetic factors associated with reducing mass. While certain input variable combinations may lead to an inflated radius of low mass, the reverse is not always true. In fact, different design spaces can result in the same inflated radius but with distinct geometries. Nevertheless, since the deviation is reasonably small, the optimization does identify a near-optimum case. After the 52 generations shown in Figure 6.31, the solver is forcefully stopped, and the resulting near-optimum case is shown in Table 6.11.

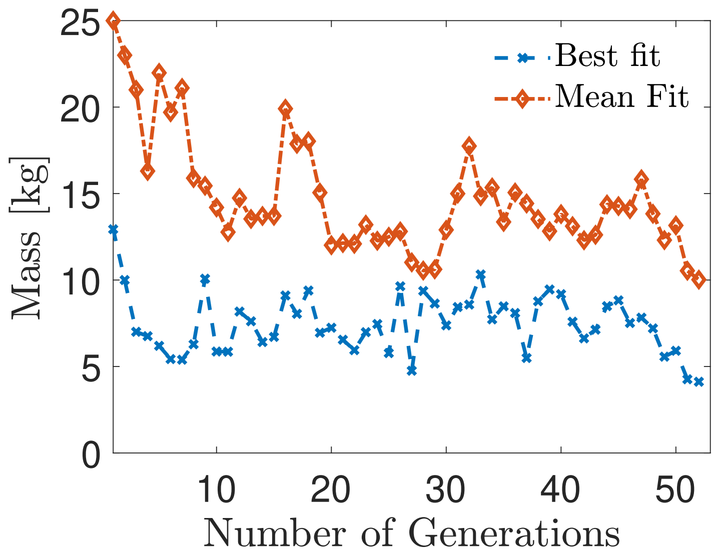

Figure 6.31.: GA convergence with a single variable in the design space

Generation Number	$r_{inflated}$ $[m]$	N $[-]$	r_{torus} $[m]$	$r_{out,torus}$ $[m]$	θ_c $[deg]$	m_{tot} $[kg]$
52	0.9633	9	0.0489	0.0055	66.0	4.11

Table 6.11.: Near-Optimum design space with a single input variable of stacked-toroid

Although the mass is slightly larger than the optimum case identified with a design space comprising four variables instead of one, the optimum design dimensions are in agreement with the discussion made for the optimum case. In both cases, configurations with a large number of tori of small radii are preferred. Additionally, the outer shoulder radius is almost zero, and the half-cone angle is in the vicinity of 70°. This demonstrates that a single variable can successfully approximate the entire design space and simplify the analysis at the cost of a slight loss in optimization fitness. It is inferred that if the GA solver is allowed to run for a sufficiently long time, it will eventually explore enough configurations to statistically determine the optimum design identified with the four-variable design space. However, this would require much longer optimization times as the GA solver fails to recognize the unique characteristics to maintain across the different generations, which are not solely captured by the inflated radius alone. While a gradient-based solver could improve efficiency, given that a single variable is used, narrowing down the design space or initiating the optimizer with a suitable initial guess is necessary to make the optimization computationally feasible within desirable time-frames.

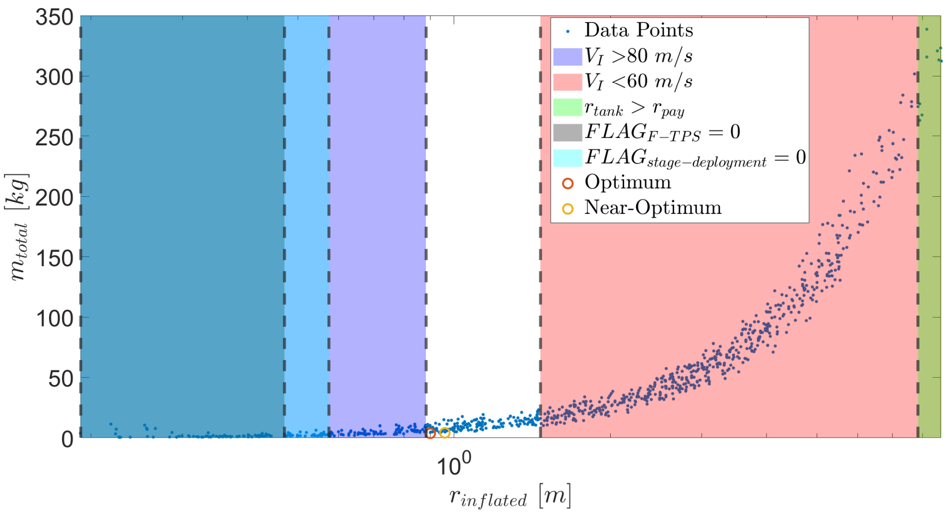

Figure 6.32.: Visualization of optimisation constraints on feasible design space

It is important to acknowledge that the use of the inflated radius is specifically suitable for this particular case where the payload remains fixed, thus allowing the design space to be fully encompassed by the inflated radius. While the expression for the inflated radius in Equation 3.3 and Equation 3.4 does take into account the payload radius, it does not consider the payload height. Consequently, greater deviations in the correlations shown in Figure 6.30 would be expected for angles of attack significantly larger than zero. In fact, during a ballistic entry, the payload would be entirely shielded by the front aeroshell, rendering its aerodynamic contribution negligible when viewed from a local panel method perspective.

The environment also allows for visualizing how constraints shape the optimization problem and define the feasibility envelope within the design space. In the case of the MiniPINS optimization scenario, the primary constraints are depicted in Figure 6.32 for the scatter plot of inflated radius versus total mass. It is intriguing to observe that the inflated radius is primarily constrained by the impact velocity requirements necessary for the penetrator to withstand the shock at impact and achieve the desired depth during emplacement. Interestingly, the upper range of the inflated radius is limited by the tank radius surpassing the payload radius. This outcome is expected since a larger diameter results in increased aerodynamic drag, which must be compensated for by the internal inflation pressure. This constraint represents the upper limit of the inflated radius for the current configuration, assuming a payload diameter of 0.3 m. However, the lower end of the inflated radius exhibits two additional constraints. Firstly, the diameter of the stacked-toroid becomes too small to generate sufficient aerobraking, leading to thermal loads that cannot be reduced to acceptable levels for the F-TPS. Secondly, the second-stage deployment at Mach 0.8 becomes unachievable at the smaller end of the inflated radius spectrum. The remaining region in the figure represents the feasible design region, where the constraints are met and a range of design options exists. The visualization of these constraints provides valuable insights into the limits and trade-offs within the design space, aiding in the identification of feasible design configurations that satisfy the desired performance criteria. Unsurprisingly, the inflated radius

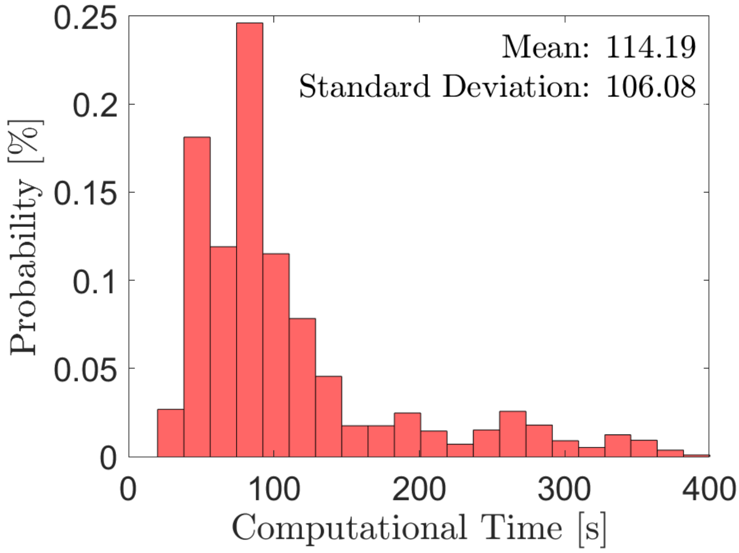

Figure 6.33.: Histogram of probable computational time for each simulation

of the optimised design, computed by substituting the optimised design space in Table 6.4 into Equation 3.3 is 0.9038, corresponding to the first lowest value available after the purple constraint in Figure 6.32 indicated in the legend as the optimum. The near-optimum case, obtained with the a single design-space input is shown as the near-optimum, with an inflated radius of 0.96 m.

The advantages offered by the present multidisciplinary framework are self-evident when compared to single high-fidelity simulations that provide only a limited perspective on the problem at hand. This framework, as demonstrated by the results discussed in this chapter, brings forth significant benefits that facilitate multidisciplinary design optimization and analysis across a broad range of design space variables, mission requirements, operational constraints, and manufacturing limitations. One of the most notable advantages of the proposed environment is its computational efficiency. As depicted in Figure 6.33, the average time required for a single simulation, including the inner F-TPS optimization loop, is less than two minutes on a 11th-generation Intel Core i7-11800H processor with a base speed of 2.30GHz and 8.00 GB of installed RAM. The system runs on a 64-bit operating system and has an x64-based processor.

Longer periods of time may be required in case the inner optimisation does not rapidly reach convergence and might require further iterations. In contrast, high-fidelity simulations can consume hours or even days to complete. This stark contrast in computational time positions the proposed method as a highly effective approach for early design stages and conceptual design exploration. Although the code has not been specifically optimized for speed, its advantage is already apparent, as it can generate 1000 data points in approximately three days of simulations using a single CPU. The substantial reduction in computational time achieved by the proposed framework enables designers to rapidly explore and analyze a vast design space, thereby enhancing the efficiency of the design process. It allows for quicker iterations and informed decision-making during the early stages of design, ultimately accelerating the development of optimized solutions.

7. Conclusion

This research was primarily motivated by the need for alternative EDL systems for safely delivering scientific instruments to the surface of Mars, including the MiniPINS penetrator. Parachutes, although commonly used, have strict deployment conditions that limit their scalability for larger payloads. On the other hand, rigid blunt aeroshells have been used for Mars entry for many years to provide shielding and aerobraking, but their volume constraints pose challenges for fitting them within the launch vehicle. Inflatable aeroshells, emerging as promising technologies, not only overcome the limitations of conventional approaches but also offer the advantages of flexibility and resistance to high temperatures, enabling their application in various space exploration missions. Several research groups have renewed their efforts in developing the stacked-toroid configuration, which has shown promise in recent years across various development programs like PAIDAE and IRDT for planetary exploration. However, the design parameters of the stacked-toroid are intricately interconnected, requiring a multidisciplinary analysis throughout its trajectory. Although numerous (re-)entry engineering tools are available in the literature, none can comprehensively address the stacked-toroid configuration. To this end, the present work introduces a novel fully-integrated MDAO framework which has the potential to be widely implemented by researchers, academia, industries, and space agencies to facilitate the design, optimization, feasibility studies, and exploration of stacked-toroids in space missions. The objectives of the research outlined in the introduction have all been entirely met, and the research questions posed in section 1.2 can ultimately be answered.

RQ1 How can a robust MDAO framework be developed to effectively integrate aerothermoelastic models for a parametrized stacked-toroid IAD design?

The proposed MDAO framework integrates aerothermoelastic models into the design process of a parametrized stacked-toroid IAD. It introduces an innovative approach to parameterize the geometry by simplifying the major structural elements into shapes described by dimensions. Notably, this approach introduces the analysis of an additional shoulder torus, which has not been previously explored in the literature. This enables comprehensive design exploration and seamless data exchange between disciplines. The parametric representation allows analysis of variations in aerodynamics, aerothermodynamics, and deflection responses, providing insights into influential design inputs. To assess performance, a mesh is generated based on the discretized geometry, and local panel methods analyze aerodynamic characteristics. Semi-empirical correlations are incorporated to account for surface flexing, ensuring accurate representation of behaviour. The framework employs a 1D FDM scheme with an inner optimization process to minimize F-TPS mass, considering material survivability and reduction. An outer optimizer, combining gradient-based and GA solvers, efficiently explores the parametrized design space, considering interactions between aerodynamics, aerothermodynamics, and structure. This MDAO environment streamlines the integration of parametrized design space, seeking optimal solutions considering the interactions between the aerodynamic, aerothermodynamic and structural aspects of the stacked-toroid IAD.

RQ1 a) How can optimisation of a stacked-toroid be effectively integrated into the holistic mission design process?

To effectively integrate the optimization of a stacked-toroid into the mission design process, the proposed MDAO environment offers a comprehensive toolset across aerothermoelastic disciplines. This holistic approach considers overall mission performance, customizing constraints like launcher type and atmospheric model. Unlike traditional designs, the MDAO environment allows for flexible tank geometries, offering design adaptability. Fine-tuning the F-TPS optimization adjusts the bondline temperature for desired payload temperature. The MDAO environment utilizes a genetic algorithm for simultaneous optimization of multiple objectives, such as volume, mass, heat flux, g-load, aerodynamic stability, and deployment altitude. This algorithm efficiently manages these objectives to meet mission-specific requirements. The integrated disciplines within the MDAO framework operate modularly, facilitating data exchange and adaptability to diverse missions. Other disciplines and interfaces, like internal heat management and communications, can be implemented to further constrain the optimization process. This modular approach ensures seamless integration while maintaining focus on the holistic mission design process.

RQ1 b) What is the extent of agreement between the simulated aerodynamic performance and the high-fidelity results from the literature?

The aerodynamic performance simulation accuracy was evaluated by comparing it to experimental results from literature for two flight configurations: IRVE-II and IRVE-3. The simulation approach integrated the local inclination panel method with the modified Newtonian method in the continuum regime. For IRVE-II, numerical predictions matched the experimental data up to Mach 6, with a mean percentage error of axial and normal force coefficients at 14.56%. The modified Newtonian method, accurate at high Mach numbers, was affected by aeroshell deflection at high Mach numbers due to dynamic pressure influence. Comparisons with rigid model databases showed better agreement. IRVE-3, which flew at higher dynamic pressures and Mach numbers, had less pronounced deflection, resulting in good agreement with the local inclination method. Mean percentage errors for drag coefficient and lift coefficient were 7% and 10%, respectively, indicating suitable performance. The model performed best at high speeds beyond Mach 5, with percentage errors below 3.4%. However, at subsonic speeds, errors reached up to 28%. Empirical relations from surface deflection yielded slightly lower percentage errors for both IRVE-II and IRVE-3. Extrapolating dynamic pressure beyond the region of IRVE-II caused adverse effects. Due to the lack of flight data in rarefied and transitional regimes, high-fidelity DSMC data was utilized. The investigated models (Schaaf and Chambre, Cook, CCL, Sentman, and Storch) provided reasonable results and agreed well with high-fidelity DSMC data for various angles of attack conditions. The CLL model, the most accurate, had mean percentage errors below 4% for the normal force coefficient and below 10% for the axial force coefficient. However, it couldn't be applied to Mars due to the lack of model coefficients for Martian atmospheric species (CO_2 and CO). The preferred choice was the Schaaf and Chambre model, despite slightly larger mean errors of around 23% for both aerodynamic coefficients. It lost accuracy at angles close to 90° due to the inclination angles of the panels, which didn't account for flow separation. The same applied to Wilmoth's bridging function in the transitional regime, accurate for all angle of attack values except 90°. This behaviour was also observed in the moment coefficient for aerostability, which showed good agreement for low angles of attack.

RQ1 c) How does the accuracy of the simulated aerothermal performance compare to high-fidelity results retrieved from the literature?

Comparing convective heat flux measurements with IRVE-II and IRVE-3 flight data, Fay-Riddell, Detra-Kemp-Riddell, Van-Driest, and Chapman's methods accurately predicted the maximum heat flux with errors of 0.8-6.4%. Sutton-Grave's formula overestimated it by 16%, indicating a more conservative approach, while Van Driest underestimated it because of its non-catalytic wall assumption. Sutton-Graves is integrated into the design framework as it overpredicts both heat flux and load, resulting in a conservative approach. Schaaf and Chambre's model, integrated into FMF with extrapolated DSMC data, exhibits an 11% error against extrapolated data but requires further validation. Wilmoth's function accurately captures the heat flux in the transitional regime. SCARAB and Krasnov methods effectively model heat distribution on the vehicle's surface for spherical and conical bodies, reducing the error against CFD data from approximately 80% to around 10%. In the presence of scallops, Hollis augmented heat flux is integrated with SCARAB and Krasnov methods, but it's less accurate for large scallop angles. SCARAB is deemed the most suitable model for large scallops, being the most conservative. Schaaf and Chambre's model is integrated in FMF, using extrapolated DSMC data with an 11% error but further validation may be required. Wilmoth's function adequately captures the heat flux in the transitional regime when compared to DSMC and CFD data. The stagnation heat flux is used for sizing the F-TPS as it represents the most critical condition. Although radiative heating is a minimal fraction of the convective contribution, it is reasonably predicted for conceptual studies, with most errors ranging from 4% to 43%.

RQ2 What is the optimal conceptual design of a stacked toroid for the MiniPINS penetrator that minimizes the total mass of the decelerator?

The optimized design consists of 7 tori, a half-cone angle of 71.6 degrees, and an inner tori radius of 0.0563 m. Notably, there is no shoulder torus included in this design. Considering the payload dimensions, which remain unchanged, a cylinder with a radius of 0.15 m and a height of 0.8 m is used. The overall size of the vehicle, encompassing all design variables, has an inflated radius of 0.9 m. Through this optimization process, the total mass of the decelerator has been minimized, resulting in an optimized mass of 3.7 kg for the MiniPINS penetrator's stacked toroid design.

RQ2 a) How can the design space of a stacked-toroid be described?

The parametrization challenge revolves around identifying the most relevant design variables that significantly influence the vehicle's topology and performance. To address this, the outer aeroshell can be treated as a sphere-cone geometry while considering the concave aft-body and approximating the payload as a cylindrical forebody. Furthermore, the inclusion of an outer shoulder torus takes into account the shoulder curvature. By defining the payload size, the configuration's number of design inputs is reduced to four: the half-cone angle (θ_c), the radius of the internal tori (r_{torus}), the number of internal tori (N), and the radius of the outer torus ($r_{out,torus}$) that is smaller than the inner tori's diameter. However, if further analysis reveals that the recent configurations of the stacked toroid are not suitable for the outer torus, the number of parameters can be reduced to three. The inflated radius can alternatively be used as a global variable. Additionally, if the payload dimensions are undefined, two additional design parameters are included: the payload radius and height. The inflated radius can be used as a single input variable to rapidly obtain near-optimal solutions.

RQ2 b) What is the most suitable characterisation of the EDL design space that complies with the MiniPINS requirements?

The EDL design space for the MiniPINS mission is characterized by a novel architecture that incorporates a stacked-toroid for the first stage. This stacked-toroid design serves the purpose of aerobraking deceleration during entry and descent, providing thermal protection to the penetrator. Once Mach 0.8 is reached, the MetNet tension cone is deployed as the second stage. In the optimized scenario, the deployment stage takes place at 14.4 km, which is more than 10 km higher than the deployment altitude of MetNet. The higher deployment altitude offers advantages such as landing at higher altitudes and enabling terrain mapping before the penetrator's impact. The structural loads experienced by the stacked-toroid are significantly lower than the yield strength of the materials used, with a g-load of 21.7 and a peak dynamic pressure of 622 Pa. To ensure aerostability, a CoG position located 0.05 m from the nose cone is proposed, resulting in a positive SM of 15%. The mass of the optimized design is 3.72 kg, which is 58% lower than the rigid capsule advocated by MetNet. While the absolute mass value may have some inaccuracies based on the depth of analysis, the relative variation of mass across different design iterations is accurately modelled. The F-TPS for the stacked-toroid design requires a total thickness of 3.56 mm across all layers to maintain temperatures within their allowable limits. The peak heat flux is 144.1 kW/m^2, and the heat load is 7.64 MJ/m^2. Finally, a predicted total flight time of 387 seconds is estimated, covering a downrange distance of 560 km.

RQ2 c) How does the variation of design space impact the responses of the MDAO model?

Through a Monte Carlo analysis comprising 8034 simulations, a comprehensive exploration of the design space is conducted to uncover relationships between design inputs and performance parameters. The number of tori and inner tori are critical factors in designing a Martian decelerator. They significantly impact the total mass and deployment altitude of the system. More tori contribute to higher deployment altitudes due to increased drag, but heavier designs are unlikely to have a low number of tori. The radius of the inner tori demonstrates stronger correlations with model responses, with smaller radii resulting in increased thermal loads, heat flux, and impact speed. However, smaller radii also yield lower g-loads and structural loads, requiring a trade-off analysis. The outer shoulder radius's influence on model responses is intriguing, but its advantages over an additional torus remain unclear. The half-cone angle does not exhibit significant correlations with most model responses, except for an increase in IAD mass and toroidal load with higher angles. To evaluate the joint effect of two design inputs on model responses, the same dataset of over 8000 random data points is utilized. The parameter $r_{inflated}$ reveals a one-to-one correlation with performance parameters, suggesting the use of a single global variable for rapid estimations. Nevertheless, this single variable contains insufficient genes to rapidly perform a global GA optimization, leading to either near-optimum solutions or excessively long optimization processes. Visualizing constraints within the design space provides valuable insights into limits and trade-offs, enabling designers to optimize vehicle performance characteristics based on desired outcomes and trade-offs.

RQ3 How robust is the entry performance of the optimised stacked-toroid design space?

A sensitivity analysis is conducted to evaluate the robustness of the optimized stacked-toroid design in entry performance. The analysis examines the vehicle's performance under varying entry conditions and atmospheric characteristics, focusing on varying reference parameters like entry velocity, entry angle, trim angle of attack, and atmospheric density.

The analysis provides insights into the design's ability to adapt and maintain performance across different conditions. The results highlight trade-offs and operational implications of design choices, such as impacting payload safety and affecting mission schedules and resource allocation. The optimized decelerator's trajectory remains robust under entry conditions and trim angle of attack, with no significant changes needed for EDL requirements. The sensitivity is further addressed in the following three subquestions.

RQ3 a) How do the trajectory entry conditions of the MiniPINS mission affect the design choices of the stacked-toroid?

Higher entry speeds result in aerobreaking occurring at a lower rate, so the stacked-toroid must be capable of withstanding larger or lower decelerations. Maintaining the desired impact speed and deployment altitude across different trajectories is crucial, and the design should ensure these parameters remain consistent to meet mission requirements. The sensitivity analysis shows that the stacked-toroid design effectively compensates for varying entry speeds, allowing it to accommodate a range of velocity scenarios without major alterations. However, further analysis is required for the F-TPS and structural design in cases of increased or decreased loading conditions resulting from different entry speeds. The change in heat flux is non-linear with respect to entry speed. An increase in entry speed by 20% leads to a 59.4% increase in heat flux and a 53.13% increase in heat load. Conversely, a reduction in entry speed by 20% is associated with a 64% reduction in heat flux and a 40% reduction in heat load. This may involve incorporating stronger structural elements or implementing active systems to manage excessive heat fluxes, ensuring the stacked-toroid can withstand up to 50 W/cm^2. While the MiniPINS mission has minimal downrange variation and flight time differences, other missions may prioritize landing location accuracy. In such cases, appropriate guidance and control systems can be implemented to account for downrange variations caused by different entry speeds, facilitating precise landing.

Furthermore, a $\pm$20% variation from the nominal entry angle is investigated. The most significant variation occurs during the descent phase between 80 and 30 km, where most aerobraking occurs. A steeper entry angle decelerates at lower altitudes, but all curves ultimately reach the same landing speeds and configurations. Decreasing the entry angle by 20% from the nominal value results in a decrease of 20% in maximum heat flux, but increased flight time and heat load. Additionally, reducing the entry angle leads to a significant increase in downrange by 40%. When the entry angle is increased to -13.2°, the g-load experiences an increase of 32% in alignment with the increase in dynamic pressure. Other quantities, such as downrange, flight time, and heat load, exhibit reduced variations. The optimized vehicle design satisfies all the requirements for $\pm$20% in entry angles.

RQ3 b) How does the trimmed angle of attack influence the entry trajectory of the optimized stacked-toroid design?

The trimmed angle of attack is varied from $\alpha = 0°$ to $\alpha = 20°$. The deployment altitude of the second stage decreases as the angle of attack increases. For $\alpha = 20°$, the deployment altitude can reach as low as 13.4 km. This indicates that a higher angle of attack results in a steeper descent trajectory during the entry phase. With increasing angles of attack, the impact speed increases. For example, at $\alpha = 10°$ and $\alpha = 20°$, the impact speeds are reported to be 81.7 m/s and 87.1 m/s, respectively. These values exceed the specified requirement of an impact speed below 80 m/s, potentially compromising the penetrator's survivability. Additionally, the trajectory performance is significantly affected by the trimmed angle of attack. Specifically, the maximum dynamic pressure experiences a

15% increase when comparing $\alpha = 20^\circ$ to the reference angle. Similarly, the heat flux and heat load encounter an approximate 8% increase at $\alpha = 20^\circ$. These variations indicate that higher angles of attack result in increased aerodynamic and thermal loads on the vehicle.

RQ3 c) How does the variation in atmospheric density impact the entry trajectory of the optimized stacked-toroid design?

As the atmospheric density changes, the trajectories of the stacked-toroid design experience noticeable shifts, which are more pronounced at lower altitudes where the density is higher. For lower densities, the deployment altitude is 12.9 km, while for higher densities, it increases to 16.5 km. This means that the optimized design allows for higher deployment altitudes when the atmospheric density is lower. Furthermore, the impact velocities during entry are affected by changes in atmospheric density. For lower densities, the impact velocity is 90.5 m/s, while for higher densities, it reduces to 72.6 m/s. It is worth noting that the impact speed for the higher-density case complies with the desired landing speed within the specified limits. However, the lower-density case results in an impact speed that exceeds the minimum requirements, indicating that the optimized design is more vulnerable to low densities. To address this sensitivity to low densities, an improved version of the design could establish a lower bound for the objective landing speed, such as 70 m/s, allowing for a greater margin on the upper bound. A more accurate estimation of the atmospheric profile should be made once the interplanetary trajectory and mission date are fully defined.

7.0.1. Future Work and Recommendations

The methodology presented here, applied to the MiniPINS penetrator, has potential for broader applications. The integrated environment can be adapted to various mission scenarios and EDL architectures, offering versatility. By adjusting constraints and objectives, the parametric design space of stacked-toroids can be explored for different missions and celestial bodies such as Venus or Titan, enabling mission planning for future exploration endeavors.

To improve prediction accuracy, efforts should focus on aerodynamic corrections due to scalloping and vehicle deflection. Implementing a coupled FSI solver would provide more accurate estimations of structural deformation and loads. Recent advancements in surrogate modelling and neural networks can enhance computational efficiency. Conducting uncertainty analysis would identify significant sources of uncertainty and establish boundaries and confidence intervals for analysis, which would increase the model's reliability and robustness, facilitating risk-informed decision-making. Moreover, implementing 6 DOF trajectories would enable investigation of control strategies and optimization responses.

Lastly, further feasibility and viability studies are recommended, building upon the preliminary case study conducted for MiniPINS. These studies should assess the technical and operational feasibility of implementing the proposed designs and systems in real-world scenarios. Considering factors such as manufacturing constraints, operational requirements, and cost-effectiveness, these studies would offer valuable insights into the practicality and potential of the proposed solutions.

Bibliography

[1] M. Genzer et al., "MiniPINS-Miniature Planetary In-situ Sensor Packages for Mars and Moon," Copernicus Meetings, Tech. Rep., 2021. DOI: 10.5194/epsc2021-69.

[2] R. Worth, "Descent and landing systems for unmanned mars entry.," Journal of Spacecraft and Rockets, vol. 3, no. 12, pp. 1744–1748, 1966. DOI: 10.2514/3.28741.

[3] C. Gillis, "Deployable aerodynamic decelerators for space missions," 5th Annual Meeting and Technical Display, 1968. DOI: 10.2514/6.1968-1081.

[4] N. CR-66727-1, "Titan/Mars Hard Lander, Volume 1: 1400 lb Capsule System Design Study"," 1969.

[5] J. Cruz and J. Lingard, "Aerodynamic decelerators for planetary exploration: Past, present, and future," AIAA Guidance, Navigation, and Control Conference and Exhibit, 2006. DOI: 10.2514/6.2006-6792.

[6] H. Bohon and R. Miserentino, "Attached inflatable decelerator performance evaluation and mission-application study," 3rd Aerodynamic Deceleration Systems Conference, 1970. DOI: 10.2514/6.1970-1163.

[7] A. M. Dwyer Cianciolo et al., "Entry, descent and landing systems analysis study: Phase 1 report," Tech. Rep., 2010.

[8] A. M. Dwyer Ciancolo et al., "Entry, descent and landing systems analysis study: Phase 2 report on exploration feed-forward systems," Tech. Rep., 2011.

[9] J. T. McShera, Wind-tunnel Investigation of a Balloon as a Towed Deceleration at Mach Numbers from 1.47 to 2.50. National Aeronautics and Space Administration, 1961.

[10] W. Alexander, "Investigation to determine the feasibility of using inflatable balloon type drag devices for recovery applications in the transonic, supersonic, and hypersonic flight regime. part 2. mach 4 to mach 10 feasibility investigation," Goodyear Aircraft Corporation, Akron Ohio, Tech. Rep., 1962.

[11] L. Kayser, "Pressure distribution, heat transfer, and drag tests on the goodyear ballute at mach 10," Arnold Engineering Development Center, Arnold AFB TN, Tech. Rep., 1962.

[12] D. Bell, "Pressure measurements on the rigid model of a balloon decelerator in the wake of a simulated missile payload at mach numbers 1.5 to 6.0," Arnold Engineering Development Center, Arnold AFB TN, Tech. Rep., 1964.

[13] R. R. Rohrschneider and R. D. Braun, "Survey of ballute technology for aerocapture," Journal of Spacecraft and Rockets, vol. 44, no. 1, pp. 10–23, 2007. DOI: 10.2514/1.19288.

[14] F. Nebiker, A. Aebischer, J. Dean, F. Floetscher, and W. Sowa, "Aerodynamic deployable decelerator performance-evaluation program," Goodyear Aircraft Corporation, Akron Ohio, Tech. Rep., 1965.

[15] E. Bloetscher, "Aerodynamic deployable decelerator performance-evaluation program: Phase 2," Air Force Flight Dynamics Laboratory, Research and Technical Division, 1967.

[16] A. Jordan and J. Robinson, “Exploratory experimental aerodynamic investi-gation of tension shell shapes at mach 7,” Tech. Rep., 1965.

[17] W. J. Stroud and G. W. Zender, Experimental investigation to determine utility of tension shell concept. National Aeronautics and Space Administration, 1966.

[18] T. R. Creel, Longitudinal aerodynamic characteristics of a tension shell entry configuration at Mach 20. National Aeronautics and Space Administration, 1966.

[19] W. D. Deveikis and J. W. Sawyer, “Aerodynamic characteristics of tension shell shapes at mach 3.0,” Tech. Rep., 1966.

[20] D. Bushnell, J. Hunt, and R. Jones, “Experimental flow field and heat-transfer investigation of several tension shell configurations at a mach number of 8,” Tech. Rep., 1967.

[21] J. W. Sawyer, Effects of configuration modifications on aerodynamic characteristics of tension shell shapes at Mach 3.0. National Aeronautics and Space Administration, 1967.

[22] C. D. Harris, “Transonic aerodynamic investigation of tension shell and blunted 100 deg conical shapes for unmanned entry vehicles,” Tech. Rep., 1966.

[23] B. Walker and R. W. Weaver, “Static aerodynamic characteristics of blunted cones in the mach-number range from 2.2 to 9.5,” Tech. Rep., 1967.

[24] A. McRonald, “A light weight inflatable hypersonic drag device for planetary entry,” 1999.

[25] R. Miserentino, Drag Characteristics of Several Towed Decelerator Models at Mach 3. National Aeronautics and Space Administration, 1970.

[26] B. P. Smith, C. L. Tanner, M. Mahzari, I. G. Clark, R. D. Braun, and F. M. Cheatwood, “A historical review of inflatable aerodynamic decelerator technology development,” 2010 IEEE Aerospace Conference, 2010. DOI: 10.1109/aero.2010.5447013.

[27] P. Bouchet, Mars habitat module entering Mars atmosphere with Low Density Supersonic Decelerator. 2014. [Online]. Available: http://manchu-sf.blogspot.com/.

[28] B. D. Goldman and E. Dowell, “In-flight aeroelastic stability of the thermal protection system on the NASA HIAD, part II: Nonlinear theory and extended aerodynamics,” 56th AIAA/ASCE Structures, Structural Dynamics, and Materials Conference, 2015. DOI: 10.2514/6.2015-1422.

[29] J. Guo, G. Lin, J. Zhang, X. Bu, and H. Li, “Hypersonic aerodynamics of a deformed aeroshell in continuum and near-continuum regimes,” Aerospace Science and Technology, vol. 93, p. 105 296, 2019. DOI: 10.1016/j.ast.2019.07.029.

[30] J. Del Corso, F. Cheatwood, W. Bruce, S. Hughes, and A. Calomino, “Advanced high-temperature flexible tps for inflatable aerodynamic decelerators,” 21st AIAA Aerodynamic Decelerator Systems Technology Conference and Seminar, 2011. DOI: 10.2514/6.2011-2510.

[31] J. A. Del Corso et al., “Flexible thermal protection system development for hypersonic inflatable aerodynamic decelerators,” in International Planetary Probe Workshop 9, 2012.

[32] J. Del Corso, W. Bruce, K. Liles, and S. Hughes, “Thermal analysis and testing of candidate materials for paidae inflatable aeroshell,” 20th AIAA Aerodynamic Decelerator Systems Technology Conference and Seminar, 2009. DOI: 10.2514/6.2009-2925.

[33] V. Finchenko, K. Pitchkhadze, L. Marraffa, D. Vennemman, and D. Wilde, “Thermal and aerodynamic experimental testing for full scale models of descent modules with inflatable braking device,” in Fourth Symposium on Aerothermodynamics for Space Vehicles, vol. 487, 2002, p. 465.

[34] T. Chen, M. R. Moholt, and L. D. Hudson, “Hypersonic Inflatable Aerodynamic Decelerator (HIAD) Torus Mechanical Testing,” Tech. Rep., 2017.

[35] J. Guo, G. Lin, X. Bu, S. Fu, and Y. Chao, “Effect of static shape deformation on aerodynamics and aerothermodynamics of hypersonic inflatable aerodynamic decelerator,” Acta Astronautica, vol. 136, pp. 421–433, 2017. DOI: 10.1016/j.actaastro.2017.03.019.

[36] R. K. Johnson et al., “Hiad advancements and extension of mission applications,” in International Planetary Probe Workshop, 2016.

[37] F. M. Cheatwood et al., “Manufacturing challenges and benefits when scaling the hiad stacked-torus aeroshell to a 15m-class system,” 2016 IEEE Aerospace Conference, 2016. DOI: 10.1109/aero.2016.7500773.

[38] A. Olds et al., “IRVE-3 Post-Flight Reconstruction,” in AIAA Aerodynamic Decelerator Systems (ADS) Conference, 2013, p. 1390. DOI: 10.2514/6.2013-1390.

[39] R. Dillman et al., “Flight performance of the inflatable reentry vehicle experiment II,” in International Planetary Probe Workshop (IPPW-10), 2013.

[40] N. Houtz, “Optimization of inflatable drag devices by isotensoid design,” 1st Annual Meeting, 1964. DOI: 10.2514/6.1964-437.

[41] M. S. Anderson, J. C. Robinson, H. S. Bush, and R. W. Fralich, “A tension shell structure for application to entry vehicles,” No. NASA-TN-D-2675, Tech. Rep., 1965.

[42] E. Axdahl, J. Cruz, M. Schoenenberger, and A. Wilhite, “Flight dynamics of an aeroshell using an attached inflatable aerodynamic decelerator,” 20th AIAA Aerodynamic Decelerator Systems Technology Conference and Seminar, 2009. DOI: 10.2514/6.2009-2963.

[43] I. G. Clark, Aerodynamic design, analysis, and validation of a supersonic inflatable decelerator. Ph.D. dissertation, Georgia Institute of Technology, 2009.

[44] C. J. Player, F. M. Cheatwood, and J. Corliss, “Development of inflatable entry systems technologies,” in 3rd International Planetary Probe Workshop, 2005.

[45] C. A. Graves et al., “Inflatable aeroshells as an alternative aerodynamic decelerator,” Advances in the Astronautical Sciences, vol. 121, pp. 279–291, 2005.

[46] B. R. Starr, D. M. Bose, M. Thornblom, and D. Kilcoyne, “Inflatable reentry vehicle experiment flight performance simulations,” in 53rd JANNAFF Propulsion Meeting, Monterey, CA. Dec, 5-8, 2005.

[47] J. R. Martins and A. B. Lambe, “Multidisciplinary design optimization: A survey of architectures,” AIAA Journal, vol. 51, no. 9, pp. 2049–2075, 2013. DOI: 10.2514/1.j051895.

[48] N. J. Falkiewicz and C. E. Cesnik, “Proper orthogonal decomposition for reduced-order thermal solution in hypersonic aerothermoelastic simulations,” AIAA Journal, vol. 49, no. 5, pp. 994–1009, 2011. DOI: 10.2514/1.j050701.

[49] K. Decker and D. N. Mavris, “A multidisciplinary analysis framework for the sizing and synthesis of hypersonic aerial systems,” in AIAA SciTech 2023 Forum, 2023, p. 2365. DOI: 10.2514/6.2023-2365.vid.

[50] J. Sobieszczanski-Sobieski and R. Haftka, “Multidisciplinary aerospace design optimization - survey of recent developments,” 34th Aerospace Sciences Meeting and Exhibit, 1996. DOI: 10.2514/6.1996-711.

[51] G. J. Harloff and B. M. Berkowitz, “HASA: Hypersonic Aerospace Sizing Analysis for the preliminary design of aerospace vehicles,” No. NASA-CR-182226, Tech. Rep., 1988.

[52] H. V. Dean, B. E. Robertson, and D. N. Mavris, "Multidisciplinary design analysis and optimization of a hypersonic inflatable aerodynamic decelerator," in AIAA SciTech 2023 Forum, 2023, p. 2364. DOI: 10.2514/6.2023-2364.vid.

[53] B. R. Hollis, S. A. Berry, K. E. Hollingsworth, and S. A. Wright, "Experimental Study of Convective Heating on the Back Face and Payload of a Hypersonic Inflatable Aerodynamic Decelerator (HIAD) Aeroshell," Tech. Rep., 2017.

[54] NASA, Software Catalog. Date Accessed: 12-02-2023. [Online]. Available: https://software.nasa.gov/.

[55] A. Falchi, V. Renato, E. Minisci, and M. Vasile, "Fostrad: An advanced open source tool for re-entry analysis," in 15th Reinventing Space Conference, 2017.

[56] J. N. Moss, C. E. Glass, B. R. Hollis, and J. W. Van Norman, "Low-density aerodynamics for the inflatable reentry vehicle experiment," Journal of Spacecraft and Rockets, vol. 43, no. 6, pp. 1191–1201, 2006. DOI: 10.2514/1.22707.

[57] V. Davydov and G. Skuridin, "Penetrators (penetrating sondes) and new possibilities for study of the planets," Tech. Rep., 1979.

[58] T. Nakajima, M. Hinada, H. Mizutani, H. Saitoh, J. Kawaguchi, and F. Akio, "Lunar penetrator program: LUNAR-A," Acta Astronautica, vol. 39, no. 1-4, pp. 111–119, 1996. DOI: 10.1016/S0094-5765(96)00128-2.

[59] E. Galimov, "Luna-glob project in the context of the past and present lunar exploration in russia," Journal of earth system science, vol. 114, no. 6, pp. 801–806, 2005. DOI: 10.1007/BF02715966.

[60] T. J. Mosher and P. Lucey, "Polar night: A lunar volatiles expedition," Acta Astronautica, vol. 59, no. 8-11, pp. 585–592, 2006. DOI: 10.1016/j.actaastro.2005.07.033.

[61] Y. Gao et al., "Lunar science with affordable small spacecraft technologies: MoonLITE and Moonraker," Planetary and Space Science, vol. 56, no. 3-4, pp. 368–377, 2008. DOI: 10.1016/j.pss.2007.11.005.

[62] H. Shiraishi, S. Tanaka, A. Fujimura, and H. Hayakawa, "The present status of the Japanese penetrator mission: LUNAR-A," Advances in Space Research, vol. 42, no. 2, pp. 386–393, 2008. DOI: 10.1016/j.asr.2007.08.022.

[63] S. Yi et al., "Research on impact type penetrator for lunar regolith exploration project,", vol. 2, no. 3, pp. 213–217, 2015. DOI: 10.15982/j.issn.2095-7777.2015.03.004.

[64] J. Shengyuan et al., "Research Progress of Penetration and In-Situ Detection of Planetary Regolith Physical Properties,", vol. 9, no. 2, pp. 114–122, 2022. DOI: 10.15982/j.issn.2096-9287.2022.20191106001.

[65] S. Miao et al., "Ground Simulation Test of Penetrator for Lunar Soil Exploration,", vol. 9, no. 2, pp. 141–149, 2022. DOI: 10.15982/j.issn.2096-9287.2022.20210149.

[66] A. Friedlander, J. Niehoff, and D. Davis, "Penetrator mission concepts for exploration of the galilean satellites," Astrodynamics Conference, 1976. DOI: 10.2514/6.1976-800.

[67] A. Coustenis et al., "TandEM: Titan and Enceladus mission," Experimental Astronomy, vol. 23, no. 3, pp. 893–946, 2009. DOI: 10.1007/s10686-008-9103-z.

[68] O. Witasse, "JUICE (Jupiter Icy Moon Explorer): A European mission to explore the emergence of habitable worlds around gas giants," Copernicus Meetings, Tech. Rep., 2020.

[69] Y. Langevin, "The vesta project: Combined studies of mars and small bodies of the solar system," Advances in Space Research, vol. 7, no. 12, pp. 205–211, 1987. DOI: 10.1016/0273-1177(87)90219-5.

[70] E. S. Agency, "Vesta – a mission to the small bodies in the solar system," ESA-SCI(88)6, vol. 7, 1988.

[71] P. Ulivi and D. M. Harland, Robotic Exploration of the Solar System: Part 2: Hiatus and Renewal, 1983-1996. Springer Science & Business Media, 2009.

[72] N. R. Council, "On the scientific viability of a restructured craf science payload: Letter report," 1930.

[73] A. Castro, "Comet nucleus impact probe feasibility study," Tech. Rep., 1980.

[74] D. Stetson, "Near-nucleus trajectory design for comet penetrator-lander data relay," Astrodynamics Conference, 1988. DOI: 10.2514/6.1988-4267.

[75] В. Дерюгин, К. Пичхадзе, В. Финченко, and С. Шматов, "Оценка возможности безымпульсного спуска объектов с орбит исз на поверхность земли," in Российская академия космонавтики им. КЭ Циолковского, НПО им. СА. Лавочкина, 2000, p. 9.

[76] В. Финченко, А. Иванков, and С. Шматов, "Проект ка, оснащённого системой удаления космического мусора (аэротермодинамика, габаритно-массовые характеристики и траектории спуска ка с околоземных орбит)," Вестник НПО им. СА Лавочкина, no. 1, pp. 10–18, 2018.

[77] R. Dillman et al., "Planned flight of the terrestrial HIAD orbital reentry (THOR)," in International Planetary Probe Workshop, 2014.

[78] C. Rapisarda, Literature Review of Inflatable Aerodynamic Decelerators for a Martian Penetrator Mission. Delft University of Technology, Research Methodologies, 2022.

[79] К. Пичхадзе, В. Финченко, С. Алексашкин, and Б. Острешко, "Трансформируемые аппараты, спускаемые в атмосферах планет," Вестник НПО им. СА Лавочкина, no. 2, pp. 4–13, 2015.

[80] A. Ivankov, "IRDT: Inflatable re-entry and Descent Technology for mars missions," 54th International Astronautical Congress of the International Astronautical Federation, the International Academy of Astronautics, and the International Institute of Space Law, 2003. DOI: 10.2514/6.iac-03-iaa.13.1.06.

[81] L. Marraffa et al., "IRDT-Inflatable Re-entry and Descent Technology," in Hot Structures and Thermal Protection Systems for Space Vehicles, vol. 521, 2003, p. 19.

[82] D. Wilde, S. Walther, K. Pitchadze, S. Alexsaschkin, D. Vennemann, and L. Marraffa, "Flight test and ISS application of the Inflatable Reentry and Descent Technology (IRDT)," Acta Astronautica, vol. 51, no. 1-9, pp. 83–88, 2002. DOI: 10.1016/S0094-5765(02)00078-4.

[83] V. Finchenko, L. M. Pitchkadze, D. Vennemann, S. Walter, and D. Wilde, "Inflatable reentry and descent technology, advanced state and prospects of development," in 1st European Workshop on Space Inflatable Structures, ESA, 2002.

[84] V. Finchenko and A. Ivankov, "Calculation of constructive heat protection characteristics for inflatable braking devices moving in planet's atmospheres," in Procedures of the European Workshop on Inflatable Space Structures, 2002, pp. 21–22.

[85] V. Finchenko, “Methodology of thermal protection design for descent modules inflatable braking device,” 54th International Astronautical Congress of the International Astronautical Federation, the International Academy of Astronautics, and the International Institute of Space Law, 2003. DOI: 10.2514/6.iac-03-i.6.05.

[86] С. Карпенко and И. Афанасьев, “Первое плавание «фрегата»,” Новости космонавтики, vol. 10, no. 4, p. 207, 2000.

[87] O. Alifanov, V. Outchvatov, and K. Pichkhadze, “Thermal protection of re-entry vehicles with the usage of inflatable systems,” Acta Astronautica, vol. 53, no. 4–10, pp. 541–546, 2003. DOI: 10.1016/s0094-5765(03)80015-2.

[88] M. Lindell, S. Hughes, M. Dixon, and C. Willey, “Structural analysis and testing of the inflatable re-entry vehicle experiment (IRVE),” 47th AIAA/ASME/ASCE/AHS/ASC Structures, Structural Dynamics, and Materials Conference 14th AIAA/ASME/AHS Adaptive Structures Conference, 2006. DOI: 10.2514/6.2006-1699.

[89] R. Wang, A. Hou, and Y. Niu, “The optimal design and analysis of the irdt system based on two-dimensional ballistic trajectory in atmosphere reentry,” in 20th AIAA International Space Planes and Hypersonic Systems and Technologies Conference, 2015, p. 3672. DOI: 10.2514/6.2015-3672.

[90] D. Wilde, “Applications of inflatable re-entry Technologies - IRT,” 54th International Astronautical Congress of the International Astronautical Federation, the International Academy of Astronautics, and the International Institute of Space Law, 2003. DOI: 10.2514/6.iac-03-u.2.a.03.

[91] V. Finchenko, “Methodology of thermal protection design for descent modules inflatable braking device,” in 54th International Astronautical Congress of the International Astronautical Federation, the International Academy of Astronautics, and the International Institute of Space Law, 2004, pp. I–6.

[92] V. Finchenko, K. Pitchkhadze, A. Ivankov, and N. Voron, “Inflatable re-entry technology for manned martian mission,” in International Astronautical Federation-55th International Astronautical Congress 2004, 2004, pp. 2163–2169.

[93] V. Finchenko, S. Alexashkin, K. Pichkhadze, and S. Ustinov, “Achivements and problems of the inflatable re-entry descent technology development,” in 61st International Astronautical Congress 2010, IAC 2010, 2010, pp. 2045–2055.

[94] K. Pichkhadze, V. Finchenko, S. Aleksashkin, and B. Ostreshko, “Transformable descent vehicles,” Solar System Research, vol. 50, no. 7, pp. 489–497, 2016.

[95] V. S. Finchenko, A. A. Ivankov, M. M. Golomazov, and S. I. Shmatov, “On the use of inflatable decelerators in the design of spacecraft intended for the study of venus,” Solar System Research, vol. 54, no. 7, pp. 595–602, 2020. DOI: 10.1134/s0038094620070059.

[96] В. Финченко, К. Пичхадзе, and В. Ефанов, “Надувные элементы в конструкциях космических аппаратов-прорывная технология в ракетно-космической технике,” 2019.

[97] L. Yates and G. Chapman, “Analysis of data from ballistic range tests of pai-dae vehicles,” Aerospace Computing, Inc., Report, 2007.

[98] S. M. Murman, “Dynamic simulations of atmospheric-entry capsules,” Journal of Spacecraft and Rockets, vol. 46, no. 4, pp. 829–835, 2009. DOI: 10.2514/1.41078.

[99] S. Hughes et al., “Inflatable re-entry Vehicle experiment (IRVE) design overview,” 18th AIAA Aerodynamic Decelerator Systems Technology Conference and Seminar, 2005. DOI: 10.2514/6.2005-1636.

[100] S. O'Keefe and D. Bose, "IRVE-II post-flight trajectory reconstruction," AIAA Atmospheric Flight Mechanics Conference, 2010. DOI: 10.2514/6.2010-7515.

[101] D. L. Lichodziejewski, R. A. Dillman, D. A. Jurewicz, K. Johnson, A. Cassell, and B. A. Tutt, "Ground and flight testing of a stacked torus hypersonic inflatable aerodynamic decelerator configuration," in 54th AIAA/ASME/ASCE/AHS/ASC Structures, Structural Dynamics, and Materials Conference, 2013, p. 1864.

[102] D. Lichodziejewski et al., "Design and testing of the inflatable aeroshell for the irve-3 flight experiment," 53rd AIAA/ASME/ASCE/AHS/ASC Structures, Structural Dynamics and Materials Conference; 20th AIAA/ASME/AHS Adaptive Structures Conference 14th AIAA, 2012. DOI: 10.2514/6.2012-1515.

[103] D. Litton et al., "Inflatable re-entry Vehicle experiment (IRVE) - 4 overview," 21st AIAA Aerodynamic Decelerator Systems Technology Conference and Seminar, 2011. DOI: 10.2514/6.2011-2580.

[104] G. Brown, "Estimating minimum inflation pressure for inflatable aerodynamic decelerators," in 20th AIAA Aerodynamic Decelerator Systems Technology Conference and Seminar, 2009, p. 2970. DOI: 10.2514/6.2009-2970.

[105] J. A. Samareh, "Estimating mass of inflatable aerodynamic decelerators using dimensionless parameters," in 8th International Planetary Probe Workshop 2011 (IPPW-8), NF1676L-12864, 2011.

[106] D. Jurewicz et al., "Design and development of inflatable aeroshell structure for irve-3," 21st AIAA Aerodynamic Decelerator Systems Technology Conference and Seminar, 2011. DOI: 10.2514/6.2011-2522.

[107] E. F. Sheta, V. Venugopalan, X. Tan, P. A. Liever, and S. D. Habchi, "Aero-structural assessment of an inflatable aerodynamic decelerator," Tech. Rep., 2010.

[108] B. R. Hollis, "Surface heating and boundary-layer transition on a hypersonic inflatable aerodynamic decelerator," Journal of Spacecraft and Rockets, vol. 55, no. 4, pp. 856–876, 2018. DOI: 10.2514/1.a34046.

[109] S. P. Schneider, "Laminar-turbulent transition on reentry capsules and planetary probes," Journal of Spacecraft and Rockets, vol. 43, no. 6, pp. 1153–1173, 2006. DOI: 10.2514/1.22594.

[110] Y. Zhao, H. Liu, Z. Liu, and C. Yan, "Numerical study of the cone angle effects on transition and convection heat transfer for hypersonic inflatable aerodynamic decelerator aeroshell," International Communications in Heat and Mass Transfer, vol. 110, p. 104 406, 2020. DOI: 10.1016/j.icheatmasstransfer.2019.104406.

[111] Y. Zhao, J. Chen, and H. Liu, "Application of improved k-- model to deformed hypersonic inflatable aerodynamic decelerator aeroshell," Applied Thermal Engineering, vol. 214, p. 118 794, 2022. DOI: 10.1016/j.applthermaleng.2022.118794.

[112] Y. Zhao, C. Yan, H. Liu, and Y. Qin, "Assessment of laminar-turbulent transition models for hypersonic inflatable aerodynamic decelerator aeroshell in convection heat transfer," International Journal of Heat and Mass Transfer, vol. 132, pp. 825–836, 2019. DOI: 10.1016/j.ijheatmasstransfer.2018.11.025.

[113] J. J. McNamara and P. P. Friedmann, "Aeroelastic and aerothermoelastic analysis in hypersonic flow: Past, present, and future," AIAA Journal, vol. 49, no. 6, pp. 1089–1122, 2011. DOI: 10.2514/1.j050882.

[114] S. Hughes et al., "Hypersonic inflatable aerodynamic decelerator (HIAD) technology development overview," 21st AIAA Aerodynamic Decelerator Systems Technology Conference and Seminar, 2011. DOI: 10.2514/6.2011-2524.

[115] H. Wright et al., "Heart flight test overview," in 9th International Planetary Probe Workshop, Toulouse, France, 2012.

[116] A. Cassell et al., "Design and execution of the hypersonic inflatable aerodynamic decelerator large-article wind tunnel experiment," AIAA Aerodynamic Decelerator Systems (ADS) Conference, 2013. DOI: 10.2514/6.2013-1304.

[117] A. Mazaheri, "HEART Aerothermodynamic Analysis," No. NASA/TM-2012-217568, Tech. Rep., 2012.

[118] A. Mazaheri, "High-energy atmospheric reentry test aerothermodynamic analysis," Journal of Spacecraft and Rockets, vol. 50, no. 2, pp. 270–281, 2013. DOI: 10.2514/1.a32407.

[119] J. Guo, G. Lin, X. Bu, S. Fu, and Y. Chao, "Influence of surface temperature on aerodynamics and aerothermodynamics of an inflatable decelerator," in 2017 8th International Conference on Mechanical and Aerospace Engineering (ICMAE), IEEE, 2017, pp. 463–471.

[120] S. Hughes et al., "Terrestrial HIAD Orbital Reentry (THOR) Flight Test Opportunity," in 11th International Planetary Probe Workshop, vol. 1795, 2014, p. 8113.

[121] R. Dillman et al., "Planned orbital flight test of a 6m hiad," in 15th International Planetary Probe Workshop, 2018.

[122] G. Swanson et al., "LOFTID Aeroshell Engineering Development Unit Structural Testing," in International Planetary Probe Workshop, 2019.

[123] J. Herath, J. Del Corso, N. Cheatwood, J. DiNonno, and D. K. Colter, "Low-earth orbit flight test of an inflatable decelerator (loftid): Robert j. collier trophy presentation," in Collier Trophy Finalist Presentation.

[124] K. B. Thompson, A. J. Wise, and B. R. Hollis, "Improvements to the laura mesh adaptation algorithm," AIAA AVIATION 2023 Forum, 2023. DOI: 10.2514/6.2023-4332.

[125] D. Raymer, Aircraft design: a conceptual approach. American Institute of Aeronautics and Astronautics, Inc., 2012. DOI: 10.1002/9781118352700.ch3.

[126] J. R. Martins and J. T. Hwang, "Review and unification of methods for computing derivatives of multidisciplinary computational models," AIAA Journal, vol. 51, no. 11, pp. 2582–2599, 2013. DOI: 10.2514/1.j052184.

[127] A. Sengupta, M. Wernet, J. Roeder, R. Kelsch, A. Witkowski, and T. Jones, "Supersonic testing of 0.8 m disk gap band parachutes in the wake of a 70 deg sphere cone entry vehicle," 20th AIAA Aerodynamic Decelerator Systems Technology Conference and Seminar, 2009. DOI: 10.2514/6.2009-2974.

[128] V. Carandente, G. Zuppardi, and R. Savino, "Aerothermodynamic and stability analyses of a deployable re-entry capsule," Acta Astronautica, vol. 93, pp. 291–303, 2014. DOI: 10.1016/j.actaastro.2013.07.030.

[129] K. Cornick, B. E. Robertson, and D. N. Mavris, "Parameterization and design space exploration of a hypersonic inflatable aerodynamic decelerator," AIAA SciTech 2023 Forum, 2023. DOI: 10.2514/6.2023-1786.

[130] The Boeing Company, "Delta IV Payload Planners Guide, Citeseer," 1998.

[131] SpaceX, 2020. [Online]. Available: https://www.spacex.com/media/starship_users_guide_v1.pdf.

[132] K. Erlich, E. Wagner, and H. Smith, "New Glenn: Enabling Novel Science with Heavy Lift and a 7-Meter Fairing," in AGU Fall Meeting Abstracts, vol. 2019, 2019, P34C–18.

[133] United Launch Alliance, Atlas V Launch Services User's Guide, 2010. [Online]. Available: https://www.ulalaunch.com/rockets/atlas-v.

[134] R. Lagier, Ariane 5 user's manual, Jul. 2020. [Online]. Available: https://preprod.arianespace.com/publication/ariane-5-users-manual/.

[135] M. S. Anderson, "A structural merit function for aerodynamic decelerators," No. NASA TN D-5535, Tech. Rep., 1969.

[136] E. Mooij, J.-P. Huot, and G. Ortega, "Entry trajectory simulation using ESA Mars Climate Database version 4.1," AIAA/AAS Astrodynamics Specialist Conference and Exhibit, 2006. DOI: 10.2514/6.2006-6023.

[137] T. Forget, E. Millour, T. Pierron, and A. Bierjon, "Mars Climate Database v6.1 Validation Document," ESA Contract No.4000128572/19/NL/AS, Tech. Rep., 2022.

[138] M. D. Smith, "Interannual variability in tes atmospheric observations of mars during 1999–2003," Icarus, vol. 167, no. 1, pp. 148–165, 2004. DOI: 10.1016/j.icarus.2003.09.010.

[139] A. Kleinböhl et al., "Mars climate sounder limb profile retrieval of atmospheric temperature, pressure, and dust and water ice opacity," Journal of Geophysical Research: Planets, vol. 114, no. E10, 2009. DOI: 10.1029/2009je003358.

[140] M. D. Smith et al., "Emirs observations of the aphelion-season Mars Atmosphere," Geophysical Research Letters, vol. 49, no. 15, 2022. DOI: 10.1029/2022gl099636.

[141] L. Lange et al., "Insight pressure data recalibration, and its application to the study of long-term pressure changes on mars," 2022. DOI: 10.1002/essoar.10510225.1.

[142] E. Millour et al., "The Mars Climate Database (version 6.1)," European Space Agency, 2022. DOI: 10.5194/epsc2022-786.

[143] U. C. for Atmospheric Research, Network Common Data Form (NetCDF). [Online]. Available: https://www.unidata.ucar.edu/software/netcdf/.

[144] M. Aznar et al., "Raman-IR Spectroscopic, and XRD analysis of selected samples from Fogo Island, Cabo Verde: Implications for ancient Martian volcanology," Advances in Space Research, 2023.

[145] B. K. Muirhead, A. K. Nicholas, J. Umland, O. Sutherland, and S. Vijendran, "Mars sample return campaign concept status," Acta Astronautica, vol. 176, pp. 131–138, 2020. DOI: 10.1016/j.actaastro.2020.06.026.

[146] S. W. Albert, H. Schaub, and R. D. Braun, "Co-delivery of multiple small probes to the martian surface," AIAA SCITECH 2022 Forum, 2022. DOI: 10.2514/6.2022-1653.

[147] L. Boltzmann, Lectures on gas theory. Univ of California Press, 2022.

[148] B. J. McBride, Coefficients for calculating thermodynamic and transport properties of individual species. National Aeronautics and Space Administration, Office of Management, 1993, vol. 4513.

[149] G. A. Bird, "Molecular gas dynamics and the direct simulation of gas flows," Molecular gas dynamics and the direct simulation of gas flows, 1994.

[150] J. O. Hirschfelder, C. F. Curtiss, and R. B. Bird, “Molecular theory of gases and liquids,” Molecular theory of gases and liquids, 1964. DOI: 10.1002/pol.1955.120178311.

[151] G. A. Bird, “Definition of mean free path for real gases,” Physics of Fluids, vol. 26, no. 11, p. 3222, 1983. DOI: 10.1063/1.864095.

[152] N. X. Vinh, A. Busemann, and R. D. Culp, “Hypersonic and planetary entry flight mechanics,” NASA Sti/Recon Technical Report A, vol. 81, p. 16 245, 1980.

[153] Journal of the Franklin Institute, vol. 276, no. 2, p. 176, 1963. DOI: 10.1016/0016-0032(63)90423-x.

[154] E. Mooij, AE4870B - Re-entry Systems. Delft University of Technology, Lecture Notes, 2017.

[155] E. Mooij, J.-P. Huot, and G. Ortega, “Entry trajectory simulation using ESA Mars Climate Database version 4.1,” AIAA/AAS Astrodynamics Specialist Conference and Exhibit, 2006. DOI: 10.2514/6.2006-6023.

[156] L. V. Lorenzoni, M. SanMartin, A. Steltzner, and A. Chen, “Preliminary assessment of msl edl sensitivity to martian environments,” 2007 IEEE Aerospace Conference, 2007. DOI: 10.1109/aero.2007.352822.

[157] F. J. Regan, Dynamics of atmospheric re-entry. AIAA, 1993.

[158] N. A. F. Senan, “A brief introduction to using ode45 in matlab,” University of California at Berkeley, USA, 2007. DOI: 10.1016/b978-0-444-63363-7.00008-8.

[159] W. H. Press, S. A. Teukolsky, W. T. Vetterling, and B. P. Flannery, Numerical recipes 3rd edition: The art of scientific computing. Cambridge university press, 2007.

[160] M. Grant and R. Braun, “Analytic hypersonic aerodynamics for conceptual design of entry vehicles,” 48th AIAA Aerospace Sciences Meeting Including the New Horizons Forum and Aerospace Exposition, 2010. DOI: 10.2514/6.2010-1212.

[161] G. Pezzella, P. Catalano, and A. Bourgoing, “Computational flowfield analysis of a sample return capsule,” 18th AIAA/3AF International Space Planes and Hypersonic Systems and Technologies Conference, 2012. DOI: 10.2514/6.2012-5818.

[162] A. Viviani and G. Pezzella, “Aerodynamic analysis of a capsule vehicle for a manned exploration mission to mars,” 16th AIAA/DLR/DGLR International Space Planes and Hypersonic Systems and Technologies Conference, 2009. DOI: 10.2514/6.2009-7386.

[163] L. A. Sinpetru, N. H. Crisp, D. Mostaza-Prieto, S. Livadiotti, and P. C. Roberts, “ADBSAT: Methodology of A novel panel method tool for aerodynamic analysis of satellites,” Computer Physics Communications, vol. 275, p. 108 326, 2022. DOI: 10.1016/j.cpc.2022.108326.

[164] D. Mostaza-Prieto, “Characterisation and applications of aerodynamic torques on satellites,” Ph.D. dissertation, The University of Manchester (United Kingdom), 2017.

[165] J. D. Anderson, Hypersonic and high-temperature gas dynamics. American Institute of Aeronautics and Astronautics, 2006.

[166] P.-O. Persson and G. Strang, “A simple mesh generator in matlab,” SIAM Review, vol. 46, no. 2, pp. 329–345, 2004. DOI: 10.1137/s0036144503429121.

[167] I. Newton, The Principia: mathematical principles of natural philosophy. Univ of California Press, 1999.

[168] S. Livadiotti et al., "A review of gas-surface interaction models for orbital aerodynamics applications," Progress in Aerospace Sciences, vol. 119, p. 100 675, 2020. DOI: 10.1016/j.paerosci.2020.100675.

[169] D. Mostaza Prieto, B. P. Graziano, and P. C. Roberts, "Spacecraft drag modelling," Progress in Aerospace Sciences, vol. 64, pp. 56–65, 2014. DOI: 10.1016/j.paerosci.2013.09.001.

[170] R. W. Shane and R. H. Tolson, "Aerothermodynamics of the mars global surveyor spacecraft," Tech. Rep., 1998.

[171] F. J. Cestero and R. H. Tolson, "Magellan aerodynamic characteristics during the termination experiment including thruster plume-free stream interaction," Tech. Rep., 1998.

[172] R. H. Tolson, M. T. Patterson, and D. T. Lyons, "Magellan windmill and termination experiments," in Spaceflight Dynamics, CNES June 1995 Conference, Toulouse, France, vol. 9, 1995.

[173] R. H. Tolson, R. A. Lugo, D. T. Baird, A. D. Cianciolo, S. W. Bougher, and R. M. Zurek, "Atmospheric Modeling Using Accelerometer Data During Mars Atmosphere and Volatile Evolution (MAVEN) Flight Operations," in AAS/AIAA Space Flight Mechanics Meeting, 2017.

[174] L. A. Sinpetru et al., "ADBSAT: Verification and validation of a novel panel method for quick aerodynamic analysis of satellites," Computer Physics Communications, vol. 275, p. 108 327, 2022. DOI: 10.1016/j.cpc.2022.108327.

[175] L. H. Sentman, Free molecule flow theory and its application to the determination of aerodynamic forces, 1961. DOI: 10.21236/ad0265409.

[176] R. W. Jeffery, "The aerodynamics of wings in low density hypersonic flow," Ph.D. Dissertation, Imperial College London (United Kingdom), 1975.

[177] P. A. Chambre and S. A. Schaaf, Flow of rarefied gases, 1961. DOI: 10.1515/9781400885800.

[178] C. Cercignani and M. Lampis, "Kinetic models for gas-surface interactions," Transport Theory and Statistical Physics, vol. 1, no. 2, 1971. DOI: 10.1080/00411457108231440.

[179] A. Walker, P. Mehta, and J. Koller, "Drag coefficient model using the cercignani–lampis–lord gas–surface interaction model," Journal of Spacecraft and Rockets, vol. 51, no. 5, pp. 1544–1563, 2014. DOI: 10.2514/1.a32677.

[180] J. A. Storch, Aerodynamic disturbances on spacecraft in free-molecular flow, 2002. DOI: 10.21236/ada410696.

[181] G. Cook, "Satellite drag coefficients," Planetary and Space Science, vol. 13, no. 10, pp. 929–946, 1965. DOI: 10.1016/0032-0633(65)90150-9.

[182] R. Wilmoth, R. Mitcheltree, J. Moss, R. Wilmoth, R. Mitcheltree, and J. Moss, "Low-density aerodynamics of the stardust sample return capsule," 32nd Thermophysics Conference, 1997. DOI: 10.2514/6.1997-2510.

[183] R. Wilmoth, R. Blanchard, and J. Moss, "Rarefied transitional bridging of blunt body aerodynamics," in 21st International Symposium on Rarefied Gas Dynamics, 1998.

[184] R. C. Blanchard, "Rarefied flow lift-to-drag measurements of the shuttle orbiter," 1986.

[185] R. C. Blanchard, "Rarefied-flow aerodynamics measurement experiment on the aeroassist flight experiment vehicle," Journal of Spacecraft and Rockets, vol. 28, no. 4, pp. 368–375, 1991. DOI: 10.2514/3.26256.

[186] J. D. Fuller and R. H. Tolson, "Improved method for the estimation of spacecraft free-molecular aerodynamic properties," Journal of Spacecraft and Rockets, vol. 46, no. 5, pp. 938–948, 2009. DOI: 10.2514/1.43205.

[187] G. Benedetti, N. Viola, E. Minisci, A. Falchi, and M. Vasile, "Low-fidelity modelling for aerodynamic characteristics of re-entry objects," Astrophysics and Space Science Proceedings, pp. 247–264, 2018. DOI: 10.1007/978-3-319-69956-1_15.

[188] D. Mostaza-Prieto and P. C. Roberts, "Methodology to analyze attitude stability of satellites subjected to aerodynamic torques," Journal of Guidance, Control, and Dynamics, vol. 39, no. 3, pp. 437–449, 2016. DOI: 10.2514/1.g001481.

[189] L. Sinpetru, "Optimising satellite geometries to minimise drag in very low earth orbits," Ph.D. dissertation, University of Manchester, 2022.

[190] T. K. West and A. M. Brandis, "Updated stagnation point aeroheating correlations for mars entry," 2018 Joint Thermophysics and Heat Transfer Conference, 2018. DOI: 10.2514/6.2018-3767.

[191] A. M. Brandis and C. O. Johnston, "Characterization of stagnation-point heat flux for earth entry," 45th AIAA Plasmadynamics and Lasers Conference, 2014. DOI: 10.2514/6.2014-2374.

[192] L. LEES, "Laminar heat transfer over blunt-nosed bodies at hypersonic flight speeds," Journal of Jet Propulsion, vol. 26, no. 4, pp. 259–269, 1956. DOI: 10.2514/8.6977.

[193] J. A. Fay and F. R. Riddell, "Theory of stagnation point heat transfer in dissociated air," Journal of the Aerospace Sciences, vol. 25, no. 2, pp. 73–85, 1958. DOI: 10.2514/8.7517.

[194] J. Bertin, Hypersonic aerothermodynamics, 1994. DOI: 10.2514/4.470363.

[195] N. H. Kemp and F. R. Riddell, "Heat transfer to satellite vehicles re-entering the atmosphere," Journal of Jet Propulsion, vol. 27, no. 2, pp. 132–137, 1957. DOI: 10.2514/8.12603.

[196] E. Reshotko and C. B. Cohen, "Heat transfer at the forward stagnation point of blunt bodies," Tech. Rep., 1955.

[197] K. Sutton and R. A. Graves Jr, "A general stagnation-point convective heating equation for arbitrary gas mixtures," Tech. Rep., 1971.

[198] C. Catalfamo, D. Bruno, G. Colonna, A. Laricchiuta, and M. Capitelli, "High temperature mars atmosphere. part ii: Transport properties," The European Physical Journal D, vol. 54, no. 3, pp. 613–621, 2009. DOI: 10.1140/epjd/e2009-00193-6.

[199] T. K. West IV and A. M. Brandis, "Stagnation-Point Aeroheating Correlations for Mars Entry," Journal of Spacecraft and Rockets, vol. 57, no. 2, pp. 319–327, 2020. DOI: 10.2514/1.A34602.

[200] F. De Filippis and M. Serpico, "Air high-enthalpy stagnation point heat flux calculation," Journal of Thermophysics and Heat Transfer, vol. 12, no. 4, pp. 608–610, 1998. DOI: 10.2514/2.6386.

[201] R. Detra, "Addendum to heat transfer to satellite vehicle reentering the atmosphere," Jet Propulsion, pp. 1256–1257, 1957.

[202] P. H. ROSE and W. I. STARK, "Stagnation point heat-transfer measurements in dissociated air," Journal of the Aerospace Sciences, vol. 25, no. 2, pp. 86–97, 1958. DOI: 10.2514/8.7519.

[203] E. R. Van Driest, The problem of aerodynamic heating. Institute of the Aeronautical Sciences, 1956.

[204] D. R. Chapman, An approximate analytical method for studying entry into planetary atmospheres. US Government Printing Office, 1959.

[205] A. Diwakar and K. Bodi, "Numerical and empirical studies of heat transfer in high-enthalpy argon–air mixtures," Journal of Thermophysics and Heat Transfer, vol. 36, no. 3, pp. 694–706, 2022. DOI: 10.2514/1.t6311.

[206] E. Mooij, "Dynamic inversion heat-flux tracking for hypersonic entry," AIAA SCITECH 2023 Forum, 2023. DOI: 10.2514/6.2023-2499.

[207] S. K. Martinelli and R. D. Braun, "Centerline heating methodology for use in preliminary design studies," 2011 Aerospace Conference, 2011. DOI: 10.1109/aero.2011.5747498.

[208] A. Falchi, L. Gentile, E. Minisci, M. Tirelli, and P. Perugini, "Launcher vehicle aerothermodynamics and fairing separation altitude effects on payload temperature," in 8th European Conference for Aeronautics and Space Sciences (EUCASS), 2019.

[209] G. Koppenwallner, B. Fritsche, T. Lips, and H. Klinkrad, "Scarab-a multi-disciplinary code for destruction analysis of space-craft during re-entry," in Fifth European Symposium on Aerothermodynamics for Space Vehicles, vol. 563, 2005, p. 281.

[210] H. Legge, "Hypersonic approximations for heat transfer and shear stress applied to continuum and rarefied plume impingement," DFVLR-ib, vol. 222, 1987.

[211] P. Mehta, E. Minisci, M. Vasile, A. C. Walker, and M. Brown, "An open source hypersonic aerodynamic and aerothermodynamic modelling tool," in 8th European Symposium on Aerothermodynamics for Space Vehicles, 2015.

[212] N. Singh and T. E. Schwartzentruber, "Heat flux correlation for high-speed flow in the transitional regime," Journal of Fluid Mechanics, vol. 792, pp. 981–996, 2016. DOI: 10.1017/jfm.2016.118.

[213] C. Johnston and A. Brandis, "Modeling of nonequilibrium co fourth-positive and cn violet emission in co 2 –n 2 gases," Journal of Quantitative Spectroscopy and Radiative Transfer, vol. 149, pp. 303–317, 2014. DOI: 10.1016/j.jqsrt.2014.08.025.

[214] N. H. Kemp, P. H. Rose, and R. W. Detra, "Laminar heat transfer around blunt bodies in dissociated air," Journal of the Aerospace Sciences, vol. 26, no. 7, pp. 421–430, 1959. DOI: 10.2514/8.8128.

[215] N. F. Krasnov, "Aerodynamics of bodies of revolution," Elsevier, New York, Chaps 6 and 7, Tech. Rep., 1970.

[216] M. J. Santos, S. Hosder, and T. K. West, "Multifidelity turbulent heating prediction of hypersonic inflatable aerodynamic decelerators with surface scalloping," Journal of Spacecraft and Rockets, vol. 58, no. 5, pp. 1325–1338, 2021. DOI: 10.2514/1.a34936.

[217] J. Wu, Q. Xu, Z. Zhang, and A. Hou, "Aeroelastic characteristics of inflatable reentry vehicle in transonic and supersonic regions," Computers & Fluids, vol. 237, p. 105 338, 2022. DOI: 10.1016/j.compfluid.2022.105338.

[218] J. Wu, Z. Zhang, A. Hou, X. Xue, and X. Cao, "Thermal aeroelastic characteristics of Inflatable Reentry Vehicle Experiment (IRVE) in Hypersonic Flow, volume=2021," International Journal of Aerospace Engineering, pp. 1–17, 2021. DOI: 10.1155/2021/6673818.

[219] H. Schlichting and J. Kestin, Boundary layer theory. Springer, 1961, vol. 121.

[220] A. Flinton et al., "Developing a flexible thermal protection system for mars entry: Thermal design and testing," 2nd International Conference on Flight Vehicles, Aerothermodynamics and Re-entry Missions Engineering, 2022.

[221] B. III and E. Walter, "Aeroassist Inflatable Re-entry System (AIRS) Thermal Protection System (TPS) Thermal Analysis," STSB-2006-002, Tech. Rep., February 2006.

[222] T. Miyakita, R. Hatakenaka, H. Sugita, M. Saitoh, and T. Hirai, "Evaluation of thermal insulation performance of a new multi-layer insulation with non-interlayer-contact spacer," 45th International Conference on Environmental Systems, 2015.

[223] M. Ferraiuolo and O. Manca, "Heat transfer in a multi-layered thermal protection system under aerodynamic heating," International Journal of Thermal Sciences, vol. 53, pp. 56–70, 2012. DOI: 10.1016/j.ijthermalsci.2011.10.019.

[224] Y. Tanigawa, T. Akai, R. Kawamura, and N. Oka, "Transient heat conduction and thermal stress problems of a nonhomogeneous plate with temperature-dependent material properties," Journal of Thermal Stresses, vol. 19, no. 1, pp. 77–102, 1996. DOI: 10.1080/01495739608946161.

[225] H. Zhu, B. V. Sankar, R. T. Haftka, S. Venkataraman, and M. Blosser, "Optimization of functionally graded metallic foam insulation under transient heat transfer conditions," Structural and multidisciplinary optimization, vol. 28, pp. 349–355, 2004. DOI: 10.1007/s00158-004-0463-3.

[226] W. Sobieski and A. Trykozko, "Discretisation of thermal diffusion equation in multilayer structures with variable material parameters and different thicknesses," Journal of Applied Computer Science, Vol. 26, No. 2, Wydawnictwo Politechniki Łódzkiej, Łódź 2018, ISSN 1507-0360., 2018.

[227] S. V. Patankar, "Numerical heat transfer and fluid flow," 2018. DOI: 10.1201/9781482234213.

[228] J. P. Holman, Heat transfer. McGraw Hill Higher Education, 2010.

[229] A. M. Albaghdadi, M. B. Baharom, and S. A. bin Sulaiman, "Parameter design optimization of the crank-rocker engine using the FMINCON function in MATLAB," in IOP Conference Series: Materials Science and Engineering, IOP Publishing, vol. 1088, 2021, p. 012 072. DOI: 10.1088/1757-899x/1088/1/012072.

[230] D. Bose, M. Toniolo, S. O'Keefe, F. Cheatwood, S. Hughes, and R. Dillman, "Impact of vehicle flexibility on irve-ii flight dynamics," 21st AIAA Aerodynamic Decelerator Systems Technology Conference and Seminar, 2011. DOI: 10.2514/6.2011-2571.

[231] B. R. Hollis, "Surface heating and boundary-layer transition on a hypersonic inflatable aerodynamic decelerator," Journal of Spacecraft and Rockets, vol. 55, no. 4, pp. 856–876, 2018. DOI: 10.2514/1.a34046.

[232] Z. Xiaoshun, Y. Li, and Y. Xue, "The prediction of aerodynamic performance of inflatable reentry vehicle at various speeds and attack angles," Spacecraft Recovery & Remote Sensing, vol. 37, no. 5, p. 27, 2016. DOI: 10.3969/j.issn.1009-8518.2016.05.004.

[233] D. Wilde and S. Walther, "Inflatable re-entry and descent technology (IRDT)-further developments," in Proceedings of the 2nd International Symposium of Atmospheric Reentry Vehicles and Systems, 2001.

[234] J. Moss, R. Wilmoth, J. Price, J. Moss, R. Wilmoth, and J. Price, "DSMC simulations of blunt body flows for Mars entries - mars pathfinder and Mars microprobe capsules," 32nd Thermophysics Conference, 1997. DOI: 10.2514/6.1997-2508.

[235] D. M. Bose, J. Shidner, R. Winski, C. Zumwalt, F. Cheatwood, and S. J. Hughes, "The hypersonic inflatable aerodynamic decelerator (HIAD) mission applications study," in AIAA Aerodynamic Decelerator Systems (ADS) Conference, 2013, p. 1389. DOI: 10.2514/6.2013-1389.

[236] C. O. Johnston, A. Mazaheri, P. Gnoffo, B. Kleb, and D. Bose, "Radiative heating uncertainty for hyperbolic earth entry, part 1: Flight simulation modeling and uncertainty," Journal of Spacecraft and Rockets, vol. 50, no. 1, pp. 19–38, 2013. DOI: 10.2514/1.a32254.

[237] A. Mazaheri, C. O. Johnston, and S. Sefidbakht, "Three-dimensional radiation ray-tracing for shock-layer radiative heating simulations," Journal of Spacecraft and Rockets, vol. 50, no. 3, pp. 485–493, 2013. DOI: 10.2514/1.a32448.

[238] A. J. Brune, T. K. West IV, S. Hosder, and K. T. Edquist, "Uncertainty analysis of mars entry flows over a hypersonic inflatable aerodynamic decelerator," Journal of Spacecraft and Rockets, vol. 52, no. 3, pp. 776–788, 2015. DOI: 10.2514/1.a33131.

[239] R. J. Hull and M. L. Lander, "Laser hardened materials evaluation laboratory (lhmel)," International Congress on Applications of Lasers and Electro-Optics, 1994. DOI: 10.2351/1.5058837.

[240] G. Xie, Q. Wang, B. Sunden, and W. Zhang, "Thermomechanical optimization of lightweight thermal protection system under aerodynamic heating," Applied Thermal Engineering, vol. 59, no. 1-2, pp. 425–434, 2013. DOI: 10.1016/j.applthermaleng.2013.06.002.

[241] B. M. Betsy, P. K. Mereena, R. M. Rincy, K. K. Vishnupriya, and D. Deepak, "Design of thermal protection system for low ballistic coefficient ballute for ballistic earth re-entry," International Research Journal of Engineering and Technology (IRJET), vol. 7, no. 9, pp. 211–230, Sep. 2020.

[242] R. D. Lorenz, "Planetary penetrators: Their origins, history and future," Advances in Space Research, vol. 48, no. 3, pp. 403–431, 2011. DOI: 10.1016/j.asr.2011.03.033.

[243] Е. В. Леун, И. М. Нестерин, К. М. Пичхадзе, А. А. Поляков, and В. К. Сысоев, "Обзор схем пенетраторов для контактных исследований космических объектов," Космическая техника и технологии, no. 2 (37), pp. 103–117, 2022.

[244] L. Charles K, "Mars penetrator: Subsurface science mission," Tech. Rep., 1974.

[245] G. Scoon and G. Whitcomb, "Marsnet: A precursor to the surface exploration of mars," Acta Astronautica, vol. 29, no. 10-11, pp. 823–831, 1993.

[246] A. Chicarro, G. Scoon, and M. Coradini, "Marsnet-a network of stations on the surface of mars.," ESA Journal, vol. 17, no. 3, pp. 225–237, 1993.

[247] L. A. Manning, "Mars surface penetrator: System description," Tech. Rep., 1977.

[248] A.-M. Harri et al., "The metnet vehicle: A lander to deploy environmental stations for local and global investigations of mars," Geoscientific Instrumentation, Methods and Data Systems, vol. 6, no. 1, pp. 103–124, 2017. DOI: 10.5194/gi-6-103-2017.

[249] M. Genzer et al., "Miniature planetary in-situ sensors (minipins)–design status and the latest activities," Copernicus Meetings, Tech. Rep., 2022.

[250] I. Arruego, M. Genzer, V. Apéstigue, J. Martìnez-Oter, A. Gonzalo, and M. Hieta, "Miniature sensors packages and delivery system for mars exploration," Low-Cost Science Mission Concepts, 2022.

[251] M. Genzer, "Miniature Planetary In-situ Sensors (MiniPINS) - MINS lander," Moving to Mars: 2022 International Workshop on Technology Development for Mars Human Exploration. Montreal, Canada, Nov. 2022.

[252] S. M. Curry and D. J. Banfield, Low-Cost Science Mission Concepts for Mars Exploration: March 29–31, 2022, Pasadena, California, 2022.

[253] H. Haukka, "Mars-laskeutujan sähköisten järjestelmien mitoitus tieteellisten operaatioiden optimoimiseksi," Aalto-yliopisto, 2021. [Online]. Available: https://helda.helsinki.fi/handle/10138/342351.

[254] A. Alekseev, P. G.A., and F. V.S., "Aerodynamics of a penetrator in the martian atmosphere," Cosmic Research, vol. 34, no. 1, pp. 90–92, 1996.

[255] J. Samareh and D. Komar, "Parametric mass modeling for mars entry, descent and landing system analysis study," 49th AIAA Aerospace Sciences Meeting including the New Horizons Forum and Aerospace Exposition, 2011. DOI: 10.2514/6.2011-1038.

[256] G. Brown, "Inflatable structures for deployable aerocapture decelerators," in Proceedings of JANNAF Conference, 2005.

[257] L. Bianchi, M. Dorigo, L. M. Gambardella, and W. J. Gutjahr, "A survey on metaheuristics for stochastic combinatorial optimization," Natural Computing, vol. 8, no. 2, pp. 239–287, 2008. DOI: 10.1007/s11047-008-9098-4.

[258] Y. Xin-She, "An introduction with metaheuristic applications," Engineering Optimization, 2010.

[259] M. Dorigo, "Optimization, learning and natural algorithms," Ph. D. Thesis, Politecnico di Milano, 1992.

[260] Z. W. Geem, J. H. Kim, and G. Loganathan, "A new heuristic optimization algorithm: Harmony search," Simulation, vol. 76, no. 2, 2001. DOI: 10.1177/003754970107600201.

[261] D. Karaboga et al., "An idea based on honey bee swarm for numerical optimization," Technical report-TR06, Erciyes university, engineering faculty, computer science, Tech. Rep., 2005.

[262] J. Kennedy and R. Eberhart, "Particle swarm optimization," Proceedings of ICNN'95 - International Conference on Neural Networks, 1995. DOI: 10.1109/icnn.1995.488968.

[263] D. Wolpert and W. Macready, "No free lunch theorems for optimization," IEEE Transactions on Evolutionary Computation, vol. 1, no. 1, pp. 67–82, 1997. DOI: 10.1109/4235.585893.

[264] A. K. Kar, "Bio inspired computing – a review of algorithms and scope of applications," Expert Systems with Applications, vol. 59, pp. 20–32, 2016. DOI: 10.1016/j.eswa.2016.04.018.

[265] S. Sivanandam and S. Deepa, "Applications of genetic algorithms," Introduction to Genetic Algorithms, pp. 317–402, 2008. DOI: 10.1007/978-3-540-73190-0_10.

[266] D. A. Coley, "An introduction to genetic algorithms for scientists and engineers," World Scientific, 1999. DOI: 10.1142/3904.

[267] K. Deep, K. P. Singh, M. Kansal, and C. Mohan, "A real coded genetic algorithm for solving integer and mixed integer optimization problems," Applied Mathematics and Computation, vol. 212, no. 2, pp. 505–518, 2009. DOI: 10.1016/j.amc.2009.02.044.

[268] C. Dai, Y. Zhu, and W. Chen, “Adaptive probabilities of crossover and mutation in genetic algorithms based on cloud model,” 2006 IEEE Information Theory Workshop, 2006. DOI: 10.1109/itw.2006.322912.

[269] S. Koziel and X.-S. Yang, Computational optimization, methods and algorithms. Springer, 2011, vol. 356.

[270] D. Litton et al., “Inflatable re-entry Vehicle experiment (IRVE) - 4 overview,” 21st AIAA Aerodynamic Decelerator Systems Technology Conference and Seminar, 2011. DOI: 10.2514/6.2011-2580.

[271] A. Falchi, “Atmospheric re-entry analysis of space objects,” Ph.D. dissertation, University of Strathclyde, 2020.

[272] N. Donaldson, “Hypersonic modelling and testing of space debris during planetary entry,” Ph.D. dissertation, University of Oxford, 2019.

[273] T. Lips and B. Fritsche, “A comparison of commonly used re-entry analysis tools,” Acta Astronautica, vol. 57, no. 2–8, pp. 312–323, 2005. DOI: 10.1016/j.actaastro.2005.03.010.

[274] J. Annaloro et al., “Aerothermodynamics modelling of complex shapes in the debrisk atmospheric reentry tool: Methodology and validation,” Acta Astronautica, vol. 171, pp. 388–402, 2020. DOI: 10.1016/j.actaastro.2020.03.006.

[275] F. Sourgen, Y. Prévereaud, J.-L. Vérant, E. Laroche, and J.-M. Moschetta, “Music/fast, a pre-design and pre-mission analysis tool for the earth atmospheric re-entry of spacecraft, capsules and de-orbited satellites,” 2015.

[276] W. Rochelle, B. Kirk, and B. Ting, “User’s guide for object reentry analysis tool (ORSAT) version 5.0, vol. 1, jsc-28742, NASA,” Johnson Space Center, 1999.

[277] J. Annaloro, P. Omaly, V. Rivola, and M. Spel, “Elaboration of a new spacecraft-oriented tool: Pampero,” in Proceedings of the 8th European Symposium on Aerothermodynamics for Space Vehicles, 2014.

[278] J. Merrifield, J. Beck, G. Markelov, and R. Molina, “Simplified aerothermal models for destructive entry analysis,” in 8th European Symposium and Aerothermodynamics for Space Vehicles, 2015.

[279] I. Pontijas Fuentes et al., “Upgrade of ESA’s debris risk assessment and mitigation analysis (Drama) tool: Spacecraft entry survival analysis module,” Acta Astronautica, vol. 158, pp. 148–160, 2019. DOI: 10.1016/j.actaastro.2017.12.001.

[280] D. Litton et al., “Inflatable re-entry Vehicle experiment (IRVE) - 4 overview,” 21st AIAA Aerodynamic Decelerator Systems Technology Conference and Seminar, 2011. DOI: 10.2514/6.2011-2580.

[281] A. Niehoff J; Friedlander, “Pioneer mars 1979 mission options,” Mechanics and Control of Flight Conference, 1974. DOI: 10.2514/6.1974-783.

[282] Y. A. Surkov and R. Kremnev, “Mars-96 mission: Mars exploration with the use of penetrators,” Planetary and Space Science, vol. 46, no. 11-12, pp. 1689–1696, 1998. DOI: 10.1016/s0032-0633(98)00071-3.

[283] A. V. Zakharov and H. Fechtig, “The Mars-94 and Mars-96 missions,” Philosophical Transactions of the Royal Society of London. Series A: Physical and Engineering Sciences, vol. 349, no. 1690, pp. 295–307, 1994. DOI: 10.1098/rsta.1994.0133.

[284] V. Linkin et al., “A sophisticated lander for scientific exploration of mars: Scientific objectives and implementation of the Mars-96 small station,” Planetary and Space Science, vol. 46, no. 6-7, pp. 717–737, 1998. DOI: 10.1016/s0032-0633(98)00008-7.

[285] B. Harvey, Russian planetary exploration: history, development, legacy and prospects. Springer Science & Business Media, 2007.

[286] H. Shiraishi et al., “Investigation of martian surface and interior structures by multiple penetrator probes,” Transaction of the Japan Society for Aeronautical and Space Sciences, Aerospace Technology Japan, vol. 12, no. 29, pp. 71–76, 2014.

[287] O. Alifanov, N. Anfimov, V. Belyaev, B. Bodin, et al., “Fundamental’nye kosmicheskie issledovaniya,” Astrofizika,

[288] A. Albee et al., “Report on the loss of the mars polar lander and deep space 2 missions,” 2000.

[289] R. Gowen et al., “An update on MoonLITE,” in Proceedings of 59th International Astronautical Congress, vol. 7, 2008, pp. 4359–4369.

[290] P. Wurz et al., “An impacting descent probe for europa and the other galilean moons of jupiter,” Earth, moon, and planets, vol. 120, no. 2, pp. 113–146, 2017. DOI: 10.48550/arXiv.1711.02452.

[291] R. A. Gowen et al., “Penetrators for in situ subsurface investigations of Europa,” Advances in Space Research, vol. 48, no. 4, pp. 725–742, 2011. DOI: 10.1016/j.asr.2010.06.026.

[292] A. Galeev, E. Gusev, V. Rodchenko, and E. Sadretdinova, “Vybor parametrov penetratora, vkhodiashchego v lunnyi grunt s nulevoi skorost’iu [choice of parameters of penetrator with jet thruster that enters into lunar ground with zero impact velocity],” Trudy MAI, no. 64, pp. 1–23, 2013.

[293] E. Sadretdinova, “Metod vybora proektnykh parametrov reaktivnykh penetratorov dlia dvizheniia v lunnom grunte [design of penetrator with jet thrusteras applied to motion in lunar ground],” Dissertatsiia na soiskanie uchenoi stepeni kandidata tekhnicheskikh nauk. Moskovskii aviatsionnyi institut, 2014.

[294] A. Bagrov, “Sysoev vk kontseptsiya skorostnogo penetratora dlya dostavki poleznoi nagruzki na kosmicheskie tela [a concept of a high-velocity penetrator to deliver payloads to space bodies],” Kosmicheskie issledovaniya, vol. 53, no. 6, pp. 521–529, 2015.

[295] J. Bibring et al., “The ROSETTA lander (“PHILAE”) investigations,” Space science reviews, vol. 128, no. 1, pp. 205–220, 2007.

[296] R. Winglee, C. Truitt, and R. Shibata, “High velocity penetrators used a potential means for attaining core sample for airless solar system objects,” Acta Astronautica, vol. 137, pp. 274–286, 2017. DOI: 10.1016/j.actaastro.2017.04.022.

[297] R. Winglee, T. Robinson, M. Danner, and J. Koch, “Cryo-braking using penetrators for enhanced capabilities for the potential landing of payloads on icy solar system objects,” Acta Astronautica, vol. 144, pp. 136–146, 2018. DOI: 10.1016/j.actaastro.2017.12.019.

[298] T. Saiki et al., “The small carry-on impactor (SCI) and the Hayabusa2 impact experiment,” Space Science Reviews, vol. 208, no. 1, pp. 165–186, 2017. DOI: 10.1007/s11214-016-0297-5.

[299] T. Saiki et al., “Small carry-on impactor of Hayabusa2 mission,” Acta Astronautica, vol. 84, pp. 227–236, 2013. DOI: 10.1016/j.actaastro.2012.11.010.

[300] T. Kimoto, "Sic material properties," Wide Bandgap Semiconductor Power Devices, pp. 21–42, 2019. DOI: 10.1016/b978-0-08-102306-8.00002-2.

[301] W.-b. Yuan, N. Yu, L.-y. Li, and Y. Fang, "Heat transfer analysis in multi-layered materials with interfacial thermal resistance," Composite Structures, vol. 293, p. 115 728, 2022. DOI: 10.1016/j.compstruct.2022.115728.

[302] G. Brown, "Estimating minimum inflation pressure for inflatable aerodynamic decelerators," 20th AIAA Aerodynamic Decelerator Systems Technology Conference and Seminar, 2009. DOI: 10.2514/6.2009-2970.

[303] G. Brown, C. Epp, C. Graves, S. Lingard, M. Darley, and K. Jordan, "Hypercone inflatable supersonic decelerator," 17th AIAA Aerodynamic Decelerator Systems Technology Conference and Seminar, 2003. DOI: 10.2514/6.2003-2167.

[304] G. J. Brown and G. C. Sharpless, Braided airbeam structure, US Patent 5,735,083, Apr. 1998.

[305] J. L. Sanders and A. A. Liepins, "Toroidal membrane under internal pressure," AIAA Journal, vol. 1, no. 9, pp. 2105–2110, 1963. DOI: 10.2514/3.2001.

[306] Z. Ilich, G. Grossir, and O. Chazot, "Evaluation of the stagnation-point velocity gradient in low-enthalpy hypersonic flows," 33rd AIAA Aerodynamic Measurement Technology and Ground Testing Conference, 2017. DOI: 10.2514/6.2017-3984.

A. State-of-the Art of (Re-)Entry Codes

The literature review in chapter 2 provides an in-depth analysis of the technological advancements and modelling challenges associated with stacked-toroid IADs. However, to further enhance the understanding and motivation behind the current study, a concise summary of the state-of-the-art (re-)entry codes and their respective capabilities is presented in Table A.1. For a more detailed exploration of each code, readers are encouraged to refer to the PhD theses of Falchi [271] and Donaldson [272], which served as the primary sources for extending the information in Table A.1.

The research presented in this study introduces a novel and comprehensive environment that offers several key advantages. Firstly, it facilitates the rapid evaluation of aerodynamics, aerothermodynamics, and thermal characteristics of an entry vehicle in various flow conditions, spanning from rarefied to continuum regimes. This integrated environment is particularly noteworthy because it allows for multidisciplinary optimization while considering the deformation of the stacked-toroid structure. Moreover, it is important to highlight that the current landscape of available codes is primarily focused on Earth re-entry applications. While these codes excel in modeling structural breakup for demise, none of them possess the capability to model and optimize the performance of a stacked-toroid on Mars across all flow conditions, while accounting for the scalloping phenomenon.

Code	Developer	Geometry	Aerodynamics	Aerothermodynamics	Flight Dynamics	Deformation	Optimisation	Planet
ADBSat [163]	University of Manchester	Complex Shapes	Panel Method	N/A	N/A	N/A	N/A	Earth
DAS [273]	NASA	Simple Shapes	Fixed Aerodynamic Coefficients	Lumped mass	3DOF Ballistic	Break-up at defined altitude	N/A	Earth
DEBRISK [274]	CNES	Simple Shapes	Tumble-averaged	Lumped Mass Material Ablation	3DOF	Break-up at defined altitude	N/A	Earth
FOSTRAD [55]	University of Strathclyde	Comples Shapes 3D Meshes	Panel Method with Surrogate Model	1D Finite Element Material Ablation	3DOF	N/A	N/A	Earth
GT-Hypersonics [49]	Georgia Institute of Technology	Comples Shapes 3D Meshes	Inviscid CFD	Inviscid CFD	3DOF	N/A	Surrogate Optimisation	Earth Mars
MUSIC/FAST [275]	ONERA	Complex Shapes	Panel Method with Surrogate Model	N/A	6DOF	N/A	N/A	Earth
ORSAT [276]	NASA and Lockeed-Martin	Simple Shapes	Tumble-Averaged	1D Finite Element	3DOF	Break-up at defined altitude	N/A	Earth
PAMPERO [277]	CNES	Complex Shapes 3D Meshes	Panel Method	3D Finite Element	6DOF	N/A	N/A	Earth
RAC [272]	University of Oxford	Complex Shapes	Panel Method	N/A	3DOF	N/A	N/A	Earth
SAM [278]	NASA	Complex Shapes	Panel Method	Heat Balance Lumped mass	3DOF 6DOF	Material Melting for Demise	N/A	Earth
SCARAB [209]	HTG gmbH	Complex Shapes	Panel Method	2D Finite Element	3DOF 6DOF	Material Melting for Demise	N/A	Earth Mars
SESAM [279]	ESA	Simple Shapes with Connections	Tumble-Averaged	Lumped Mass	3DOF	Break-up at defined altitude	N/A	Earth
Present Work	Present Author	Complex Shapes	Panel Method	Panel Method and 1D FDM	3DOF	Semi-Empirical and Analytical Corrections For Scalloping	Gradient-based and Genetic	Mars

Table A.1.: Overview of the current state-of-the-art of (re-)entry codes and their capabilities

B. Additional Figures and Tables

This appendix contains supplementary visual and tabular data to complement the main research thesis. These additional resources offer further insights, support findings, and provide additional data for reproducing the methodology used in the research. It also includes verification data, allowing for a direct comparison with existing literature data. The relevant tables and figures are referred to in the relevant sections where needed.

B.1. Auxiliary Literature Review

Region	Vehicle	Year	Reference	Payload Mass [kg]	IAD Mass [kg]	Nose Diameter [m]	Inflated Diameter [m]
United States	IRVE I-II	2004-2009	[88, 99, 100] [39, 102]	-	126	0.2095	1.465
	IRVE 3-4	2009-2013	[106, 280]	-	281	0.2350	1.50
	HEART	2009-2012	[114, 117]	4000	349	4.5	8.3
	THOR	2013-2014	[77, 120]	5000	315	2	3.7
	LOFTID	2016-2022	[121–123]	4000	1224	1.3	6
Europe	IRDT 1 IRDT 2	2002-2005	[80–83]	200	140	0.7	3.8
	IRT	2003-2004	[90]	70000	9000	0.5	1.8
Russia	Demonstrator I	1999-2000	[79]	147	33.3	2.3	3.8
	Rescue System Fregat Upper Stage	1999-2000	[79]	1820	637	6	14
	Demonstrator 2-2R	2002-2005	[33, 84]	138	33.3	2.3	3.8
	ISS Cargo Delivery Capsule	2002-2003	[96]	350	98	2.5	8.6
	Martian Capsule	2003-2004	[75, 76, 92]	70000	8800	< 10	23
	Venusian Capsule	2016-2020	[94, 95]	180	-	0.85	2.5

Table B.1.: Literature Survey of major Stacked-toroid program developments

Mission Study	Trajectory Conditions					
	Entry Altitude [km]	Entry Speed [km/s]	Entry Angle [°]	Entry Mass [kg]	Impact Speed [m/s]	Impact Angle [°]
Sandia Labs [244]	120	4.73	-12\-22.5	31	137-168	$<$15
Pioneer [281]	100	4.73	-15	40.8	144	$\sim$0
Mars-96 [282–285]	300	5.60	-10\-14	62.5	60\80	$\sim$0
JAXA [286]	300	3.00	$<$20	16	200\250	$\sim$0
MetNet [248]	120	$>$6.00	-14\-20	22.5	50	$\sim$0

Table B.2.: Trajectory conditions for inflatable EDL systems of Mars penetrator missions

Penetrator Mission	Reference	Destination	Mass [kg]	Dimensions [cm]	Max Acceleration [g]	Impact Velocity [m/s]	Max Penetration [m]
Mars-96 (USSR)	[282–285]	Mars	110	80x150	800	60-80	4-6
Luna Globe (RF)	[287]	Moon	239	14-20x104	800	100	3-6
Deep Space (US)	[288]	Mars	0.670	3.5x10.5	60	100-200	0-6
Lunar-A (Japan)	[58, 62]	Moon	13	16x142.2	3,000	300	1-5
MoonLITE (UK)	[61, 289]	Moon	13	5.6x50	16,000	300	2-5
Europe Akon-Clipper (ESA/NASA)	[290, 291]	Europa	50	20x60	3,000	100-500	305
MAI(RF)	[292, 293]	Moon	50	20x200	0	0	>10
Hyperspeed (RF)	[294]	Comets Asteroids	100-200	15x300	5,000	500-3,000	1-5
Rosetta Phile (ESA)	[295]	Comet	2	4x40	0	0	0
SCT (USA)	[296, 297]	Icy planets	100	20x200	500-3,000	600	3-5
Hayabusa (Japan)	[298, 299]	Asteroid	2.5	30x22	500	2,000	1-10

Table B.3.: Survey of mechanical characteristics of major penetrator missions

B.2. Atmospheric Properties

For reference, the latitudinal and longitudinal distribution of the pressure, temperature and density profiles are shown in Figure B.1 at the entry altitude of 120 km from Mars' sea level.

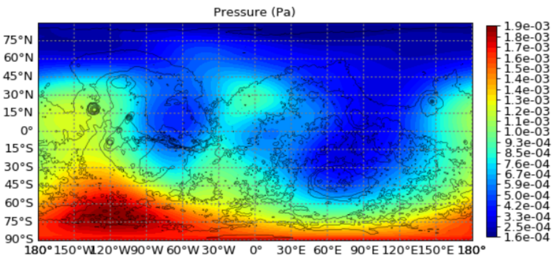

(a) Pressure

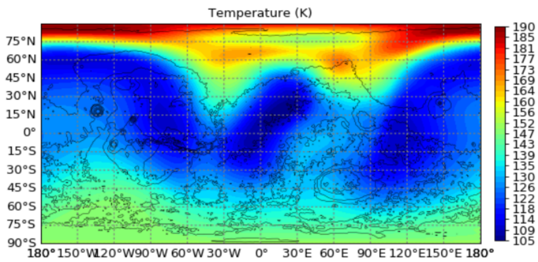

(b) Temperature

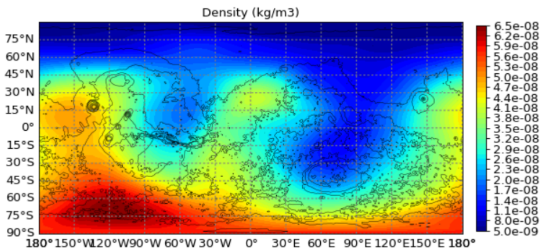

(c) Density

Figure B.1.: MCD v6.1 with climatology average solar scenario at an altitude of 120 km [142]. Julian Date 2461772.0

Gas	DOF ξ [−]	Molecular Weight M_w [g/mol]	Sutherlands Coefficient μ_0 [Pa]	Viscosity Index ω [−]	Reference Temperature T_{ref} [K]	Diameter d_m [m]	Specific Heat Ratio γ [−]
CO_2	6.7	44.01	1.37×10^{-5}	0.93	222	5.62×10^{-10}	1.289
N_2	5	28.01	1.41×10^{-6}	0.74	111	4.17×10^{-10}	1.400
O_2	5	32.00	1.69×10^{-6}	0.77	127	4.07×10^{-10}	1.400
Ar	3	39.95	2.13×10^{-5}	0.81	144	4.17×10^{-10}	1.667
CO	5	28.01	1.66×10^{-5}	0.73	136	4.19×10^{-10}	1.039
O	3	16.00	1.69×10^{-6}	0.80	127	3.00×10^{-10}	1.667
H	3	1.00	6.30×10^{-7}	0.80	72	3.00×10^{-10}	1.667

Table B.4.: Atmospheric gas properties retrieved from Appendix A of reference [149]

Gas	a_1	a_2	a_3	a_4	a_5
CO_2	2.35677352E	$8.98459677\cdot10^{-3}$	$-7.12356269\cdot10^{-6}$	$2.45919022\cdot10^{-9}$	$-1.43699548\cdot10^{-13}$
N_2	3.53100528	$-1.23660987\cdot10^{-4}$	$-5.02999437\cdot10^{-7}$	$2.43530612\cdot10^{-9}$	$-1.40881235\cdot10^{-12}$
O_2	3.78246636	$-2.99673416\cdot10^{-3}$	$9.84730200\cdot10^{-6}$	$-9.68129508\cdot10^{-9}$	$3.24372836\cdot10^{-12}$
Ar	2.59316097	$-1.32892944\cdot10^{-3}$	$5.26503944\cdot10^{-6}$	$-5.97956691\cdot10^{-9}$	$2.18967862\cdot10^{-12}$
CO	3.57953347	$-6.10353680\cdot10^{-4}$	$1.01681433\cdot10^{-6}$	$9.07005884\cdot10^{-10}$	$-9.04424499\cdot10^{-13}$
O	3.16826710	$-3.27931884\cdot10^{-3}$	$6.64306396\cdot10^{-6}$	$-6.12806624\cdot10^{-9}$	$2.11268971\cdot10^{-12}$
H	2.5	0	0	0	0

Table B.5.: Empirical coefficients for gas transport properties; Adapted from [148]

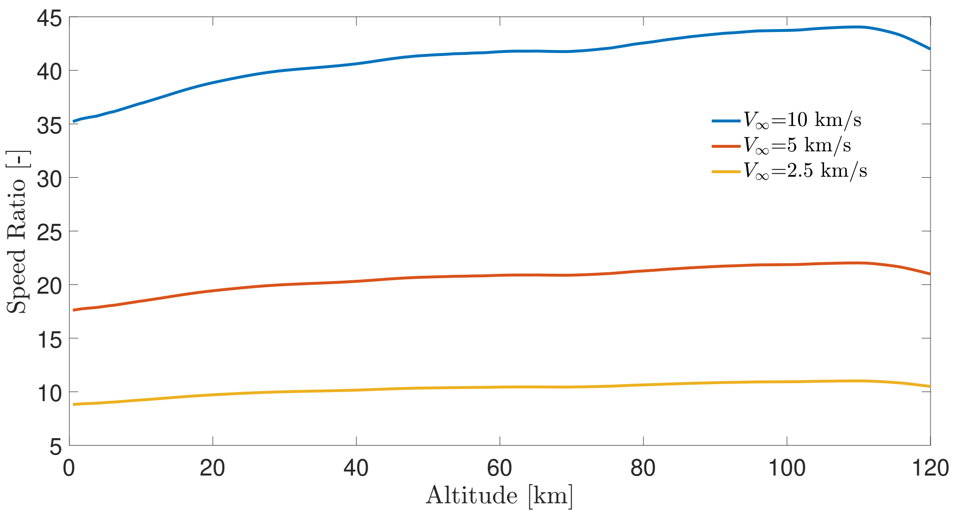

Figure B.2.: Speed ratio as a function of altitude for varying freestream velocities

B.3. Aerodynamics

B.3.1. Cercignani-Lampsi-Lord's Model

Species	ι	χ	δ	ζ
O_2	6.3	0.26	0.42	20.5
N_2	6.6	0.22	0.48	35
O	5.85	0.2	0.48	31
N	4.9	0.32	0.42	8
He	4.5	0.38	0.51	5.8
H	3.6	0.48	0.52	2.8

Table B.6.: Fitted Parameters for the CLL Closed-Form in Equation 3.59 [179]

B.3.2. Continuum Regime

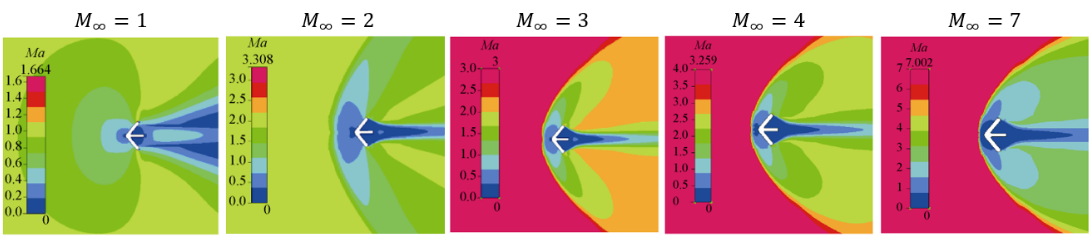

Figure B.3.: Viscid CFD simulations of IRVE-3 ($\alpha = 0°$) performed by Xiaoshun and Xue [232]

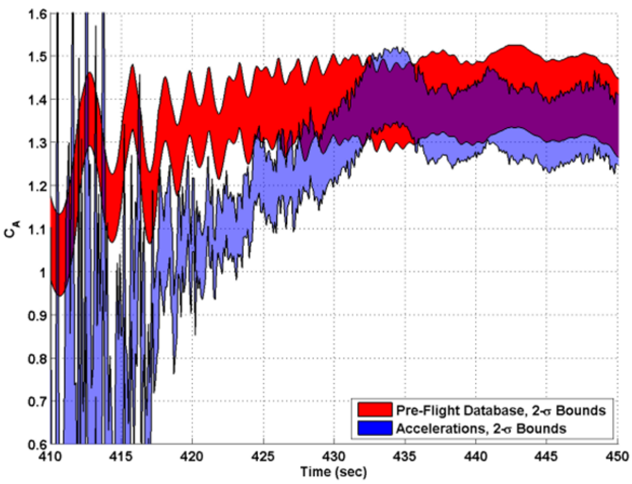

Figure B.4.: Axial Force Coefficient calculated from gyroscopes telemetry compared to the pre-flight aerodynamic database prediction [100]

Mach	α	Axial Force Coefficient $C_A[-]$			Normal Force Coefficient $C_N[-]$		
$[-]$	$[deg]$	Modified Newtonian C_A	Pre-Flight Database	Post-Flight Reconstruction	Modified Newtonian C_N	Pre-Flight Database	Post-Flight Reconstruction
1.5	6.00	1.0302	1.3573	1.3179	-0.0274	-0.0650	-0.0450
1.75	8.97	1.0682	1.4045	1.3569	-0.0427	-0.0672	-0.0455
2	10.88	1.0918	1.3921	1.3119	-0.0530	-0.0733	-0.0416
2.25	8.37	1.1292	1.4132	1.3056	-0.0421	-0.0748	-0.0257
2.5	4.99	1.1599	1.4253	1.3267	-0.0257	-0.0867	-0.0266
2.75	7.32	1.1650	1.4125	1.3505	-0.0379	-0.0853	-0.0357
3	10.38	1.1598	1.3954	1.3566	-0.0537	-0.0960	-0.0437
3.25	9.54	1.1726	1.3928	1.3340	-0.0499	-0.0849	-0.0410
3.5	5.39	1.1964	1.4102	1.3124	-0.0344	-0.0899	-0.0208
3.75	3.70	1.2072	1.3968	1.3365	-0.0198	-0.0795	-0.0108
4	6.12	1.2043	1.3774	1.3572	-0.0327	-0.0675	-0.0259
4.25	5.75	1.2092	1.3796	1.4148	-0.0309	-0.0482	-0.0182
4.5	4.90	1.2150	1.3828	1.3645	-0.0265	-0.0294	-0.0011
4.75	3.13	1.2218	1.3858	1.3079	-0.0170	-0.0124	0.0049
5	6.11	1.2158	1.3652	1.2533	-0.0330	-0.0187	-0.0266
5.25	3.51	1.2253	1.3747	1.2101	-0.0191	0.0057	-0.0191
5.5	6.22	1.2189	1.3608	1.1725	-0.0336	0.0284	-0.0305
5.75	9.31	1.2060	1.3214	1.1642	-0.0501	0.0193	-0.0584
6	2.28	1.2318	1.3698	1.1350	-0.0125	0.0802	-0.0145
6.2	20.16	1.1167	1.1864	0.9092	-0.1036	0.3249	-0.0542

Table B.7.: Comparison of modified Newtonian method with IRVE-II pre- and post-flight aerodynamic data retrieved from [100]

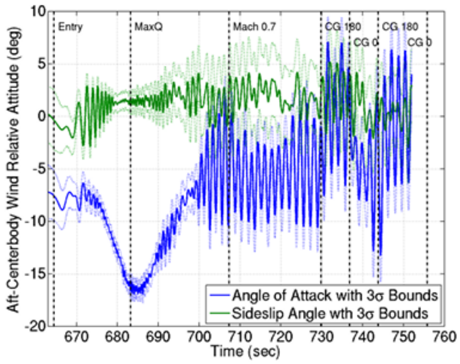

(a) Aerodynamic Angles

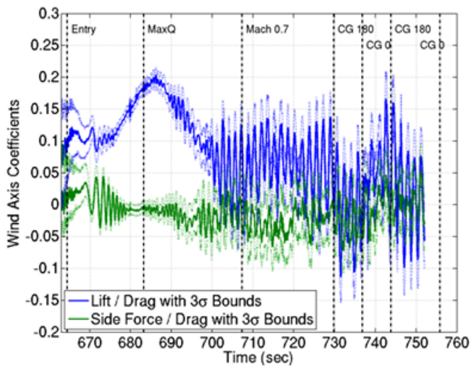

(b) Drag normalized Lift and Side Force

Figure B.5.: Reconstructed IRVE-3 Flight Data [38]

Mach [−]	Angle of Attack [deg]	Drag Coefficient C_D [−] Flight Data [38]	Modified Newtonian	$\|\delta_{\%}\|$	Lift Coefficient C_L [−] Flight Data [38]	Modified Newtonian	$\|\delta_{\%}\|$
0.8	-5.68	1.1322	0.9176	18.948	0.1334	0.0951	28.70
1	-6.68	1.3528	0.9508	29.70	0.1572	0.1161	26.18
1.5	-9.19	1.4396	1.1292	21.55	0.2162	0.1895	12.36
2	-11.59	1.4275	1.2041	15.64	0.2709	0.2549	5.89
2.5	-12.18	1.3992	1.2448	11.02	0.2899	0.2770	4.44
3	-12.77	1.3527	1.2651	6.47	0.3076	0.2590	15.81
3.5	-13.37	1.2715	1.2751	0.28	0.3233	0.2732	15.50
4	-13.91	1.2563	1.2799	1.87	0.3381	0.2854	15.58
4.5	-13.54	1.2559	1.2908	2.77	0.3316	0.2800	15.57
5	-13.16	1.2563	1.2996	3.44	0.3244	0.2740	15.55
5.5	-12.78	1.2641	1.3071	3.40	0.3151	0.2676	15.07
6	-12.34	1.2750	1.3145	3.09	0.3025	0.2590	14.37
6.5	-11.28	1.2962	1.3260	2.30	0.2778	0.2729	1.76
7	-10.23	1.3192	1.3363	1.30	0.2527	0.2494	1.29
7.5	-9.17	1.3445	1.3458	0.097	0.2269	0.2253	0.72
8	-8.16	1.3617	1.3537	0.58	0.2020	0.2016	0.24
8.5	-7.51	1.3685	1.3588	0.70	0.1854	0.1858	0.25
9	-6.87	1.4123	1.3636	3.44	0.1693	0.1692	0.06

Table B.8.: Comparison of IRVE-3 aerodynamic flight data with modified Newtonian method

Mach Number	$\theta_c = 60°$			$\theta_c = 50°$		
[−]	C_D [89]	C_D^*	$\delta_{\%}$	C_D[89]	C_D^*	$\delta_{\%}$
2	1.4344	1.2479	13.00	1.3652	1.1670	14.52
3	1.4020	1.3250	5.49	1.3174	1.2438	5.58
4	1.3887	1.3533	2.55	1.2907	1.2719	1.46
6	1.3888	1.3696	0.94	1.2537	1.2884	2.77
8	1.3829	1.3768	0.44	1.2305	1.2952	5.26
10	1.3834	1.3840	0.04	1.2187	1.3020	6.82
12	1.3840	1.3852	0.08	1.2076	1.3012	7.75
15	1.3848	1.3870	0.15	1.2017	1.3000	8.17
20	1.3862	1.3890	0.19	1.1933	1.3070	9.52

* Refers to the numerical results obtained with the modified Newtonian method coupled with the panel method, as described in section 3.5.

Table B.9.: Comparison of Drag coefficient for Panel method and CFD data of IRDT

Mach $[-]$	α $[deg]$	Modified Newtonian C_A	Pre-Flight Database [100]	$\delta_{\%,pre}$	Post-Flight Reconstruction [100]	$\delta_{\%,post}$	$C_A + \Delta C_A$	$\delta_{\%,post}$
1.5	6.00	1.0302	1.3573	24.10	1.3179	21.83	1.0512	22.56
1.75	8.97	1.0682	1.4045	23.94	1.3569	21.27	1.0906	22.35
2	10.88	1.0918	1.3921	21.57	1.3119	16.78	1.1174	19.73
2.25	8.37	1.1292	1.4132	20.10	1.3056	13.51	1.1564	18.17
2.5	4.99	1.1599	1.4253	18.62	1.3267	12.57	1.1901	16.50
2.75	7.32	1.1650	1.4125	17.52	1.3505	13.73	1.1998	15.06
3	10.38	1.1598	1.3954	16.88	1.3566	14.50	1.1981	14.14
3.25	9.54	1.1726	1.3928	15.81	1.3340	12.10	1.2147	12.79
3.5	5.39	1.1964	1.4102	15.16	1.3124	8.84	1.2425	11.89
3.75	3.70	1.2072	1.3968	13.57	1.3365	9.67	1.2584	9.91
4	6.12	1.2043	1.3774	12.57	1.3572	11.27	1.2605	8.49
4.25	5.75	1.2092	1.3796	12.35	1.4148	14.53	1.2679	8.10
4.5	4.90	1.2150	1.3828	12.14	1.3645	10.96	1.2750	7.80
4.75	3.13	1.2218	1.3858	11.83	1.3079	6.58	1.2979	6.34
5	6.11	1.2158	1.3652	10.95	1.2533	2.99	1.3140	3.75
5.25	3.51	1.2253	1.3747	10.87	1.2101	1.25	1.3680	0.49
5.5	6.22	1.2189	1.3608	10.43	1.1725	3.95	1.4057	3.30
5.75	9.31	1.2060	1.3214	8.73	1.1642	3.60	1.4243	7.79
6	2.28	1.2318	1.3698	10.07	1.1350	8.53	1.4638	6.86
6.2	20.16	1.1167	1.1864	5.87	0.9092	22.82	1.4619	23.22

Table B.10.: Comparison of panel method with IRVE-II Flight Data and Correction for Deflection

Mach [-]	α $[deg]$	Modified Newtonian C_N	Pre-Flight Database [100]	$\delta_{\%,pre}$	Post-Flight Reconstruction [100]	$\delta_{\%,post}$	$C_N + \Delta C_N$	$\delta_{\%,post}$
1.5	6.00	-0.0274	-0.0450	-39.15	-0.0650	-57.87	-0.0274	-39.15
1.75	8.97	-0.0427	-0.0455	-6.11	-0.0672	-36.40	-0.0427	-6.11
2	10.88	-0.0530	-0.0416	-27.47	-0.0733	-27.64	-0.0530	-27.47
2.25	8.37	-0.0421	-0.0257	-63.45	-0.0748	-43.77	-0.0421	-63.45
2.5	4.99	-0.0257	-0.0266	-3.46	-0.0867	-70.35	-0.0257	-3.46
2.75	7.32	-0.0379	-0.0357	-6.36	-0.0853	-55.56	-0.0379	-6.36
3	10.38	-0.0537	-0.0437	-23.04	-0.0960	-44.00	-0.0537	-23.04
3.25	9.54	-0.0499	-0.0410	-21.74	-0.0849	-41.23	-0.0499	-21.74
3.5	5.39	-0.0344	-0.0208	-65.19	-0.0899	-61.76	-0.0344	-65.19
3.75	3.70	-0.0198	-0.0108	-83.65	-0.0795	-75.08	-0.0198	-83.65
4	6.12	-0.0327	-0.0259	-26.42	-0.0675	-51.50	-0.0327	-26.42
4.25	5.75	-0.0309	-0.0182	-69.22	-0.0482	-36.05	-0.0309	-69.22
4.5	4.90	-0.0265	-0.0011	-2293.10	-0.0294	-10.15	-0.0265	-2293.14
4.75	3.13	-0.0170	0.0049	446.00	-0.0124	-36.41	-0.0170	446.05
5	6.11	-0.0330	-0.0266	-24.07	-0.0187	-76.01	-0.0330	-24.14
5.25	3.51	-0.0191	-0.0191	0.05	0.0057	435.20	-0.0195	-1.92
5.5	6.22	-0.0336	-0.0305	-10.26	0.0284	218.34	-0.0368	-20.77
5.75	9.31	-0.0501	-0.0584	14.30	0.0193	359.57	-0.0611	-4.62
6	2.28	-0.0125	-0.0145	13.79	0.0802	115.58	-0.0304	-109.71
6.25	20.16	-0.1036	-0.0542	-91.31	0.3249	131.89	-0.5245	-868.57

Table B.11.: Comparison of panel method with IRVE-3 Flight Data and Correction for Deflection

B.3.3. Transitional Regime

C_A [$-$]			C_N [$-$]		
α [deg]	R^2	RMSE	α [deg]	R^2	RMSE
5	0.9935	0.00416	0	0.9696	0.16098
15	0.9933	0.01400	15	0.96101	0.15556
30	0.9855	0.03579	30	0.95885	0.14315
45	0.9686	0.06854	60	0.91349	0.10769
60	0.9288	0.11399	90	0.1979	0.02110
90	0.8626	0.16323	120	0.87138	0.11502
120	0.9212	0.12146	150	0.91369	0.18373
150	0.9773	0.05189	165	0.93985	0.18443
165	0.9752	0.03130	180	0.95039	0.17879

Table B.12.: Agreement of Wilmoth Bridging Function at non-zero angle of attack

B.3.4. Rarefied Regime

Method	$\alpha = 0°$	$\alpha = 15°$	$\alpha = 30°$	$\alpha = 60°$	$\alpha = 90°$ *	$\alpha = 120°$	$\alpha = 150°$	$\alpha = 165°$	$\alpha = 180°$	$\delta_{\%}$
DSMC [56]	4.109	3.937	3.452	1.877	0.0335	-1.864	-3.526	-4.033	-4.215	-
CLL	3.971	3.809	3.354	1.853	0.720	-1.737	-3.334	-3.823	-3.989	3.73
Schaaf Sentman	3.215	3.074	2.683	1.435	0.428	-1.368	-2.669	-3.086	-3.229	23.42
Cook	2.813	2.745	2.228	1.767	0.383	-0.632	-2.177	-2.687	-2.794	34.32
Storch	2.375	2.247	1.891	0.830	0.1376	-0.804	-1.883	-2.250	-2.388	47.15

* 90° is excluded from error, since the denominator is close to 0°.

Table B.13.: Comparison of axial force coefficients C_A of IRVE as a function of angle of incidence

Method	$\alpha = 5°$	$\alpha = 15°$	$\alpha = 30°$	$\alpha = 45°$	$\alpha = 60°$	$\alpha = 90°$	$\alpha = 120°$	$\alpha = 150°$	$\alpha = 165°$	$\delta_{\%}$
DSMC [56]	0.226	0.660	1.220	1.603	1.808	1.890	1.779	1.1960	0.6460	-
CLL	0.166	0.571	1.110	1.516	1.758	1.375	1.821	1.171	0.633	9.58
Schaaf Sentman	0.153	0.499	0.946	1.264	1.434	1.116	1.474	0.982	0.536	23.78
Cook	0.317	0.929	1.710	2.229	2.375	1.433	2.351	1.695	0.903	33.61
Storch	0.151	0.436	0.771	0.930	0.884	0.571	0.883	0.773	0.439	42.75

Table B.14.: Comparison of normal force coefficients C_N of IRVE as a function of θ

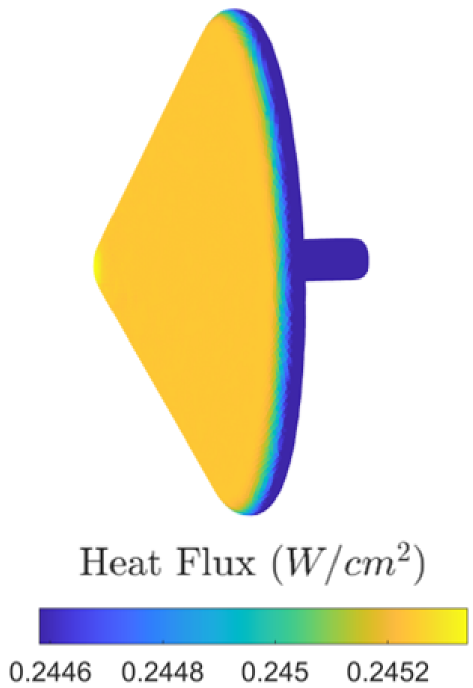

(a) Surface distribution plot

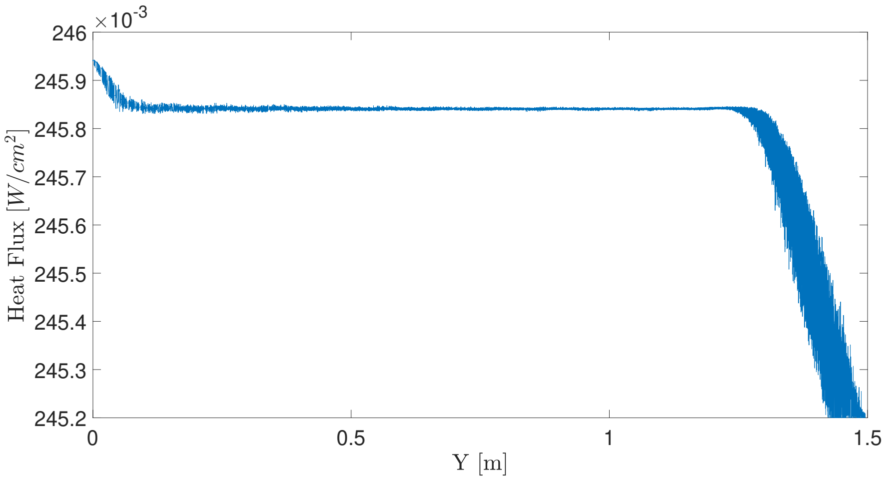

(b) Axial distribution plot

Figure B.6.: FMF Heat flux distribution along IRVE vehicle using Schaaf and Chambre's method at 150 km $\alpha = 0°$

B.4. Aerothermodynamics

B.4.1. Radiation

Term	Coefficient	Term	Coefficient	Term	Coefficient	Term	Coefficient	Term	Coefficient
Constant	-2.1851	$\ln(\rho)^2$	0.0674	Vr_N^2	$-2.7369 \cdot 10^{-3}$	$V^3\ln(\rho)$	$-6.4747 \cdot 10^{-3}$	$V\ln(\rho)^2 r_N$	$2.3530 \cdot 10^{-4}$
V	2.7138	$\ln(\rho)r_N$	-0.1056	$V\ln(\rho)r_N$	0.0108	$V^3 r_N$	$-2.9409 \cdot 10^{-3}$	$V\ln(\rho)r_N^2$	$-7.4458 \cdot 10^{-4}$
$\ln(\rho)$	0.5949	r_N^2	-0.0545	$\ln(\rho)^3$	0.0114	$V^2\ln(\rho)^2$	$4.4518 \cdot 10^{-4}$	$\ln(\rho)^4$	$2.2040 \cdot 10^{-4}$
r_N	0.0400	V^3	-0.3602	$\ln(\rho)^2 r_N$	$-3.8751 \cdot 10^{-3}$	$V^2\ln(\rho)r_N$	$2.2275 \cdot 10^{-3}$	$\ln(\rho)^3 r_N$	$-2.5058 \cdot 10^{-4}$
V^2	0.8212	$V^2\ln(\rho)$	0.0660	$\ln(\rho)r_N^2$	$2.5431 \cdot 10^{-3}$	$V^2 r_N^2$	$5.5876 \cdot 10^{-4}$	$\ln(\rho)^2 r_N^2$	$-1.5449 \cdot 10^{-4}$
$V\ln(\rho)$	0.1017	$V^2 r_N$	0.0386	r_N^3	$3.8852 \cdot 10^{-3}$	$V\ln(\rho)^3$	$2.5481 \cdot 10^{-4}$	$\ln(\rho)r_N^3$	$-5.8732 \cdot 10^{-5}$
Vr_N	-0.0220	$V\ln(\rho)^2$	0.0259	V^4	0.0326	Vr_N^3	$-2.1412 \cdot 10^{-4}$	r_N^4	$-7.0997 \cdot 10^{-5}$

Table B.15.: Low-velocity radiation correlation polynomial coefficients [190]

Term	Coefficient	Term	Coefficient	Term	Coefficient	Term	Coefficient	Term	Coefficient
Constant	-776.1295	$\ln(\rho)^2$	-0.8472	Vr_N^2	$-7.7139 \cdot 10^{-3}$	$V^3\ln(\rho)$	0.1704	$V\ln(\rho)^2 r_N$	$2.9523 \cdot 10^{-3}$
V	327.0352	$\ln(\rho)r_N$	-0.2324	$V\ln(\rho)r_N$	0.0310	$V^3 r_N$	0.0125	$V\ln(\rho)r_N^2$	$1.9937 \cdot 10^{-4}$
$\ln(\rho)$	-69.4125	r_N^2	-0.0615	$\ln(\rho)^3$	-0.0352	$V^2\ln(\rho)^2$	$3.8018 \cdot 10^{-3}$	$\ln(\rho)^4$	$1.6924 \cdot 10^{-4}$
r_N	-4.8702	V^3	2.5044	$\ln(\rho)^2 r_N$	-0.0385	$V^2\ln(\rho)r_N$	$1.3922 \cdot 10^{-3}$	$\ln(\rho)^3 r_N$	$-1.2821 \cdot 10^{-3}$
V^2	-46.6552	$V^2\ln(\rho)$	-3.6385	$\ln(\rho)r_N^2$	-0.0155	$V^2 r_N^2$	$7.4385 \cdot 10^{-4}$	$\ln(\rho)^2 r_N^2$	$-6.1914 \cdot 10^{-4}$
$V\ln(\rho)$	28.0329	$V^2 r_N$	-0.2701	r_N^3	$6.8871 \cdot 10^{-4}$	$V\ln(\rho)^3$	$9.9250 \cdot 10^{-3}$	$\ln(\rho)r_N^3$	$5.8098 \cdot 10^{-5}$
Vr_N	2.1226	$V\ln(\rho)^2$	0.2091	V^4	-0.0256	Vr_N^3	$-1.4599 \cdot 10^{-5}$	r_N^4	$-1.9117 \cdot 10^{-7}$

Table B.16.: High-velocity radiation correlation polynomial coefficients [190]

B.4.2. Heat Distribution

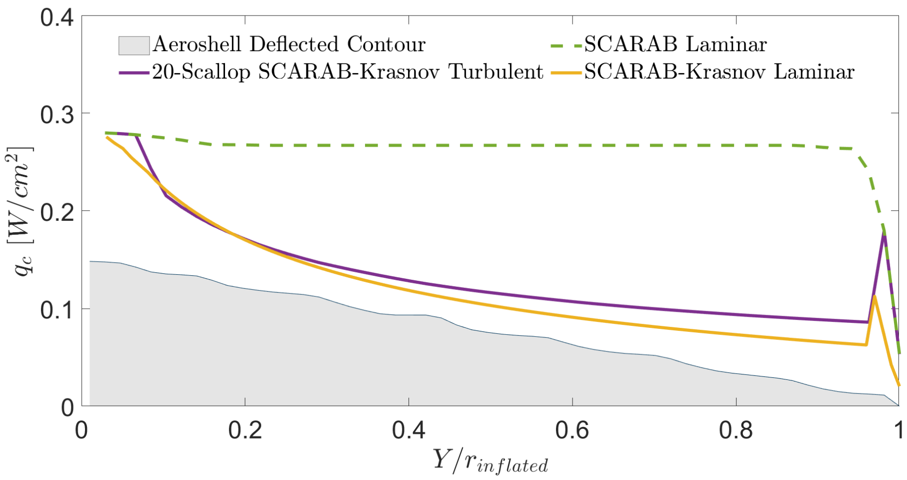

Figure B.7.: Heat flux radial distribution across optimised stacked-toroid

B.5. Flexible Thermal Protection System

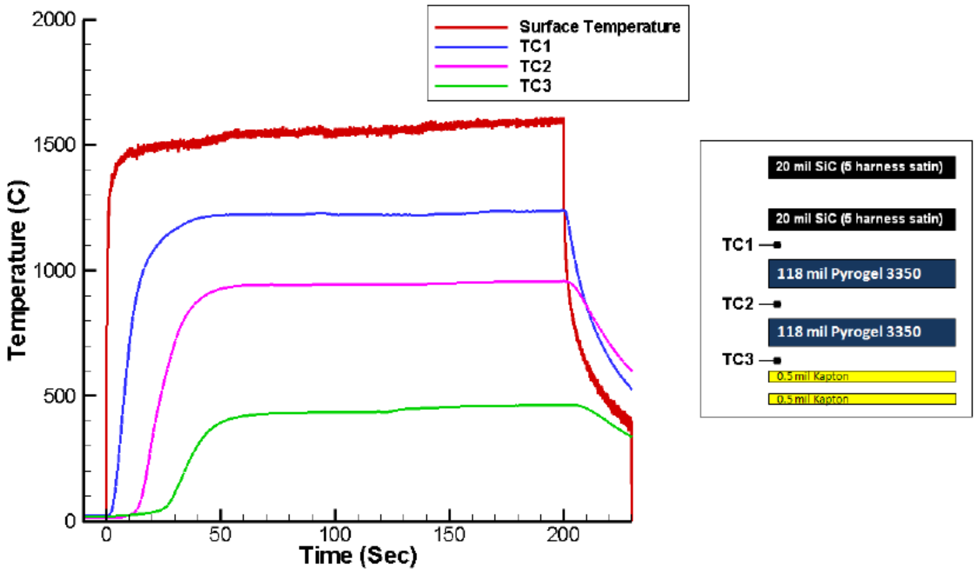

(a) Heat flux of 50 W/cm^2 for 200 seconds

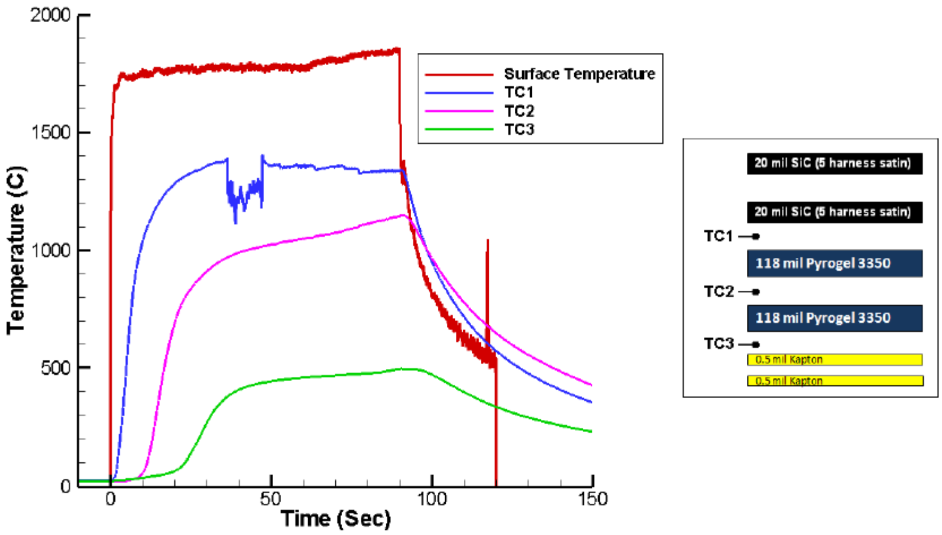

(b) Heat flux of 100 W/cm^2 for 90 seconds

Figure B.8.: SiC 5HS layup tested at 8 torr [30]

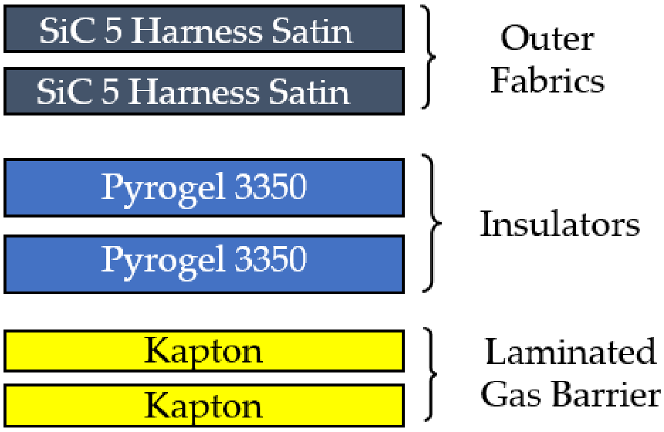

Figure B.9.: Functional aspects of the 2^{nd} generation F-TPS

B.5.1. Thermal Properties

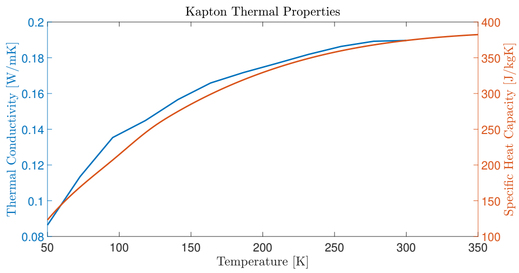

(a) Kapton [31]

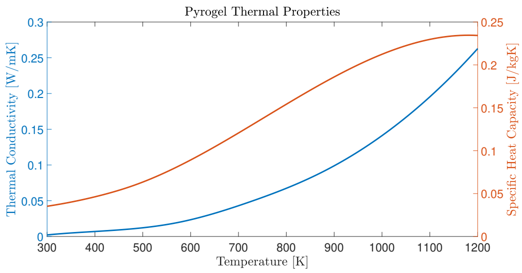

(b) Pyrogel [30]

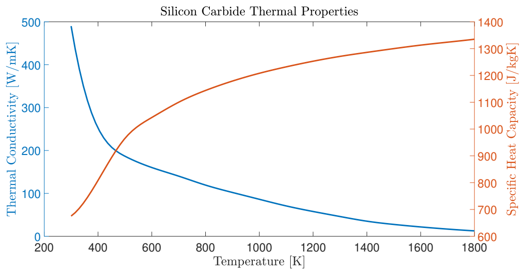

(c) SiC [300]

Figure B.10.: Variation of the thermal conductivity and specific heat capacity as a function of temperature for the F-TPS layer materials

Material	Emissivity ϵ $[-]$	Density ρ $[kg/m^3]$	Max. Temperature T_{max} $[K]$
Nicalon SiC	0.75	1468	2073
Pyrogel 3350	-	110	1373
Kapton	0.12	3100	773

Table B.17.: F-TPS Material Properties [30, 31]

B.5.2. Thermal Contact Conductance

While a constant thermal conductance value can simply be included in Ansys by creating bonded contact regions between the interfaces with a manually inputted value of the conductance, no function is available to model the variation of thermal conductance as a variable. A novel solution to this problem is proposed in this work based on the concept of virtual layer introduced by Yuan et al. [301]. This consists of a physical interface to represent the thermal resistance such that a discontinuity is caused between the two original layers as illustrated in Figure B.11. Given that this virtual layer may be very thin, it is assumed that the temperature is distributed linearly and that the flux is conserved. Given that the equation for the heat resistance R_q is given in Equation B.1 along with its inverse, equivalent to the heat contact conductance, the calculation of the heat capacity is trivial. The relationship between the contact conductance and the conductivity of the virtual material is of inverse proportionality. Given an arbitrarily chosen thickness of the virtual layer L and its cross-sectional area, the contact resistance may be modelled by setting a varying relationship for the conductivity of the virtual material.

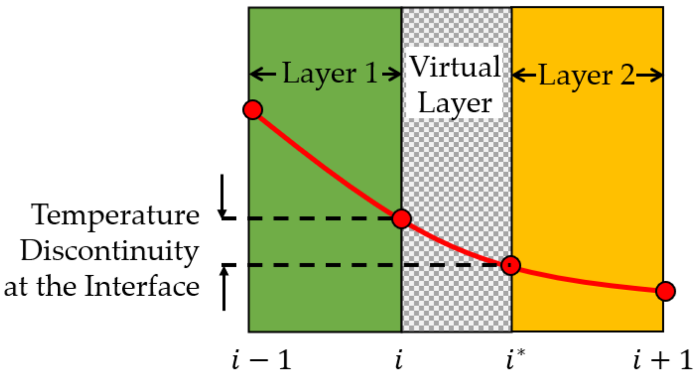

Figure B.11.: Virtual layer concept for thermal contact interface

$$R_q = \frac{L}{Ak} = \frac{1}{h_c A} \rightarrow k = Lh_c \tag{B.1}$$

For reference, virtual layers with a thickness of 1mm each are implemented in Ansys for each interface, with the equivalent values reported in Table B.18 according to Equation B.1, which yield the same solution as in Figure 4.48 for the constant values.

Contact Surfaces	Virtual Layer Thickness L [mm]	Thermal Conductivity k [W/mK]	Equivalent Contact Conductance h_c [$W/m^2/K$]
SiC-SiC	1	0.1	100
SiC-Pyrogel	1	0.1	100
Pyrogel-Pyrogel	1	0.03	30
Pyrogel-Kapton	1	0.2	200
Kapton-Kapton	1	1	1000

Table B.18.: Virtual layer thermal conductivity

However, the advantage of this method is that of enabling temperature-variant conductances. An arbitrarily chosen variation of the Sic-Pyrogel interface conductance with respect to the temperature is shown in Figure B.12 and implemented. The results, also plotted in Figure B.12 for both varying and constant h_c, reveal the significant variation of the transient temperature behaviour of the layers following the interface.

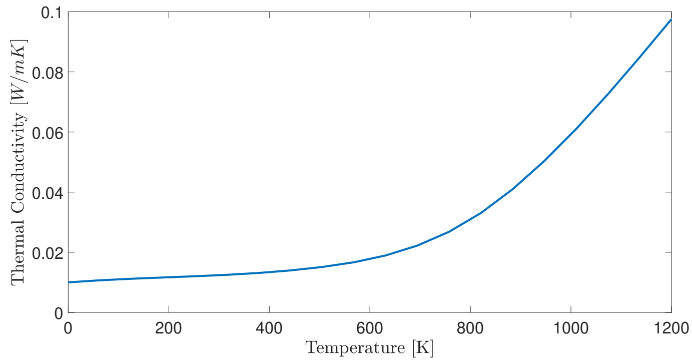

(a) Chosen profile for $k = f(T)$ at the SiC-Pyrogel interface

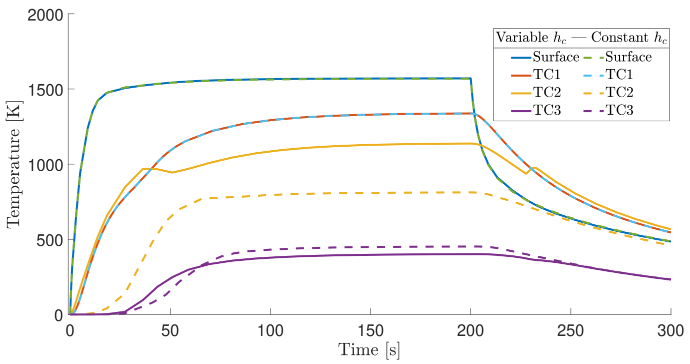

(b) Numerical results

Figure B.12.: Comparison of Ansys transient thermal results with constant and with variable contact conductance

B.6. Optimised Stacked Toroid

B.6.1. Aerodynamic Distribution

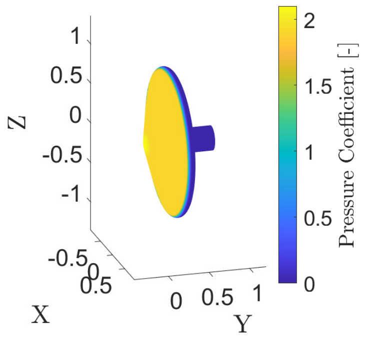

(a) FMF: Schaaf and Chambre

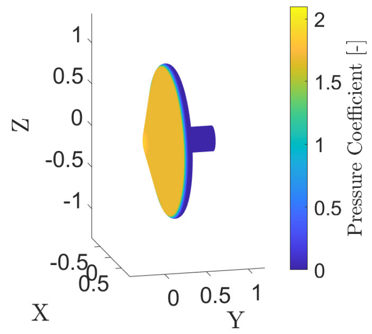

(b) Continuum: Modified Newtonian Method

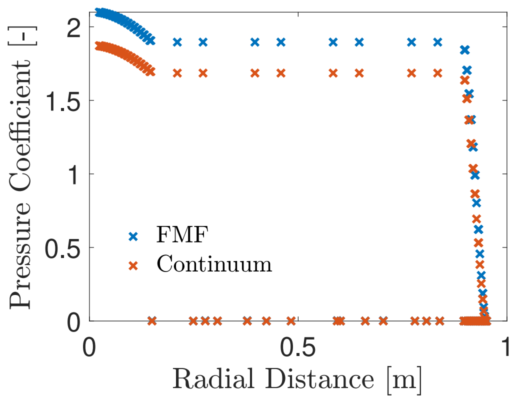

(c) Radial distribution of C_P

Figure B.13.: Pressure coefficient distribution across optimised-stacked-toroid

B.6.2. Design Space Surface Plots

By constructing a surface plot, as depicted in Figure B.14, the variation of heat flux and heat load can be visualized as a function of the inner torus radii and the number of tori. Consistent with the previous discussion, the surface plot confirms the desirability of a stacked-toroid design with both a large number of tori and a substantial radius of inner tori in order to minimize heat loads. This holds true for both the heat flux and heat load, as they exhibit a direct correlation. Similarly, when examining the surface plot of the half-cone angle and radius of inner tori, it becomes evident that the optimal design configuration should possess a large inner tori radius and, to some extent, larger half-cone angles. However, it is worth noting that the variation in half-cone angle appears to be less significant, particularly at the higher end of the spectrum for the inner tori radius.

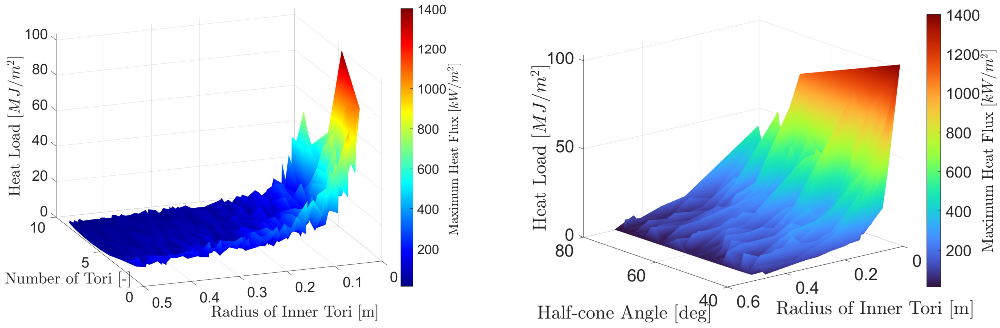

(a) Number of tori and Radius of inner tori (b) Half-cone Angle and Radius of inner tori

Figure B.14.: Surface plot of heat flux and heat load with varying design inputs

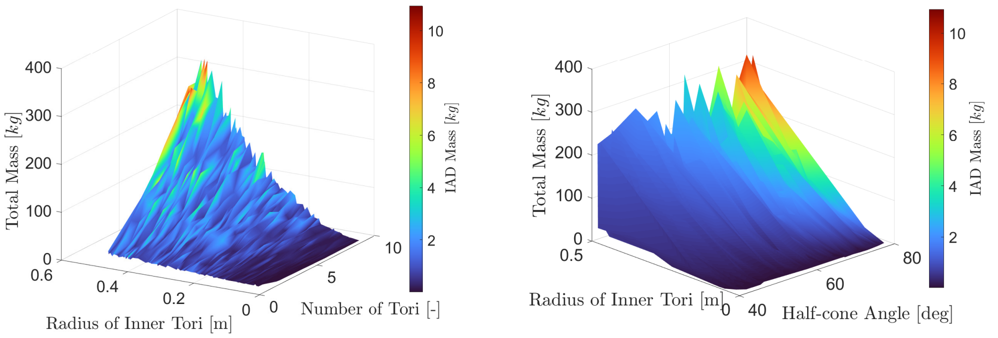

(a) Number of tori and Radius of inner tori (b) Half-cone Angle and Radius of inner tori

Figure B.15.: Surface plot of total mass and IAD mass with varying design inputs

The same approach is employed to analyze the structural and total mass, and the corresponding results are illustrated in Figure B.15, aligning with the heat-flux profile. This alignment can be attributed to the following rationale. By examining the proportion of IAD to the total mass, it becomes apparent that the majority of the mass contribution arises from the F-TPS. Consequently, the heat loads play a crucial role in determining the overall mass of the vehicle. Therefore, it is desirable to design a vehicle with a small radius of inner tori, as this helps to minimize the heat loads. Simultaneously, the influence of the number of tori on the mass is not straightforwardly advantageous or disadvantageous, as it depends on the trade-off with the structural mass. A lower number of tori seems beneficial when paired with large inner torus radii but slightly detrimental as the inner torus radii increase. When considering the effect of the half-cone angle, it is evident that the largest angles should be avoided due to the sharp increase in IAD and overall mass. However, the combination of inner torus radii and half-cone angle alone is insufficient to identify an optimum design configuration.

B.7. Effect of Zonal Wind

Since the presence of atmospheric wind is neglected in the optimisation process, its effect on the trajectory of the optimised stacked toroid vehicle is shown in Figure B.16 and the differences are listed in Table B.19. With the exception of the end speed, which would not meet the impact requirements of the penetrator, all other performance parameters show only slight variations due to the presence of wind. In fact, the greatest wind influence occurs at altitudes higher than 40 km, where the vehicle's velocity is the highest.

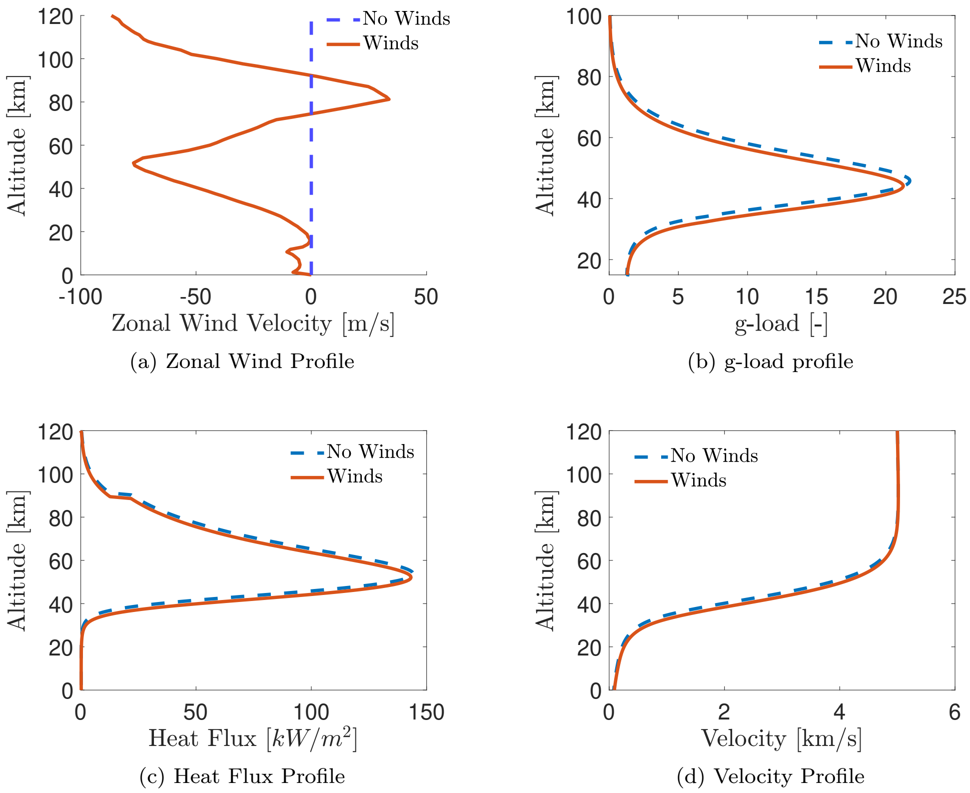

(a) Zonal Wind Profile (b) g-load profile (c) Heat Flux Profile (d) Velocity Profile

Figure B.16.: Effect of Zonal Wind on Ballistic entry trajectory of optimised stacked-toroid

Trajectory	V_I $[m/s]$	$h_{deployed}$ $[km]$	R $[km]$	$\bar{a}_{max}$ $[-]$	$q_{\infty,max}$ $[Pa]$	$q_{s,max}$ $[kW/m^2]$	Q_s $[MJ/m^2]$	t $[s]$
No Winds	80	14.4	560.6	21.7	622.8	144.1	7.64	387
Winds	90.5	12.86	576	21.26	609.9	143.2	7.67	364

Table B.19.: Effect of Zonal Wind on Entry Trajectory for optimised stacked toroid IAD

C. Derivations

This appendix details some of the lengthy derivations of the models adopted in this work. Specifically, the parametric model for the stacked toroid geometry, the structural mass model associated with the parametric geometry, the modified Newtonian method and Fay-Riddell's convective stagnation heat flux. These provide the theoretical foundations and mathematical underpinnings behind the engineering models and expressions utilized throughout the study.

C.1. Geometry Parametrization

Firstly, the area of the nose-cone can be computed in Equation C.1 given that a spherical profile is utilized.

$$A_{nose} = \pi \cdot \left(r_{\text{pay}}^2 + \left(r_{\text{pay}} \cdot \left(1/\cos\left(\theta_c\right) - \tan\left(\theta_c\right) \right) \right)^2 \right) \tag{C.1}$$

The area of the conical section upon which the TPS is mounted can be defined from two additional lengths. The first one is the outer shell length L_{shell} in Equation C.2, represented by the straight contour beneath the internal tori. The trigonometric identity $\cos\left(\arcsin\left(x\right)\right) = \sqrt{1-x^2}$ is used to simplify the mathematical expression.

$$\begin{aligned} L_{\text{shell}} &= 2N r_{\text{torus}} + \frac{1}{2}\left(r_{\text{torus}} + r_{\text{out,torus}}\right)\cos\left(\arcsin\left(\frac{r_{\text{torus}} - r_{\text{out,torus}}}{r_{\text{torus}} + r_{\text{out,torus}}}\right)\right) - r_{\text{torus}} \\ &= 2N r_{\text{torus}} + \frac{1}{2}\left(r_{\text{torus}} + r_{\text{out,torus}}\right)\left(\frac{2\sqrt{r_{\text{torus}}\, r_{\text{out,torus}}}}{r_{\text{torus}} + r_{\text{out,torus}}}\right) - r_{\text{torus}} \end{aligned} \tag{C.2}$$

The second length, defined in Equation C.3 as $L_{\text{enclosure}}$ is the distance of the gap between L_{shell} and the wall of the payload.

$$L_{\text{enclosure}} = r_{\text{torus}} \frac{1 + \tan\left(\pi/4 - \theta_c/2\right)}{\tan\left(\theta_c\right)} \tag{C.3}$$

The area of the bottom shell A_{shell} enclosing the toroidal structures can therefore be computed:

$$A_{\text{shell}} = \pi \cdot \left(2 r_{\text{pay}} \left(L_{\text{shell}} + L_{\text{enclosure}}\right) \sin\left(\theta_c\right)\right)\left(L_{\text{shell}} + L_{\text{enclosure}}\right) \tag{C.4}$$

To account for the curvature of the outer torus and its connection to the outer shell, the arc length of the shoulder is given in Equation C.5 and the flat connection created between the shoulder and the shell is expressed in Equation C.6.

$$L_{\text{shoulder}} = 2r_{\text{out,torus}} \left(\pi - 2\arcsin\left(\frac{r_{\text{torus}} - r_{\text{out,torus}}}{r_{\text{torus}} + r_{\text{out,torus}}}\right)\right) \tag{C.5}$$

$$\begin{aligned} L_{\text{shoulder,link}} &= \frac{1}{2}\left(r_{\text{torus}} + r_{\text{out,torus}}\right)\cos\left(\arcsin\left(\frac{r_{\text{torus}} - r_{\text{out,torus}}}{r_{\text{torus}} + r_{\text{out,torus}}}\right)\right) \\ &= \sqrt{r_{\text{torus}} \cdot r_{\text{out,torus}}} \end{aligned} \tag{C.6}$$

The surface area of the shoulder and the connecting link are finally provided in Equation C.7 and Equation C.8 in a similar manner to the Equation C.4 by constructing a surface of revolution. The outer area is thus found from the sum of the individual area components $A_{outer} = 2A_{\text{shell}} + A_{shoulder} + A_{shoulder,link} + A_{nose}$. The shell area is multiplied by a factor of two to account for the upper surface.

$$\begin{aligned} A_{shoulder} =& \pi L_{\text{shoulder}} \cdot \left(2\left(r_{\text{pay}} + \left(L_{\text{shell}} + L_{\text{enclosure}}\right)\sin\left(\theta_c\right)\right) - r_{\text{out,torus}} \sin\left(\pi/2 - \theta_c\right)\right. \\ &\left. + r_{\text{out,torus}} \sin\left(2\arcsin\left(\frac{r_{\text{torus}} - r_{\text{out,torus}}}{r_{\text{torus}} + r_{\text{out,torus}}}\right) - \pi/2 + \theta_c\right)\right) \end{aligned} \tag{C.7}$$

$$\begin{aligned} A_{shoulder,link} =& \pi L_{\text{shoulder,link}} \left(2\left(r_{\text{pay}} + \left(L_{\text{shell}} + L_{\text{enclosure}}\right)\sin\left(\theta_c\right)\right) - r_{\text{out,torus}} \sin\left(\pi/2 - \theta_c\right)\right. \\ & + r_{\text{out,torus}} \sin\left(2\arcsin\left(\frac{r_{\text{torus}} - r_{\text{out,torus}}}{r_{\text{torus}} + r_{\text{out,torus}}}\right) - \pi/2 + \theta_c\right) \\ &\left. - L_{\text{shoulder,link}} \cos\left(2\arcsin\left(\frac{r_{\text{torus}} - r_{\text{out,torus}}}{r_{\text{torus}} + r_{\text{out,torus}}}\right) - \pi/2 + \theta_c\right)\right) \end{aligned} \tag{C.8}$$

C.2. Structural Mass Model

Following the first step of this roadmap, the definition of the stacked toroid area is given in Equation C.9 to include only the area of the shell and disregard that of the nose cone, such that the aspect ratio of the IAD is given as $AR = \frac{A_{IAD}}{\pi r_{inflated}^2}$. The dimensionless parameters for the total toroid circumference $\bar{C}$, total surface toroid area $\bar{S}$ and total toroid volume $\bar{V}$ are also given in Equation C.10, Equation C.11 and Equation C.12 for the stacked-toroid configuration comprising of an outer smaller torus.

$$A_{IAD} = \pi(r_{inflated}^2 - r_N^2) \tag{C.9}$$

$$\bar{C} = \frac{\sum_{i=1}^{N} C_i}{2\pi r_{inflated}} = \frac{N + N\big(2r_{pay} + 4r_{out,torus}\sin(\theta_c)\big)}{2\big(2r_{pay} + 4r_{out,torus}\sin(\theta_c) + 2r_{torus}(2N\sin(\theta_c) - 2\sin(\theta_c) + 2)\big)} \tag{C.10}$$

$$\bar{S} = \frac{\sum_{i=1}^{N} S_i}{A_{\text{IAD}}} = \frac{4\,\pi\, 2r_{torus}\, N \left(\frac{2r_{torus}}{\sigma_1} + \frac{2r_{torus}\,\sin(\theta)\,(N-1)}{\sigma_1} - 1\right)}{\left(\left(\frac{2r_{torus}\,(\sin(\theta)\,(2\,N-1) - \cos(\theta)+1)}{\sigma_1} - 1\right)^2 - 1\right)\sigma_1} \tag{C.11}$$

$$\text{where} \quad \sigma_1 = 2r_{pay} + 4r_{out,torus}\sin(\theta_c) - 4r_{torus}(\sin(\theta_c) - 1) + 4r_{torus}N\sin(\theta_c))$$

$$\bar{V} = \frac{\sum_{i=1}^{N} V_i}{2r_{torus}A_{\text{IAD}}} = \frac{\bar{S}}{4} \tag{C.12}$$

Then, the dimensionless parameter for the material tensile yield σ_y is defined in Equation C.13 as a standard structural metric for the material that can be interpreted as the material breaking length. The characteristic length L_{ref} is included to attain closure in the nondimensional analysis. However, a value of unity is assumed by Samareh [105] to further simplify the problem. The magnitude of the chosen length does not affect the final solution of the analysis when the same value is consistently adopted.

$$\bar{\sigma_y} = \frac{\sigma_y}{\rho g_m L_{ref}} \tag{C.13}$$

Similarly to Equation C.13 a nondimensional metric is attained in Equation C.14 for the inflation gas. The temperature T and molar mass M_w in the expression refer to the properties of the inflation gas used in the IAD.

$$\bar{G} = \frac{g_m L_{ref}}{\frac{R}{M_w}T} \tag{C.14}$$

To compute the length of the radial straps, which start at the front of the heat shield, run through the shell and loop around the top toroid to attach back to the heat shield, a modification to Samareh's approximation is hereby proposed which includes the presence of the outer torus of smaller diameter for $r_{\text{out,torus}} \neq 0$. A schematic of the strap configuration is shown in Figure C.1 to differentiate between the structural elements accounted in the model.

$$\bar{L}_r = \frac{2r_{torus}\,(2\,N + \pi - 2)}{2r_{pay} + 4\,r_{out,torus}\,\sin(\theta_c) - 4r_{torus}\,(\sin(\theta_c) - 1) + 4r_{torus}\,N\,\sin(\theta_c)} \tag{C.15}$$

Figure C.1.: Isometric view of the strap configuration of an inflated stacked-toroid [36] (left) and bottom-view of straps [37] (right)

The area of the gores, equivalent to that of the tension shell, includes the conical section and the upper portion of the last torus. The nondimensionalised term for the gore area is expressed in Equation C.16, where the presence of the outer torus is also included.

$$\bar{A}_{\text{gores}} = \frac{1}{\sin(\theta_c)} + \frac{\pi\,4r_{torus}\left(\frac{2r_{torus}}{\sigma_2} - 1\right)}{\left(\left(\frac{2r_{torus}\,(\sin(\theta_c)\,(2\,N-1)-\cos(\theta_c)+1)}{\sigma_2} - 1\right)^2 - 1\right)\sigma_2} \tag{C.16}$$

where $\sigma_2 = 2r_{pay} + 4\,r_{out,torus}\,\sin(\theta_c) - 4r_{torus}\,(\sin(\theta_c) - 1) + 4r_{torus}\,N\,\sin(\theta_c)$

In this work, the calculation of the minimum inflation pressure is also expanded from Samareh's method [105] such that the stacked toroid configuration with the smaller outer torus is included. This is done by first defining the slanted height of the aeroshell h_{shell} as shown in Equation C.17 with the complete form of the inflated radius in Equation 3.3:

$$h_{shell} = \frac{r_{inflated}}{\sin(\theta_c)} \tag{C.17}$$

This serves the purpose of rewriting the gas volume expression in Equation C.18 without the inflated radius term. The volume approximates the internal bladders as a volume of rotation of a cylindrical section with height h_{shell} and radius r_{torus}.

$$V = 2\pi h_{shell} \cdot r_{inflated} \cdot r_{torus} = 2\pi h_{shell}^2 \cdot r_{torus}\sin(\theta_c) \tag{C.18}$$

The minimum internal pressure required to sustain the inflation of the stacked toroids is therefore estimated following Brown's approach [302] in Equation C.19 as a result of the volume change dV due to the structural displacement δ_s caused by the aerodynamic drag force D. The definition of the displacement for the stacked toroid is given in Equation C.20.

$$Dd\delta_s = -p_{min}dV \rightarrow p_{min} = -D\frac{d\delta_s}{d\theta_c}\frac{d\theta_c}{dV} \tag{C.19}$$

$$\delta_s = \frac{2}{3}h_{shell}\cos(\theta_c) = \frac{2r_{inflated}}{3\tan(\theta_c)} \tag{C.20}$$

By inspection of Equation C.19, the changes in volume and displacement have to be calculated from the corresponding expressions in Equation C.18 and Equation C.20. Their derivative with respect to the half-cone angle θ_c is calculated in Equation C.21 and Equation C.22. The author also notes a sign error in the original differential form of $d\delta_s$ in [105] which is hereby corrected.

$$\frac{dV}{d\theta_c} = 2\pi h_{shell}^2 r_{torus}\cos(\theta_c) = -\frac{4\pi r_{inflated} r_{torus}\cos(\theta_c)}{4\sin(\theta_c)^2} \tag{C.21}$$

$$\frac{d\delta_s}{d\theta_c} = \frac{2}{3}r_{inflated} \tag{C.22}$$

Finally, Equation C.21 and Equation C.22 are substituted in Equation C.19 to compute the minimum pressure, as shown in Equation C.23 [105].

$$p_{min} = \frac{D\sin(\theta_c)^2}{3r_{inflated}r_{torus}\pi\cos(\theta_c)} \tag{C.23}$$

Equation C.23 can then be rewritten in a non-dimensional form in Equation C.24, where C_D is the drag coefficient of the IAD.

$$\bar{p}_{min} = \frac{p_{min}}{qC_D} \tag{C.24}$$

The mass of the inflation gas is evaluated from Equation C.25 by employing the ideal gas law previously defined in Equation 3.1, the dimensionless gas parameter in Equation C.14, the nondimensional volume in Equation C.12 and the minimum inflation pressure in Equation C.24. It is noted that the proportion of the inflation gas mass to the total mass is likely to be marginal, especially for designs with a low number of tori and a small internal tori diameter. Nevertheless, its influence is included for completeness.

$$\bar{m}_{\text{gas}} = \left(\bar{p}_{\text{min}} + \frac{p_\infty}{qC_D}\right)\frac{2\bar{G}\cdot\bar{V}\cdot r_{torus}\cdot\eta_g}{r_{pay} + 2r_{out,torus}\sin(\theta_c) - 2r_{torus}(\sin(\theta_c)-1) + 2r_{torus}N\sin(\theta_c)} \tag{C.25}$$

Equation C.25 also includes a growth allowance parameter η_g to account for the presence of potential leaks and ullage. While the selection of the parameter depends on the type of inflation system in conjunction with the amount of gas required [303], a value of $\eta_g = 1.25$ is assumed by Samareh [105] for a 25% margin.

The fiber mass is estimated with the Brown and Sharpless [304] braided airbeam concept comprising a gas barrier, a fibre-reinforced fabric and axial straps. The calculation in Equation C.26

relates the fiber mass to the braided fiber bias angle β_{fiber}, assumed to be at 75° [105] for the braided fiber-reinforced fabric, the nondimensional yield parameter $\bar{\sigma_y}$ in Equation C.13, the minimum inflation pressure in Equation C.24, the toroid surface area in Equation C.11 and to the dimensionless geometry parameter η_{fiber} assumed to equal 4 [105].

$$\bar{m}_{fiber} = \frac{1}{\bar{\sigma_y}} \cdot \frac{r_{torus} \cdot \eta_{fiber} \cdot \bar{p}_{min} \cdot \bar{S} \left(1 + \frac{1}{\tan(\beta_{fiber})^2}\right)}{2r_{pay} + 4r_{out,torus}\sin(\theta_c) - 4r_{torus}(\sin(\theta_c) - 1) + 4r_{torus}N\sin(\theta_c)} \tag{C.26}$$

The dimensionless mass parameter of the axial straps is expressed in Equation C.27 by setting the straps' stiffness equal to the in-plane and out-of-plane buckling they are expected to resist. The terms in Equation C.27 are similar to those used for Equation C.26, including the presence of a nondimensional parameter η_{axial} assumed to be equal to 4.

$$\bar{m}_{axial} = \frac{1}{\bar{\sigma}} \cdot \frac{\bar{p}_{min} \cdot \bar{S} \cdot r_{torus} \cdot \eta_{axial}}{2r_{pay} + 4r_{out,torus}\sin(\theta_c) - 4r_{torus}(\sin(\theta_c) - 1) + 4r_{torus}N\sin(\theta_c)} \tag{C.27}$$

The dimensionless parameter for the mass of the coated fabric and film is given in Equation C.28, obtained with linear analysis which was shown by Sanders and Liepins [305] to be very close to the results obtained with nonlinear membrane theory. As for the axial and fiber components, the term η_{torus} is set equal to 4.

$$\begin{aligned} \bar{m}_{torus} &= \frac{1}{\bar{\sigma}} \frac{\bar{p}_{min} \cdot \bar{S} \cdot \eta_{torus} \left(\frac{6r_{torus}}{\sigma_3} - 2\right)}{\sigma_3 \left(\frac{8r_{torus}(\sin(\theta_c)(2N-1) - cos(\theta_c)+1)}{\sigma_3} - 4\right)} \\ \text{where} \quad \sigma_3 &= 2r_{pay} + 4r_{out,torus}\sin(\theta_c) - 4r_{torus}(\sin(\theta_c) - 1) + 4r_{torus}N\sin(\theta_c) \end{aligned} \tag{C.28}$$

The mass of the radial straps, which are constructed to carry the aerodynamic load experienced by the IAD besides connecting the heat shield to the shell of the stacked toroid, can be nondimensionalised in Equation C.29 by assuming that the tension in the straps is statically solved with the corresponding component of drag at the angle θ_c. The parameter η_{radial} is again set equal to 4 [105].

$$\bar{m}_{radial} = \frac{1}{\bar{\sigma_y}} \frac{\bar{L}_r}{\cos(\theta_c)} \frac{2r_{inflated}}{L_{ref}} \eta_{radial} \tag{C.29}$$

Finally, the gores' mass is calculated in Equation C.30 as a function of nondimensional sigma in Equation C.13, the gores area in Equation C.16, the number of radial straps I and the maximum material strain ϵ_e. A margin is also included $\eta_{gores} = 4$.

$$\bar{m}_{gores} = \frac{1}{\bar{\sigma_y}} \bar{A}_{gores} \frac{2r_{inflated}}{L_{ref}} \eta_{gores} \frac{\pi}{I} \left(\frac{4\epsilon_e^2 + 1}{8\epsilon_e}\right) \eta_{gores} \tag{C.30}$$

C.3. Modified Newtonian Method

When the method is applied to a flat plate inclined at an angle θ to the horizontal, the volumetric flow rate within the control volume can be computed using the normal velocity component and set equal to the rate of change of momentum, giving rise to the surface pressure relation in Equation C.31, which can be used to compute the pressure coefficient C_p and the aerodynamic coefficients C_D and C_L in Equation C.32. On the contrary, the shear stress coefficient is always regarded as being equal to zero for this method as in Equation C.33.

$$p = \rho_\infty V_\infty^2 \sin^2(\theta) + p_\infty \tag{C.31}$$

$$\begin{aligned} C_p &= \frac{p - p_\infty}{q_\infty} = 2\sin^2(\theta) \\ C_D &= C_p \sin(\theta) = 2\sin^3(\theta) \\ C_L &= C_p \cos(\theta) = 2\sin^2(\theta)\cos(\theta) \end{aligned} \tag{C.32}$$

$$C_\tau = 0 \tag{C.33}$$

While Equation C.32 represents the standard Newtonian method, a modified version may be implemented by relating the pressure coefficient to its equivalent value at the stagnation pressure $C_{p,max}$ [165], as in Equation 3.48. In a hypersonic flow, the pressure coefficient at the stagnation point behind a shockwave p_{02} can be calculated by considering that the local surface inclination is $\theta = 90°$, resulting in $\sin(\theta) = 1$ and thus $p_{02} = \rho V_\infty^2 + p_\infty$ from Equation C.31. $C_{p,max}$ can therefore be computed from Equation 3.48 as shown in Equation C.34:

$$C_{p,max} = \frac{p_{02} - p_\infty}{q_\infty} \tag{C.34}$$

Equation C.34 can further be modified using the Rankine-Hufoniot relation [165] in Equation C.35 to compute the ratio of stagnation pressure on the vehicle's surface to the freestream pressure, assuming the presence of a sufficiently large Mach cone in front of the body that may be treated as a normal shock [160].

$$\frac{p_{02}}{p_\infty} = \left[\frac{(\gamma+1)^2 M_\infty^2}{4\gamma M_\infty^2 - 2(\gamma-1)}\right]^{\frac{\gamma}{\gamma-1}} \left[\frac{1-\gamma+2\gamma M_\infty^2}{\gamma+1}\right] \tag{C.35}$$

By substituting Equation C.35 into Equation C.34 using $q_\infty = \frac{\gamma}{2} p_\infty M_\infty^2$, Equation 3.49 is obtained, which can finally be used in Equation 3.48 to obtain the modified Newtonian model. The aerodynamic coefficients can be obtained analogously to Equation C.32 where the new pressure distribution in Equation 3.49 is computed by combining Equation 3.48 with Equation 3.49.

$$C_{p,max} = \frac{2}{\gamma M_\infty^2}\left[\frac{p_{02}}{p_\infty} - 1\right] \tag{C.36}$$

C.4. Fay-Riddell Convective Stagnation Heat Flux

The density at the wall and at the stagnation point can be calculated as in Equation C.37 [165], where T_w is the wall temperature, T_{0s} the total stagnation temperature as defined in Equation C.38, and p_{02} is the stagnation pressure from the Rankine-Hufoniot relation in Equation C.35.

$$\rho_s = \frac{p_{02}}{RT_{0s}} \qquad\qquad \rho_w = \frac{p_{02}}{RT_w} \tag{C.37}$$

$$\frac{T_{0s}}{T_\infty} = \left(1 + \frac{(\gamma - 1)M_\infty^2}{2}\right) \tag{C.38}$$

The viscosity at the wall μ_w can be computed from Sutherland's expression in Equation 3.19 with the usage of T_w, whereas the viscosity at the stagnation point μ_s requires the application of T_{0s} in Equation C.38 as opposed to T_w for the same viscosity model in Equation 3.19. At the same time, the enthalpy at the stagnation conditions h_s and at the wall h_w can be computed according to Equation C.39 from the second law of thermodynamics. The h_D term in Equation 3.81 refers to the dissociation enthalpy, which is a quantity specific to the gas investigated.

$$h_s = c_p T_{0s} \qquad\qquad h_w = c_p T_w \tag{C.39}$$

The velocity gradient at the stagnation point $\left(\frac{du}{dy}\right)_s$, in both Equation 3.81 and Equation 3.82, can be defined from the modified Newtonian theory as in Equation C.40 which has shown to yield the best agreement with numerical and experimental results [306].

$$\left(\frac{du}{dy}\right)_s = \frac{1}{r_N}\sqrt{\frac{2(p_{02} - p_\infty)}{\rho_s}} \tag{C.40}$$